SYNTHESIS, STRUCTURE AND PROPERTIES OF SELECTED LITHIATED TRANSITION METAL OXIDES

By

ISOBEL JEAN DAVIDSON, B.Sc., M.Sc.

A Thesis

Submitted to the School of Graduate Studies

in Partial Fulfillment of the Requirements

for the Degree

Doctor of Philosophy

McMaster University

PROPERTIES OF SELECTED

LITHIATED TRANSITION METAL OXIDES

DOCTOR OF PHILOSOPHY (1997)
(Chemistry)

MCMASTER UNIVERSITY
Hamilton, Ontario

TITLE: Synthesis, Structure and Properties of Selected Lithiated Transition Metal Oxides

AUTHOR: Isobel Jean Davidson, B.Sc., M.Sc. (McMaster University)

SUPERVISOR: Professor John E. Greedan

NUMBER OF PAGES: xvii, 238

Abstract

This thesis discloses a newly discovered series of compounds, $Li_2Cr_yMn_{2-y}O_4$, wherein $0.1 \leq y \leq 1.9$. This series consists of two solid solutions regions with a cross-over occurring at a composition near $y = 1.4$. The chemical structure of these phases was identified by x-ray powder diffraction. Phases with $y \geq 1.4$ have an ordered rock salt structure in which the lithium and transition metal cations form alternating layers between the sheets of oxygen atoms. The phases with $y < 1.4$ have a different rock salt related structure in which the lithium ions and transition metal ions are arranged in interleaving chains within the cubic-close-packed oxygen framework. The resulting structures are distorted from cubic symmetry by the presence of the Jahn-Teller ion, Mn^{3+}. The compositions with $y < 1.65$ were found to be particularly useful as cathodes in lithium ion type, electrochemical cells.

The chemical and ordered magnetic structure of three materials, orthorhombic $LiMnO_2$, 1T-Li_2NiO_2 and a low temperature form of $LiFeO_2$ were determined from neutron diffraction data. LT-$LiFeO_2$ and 1T-Li_2NiO_2 are metastable phases prepared by *chimie douce* synthetic methods. A detailed study of the magnetic properties of 1T-Li_2NiO_2 and orthorhombic $LiMnO_2$ revealed complex behaviour involving a competition between two- and three-

dimensional ordering. Neutron diffaction was also employed to identify the chemical structure of Li_2NiMnO_4.

The electrochemical behaviour of orthorhombic $LiMnO_2$, LT-$LiFeO_2$, Li_2NiMnO_4 and $Li_2Ni_{1.5}Mn_{0.5}O_4$ was investigated in lithium ion cells. Orthorhombic $LiMnO_2$ proved to be particularly useful as a cathode material as it undergoes a phase transition *in situ* to the lithiated spinel phase λ-$Li_2Mn_2O_4$. Consequently, orthorhombic $LiMnO_2$ provides a convenient, air stable precursor to the electrochemically useful, but not air stable, λ-$Li_2Mn_2O_4$ phase.

Acknowledgments

It is my great pleasure to acknowledge the contribution of my supervisor. Dr. John Greedan. to the completion of this thesis. His scientific advice. constant encouragement. and enormous patience were essential to the successful completion of this work. The scientific. practical and emotional support provided by my supervisor at the National Research Council, Dr. John Murray. deserves equal credit. His unwavering support for this project through numerous corporate upheavals. and continuing faith that it would be successfully completed were indispensable.

Dr. Jeff Dahn is to be thanked for many helpful discussions. and jointly with C. A. Michal and Dr. Ulrich von Sacken. for the sample of 1T-Li_2NiO_2. I would also like to thank Dr. C. V. Stager and Dr. W. R. Mc Kinnon for access to their SQUID magnetometers. The transmission electron microscopy study on $LiFeO_2$ by Dr. Jacques Barbier is greatly appreciated. The scientific and technical staff of the Brockhouse Institute for Materials Science provided assistance in obtaining the Guinier photographs on $Li_2Cr_yMn_{2-y}O_4$ and the some of neutron data used in this thesis. I am very grateful for all their assistance.

My colleagues at the NRC have been generous with both their time and resources. Drs. Yvon Le Page and Eric Gabe were a vital source of aid in understanding the crystallographic data. My co-workers in the NRC lithium ion battery project helped in the assembly and testing of electrochemical cells.

Drs. John Murray, and Rod McMillan designed and built the electrochemical cell assembly and cycling equipment used for this project. They, along with Dr. ZhiXin Shu, also provided helpful discussions on the interpretation of electrochemical results. Dr. Shu also helped in the electrochemical study of $LiMnO_2$ versus metallic lithium. Ms. Helen Slegr provided a broad range of technical support to the electrochemical studies. I am also very grateful for the moral support and encouragement provided by my NRC colleagues.

Table of Contents

Chapter			Page
1	Introduction		1
	1.1	Applications	1
	1.2	Chemical Structures	3
	1.3	Magnetic Structures and Properties	9
2	Methods and Theory		11
	2.1	Chemical Synthesis	11
	2.2	Structure Determination	14
		2.2.1 Introduction	14
		2.2.2 Diffraction Theory	15
		2.2.3 Neutron Diffraction	28
		2.2.4 Structure Refinement	33
	2.3	Magnetic Properties	34
	2.4	Electrochemical Evaluation	42
3	Chemical Synthesis of Phases		50
	3.1	3R - $LiCrO_2$	50
	3.2	Orthorhombic - $LiMnO_2$	51
	3.3	$LiFeO_2$	56

Chapter			Page
	3.4	3R - $LiNiO_2$	59
	3.5	1T - Li_2NiO_2	59
	3.6	$Li_2Ni_yMn_{2-y}O_4$	60
	3.7	$Li_2Cr_yMn_{2-y}O_4$	67
4	Chemical Structures		73
	4.1	Orthorhombic - $LiMnO_2$	73
	4.2	$LiFeO_2$	77
	4.3	1T -Li_2NiO_2	88
	4.4	Li_2NiMnO_4	93
	4.5	$Li_2Cr_yMn_{2-y}O_4$	99
5	Magnetic Structures and Properties		116
	5.1	Orthorhombic - $LiMnO_2$	116
	5.2	$LiFeO_2$	128
	5.3	1T - Li_2NiO_2	138
6	Electrochemistry		152
	6.1	Orthorhombic - $LiMnO_2$	152
	6.2	$LiFeO_2$	174
	6.3	$Li_2Ni_yMn_{2-y}O_4$	175
	6.4	$Li_2Cr_yMn_{2-y}O_4$	182

Chapter			Page
7	Discussion		203
	7.1	Orthorhombic - $LiMnO_2$	203
	7.2	$LiFeO_2$	210
	7.3	1T -Li_2NiO_2	215
	7.4	$Li_2Ni_yMn_{2-y}O_4$	217
	7.5	$Li_2Cr_yMn_{2-y}O_4$	224
8	Conclusions		228
	Bibliography		234

List of Figures

Figure		Page
1.2.1	Comparison of ideal 3R structure and NaCl structure	5
1.2.2	Illustration of the lithiated spinel structure	7
2.2.1	Illustration of Bragg reflection from a family of planes	16
2.2.2	Illustration of Laue condition for constructive interference	17
2.2.3	Illustration of equivalence of the Bragg and Laue conditions	20
2.2.4	Phase difference between scattering from two lattice points	24
2.2.5	Phase difference between rays scattered from different points in the electronic charge	26
2.2.6	Comparison of neutron and x-ray scattering amplitudes	30
2.4.1	Typical voltage curve versus lithium for a carbon coke anode	45
2.4.2	Exploded view of coin cell assembly with spring and spacers	46
3.1.1	X-ray diffraction pattern of $LiCrO_2$	51
3.2.1	X-ray diffraction pattern of orthorhombic $LiMnO_2$	54
3.2.2	Diffraction pattern of same sample of $LiMnO_2$ after 11 months	55
3.3.1	Comparison of x-ray diffraction patterns of $LiFeO_2$ and $LiNiO_2$	58
3.6.1	Diffraction pattern of Li_2NiMnO_4 prepared at 1000°C	61
3.6.2	Diffraction pattern of Li_2NiMnO_4 prepared at 800°C	62
3.6.3	X-ray diffraction pattern of $Li_2Ni_{1.5}Mn_{0.5}O_4$	63
3.6.4	Comparison of diffraction peak intensities for $Li_2Ni_yMn_{2-y}O_4$ phases	64

Figure		Page
3.6.5	Changes in $Li_2Ni_{1.5}Mn_{0.5}O_4$ with annealing temperature	64
3.6.6	Diffraction pattern from a 2:3 mixture of $LiNiO_2$ and $LiMnO_2$	66
3.6.7	Diffraction pattern from a 1:3 mixture of $LiNiO_2$ and $LiMnO_2$	66
3.7.1	X-ray diffraction patterns for two samples of Li_2CrMnO_4	68
3.7.2	X-ray diffraction pattern of $Li_2Cr_{1.5}Mn_{0.5}O_4$	70
3.7.3	X-ray diffraction pattern of $Li_2Cr_{0.5}Mn_{1.5}O_4$	72
4.1.1	Refinement of neutron diffraction data for $LiMnO_2$	74
4.2.1	Room temperature neutron diffraction pattern of $LiFeO_2$	79
4.2.2	Hexagonal model refinement of neutron data for $LiFeO_2$	80
4.2.3	Cubic model refinement of neutron data for $LiFeO_2$	81
4.2.4	X-ray diffraction patterns demonstrating preferred orientation in $LiFeO_2$	87
4.3.1	Refinement of neutron diffraction data for 1T-Li_2NiO_2	91
4.4.1	Refinement of neutron data for Li_2NiMnO_4 (sample A)	95
4.4.2	Refinement of neutron data for Li_2NiMnO_4 (sample B)	97
4.5.1	Normalized volume versus composition for $Li_2Cr_yMn_{2-y}O_4$ phases	101
4.5.2	Diffraction patterns for $Li_2Cr_yMn_{2-y}O_4$ phases with the 3R structure	102
4.5.3	Diffraction patterns for $Li_2Cr_yMn_{2-y}O_4$ phases with the lithiated spinel structure	103

Figure		Page
4.5.4	Modeling of $Li_2Cr_{1.25}Mn_{0.75}O_4$ to lithiated spinel structure	107
4.5.5	Modeling of Li_2CrMnO_4 to lithiated spinel structure	108
4.5.6	Modeling of $Li_2Cr_{0.5}Mn_{1.5}O_4$ to lithiated spinel structure	109
4.5.7	Modeling of $Li_2Cr_{0.1}Mn_{1.9}O_4$ to lithiated spinel structure	110
4.5.8	Detailed view of diffraction patterns from 30 - 70 degrees	111
4.5.9	Plot of Jahn-Teller ratios versus composition	112
4.5.10	Plot of crystallographic and measured densities for $Li_2Cr_yMn_{2-y}O_4$ phases	115
5.1.1	Illustration of magnetic structure model for orthorhombic $LiMnO_2$	119
5.1.2	Refinement of 12 K neutron data for orthorhombic $LiMnO_2$	120
5.1.3	Magnetic susceptibility of $LiMnO_2$ at an applied field of 10^{-2} T	124
5.1.4	Plot of the inverse of the susceptibility of $LiMnO_2$	125
5.1.5	Plot of peak intensity versus temperature for the (1/2 1/2 1/2) and (1/2 1/2 3/2) reflections	126
5.1.6	Neutron diffraction pattern of $LiMnO_2$ at 271 K and inset showing fit of low angle feature of Warren function	127
5.2.1	Neutron diffraction patterns for $LiFeO_2$ from 10 K to 290 K	130
5.2.2	Comparison between neutron diffraction patterns for $LiFeO_2$ at 10 K and 290 K.	131
5.2.3	Plot of the square root of the intensity of the strongest magnetic reflection versus temperature	132

Figure		Page
5.2.4	Neutron diffraction pattern of $LiFeO_2$ at 10 K over a broader angular range	133
5.2.5	Rietveld refinement of 10 K neutron data for $LiFeO_2$	136
5.3.1	Neutron diffraction patterns for 1T-Li_2NiO_2 from 10 to 65 K	140
5.3.2	$11\bar{2}0$ projection of magnetic crystallographic unit cell	141
5.3.3	Rietveld refinement fit of 10 k neutron diffraction data with the spin perpendicular to the c-axis for 1T-Li_2NiO_2	143
5.3.4	Rietveld refinement fit of 10 K neutron diffraction data with the spin parallel to the c-axis for 1T-Li_2NiO_2	144
5.3.5	Magnetization divided by the applied field versus temperature for applied fields of 0.01 T and 1.0 T for 1T-Li_2NiO_2	148
5.3.6	Magnetic moment data for 1T-Li_2NiO_2 as a function of temperature versus applied field to 2.0 T	149
5.3.7	Magnetic moment data for 1T-Li_2NiO_2 as a function of temperature versus applied field to 5.0 T	150
5.3.8	Magnetic moment data for 1T-Li_2NiO_2 replotted versus temperature for various applied fields	151
6.1.1	X-ray diffraction pattern of $LiMnO_2$ cathode from cell at 3.04 V	153
6.1.2	X-ray diffraction pattern of $LIMnO_2$ cathode from cell charged to 3.8 V.	154
6.1.3	First five cycles of a coke/$LiMnO_2$ cell cycled to progressively higher voltage limits	156

Figure		Page
6.1.4	First five charge/discharge cycles of a coke/$LiMnO_2$ cell cycled between voltage limits of 1.5 and 4.0 V	157
6.1.5	Charge and discharge capacities as function of cycle number for a coke/$LiMnO_2$ coin cell	160
6.1.6	First cycle voltage profiles for Li/$LiMnO_2$ cells cycled at different rates	162
6.1.7	Voltage profiles of a Li/$LiMnO_2$ cell cycled to progressively higher charge limits	164
6.1.8	Derivative plot of cycling curve for a Li/$LiMnO_2$ cell conditioned by cycling over upper plateau only before cycling to 2.9 V	165
6.1.9	Derivative plot of cycling curve for a Li/$LiMnO_2$ cell conditioned by cycling lower plateau only before cycling to 4.3 V	166
6.1.10	Voltage profiles for a Li/$LiMnO_2$ cell cycled between 1.0 and 4.2 volts at various rates	170
6.3.1	Voltage profile of the first charge and discharge of a coke/Li_2NiMnO_4 coin cell	178
6.3.2	Comparative plot of the first cycle voltage profile for a typical coke/$LiCoO_2$ coin cell	179
6.3.3	Voltage profile of the third cycle of a coke/Li_2NiMnO_4 coin cell	180
6.3.4	Comparison of resistivity between cathodes based on $Li_2Ni_yMn_{2-y}O_4$ phases and those based on $LiCoO_2$ or $LiNiO_2$	181
6.4.1	Voltage profile of a coke/$Li_2Cr_{1.5}Mn_{0.5}O_4$ coin cell	185
6.4.2	Voltage profile of a coke/Li_2CrMnO_4 coin cell	188

Figure		Page
6.4.3	Voltage profile of a coke/$Li_2Cr_{0.5}Mn_{1.5}O_4$ coin cell	191
6.4.4	Voltage profiles of the fifth charge/discharge cycle for coin cells with $Li_2Cr_yMn_{2-y}O_4$ cathodes and coke anodes	192
6.4.5	Comparison of charge and discharge cathode utilization in lithium ion cells cycled between 1.5 and 4.0 V at 100 hour rate	193
6.4.6	Charge and discharge capacities as a function of cycle number for a coke/$Li_2Cr_{1.5}Mn_{0.5}O_4$ coin cell	194
6.4.7	Charge and discharge capacities as a function of cycle number for a coke/$Li_2Cr_{0.5}Mn_{1.5}O_4$ coin cell	195
6.4.8	Voltage profile for the 4^{th} cycle of a Li/$Li_2Cr_{1.5}Mn_{0.5}O_4$ cell	199
6.4.9	Voltage profile for the 4^{th} cycle of a Li/Li_2CrMnO_4 cell	200
6.4.10	Voltage profile for the 12^{th} cycle of a Li/$Li_2Cr_{0.5}Mn_{1.5}O_4$ cell	201
6.4.11	Voltage profile for the 12^{th} cycle of a Li/$Li_2Cr_{0.1}Mn_{1.9}O_4$ cell	202
7.1.1	Hexagonal view of orthorhombic $LiMnO_2$ structure	207
7.1.2	Linear chain view of orthorhombic $LiMnO_2$ structure	208

List of Tables

Table		Page
4.1.1	Rietveld refinement of room temperature neutron diffraction data for $LiMnO_2$	75
4.1.2	Bond lengths and angles in orthorhombic $LiMnO_2$	76
4.2.1	Rietveld refinement of neutron data using 3R model	82
4.2.2	Rietveld refinement of neutron data using 3R model with cation occupancy refined	83
4.2.3	Rietveld refinement of neutron data using spinel related model	84
4.2.4	Rietveld refinement of neutron data using spinel related model with cation occupancy refined	85
4.3.1	Rietveld refinement of room temperature neutron diffraction data for Li_2NiO_2	92
4.4.1	Rietveld refinement of room temperature neutron diffraction data for Li_2NiMnO_4 (sample A)	96
4.4.2	Rietveld refinement of room temperature neutron diffraction data for Li_2NiMnO_4 (sample B)	98
4.5.1	Tabulation of normalized crystallographic cell volumes	100
4.5.2	Jahn-Teller ratios in $Li_2Cr_yMn_{2-y}O_4$ phases	113
4.5.3	Crystallographic and measured densities of $Li_2Cr_yMn_{2-y}O_4$ phases	114
5.1.1	Rietveld refinement of 12 K neutron diffraction data for $LiMnO_2$ with spins aligned parallel to the b-axis	121

Table		Page
5.2.1	Rietveld refinement of 10 K neutron diffraction data for $LiFeO_2$ with spins aligned perpendicular to the c-axis	137
5.3.1	Rietveld refinement of 10 K neutron diffraction data for Li_2NiO_2 with spins aligned parallel to the c-axis	145
6.1.1	Charge and discharge capacities of Li/$LiMnO_2$ cells cycled at different rates and voltage limits in a variety of electrolytes	169
6.1.2	X-ray diffraction data for cathodes extracted from cycled coin cells after charging to 4.2 volts and after discharging to 1.0 volts	173
7.4.1	Comparison of bond lengths in "Li_2NiMnO_4' to related phases	221
7.4.2	Comparison of transition metal bonding in "$Li_2Ni_yMn_{2-y}O_4$" phases	223

Chapter 1

Introduction

1.1 Applications

Lithiated transition metal oxides in which the lithium atoms are labile and the transition metal has accessible higher oxidation states have been investigated extensively for use as cathodes or anodes in rechargeable lithium ion batteries. Materials used in this way are said to intercalate lithium. Intercalation is a topochemical reaction in which the insertion of a "guest" species into a "host" lattice is accompanied by only minimal changes in the host structure (Thomas 1974). In the ideal case of no change in the host structure, the transition states of the forward and reverse reaction are similar and consequently, the reaction is reversible. When the intercalation reaction is of the redox type, the compound may be useful as an electrode in a secondary (i.e. rechargeable) electrochemical cell.

A secondary lithium ion cell has lithium intercalation compounds for both the cathode and the anode. The intercalation material, used for the anode, is strongly reducing while the cathode material is a highly oxidizing compound. The electrochemical potential of the cell is realized by exchange of lithium ions from the anode to the cathode via an electrolyte which contains a lithium salt. The greater the difference in the free energy of lithium ions in the cathode from that

in the anode, the greater the electrochemical potential of the cell. The cell is recharged by applying a voltage from an external circuit which reverses the reaction, shifting lithium ions from the cathode to the anode. The recent commercial interest in lithium ion batteries stems from the realization that it is not possible to make a safe rechargeable battery containing metallic lithium. However, lithium, being the lightest of the very electropositive alkaline metals, is a uniquely attractive anode choice. To maintain many of the benefits of a metallic lithium anode while eliminating the hazards, interest has switched to forms of carbon, such as graphite, which reversibly intercalate one lithium atom per six carbon atoms at a potential only about 200 mV lower than metallic lithium.

Lithium ion cells are built in the discharged state with the cathode fully lithiated and the anode completely free of lithium. When the lithiated cathode material is at least 3 volts more oxidizing than metallic lithium, it is stable in ambient conditions, and then both electrode materials can be handled in air. This greatly facilitates the assembly of batteries and reduces the cost dramatically. Three such compounds, $LiNiO_2$, $LiCoO_2$ and $LiMn_2O_4$, have been seriously pursued for use in commercial products. However, the battery industry has a continuing interest in finding cheaper, and better performing electrode materials.

1.2 Chemical Structures

The essential requirements for a lithium compound to be a good cathode for a lithium ion cell are that it:

i) contain a component with accessible higher oxidation states,

ii) be highly oxidizing to provide a large cell voltage and air stability,

iii) have a wide range of composition with little change in free energy over the range to provide a large cell capacity,

iv) experience little structural change on reaction to comply with the reversibility requirement, and

v) have a high diffusivity to yield a high power density.

Other desirable properties (Murphy and Christian 1979) are good electrical conductivity and low solubility in the electrolyte to minimize resistive heat generation and to prevent self-discharge, respectively.

The materials most likely to fulfill these requirements are those in which the lithium atoms occupy layers or channels, have a high free energy of formation and an accessible and unfilled electronic band structure, and transition metal ions in their higher oxidation states (Whittingham 1978). The class of lithium intercalation compounds which have been studied the most intensely are the two-dimensional, van der Waals bonded structures such as the transition metal dichalcogenides (Murphy and Christian 1979) and dioxides (Reimers and Dahn 1992). In these materials the Van der Waals gap between the transition metal dichalcogenide layers, or the transition metal dioxide layers widens to

accommodate the lithium, thus providing enough vacant sites to permit a wide range of composition and to facilitate lithium ion diffusion. Many three-dimensional materials can reversibly intercalate lithium within channels in their structure. The best studied of these compounds include spinel-related manganese dioxide (Ohzuku, Kitagawa and Hirai 1989), and rutile-related transition metal dioxides (Davidson and Greedan 1984).

To be commercially practical, the cathode material should be light, and inexpensive. Consequently, a great deal of interest has focused on lithiated dioxides of the first row transition metals. The first lithium ion cells to be commercialized have cathodes based on $LiNiO_2$ and $LiCoO_2$ (Tarascon and Guyomard 1991). $LiNiO_2$ and $LiCoO_2$ both have a layered 3R structure, and are completely miscible (Delmas and Saadoune 1992). The ideal 3R structure is composed of cubic close-packed layers of oxygen which alternate with layers of transition metal and lithium atoms in the sequence O-TM-O-Li-O-TM-O-Li... . The lithium atoms occupy octahedral interstices between the more broadly spaced oxygen layers, while the transition metal atoms fill octahedral sites between the alternate, more closely spaced, oxygen layers (figure 1.2.1). The 3R structure belongs to the space group R-3m (D^5_{3d}). The transition metal atom occupies the 3a site at (0,0,0), the lithium, the 3b site at (0,0.1/2), and oxygen atoms, the 6c site at (0,0,z) with $z > 0.25$. The 3R structure is related to the rock salt, or NaCl, structure by ordering of the lithium and transition metal cations into separate layers normal to the body diagonal of the NaCl unit cell. This ordering

reduces the symmetry from cubic to rhombohedral. The hexagonal axis setting, as in figure 1.2.1, is more commonly used for illustrative purposes.

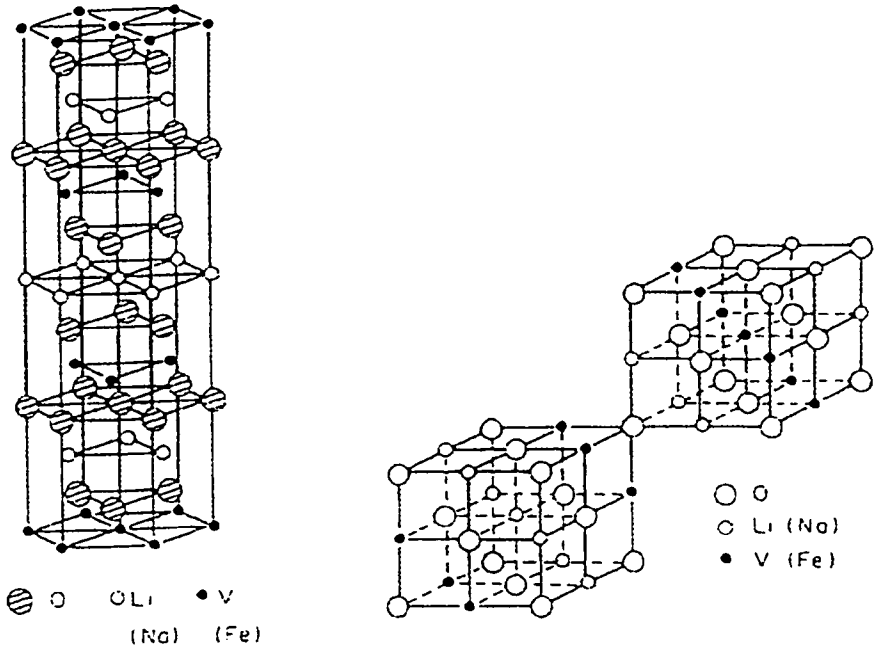

Figure 1.2.1 - Comparison of ideal 3R structure and NaCl stucture (from Wells 1975)

$LiCoO_2$, $LiCrO_2$, $LiVO_2$, and $LiNiO_2$ all have phases with the 3R structures although in the case of $LiNiO_2$ samples are generally slightly low in lithium content and there is significant disorder between the lithium and nickel atoms (Pickering, Lewandowski, Jacobson and Goldstone 1992). Solution phases of $LiNiO_2$ and $LiCoO_2$, $LiNi_{1-y}Co_yO_2$ can be prepared over the range $0 < y < 1$ in the 3R structure (Delmas and Saadoune 1992). Solution phases offer the

possibility of tuning the properties of lithiated transition metal oxides to better suit their application as high energy cathodes.

Compounds belonging to a new series of solid solution phases, $Li_2Cr_yMn_{2-y}O_4$, have been prepared. The methods of synthesis and the results of structural studies for these phases and phases in the series $Li_2Mn_yNi_{2-y}O_4$ will be presented.

An excellent review on the structures of lithiated first-row ternary oxides was written by Hewston and Chamberland (1987). $LiMnO_2$ occurs in at least three structures: an orthorhombic form first reported by Johnston and Heikes in 1956, a tetragonal form prepared by chemical or electrochemical lithiation of the spinel $LiMn_2O_4$ (Mosbah, Veraere and Tournoux 1983), and a high-pressure form with a statistical rock-salt structure (Hewston and Chamberland 1987). The tetragonal form, sometimes written λ-$LiMnO_2$ or λ-$Li_2Mn_2O_4$, has a structure similar to the atacamite structure. $Li_2Ti_2O_4$ and a high pressure form of $Li_2V_2O_4$ are known to also have this structure, in which the lithium and transition metal ions are segregated into the 16c and 16d octahedral sites of the Fd3m space group (figure 1.2.2). The larger spheres in the figure represent the oxygen atoms, and the lithium and transition metal atoms are represented by the small dashed and solid line spheres, respectively. It is a cubic-close-packed structure containing interleaved chains of lithium and transition metal octahedra. This structure can also be viewed as a rock salt structure with ordered cations. λ-$Li_2Mn_2O_4$ deviates from the ideal cubic symmetry to tetragonal as a result of a

cooperative Jahn-Teller distortion caused by the Mn^{3+} ions. Structure refinements from ambient and low temperature neutron diffraction data on the orthorhombic form of $LiMnO_2$ were conducted for this work.

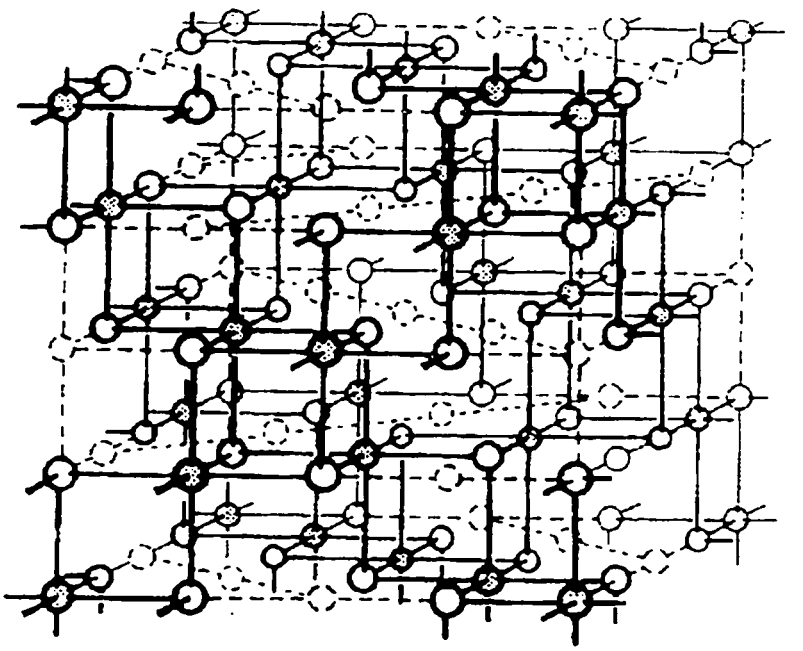

Figure 1.2.2 - Illustration of the lithiated spinel structure (from Wells 1975)

Three polymorphs are known for $LiFeO_2$. One, termed the α-form, has a disordered cubic NaCl-type structure (Anderson and Schieber 1964). Above 300 $^{\circ}C$ α-$LiFeO_2$ converts to a monoclinic β-form (Famery, Bassoul and Queyroux 1985) of symmetry C2/c. The β-form converts to an ordered, tetragonal γ-form which is isostructural with $LiScO_2$ (Wyckoff 1964) above 500 $^{\circ}C$. The

preparation, structure and properties of a fourth polymorph of $LiFeO_2$ will be presented in this report.

Although some lithiated transition metal dioxides have been prepared as single crystals, these materials are more easily prepared and studied in the form of polycrystalline powders. Their structures are determined by powder diffraction techniques. X-ray diffraction is used to identify the unit cell and the positions of the heavy atoms. Powder x-ray diffraction is not capable of locating lithium in the presence of heavy atoms because the relative scattering power of lithium is so much lower. Additionally, powder x-ray diffraction, employing conventional, non-tunable sources, is not generally able to distinguish between two different first row transition metal atoms in the same structure. For these problems, neutron powder diffraction is a highly complementary technique. Thermal neutrons have wavelengths (1-3 Å) comparable with interatomic distances in crystals. Lithium has a significant and negative scattering length for neutrons, and the neutron scattering lengths of the first row transition metal atoms vary broadly. The theory of diffraction and the methods of structure refinement will be discussed in a later chapter.

1.3 Magnetic Structures and Properties

Neutron diffraction is an invaluable tool in determining magnetic structures. The neutron has a magnetic moment of 1.9132 μ that undergoes a dipole-dipole interaction with magnetic moments of unpaired electrons. Thermal neutrons display interference effects (i.e. diffraction) when scattered from solids with ordered magnetic moments. The magnetic scattering length is of the same order of magnitude as most nuclear scattering lengths. However, since the neutron's magnetic interaction is with the unpaired electrons, the structure factor for magnetic neutron scattering contains a form factor. Thus, the intensity of magnetic scattering decreases with increasing scattering vector, Q. The magnetic unit cell can be the same or different from the chemical unit cell depending on whether or not the ordering of the magnetic moments is commensurate with the chemical unit cell, and whether or not the moments are aligned in the same direction. In the case of a ferromagnet, the magnetic unit cell is the same as the chemical unit cell, and the magnetic scattering is observed in changes in the relative intensities of Bragg reflections between the magnetically ordered and unordered states. An antiferromagnet has two, or more, sublattices of magnetic moments of equal magnitude which are aligned in opposite directions. Consequently, the magnetic unit cell of an antiferromagnet must be a multiple, or fraction, of the chemical unit cell in at least one direction. The magnetic scattering from an antiferromagnetically ordered solid appears as new peaks at positions corresponding to the magnetic unit cell.

The bulk magnetic properties reported in this thesis were measured with a SQUID magnetometer. This technique determines magnetization directly. An apparent susceptibility can be calculated by dividing the magnetization by the applied field.

Three new magnetic structures were identified by low temperature neutron diffraction. The refinement of these structures is presented in chapter 5. The bulk magnetic properties of orthorhombic $LiMnO_2$ and of a new form of Li_2NiO_2 is also discussed.

Chapter 2

Methods and Theory

2.1 Chemical Synthesis

Most of the materials discussed in this thesis were prepared by reaction of an intimate mixture of the appropriate transition metal oxide or oxides with a lithium salt which thermally decomposes to Li_2O, and a gaseous by-product which is removed by diffusion. The lithium salts most commonly used were $LiOH{\cdot}H_2O$ and Li_2CO_3. The reagent transition metal oxides and the reaction conditions were chosen such that the desired oxidation state would be achieved in the transition metal. For instance, Co_2O_3 loses oxygen at 895 °C when heated in air. Therefore, for compounds in which Co^{3+} is the desired oxidation state, should be prepared at temperatures less than 895 °C. MnO_2 does not lose oxygen until 535 °C and Mn_2O_3 begins to reduce at 1080 °C. Consequently, the reaction temperature for phases in which Mn^{3+} is required should be near 1000 °C, and the product should be cooled in an inert atmosphere to prevent oxidation to Mn^{4+}. Some of the phases containing two types of transition metals were prepared by reaction of lithiated single transition metal oxides. For example, Li_2MnNiO_4 can be prepared from $LiMnO_2$ and $LiNiO_2$.

An intimate mixture of the powders was achieved by grinding them with a mortar and pestle and then pelletizing the mixture. The pellets were then placed in high purity alumina crucibles and fired in a Kanthal wound horizontal tube furnace. The furnace was left open to air through small gaps at each end for preparations in air. For preparations requiring an atmosphere other than air, the two ends of the furnace tubes were sealed and a flow of the appropriate gas was passed through the furnace tube. A small positive pressure was maintained in the tube by placing a gas bubbler filled with diffusion pump oil on the outlet side to the tube.

Some lithiated transition metal oxides can be prepared by ion exchange of the sodium or acid analogue. For example, Clearfield (1984) demonstrated that layered group IV acid salts such as zirconium phosphate can undergo ion exchange with alkali metals such as sodium by titrations with MCl + MOH solutions. The preparation of a new phase of $LiFeO_2$ by ion exchange of α-$LiFeO_2$ in molten $LiNO_3$ is described in chapter 3.

Lithiation of transition metal oxides can also be accomplished by chemical reaction with an appropriate organometallic reagent. $LiRuO_2$ was prepared from RuO_2 by reaction with n-butyl lithium in hexane (Davidson and Greedan 1984). The sample of 1T-Li_2NiO_2 used for the chemical and magnetic structure determinations, reported in chapters 4 and 5, was made by further lithiating 3R-$LiNiO_2$ with lithium benzophenone in tetrahydrofuran (Dahn, von Sacken and Michal 1990).

Progress of reactions was followed by x-ray powder diffraction (XRD) analysis. X-ray diffraction is useful for both identifying known compounds, and for determining that the product of a reaction is a single phase. The identification of known phases, either alone or in a mixture, is accomplished by comparing the diffraction pattern of the unknown material(s) with the JCPDS data base of known x-ray powder diffraction patterns which has been compiled by the *International Centre for Diffraction Data*. The JCPDF powder diffraction file is available in both print and on computer, and can be searched by chemical compositions or by positions of diffraction peaks. The x-ray powder diffraction pattern of a well crystallized material serves as virtually a finger print to its identity, and can be used to identify major components in an intimate mixture of crystalline solids. The technique does not work well for identifying poorly crystallized materials, or those which produce only a few weak diffraction peaks due to poor scattering power or low percent composition in a mixture.

The product of a reaction is, most probably, a single phase when all the diffraction peaks can be indexed to one Bravais lattice. The relationship between diffraction peaks and the Miller indices of a Bravais lattice is described later in this chapter. Computer programs are available to conduct a trial and error search of probable unit cell dimensions and symmetries. A program called TREOR (Werner, Eriksson and Westdahl 1985) was employed in this work. Although such programs are very useful, they are not always successful in finding a match to a Bravais lattice, or they find several possible matches. With

knowledge of related structures, it is often possible to identify the dimensions and symmetry of the unit cell of a new phase by comparison to the diffraction pattern of related known phases. The match can then be verified by calculating the diffraction pattern for the proposed structure and comparing the calculated to the observed pattern. The theory behind this calculation is detailed later in this chapter. A computer program called DISPOW, which is a module of the NRCVAX Crystal Structure System written by A. C. Larson, F. L. Lee, Y. Le Page, M. Webster, J. P. Charland and E. J. Gabe, was generally used for this task.

2.2 Structure Determination

2.2.1 Introduction

In this section, the theory of x-ray and neutron diffraction as it pertains to the determination of crystal and magnetic structures will be discussed. This discussion will closely follow related chapters in Kittel (1976) and in Ashcroft and Mermin (1976). A description, taken largely from Woolfson (1970) and Cullity (1956), of the important role of symmetry in determining the unit cell shape and dimensions, and the atomic positions is presented. The theory and procedure for refining structures from x-ray and neutron powder diffraction intensities will be developed in some detail.

2.2.2 Diffraction Theory

Just as visible light is diffracted by a ruled grating, any waves will be diffracted by an evenly spaced array of scattering objects provided that the wavelength is of the same order of magnitude as the separation between the scatterers. Diffraction is an interference effect caused by mutual reinforcement of a large number of scattered waves. In a crystal, interatomic spacings are generally on the order of 1 Å. Thus any radiation which is scattered by atoms and has a wavelength of about 1 Å will be diffracted by crystals. Both x-rays and neutrons can fulfill these requirements.

The condition for constructive interference of radiation scattered from crystalline materials was determined by both Bragg and Laue. Though their approaches differ, their results are equivalent. Bragg pictured a crystal as being formed from uniformly spaced parallel planes of ions. He accounted for diffraction by envisioning an incident ray as being reflected by the planes of ions such that the angle of reflection is equal to the angle of incidence, θ. Under this condition rays reflected from successive planes interfere constructively whenever their path difference is an integral multiple of the wavelength of the radiation. From figure 2.2.1 it can be seen that the path difference is $2dsin\theta$, giving the famous Bragg condition,

$$m\lambda = 2dsin\theta$$

for integral m.

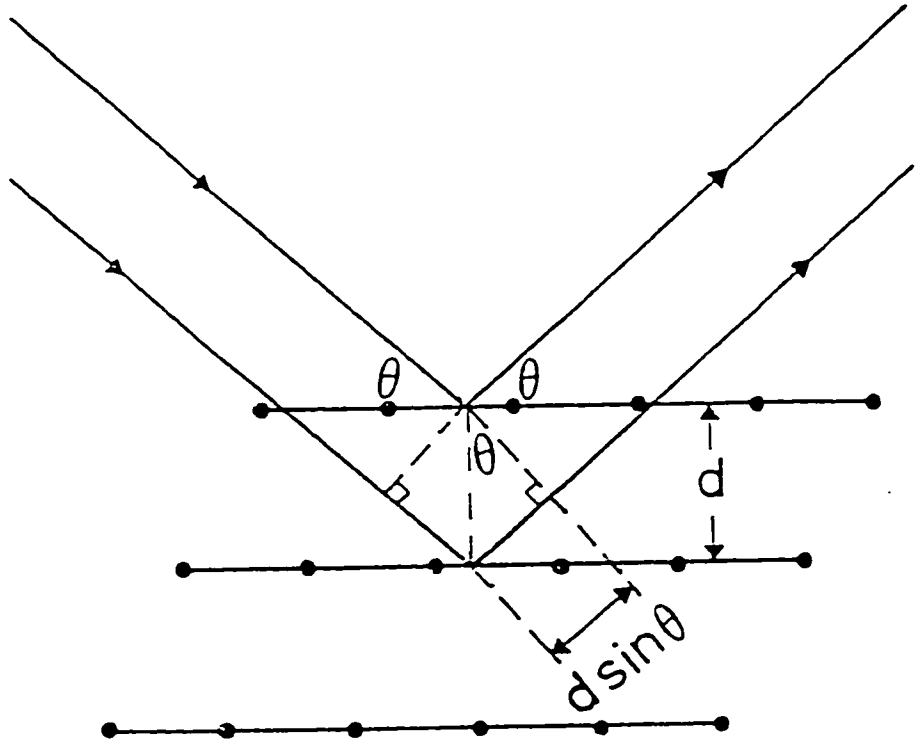

Figure 2.2.1 - Illustration of Bragg reflection from a family of planes.

The approach of Laue can be outlined by considering an incident beam traveling in direction $\hat{n}$, which is scattered by two atoms separated by a vector $\vec{d}$, without any exchange of energy. Again the scattered rays will interfere constructively when the path difference between the rays is an integral number of wavelengths. Thus, from figure 2.2.2, the condition for constructive interference is

$$\vec{d} \cdot (\hat{n}' - \hat{n}) = m\lambda$$

where $\hat{n}'$ is the direction of the scattered beam and m is an integer. In terms of the wavevectors $\vec{k}$ and $\vec{k}'$ of the incident and scattered beams respectively, this can be rewritten as

$$\vec{d} \cdot (\vec{k}' - \vec{k}) = 2\pi m.$$

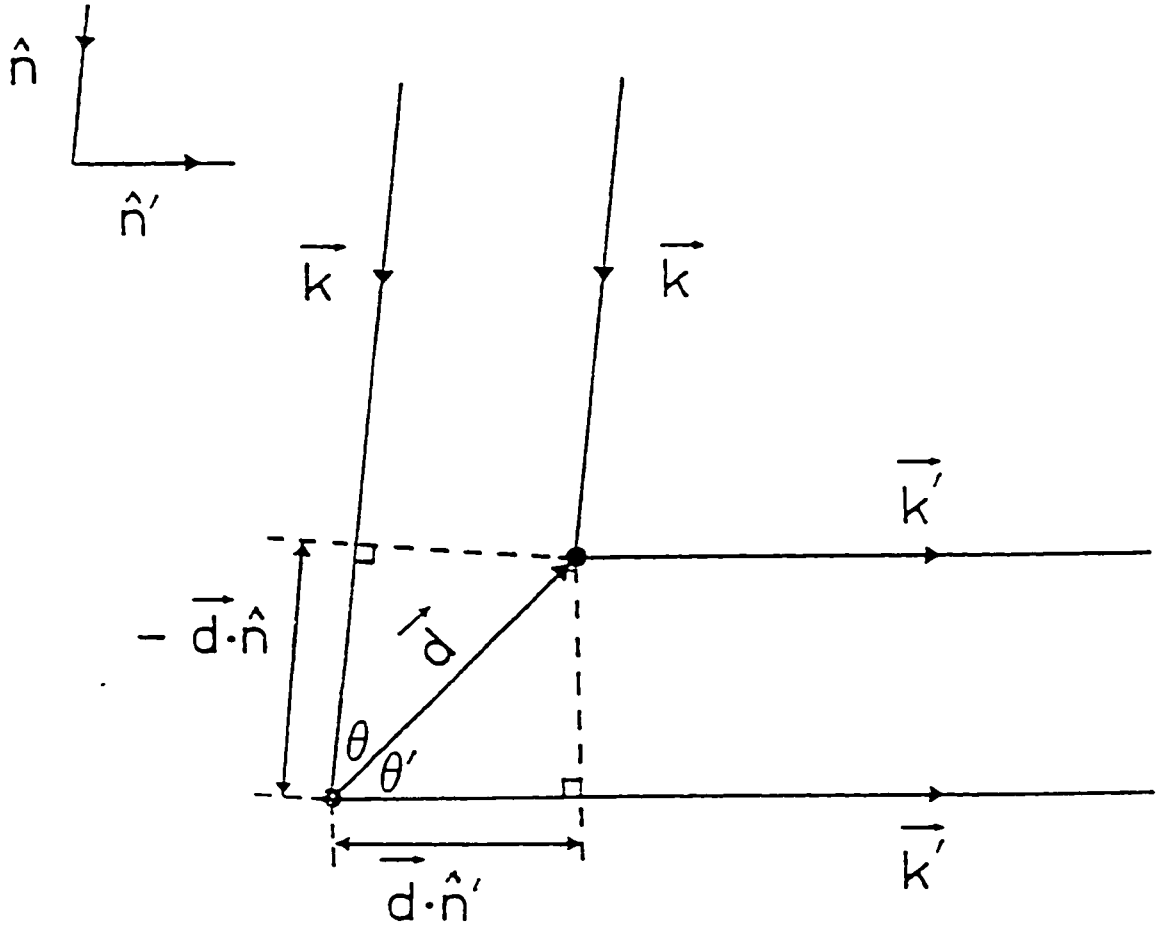

Figure 2.2.2 - Illustration of Laue condition for constructive interference.

If as in a simple Bravais lattice the atoms are separated by lattice vectors $\bar{R}$ then the requirement for constructive interference becomes

$$\bar{R}\cdot(\bar{k}'-\bar{k}) = 2\pi m$$

or

$$e^{i\Delta\bar{k}\cdot\bar{R}} = 1$$

for all $\bar{R}$, where

$$\Delta\bar{k} = \bar{k}' - \bar{k}\,.$$

This restriction is equivalent to saying that the momentum transfer. $\Delta\bar{k}$, must be the wave vector of a plane wave which has the periodicity of the Bravais lattice:

$$e^{i\Delta\bar{k}\cdot(\bar{R}+\bar{r})} = e^{i\Delta\bar{k}\cdot\bar{r}}$$

for any $\bar{r}$. The set of all wave vectors which satisfy this condition is called the reciprocal lattice. The reciprocal lattice is itself a Bravais lattice and can be described by three primitive vectors $\bar{A}$, $\bar{B}$, $\bar{C}$, which are related to the primitive vectors $\bar{a}$, $\bar{b}$, $\bar{c}$ of the direct lattice by the following relationships:

$$\bar{A} = \frac{2\pi\bar{b}\times\bar{c}}{\bar{a}\cdot(\bar{b}\times\bar{c})}\,, \qquad \bar{B} = \frac{2\pi\bar{c}\times\bar{a}}{\bar{a}\cdot(\bar{b}\times\bar{c})}\,, \text{ and } \bar{C} = \frac{2\pi\bar{a}\times\bar{b}}{\bar{a}\cdot(\bar{b}\times\bar{c})}\,.$$

Therefore any point in the reciprocal lattice can be described by a reciprocal lattice vector

$$\vec{G} = h\vec{A} + k\vec{B} + l\vec{C} .$$

The reciprocal lattice vectors are commonly used to designate families of planes in the direct lattice. From the definition of a reciprocal lattice vector, it can be shown that every family of lattice planes has a reciprocal lattice vector normal to it (Ashcroft and Mermin 1976). If the lattice planes are separated by a distance d, then, the shortest reciprocal lattice vector normal to it will be of length $2\pi d$. The coordinates of the shortest reciprocal lattice vector normal to the plane with respect to the primitive reciprocal lattice vectors are known as Miller indices. For example, a plane with Miller indices *(hkl)* is normal to the reciprocal lattice vector

$$\vec{G} = h\vec{A} + k\vec{B} + l\vec{C} .$$

In terms of the direct lattice, the Miller indices are the reciprocals of the fractional intercepts between the plane and the crystallographic axes a, b, c. Therefore the plane described by the Miller indices *(hkl)* has intercepts $a\,h$, $b\,k$, $c\,l$.

The Laue condition for constructive interference requires that

$$\Delta\vec{k} = \vec{k}' - \vec{k} = \vec{G}$$

be a reciprocal lattice vector. Since the scattering is elastic $\vec{k}$ and $\vec{k}'$ must have the same magnitude, and therefore, must make the same angle θ with respect to the plane perpendicular to $\vec{G}$. Thus, from figure 2.2.3 it can be seen that

$$G = 2k \sin\theta .$$

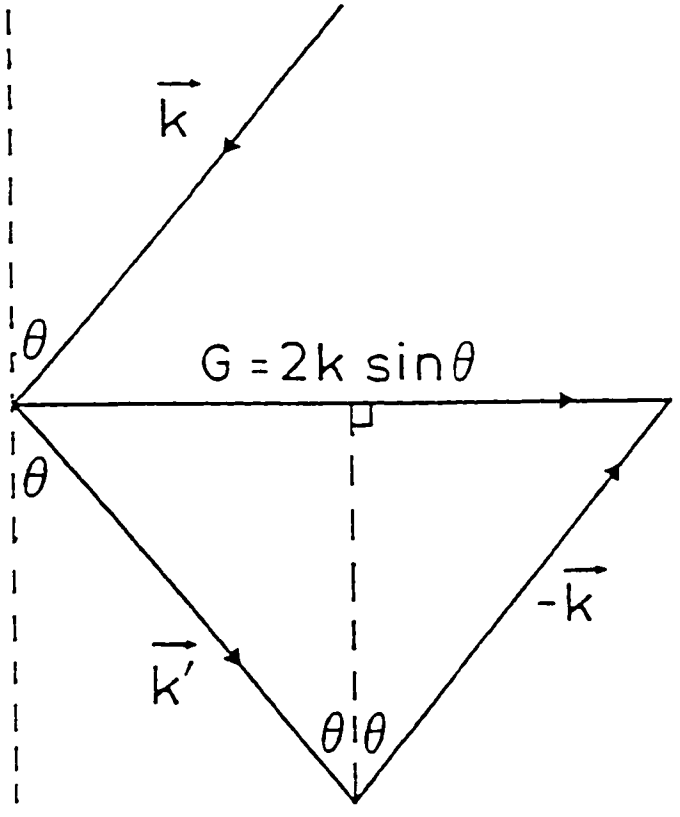

Figure 2.2.3 - Illustration of the equivalence of the Bragg and Laue conditions.

If $\vec{G}$ is a reciprocal lattice vector, its length must be an integral multiple of the length of the shortest reciprocal lattice vector parallel to it; hence,

$$G = m2\pi / d$$

for integral m. Since

$$k = 2\pi / \lambda ,$$

equating the two expressions for G results in the Bragg law.

$$m\lambda = 2d\sin\theta .$$

Thus, the Laue condition,

$$\Delta\bar{k} = \bar{G}$$

for constructive interference is equivalent to the condition for Bragg reflection from the family of planes normal to $\bar{G}$.

The integer m is generally called the order of the reflection. Rewriting the Bragg equation as

$$\lambda = 2\frac{d'}{m}\sin\theta ,$$

it can be seen that an m^{th} order reflection from planes separated by a distance d' can be regarded as a first order reflection from real or fictitious planes at a spacing of d'/m. For convenience the Bragg equation is often written as

$$\lambda = 2d\sin\theta ,$$

where $d = d'/m$, and an m^{th} order reflection from the planes *(hkl)* is regarded as a first order reflection from the planes *(mh mk ml)*.

In the powder diffraction method, the material is ground into a fine powder, such that the crystal particles are randomly oriented with respect to the monochromatic incident beam. In this situation, some of the particles will be in the correct orientation to reflect the incident beam from, for example, their (100) planes and others will be correctly oriented to reflect from their (110) planes etc. The net result is that some particles will be in the correct orientation for reflection from any plane and all possible reflections will be observed.

From the Bragg equation, it can be seen that the peak positions, measured in terms of the scattering angle, 2θ, give the interplanar spacings between families of planes with a given set of Miller indices. These spacings can, in turn, be used to determine which crystal system a unit cell belongs to. There are 32 distinct symmetry point groups which a unit cell can have and these are associated with seven crystal systems. The seven crystal systems, each represented by a parallelepiped, are described by the relationship between the lengths of the three axes a, b, c and by the values of the three angles between the axes α, β, and γ.

The relationship between the interplanar spacings, d, and the lattice parameters (a, b, c, α, β, γ) is well known for each crystal system (Woolfson 1970). However, to fit the lattice parameters, one must assign Miller indices to all the observed reflections and this requires that one first make some intuitive guess at which crystal system the material belongs to and the approximate values of the lattice parameters. Fitting programs which search through all crystal systems for a reasonable fit to the observed d-spacings are available, but they require a large number of reflections to be used successfully. Generally, some *a priori* knowledge of the crystal structure is required for determining the lattice parameters from powder data only.

The best choice of unit cell is not necessarily a primitive one; sometimes a non-primitive cell has a more obvious connection to the point symmetry elements. Bravais has shown that there are only 14 distinct space lattices, 7

primitive and 7 non-primitive, which can completely define the repetition characteristics of a three dimensional pattern without any reference to the repeated motif.

In addition to having a particular point symmetry, a crystal lattice has elements of translational symmetry. When all the possible symmetry elements of a three dimensional array are considered, there are 230 distinct combinations possible; these combinations are called the space groups.

Once the lattice parameters of the unit cell have been determined and the observed Bragg reflections have been assigned Miller indices, a study of the missing reflections can reveal the lattice type (primitive, body-centered, etc.) and the translational symmetry elements of the unit cell. For example, if all the reflections whose Miller indices sum to an odd number are absent (and the apparently absent reflections are not simply too weak to be seen) then the unit cell is body centered. Similarly, consideration of the absence of particular sets of reflections called systematic absences can be helpful in narrowing down the choice of space group.

A crystal structure is defined by its Bravais lattice and by the arrangement of atoms in the unit cell. Information about the arrangement of atoms, or basis, at any lattice point is obtained from the relative intensities of the Bragg peaks.

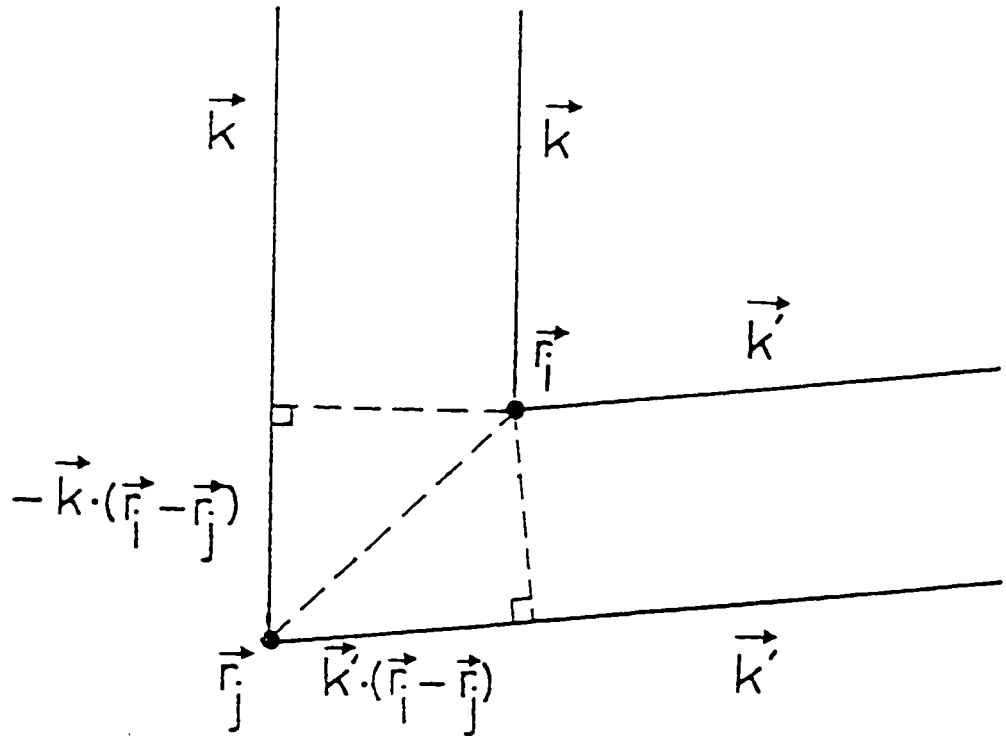

Figure 2.2.4 - Phase difference between scattering from two lattice points.

If an incoming wave is scattered from two points r_i and r_j (figure 2.2.4), the path difference between the scattered rays will be $\Delta\bar{k}\cdot(\bar{r}_i-\bar{r}_j)$ and the phases of the two rays will differ by the factor $e^{i\Delta\bar{k}\cdot(\bar{r}_i-\bar{r}_j)}$. Similarly the rays scattered from $\bar{r}_1 \ldots . \bar{r}_n$ will have phases in the ratio $e^{i\Delta\bar{k}\cdot\bar{r}_1} \ldots . e^{i\Delta\bar{k}\cdot\bar{r}_n}$, and thus, the amplitude of the rays scattered from the entire primitive cell will contain the factor

$$S_{\Delta\vec{k}} = \sum_{j=1}^{n} e^{i\Delta\vec{k}\cdot\vec{r}_j}.$$

The Laue condition for constructive interference requires that $\Delta\vec{k}$ be a reciprocal lattice vector, $\vec{G}$, and therefore this factor, which is called the structure factor, is associated with a particular Bragg reflection and can be expressed in terms of the reciprocal lattice vector

$$S_{\vec{G}} = \sum_{j=1}^{n} e^{i\vec{G}\cdot\vec{r}_j}.$$

The structure factor indicates the extent to which a particular Bragg reflection is diminished by interference effects between identical ions in the basis. In the case of x-rays, which are electromagnetic radiation, the scattering particles are the electrons, and therefore the total amplitude of the wave scattered from a volume element dV is proportional to the electron concentration in that volume element. Since in general all the atoms in the basis are not identical, the structure factor is modulated by the Fourier transform of the electron concentration n_j associated with each atom j. This modulating factor, which is called the atomic scattering factor, is the integral over all space of the electron concentration associated with the j^{th} atom multiplied by a phase factor which depends on the position of the charge relative to the center of the atom. If $r = 0$ at one corner of the cell and $\vec{r}_j$ is the vector from the corner of the cell to the center of atom j (figure 2.2.5), then the x-ray atomic scattering factor may be written as

$$f_j = \int dV n_j(\vec{r} - \vec{r}_j) e^{i\vec{G}\cdot(\vec{r}-\vec{r}_j)} .$$

The x-ray structure factor for any basis is then given by

$$S_{\vec{G}} = \sum_{j=1}^{n} e^{i\vec{G}\cdot\vec{r}_j} \int_{cell} dV n_j(\vec{r} - \vec{r}_j) e^{i\vec{G}\cdot(\vec{r}-\vec{r}_j)}$$

or

$$S_{\vec{G}} = \sum_{j=1}^{n} f_j e^{i\vec{G}\cdot\vec{r}_j} .$$

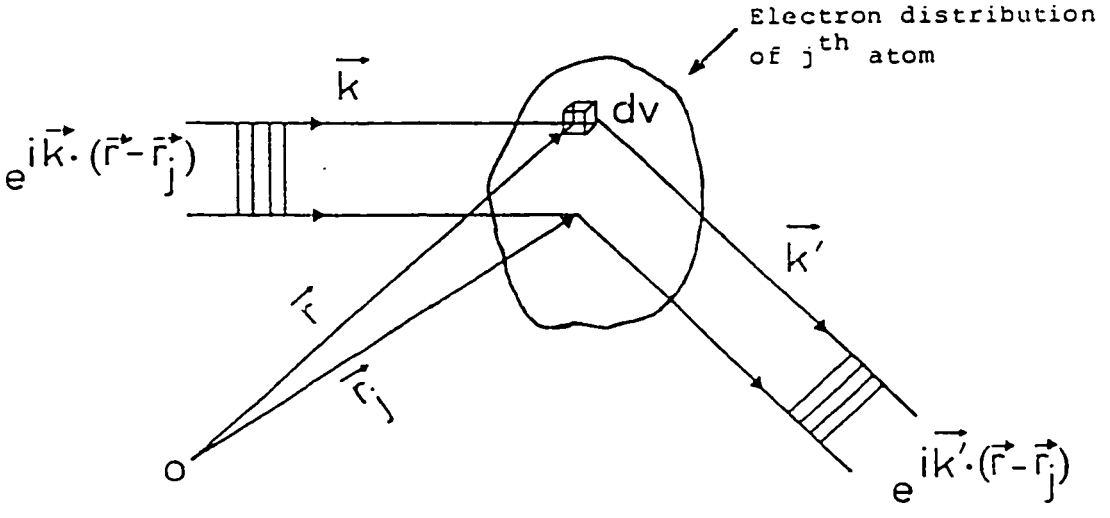

Phase difference between rays scattered from electronic charge in a volume element dV and from a charge located at the atomic center, r_j. Since the path difference between the rays is $\Delta k \cdot (r - r_j)$, their phases differ by a factor $e^{i\Delta k \cdot (r - r_j)}$.

Figure 2.2.5 - Phase difference between rays scattered from different points in the electronic charge.

The structure factor can be rewritten in terms of the Miller indices of the reciprocal lattice vector and the fractional coordinates of the atoms in the unit cell:

$$S_{\vec{G}} = \sum_{j=1}^{n} f_j \exp i(h\vec{A} + k\vec{B} + l\vec{C}) \cdot (x_j\vec{a} + y_j\vec{b} + z_j\vec{c}).$$

Using the definitions of the primitive reciprocal lattice vectors $\vec{A}, \vec{B}, \vec{C}$, this expression can be reduced to

$$S_{hkl} = \sum_{j=1}^{n} f_j \exp[2\pi i(hx_j + ky_j + lz_j)].$$

Thus, if the structure factor were known for enough reflections, it would be possible to calculate the positions of all the atoms in the cell. Though the structure factor can not be measured directly, it is proportional to the amplitude of the rays scattered from a unit cell. Since intensity is proportional to the square of the absolute value of the amplitude, the relative intensities of the Bragg peaks will indirectly provide information about the positions of the atoms in the unit cell.

In the calculation of the structure factor it was tacitly assumed that the atoms in the crystal are tightly bound and not free to move. However, in reality the atoms are subject to thermal vibrations about their equilibrium positions and this motion has the effect of diminishing the amplitude of the coherent scattering by a factor $\exp(-B_j \sin^2 \theta / \lambda^2)$, where B_j is a measure of the average displacement of the j^{th} atom and is called the temperature factor. The structure factor thus becomes

$$S_{hkl} = \sum_{j=1}^{n} f_j \exp[2\pi i(hx_j + ky_j + hz_j)]\exp(-B_j \sin^2\theta/\lambda^2).$$

This correction appears as its square, $\exp(-2B_j \sin^2\theta/\lambda^2)$, in the intensity and is then called the Debye-Waller factor.

The x-ray atomic scattering factor is the Fourier transform of the electronic charge distribution of an atom and is dependent on the reciprocal lattice vector. It represents the ratio of the amplitude of the coherent scattered radiation from an atom to that from a single electron situated at the center of the atom.

2.2.3 Neutron Diffraction

Coherent elastic scattering of neutrons from atoms also produces Bragg peaks, but in the case of non-magnetic neutron scattering it is the nuclei rather than the electrons which are the predominant scatterers. The interaction potential between the nucleus and the neutron is of very short range, falling to zero outside a distance on the order of nuclear dimensions (~10^{-8} cm). Consequently, the nucleus acts as a point scatterer to neutrons and therefore. the ratio of the amplitude of the coherent scattered radiation from an atom to that of a unit scatterer located at the atomic center is a constant and has no dependence on the reciprocal lattice vector. The neutron structure factor for any basis is given by

$$S_{hkl} = \sum_{j=1}^{n} b_j \exp[2\pi i(hx_j + ky_j + hz_j)]\exp(-B_j \sin^2\theta/\lambda^2),$$

where b_j is a constant dependent only on the average nuclear structure of the j^{th} atom and is called the neutron scattering length. The scattering length i specific to a given nuclide, and for elements which contain more than one isotope the effective scattering length, $\bar{b}$, is the average value of b weighting each isotope, r, by its relative abundance, w_r, so $\bar{b} = \sum_r w_r b_r$.

The neutron scattering length differs from the x-ray scattering factor in another respect. The x-ray scattering factor is the Fourier transform of the electron charge distribution of a given atom. Therefore, considering only atoms in their zeroth oxidation state. the x-ray scattering factor increases with increasing atomic number through the concommittal addition of an electron. This results in a dramatic difference in the scattering amplitudes of light and heavy atoms. For example, the x-ray scattering amplitude of a lead atom is about 20 times that of a carbon atom (Bacon 1962). The neutron scattering length. however, varies more or less randomly through the periodic table such that atoms with quite different atomic numbers can have very similar scattering lengths and vice versa. Figure 2.2.6 taken from Bacon (1962) graphically demonstrates this fact.

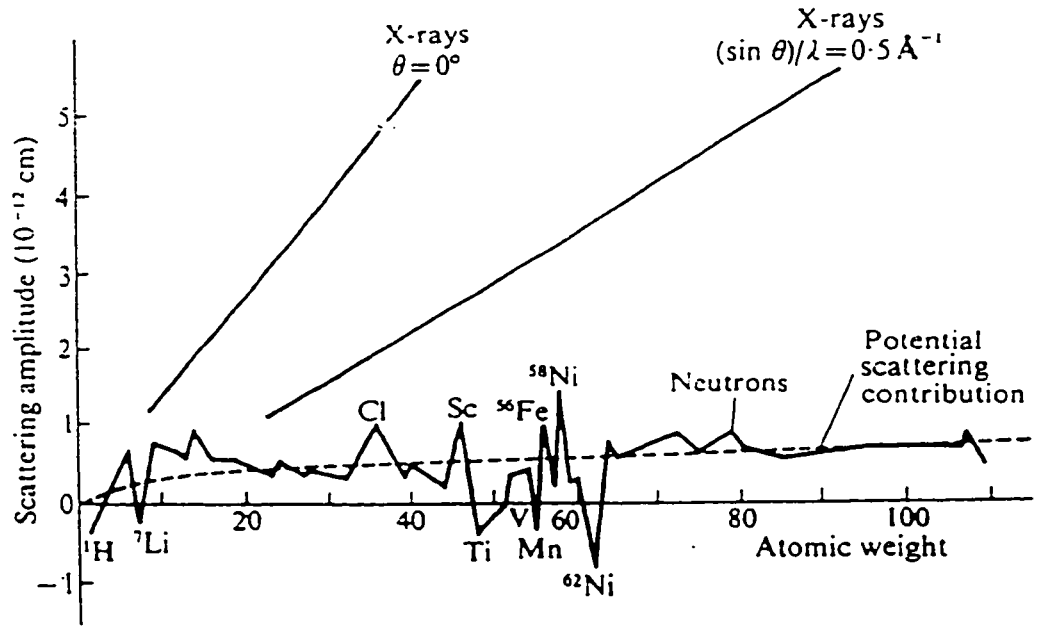

Figure 2.2.6 - Comparison of neutron and x-ray scattering amplitudes.

One of the powerful applications of neutron diffraction results from the fact that the neutron has a magnetic moment of 1.9132 μ that undergoes a dipole-dipole interaction with magnetic moments of unpaired electrons. This interaction makes neutron scattering particularly useful in the study of magnetically ordered crystals, for which the scattering will reflect interactions with both the atomic lattice and the lattice of magnetic moments. Each magnetic atom has a magnetic scattering length, *p*, which is determined by its magnetic moment such that

$$p = \frac{e^2\gamma}{2mc^2} gJf$$

$$= 0.27 gJf \times 10^{-12} cm$$

where, the constants in the expression, *e* and *m* are the charge and mass of the electron, *c* is the speed of light and γ is the magnetic moment of the neutron expressed in nuclear magnetons. The other quantities are the Landé spitting factor, *g*, the total quantum number, *J*, and *f* is a form factor which depends on the scattering angle, 2θ. The form factor arises from the fact that the neutron's magnetic interaction is with the unpaired electrons and the spatial distribution of magnetic electrons about the center of the ion is comparable to the interatomic spacing, and consequently, to the wavelength of the scattering neutron. Thus, the intensity of magnetic scattering decreases with increasing scattering vector, *Q*. This equation is for the general case in which the magnetic moment has both spin and orbital contributions. In many of the compounds of the first row transition metals the orbital momentum is quenched by the crystal field and magnetic moment is due only to the spin of the electron. Then the magnetic moment, *gJ*, can be represented as *2S*, where *S* is the spin quantum number, and the equation for the magnetic scattering length becomes

$$p = 0.54 Sf \times 10^{-12} cm .$$

This expression shows that the magnetic scattering length is of comparable magnitude to the nuclear scattering length, *b*.

For unpolarized neutrons, the scattering cross-section is the sum of the nuclear and magnetic contributions. The magnetic scattering of a paramagnetic ion has a cross section per unit solid angle, Ω, defined as

$$\frac{d\sigma_m}{d\Omega} = \frac{2}{3} S(S+1)\left(\frac{e^2\gamma}{mc^2}\right)^2 f^2.$$

In a paramagnetic material, the magnetic moments vary randomly from ion to ion and therefore do not contribute to the Bragg diffraction peaks. The magnetic scattering appears as an increase in the background of the diffraction pattern which decreases with increasing scattering angle as a consequence of the form factor, *f*.

However, when the magnetic moments are ordered in a fixed orientation, the scattering cross section becomes

$$\frac{d\sigma_m}{d\Omega} = q^2 S^2 \left(\frac{e^2\gamma}{mc^2}\right)^2 f^2$$

where the magnetic interaction vector, $\vec{q}$, is defined as

$$\vec{q} = \vec{\varepsilon}\left(\vec{\varepsilon}\cdot\vec{K}\right) - \vec{K},$$

in which $\vec{K}$ is a unit vector in the direction of the spin of the atomic moment and $\vec{\varepsilon}$ is the scattering vector.

For the simple case of a magnetic system in which all the moments are aligned parallel or antiparallel to a single direction, the total neutron scattering cross-section for an unpolarized beam can be written as

$$\frac{d\sigma}{d\Omega} = b^2 + p^2\bar{q}^2 .$$

A magnetic unit cell structure factor can then be defined as

$$S_{magn} = \sum_{j=1}^{n} \bar{q}_j p_j \exp[2\pi i(hx_j + ky_j + hz_j)]\exp(-B_j \sin^2\theta/\lambda^2) .$$

The first step to determining a magnetic structure involves identifying the magnetic propagation vector, *k*, from the positions of the magnetic Bragg reflections. The value of *k* can range from (0 0 0), as is the case when the chemical and magnetic unit cells are identical, to a fractional value of the reciprocal lattice vector, such as (0 0 1/2) when the magnetic unit cell is double the length of the chemical cell along the c-axis but the same as the chemical cell along the a-axis and b-axis. In some cases the value of *k* is so complicated, that it is best represented as a magnetic cell incommensurate with the chemical cell.

2.2.4 Structure Refinement

At the point where the structure refinement procedure can commence, the chemical composition of the material, and the shape and dimensions of the unit cell (from the fitting of the d-spacings) are known, and the choices of space groups have been narrowed down by identifying the systematic absences. In this work, the structure refinement was carried out with the aid of a computer program called "Rietan" (Izumi 1989) which performs a least squares fit to the diffraction pattern profile. The least squares refinement attempts to minimize a

weighted R-factor, R_{wp}. The weighed R-factor represents the normalized weighed sum of the differences between the observed x-ray or neutron powder diffraction profile and the profile calculated from a model structure for the atomic positions. R_{wp} is expressed as

$$R_{wp} = \left[\frac{\sum_i w_i \left(Y_i(obs) - Y_i(cal) \right)^2}{\sum_i w_i \left((Y_i(obs) \right)^2} \right]^{1/2} \times 100$$

where the sums are taken over all data points, $Y_i(obs)$ and $Y_i(cal)$ are the observed and calculated profile points, and $w_i = (Y_i(obs))^{-1}$, is the weighting factor. The parameters, with respect to which R_{wp} is minimized, include a scale factor and the fractional coordinates and temperature factors of the individual atoms. To choose a suitable space group and probable atomic sites, a rough model of the structure, usually based on compounds of similar composition or some knowledge of the history of the compound is required.

2.3 Magnetic Properties

The magnetic moment of a free atom has three main sources: the spin of the electrons, their orbital angular momentum about the nucleus, and the change in angular moment induced by an applied field. The first two effects contribute to the *paramagnetic* susceptibility and the last, to the *diamagnetic* susceptibility.

The magnetization, M, is defined as the magnetic moment per unit volume. The magnetic susceptibilty per unit volume is defined by

$$\chi = \frac{M}{B},$$

where B is the macroscopic magnetic field intensity.

Diamagnetism is a property of all matter and arises from the interaction of paired electrons with a magnetic field. It is particularly important in the consideration of materials with completely filled electronic shells. Diamagnetic susceptibilities do not depend on field strength or temperature. Since transition metal substances with unpaired electrons also have a number of filled shells, they too have a diamagnetic contribution to their susceptibility. Diamagnetic susceptibilities are much smaller, of the order of (-1 to -100) x 10^{-6} emu/mol, than paramagnetic susceptibilities which increase with decreasing temperature and are normally in the range of (10^2 to 10^4) x 10^{-6} emu/mol at room temperature. The diamagnetic contribution to the susceptibility can usually be separated from the paramagnetic susceptibility by measuring the temperature dependence, but the difference in their size, particularly at low temperature, often makes the exact calculation of the diamagnetic contribution unimportant. Diamagnetic susceptibilities of atoms in molecules are largely additive, and therefore can be estimated for a given compound using values from published tables.

The diamagnetic contribution to the susceptibilty can also be calculated from theoretical considerations. If the average electron current about a nucleus is initially zero, the application of a magnetic field will result in a finite current

around the nucleus. This current is equivalent to a magnetic moment opposed to the applied field. According to the Larmor theorem, the application of a magnetic field, B, causes the electrons to precess with an angular frequency, $\omega = eB / 2mc^2$. The precession of Z electrons is equivalent to a current of

$$I = -\frac{Ze^2 B}{4\pi mc^2}.$$

The magnetic moment, μ, of a current loop is given by the product of the current times the area of the loop. The area of a loop of radius p is πp^2, so

$$\mu = -\frac{Ze^2 B}{4mc^2}\langle p^2 \rangle.$$

It is conventional to present the Langevin equation for diamagnetic susceptibility in terms of the mean square distance of the electrons from the nucleus, $\langle r^2 \rangle$. For a spherically symmetric distribution of charge, $\langle r^2 \rangle = 3/2 \langle p^2 \rangle$. The diamagnetic susceptibility for a unit volume containing N atoms is

$$\chi = -\frac{NZe^2}{6mc^2}\langle r^2 \rangle.$$

The problem of calculation of the diamagnetic susceptibility for an isolated atom is reduced to the calculation of $\langle r^2 \rangle$ for the electron distribution within the atom.

Paramagnetism is a property exhibited by substances containing unpaired electrons. This includes the oxygen molecule, nitric oxide and a large number of organic free radicals, but for the purpose of this work, transition metal compounds are the main concern. Paramagnetic susceptibilities are usually

temperature dependent. To a first approximation, the susceptibility varies inversely with temperature, giving the Curie law $\chi = C/T$.

χ is the measured susceptibility corrected, if necessary, for diamagnetic contributions, C is called the Curie constant, and T is the absolute temperature. Since the magnitude of χ at room temperature is an inconvenient number, it is common to report the effective magnetic moment, μ_{eff}, which is defined as

$$\mu_{eff} = (3k/N)^{1/2}(\chi T)^{1/2}$$

where k is the Boltzmann constant and N is Avogadro's number. For the spin only case in which the orbital angular momentum is quenched by the ligand field,

$$\mu_{eff} = \left[g^2 s(s+1)\right]^{1/2} \mu_B$$

where μ_B, is the Bohr magneton, 9.27×10^{-24} JT^{-1}, g is the Lande constant, and s is the spin quantum number equal to ½ times the number of unpaired electrons in the magnetic ion. The Lande constant is characteristic of each system but is generally close to 2.

Similarily, for the spin-only case, the Curie constant can be written as

$$C = Ng^2\mu_B{}^2 s(s+1)/3k = 0.125g^2 s(s+1) \ .$$

The maximum or saturation magnetization which such a spin system can exhibit is

$$M_{sat} = Ng\mu_B s.$$

This situation corresponds to the complete alignment of magnetic dipoles by the field.

There are many situations in which the Curie law is not strictly obeyed. One source of deviation results from the interactions which can occur between paramagnetic ions, another source is the presence of an energy level whose population changes over the measured temperature range. To the simplest approximation, this behaviour is expressed by a small modification of the Curie law, to the Curie-Weiss law,

$$\chi = C / (T - \theta),$$

where the correction term, θ, has units of temperature.

A ferromagnet has a spontaneous magnetic moment. That is to say it has a magnetic moment even in the absence of an applied magnetic field. A spontaneous moment suggests that the electron spins and magnetic moments are arranged in a regular array, although not necessarily a simple one. An internal interaction is postulated to be responsible for aligning the magnetic moments. The internal interaction is called the exchange field or the molecular field, and is treated as equivalent to a magnetic field, H_{int}. The exchange field is assumed to be proportional to the magnetization, M, so it is assumed that

$$H_{int} = \lambda M,$$

where λ is a constant, independent of temperature. In this model each spin sees the average magnetization of all the other spins.

The orienting effect of the exchange field is opposed by thermal agitation, and at some critical temperature, the spin order is destroyed. The Curie temperature, T_C, separates the disordered paramagnetic phase at $T > T_C$, from the ordered ferromagnetic phase at $T < T_C$. Within the paramagnetic phase an applied field H will cause a finite magnetization, which will in turn cause a finite exchange field, H_{int}. Now the total magnetic field, H_T, acting on sample is the sum of H_{int} and the external field, H_{ext}.

$$H_T = H_{ext} + H_{int}$$

so

$$M / H_T = M / (H_{ext} + \lambda M) = C / T,$$

or by multiplying through and rearranging,

$$M\left[1 - (\lambda C / T)\right] = C H_{ext} / T.$$

Thus

$$\chi = M / H_{ext} = C / (T - \lambda C)$$

and when $H_{ext}=0$, M is not zero at T_C (because of H_{int}) so under these conditions, $T_C=\lambda C$ and

$$\chi = C / (T - T_c).$$

This is the Curie-Weiss law where $\theta = T_C$, however, no materials obey the relationship between θ and T_C exactly.

Ferromagnetic ordering is relatively rare amongst transition metal compounds. Rather, neighbouring spins are found more frequently to adopt an

anti-parallel or antiferromagnetic arrangement. The paramagnetic-antiferromagnetic transition is a cooperative one, accompanied by a characteristic long-range ordering temperature usually called the Neel temperature, T_N.

The typical antiferromagnet may be considered to consist of two interpenetrating sublattices, with each sublattice uniformly magnetized with spins aligned parallel, but with the spins on one sublattice antiparallel to those on the other. The sublattice magnetizations can not be measured by a macroscopic technique such as magnetic susceptibility, but can be by microscopic procedures such as neutron scattering and nuclear resonance.

Molecular field theory can be used to explain antiferromagnetism in a manner analogous to the discussion of ferromagnetism. However, in an antiferromagnet it is assumed that ions on one sublattice (A) interact only with ions on the B sublattice, and visa versa. Then the field acting on sublattice A is

$$H_A = H_{ext} + H_{\text{int}\,B} = H_{ext} - \lambda M_B$$

and similarily,

$$H_B = H_{ext} - \lambda M_A .$$

The negative signs are used because antiferromagnetic exchange tends to destroy the alignment parallel to the field. Above the ordering temperature, T_N, the Curie law is assumed, and the magnetization of each sublattice can be written as

$$M_A = \tfrac{1}{2} C(H_{ext} - \lambda M_B)/T$$
$$M_B = \tfrac{1}{2} C(H_{ext} - \lambda M_A)/T$$

and the total magnetiziation is $M = M_A + M_B$. By multiplying and rearranging as before, a modified Curie-Weiss law is derived,

$$\chi = C/(T + \lambda C/2),$$

where the Weiss constant is negative and given by $\theta = -\lambda C/2$.

The constant, θ, in the Curie-Weiss law is positive for systems with dominant ferromagnetic interactions, and negative for ones with antiferromagnetic interactions.

Many more complex forms of long range magnetic ordering are known. For instance, ferrimagnetism occurs when the magnitudes of the moments associated with two antiferromagnetically aligned sublattices are not exactly the same. The result is that the two sublattices cannot balance each other out, and a weak moment persists below the ordering temperature, T_C. Sometimes the magnetic ordering in a compound is dependent on the strength of the applied magnetic field. Metamagnets are an example of such behaviour which results from competing interactions within the compound.

The magnetic properties of 1T-Li_2NiO_2 and 3R-$LiNiO_2$ were examined by dc-magnetization. The magnetic structures of several compounds were elucidated by low temperature powder neutron diffraction. The results of these studied are presented in chapter 5.

2.4 Electrochemical Evaluation

The phases being studied for this thesis were chosen on the basis that they are materials with characteristics which suggest that they will be suitable for use as cathodes in lithium ion cells. At the start of this work only one of the phases being studied, 1T-Li_2NiO_2, had been evaluated electrochemically (Dahn, von Sacken and Michal 1990). All of the other phases have high enough oxidizing potentials to be stable in ambient conditions. The carbon anodes of lithium ion cells are also air stable. However, once a lithium ion cell is charged the lithiated carbon anode becomes a very strong reducing agent with a potential close to that of metallic lithium. Consequently, lithium ion cells require non-aqueuos electrolyte solutions with a very broad range of electrochemical stability. The electrolyte must contain a reasonable concentration, usually 1 - 2 molar, of a lithium salt. Both the electrolyte solution and the anion of electrolyte salt must be stable in the presence of both a strong reducing agent, the charged anode, and a strong oxidizing agent, the charged cathode. The rather demanding requirements of lithium ion cells for electrolyte solutions can be satisfied using a mixture of organic solvents with highly stable lithium salt such as $LiClO_4$, $LiPF_6$ or lithium bis(trifluoromethylsulfonyl)imide, $LiN(CF_3SO_2)_2$. The organic solvent mixture usually contains a high dielectric solvent to solvate the lithium salt and a miscible cosolvent of lower viscosity to improve the ionic conductivity. Propylene carbonate (PC) and/or ethylene carbonate (EC) are

commonly used for the high dielectric component, and dimethoxyethane (DME), dimethly carbonate (DMC) or diethyl carbonate (DEC) are often chosen for the cosolvent. The resulting electrolyte solutions are both hygroscopic and volatile. Thus, even though the electrodes materials are initially air stable, lithium ion cells must be assembled in a glove box to prevent degradation of the electrolyte. The seal of the cells should be nearly hermetic to prevent loss of the volatile electrolyte solvent or ingress of water or air. At the research level, it is most convenient to use an electrochemical cell which requires only small amounts of materials. Consequently, a coin cell format was chosen. The coin cells used are made of stainless steel and have a diameter of 23 mm and a height of 2.5 mm. They are sealed in the glove box by crimping with a polypropylene grommet.

Most of the electrochemical experiments described in chapter 6 involved relatively thick electrodes, typically about 1 mm, and anodes based on petroleum cokes. Petroleum cokes are non-graphitic carbons which can intercalate up to approximately one lithium ion per twelve carbon atoms (Dahn, Sleigh, Shi, Reimers, Zhong and Way 1993). In these studies the electrodes were formed as pressed pellets. The finely ground active materials were mixed with 5 - 10 weight percent of Super-S carbon black, and coated with about 2 weight percent of ethylene propylene diene monomer (EPDM). The EPDM served as a binder and the carbon black as a conductivity enhancer and a wick for the electrolyte solution. Pellets of 17 mm diameter were formed by pressing about 300 mg of the mixture in a hardened steel die to 3500 psi. The cell stack consisted of a

three layer sandwich of the cathode, a cell separator, and a carbon anode. The separator which is needed to prevent the two electrodes from contacting directly was a non-woven polypropylene felt, from Web Dynamics. The separator also provides a reservoir for the electrolyte solution. For the thick electrode studies, a 50/50 mixture by volume of propylene carbonate and dimethoxyethane containing 1 M $(CF_3SO_2)_2N^-Li^+$ from the 3M company was used. The salt was dried under vacuum at 160 ^oC for 24 hours as recommended by the manufacturer. The propylene carbonate was vacuum distilled and the dimethoxyethane was distilled from lithium/naphthalide under helium. The water content of the electrolyte was under 30 ppm as determined by Karl-Fischer titration. About 300 µl of electrolyte was typically required to properly wet the electrode stack .

Electrochemical studies employing carbon coke anodes are very useful for demonstrating that a cathode material has true commercial applicability. However the coke anodes have a disadvantage relative to metallic lithium anodes in that they have a sloping voltage curve as a function of their state of charge and they have an intrinsic irreversible capacity. Figure 2.4.1,from Dahn *et al* (1993), is a typical voltage curve for a carbon coke electrode cycled against metallic lithium. The coke electrode can be discharged to a composition near LiC_{12}, or about 186 mAh/g of carbon, but on recharge and subsequent cycling, only about 80% of the initial capacity can be obtained. The capacity loss is the result of the formation of a passivation film on the surface of

the now, lithiated, carbon electrode. A stable passivation film is essential to the function of the anode because the electrolyte solutions are not thermodynamically stable at the potential of the lithiated carbon anode. Cathodes evaluated against coke anodes will have voltage curves which reflect changing potentials in both electrodes and an irreversible capacity region at the higher lithium end of their cycleable composition range. Consequently, in addition to evaluating cathode materials against coke anodes, some of the materials were also tested with metallic lithium anodes.

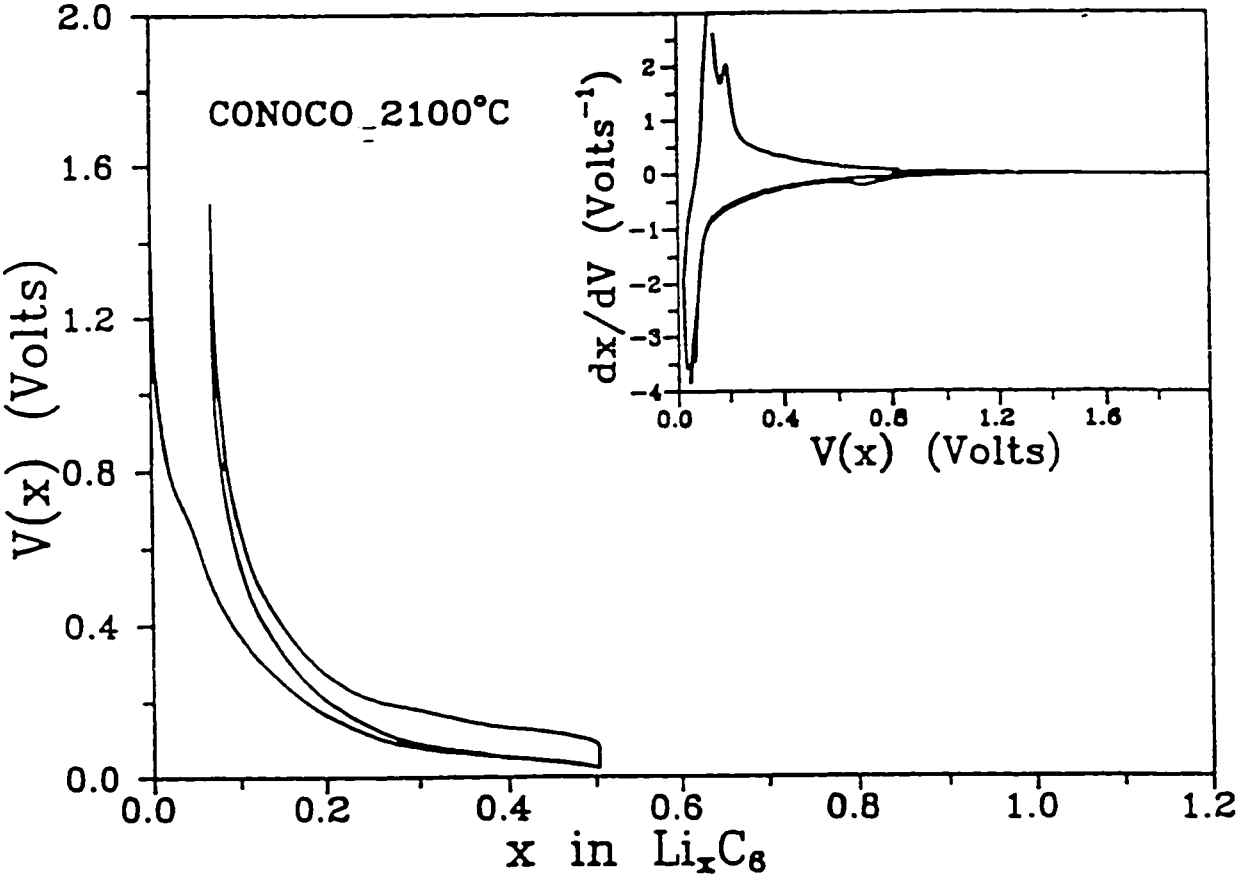

Figure 2.4.1 - Typical voltage curve versus lithium for a carbon coke anode.

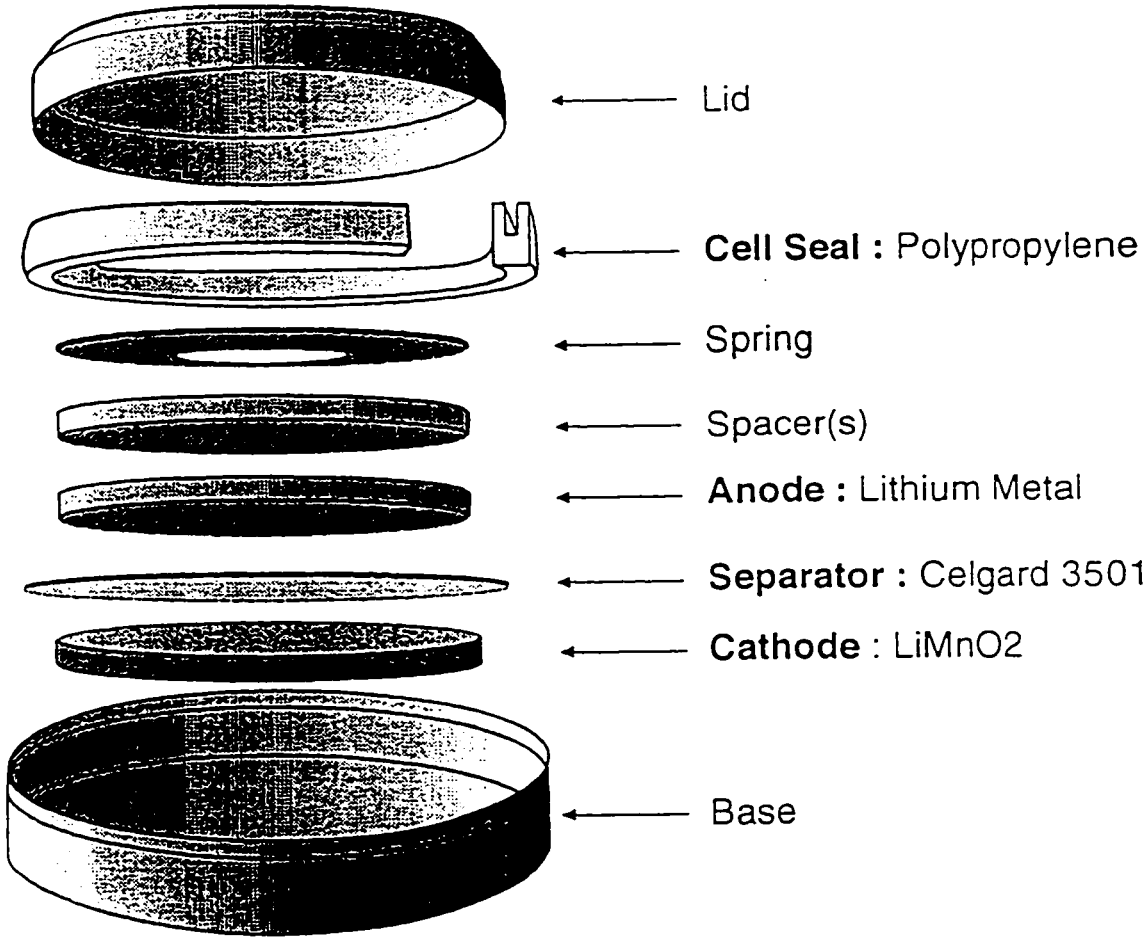

Figure 2.4.2 - Exploded view of coin cell assembly with spring and spacers.

For the lithium cells, the thinner cathodes were prepared by slurry casting a mixture of active material, carbon black, and polyvinylidene fluoride (PVDF) in the weight ratio 88:9:3 from a solvent such as N-methyl pyrrolidinone (NMP). A doctor blade was used to achieve a cast of uniform density and the solvent was removed by gentle heating. The electrode sheet was then cut into pellets having a diameter of 1.1 cm and a thickness between 0.005 and 0.010 cm. The lithium anodes were punched from a 5 mm thick sheet of lithium metal (Foote Mineral Co.), and had a diameter of 1.65 cm. Two layers of microporous polypropylene (Celgard 3501 or 2500) were used for the separators. The 2325 coin cells described above were used for the lithium cells; however stainless steel disc springs (Belleville) and disc spacers were inserted in the cells to establish enough force on the cell assembly (18 kg) to ensure reliable internal contact. An exploded view of the coin cell assembly is shown in figure 7.4.2. These cells were assembled and crimped in a helium filled glove box.

Several different electrolytes were used in the cells having lithium metal anodes. They were 1M $LiPF_6$ (Hashimoto) in ethylene carbonate (EC, Aldrich)/-dimethyl carbonate (DMC) (1/2), 1M $LiClO_4$ in propylene carbonate (PC, Anachemia)/dimethoxyethane(DME, Anachemia) (1/1), 1M $LiClO_4$ in EC/diethyl carbonate (DEC, Aldrich) (1/1) and 1M $LiClO_4$ in PC/EC (1/1). The electrolyte solvents were first dried for 24 hours over activated molecular sieves and were then distilled using a spinning band column. In the case of PC and EC, distillations were carried out under vacuum. $LiPF_6$ was used without further

purification. $LiClO_4$ was dried under vacuum at 120 °C overnight. The water contents of the electrolyte solutions were measured using Karl-Fisher titration and were less than 50 ppm.

In some cases, x-ray powder diffraction patterns were obtained on cathodes extracted from previously cycled coin cells. A Scintag XDS 2000 with a theta-theta geometry and a copper x-ray tube was used to obtain the data. The diffractometer has a pyrolytic graphite monochromator in front of the detector. The samples were mounted on a zero background sample holder made from an oriented silicon wafer. The air sensitive samples were removed from the cells in an argon filled dry box and heat sealed in a polyethylene bag for the diffraction studies. In some cases, the cathodes could not be removed from the microporous polypropylene separator film. For these diffraction patterns, the second layer of separator from the same cell was used to establish an appropriate background correction which also includes contributions from dried electrolyte. Lattice parameters were calculated from the measured peak positions with the program TREOR (Werner, Eriksson and Westdahl 1985). Relative intensities of peaks were obtained by profile fitting to a Pearson VII curve shape.

The coin cells were cycled (i.e. charged and discharged) on cell cyclers custom built for the National Research Council. These fully automated and fully programmable cyclers were designed and built by John Murray and Rod McMillan of NRC, and Tom Felton of the University of British Columbia's

Department of Physics. They operate at a constant current anywhere from 0.1 μ A to 100 mA with the current controlled to 0.1 μA, or to 1 part in 4000 for higher currents. The current and voltage are measured every 30 s. The voltage can be resolved to 10 μV over the range 0 to 12 V.

All cell cycling was done galvanostatically between voltage limits. The results of the electrochemical evaluation of compounds in the series $Li_2Ni_yMn_{2-y}O_4$, $Li_2Cr_yMn_{2-y}O_4$, and of $LiFeO_2$ and orthorhombic $LiMnO_2$ are reported in chapter 6.

Chapter 3

Chemical Synthesis of Phases

3.1 3R - $LiCrO_2$

Samples of $LiCrO_2$ were prepared by heating an intimate mixture of fine powders of Cr_2O_3 and $LiOH{\cdot}H_2O$ or Li_2CO_3 in air. A sample made from Fisher Scientific Certified Cr_2O_3 and Anachemia Reagent $LiOH{\cdot}H_2O$ was heated slowly to 700 °C with thermal soaks, of several hours each, at 150 °C and at 400 °C. The sample was left at 700 °C for 3 days and then cooled back to room temperature in the furnace by shutting off the power. The product was a uniform olive green. The x-ray powder diffraction pattern of the product matched the pattern calculated for a 3R-type structure with the NRCVAX crystal structure system and the JCPDF card file for $LiCrO_2$.

Similarly, other samples of $LiCrO_2$ were prepared from Fisher Scientific Certified Cr_2O_3 and Aldrich 99.997% pure Li_2CO_3 by reaction for several days, in air, at 700 °C. Products prepared in this way had x-ray powder patterns which matched well to the that of the known structure. A typical example is shown in figure 3.1.1. These samples were used in the preparation of the $Li_2Cr_yMn_{2-y}O_4$ phases discussed in later section.

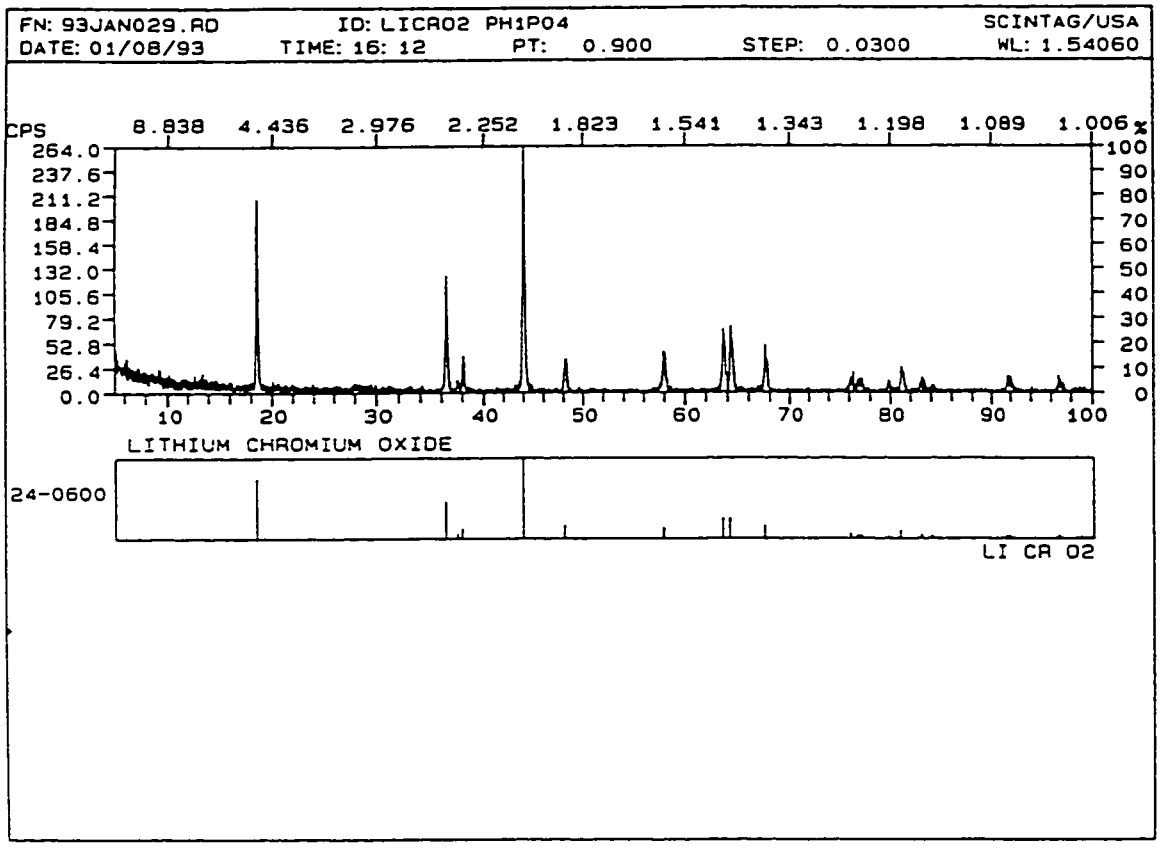

Figure 3.1.1 - X-ray diffraction pattern of $LiCrO_2$.

3.2 Orthorhombic - $LiMnO_2$

$LiMnO_2$ is known to exist in several phases. Two phases, whose crystal structures have been well characterized, are a high temperature orthorhombic phase and a tetragonal phase. Both structures involve cubic closest packing but they differ in the arrangement of the ordering of the lithium and manganese cations. The tetragonal form is normally written as $Li_2Mn_2O_4$ or λ-$LiMnO_2$. It has an atacamite-type structure which is often referred to as being spinel related.

Another type of lithium manganate has a spinel structure of composition $LiMn_2O_4$.

Both $LiMn_2O_4$ and λ-$Li_2Mn_2O_4$ have been used as cathodes in lithium ion cells (Tarascon and Guyomard 1991, and Tarascon *et al* 1991). λ-$Li_2Mn_2O_4$ has twice the nominal capacity of $LiMn_2O_4$ but it is reported to be hydroscopic and metastable (Mosbah, Verbaere and Tournoux 1983). Tarascon and Guyomard (1991) reported that λ-$Li_2Mn_2O_4$ slowly decomposes in ambient conditions to $LiMn_2O_4$. λ-$Li_2Mn_2O_4$ converts to the high temperature orthorhombic form, $LiMnO_2$, when heated in an argon atmosphere to 600 ^oC. It is prepared by intercalating lithium electrochemically, or chemically, into the $LiMn_2O_4$ spinel structure, as described in the two preceding references.

Samples of the orthorhombic form of $LiMnO_2$ were prepared from Fisher Scientific Certified MnO_2 and Aldrich 99.997% pure Li_2CO_3. The powdered reagents were intimately mixed by grinding and pelletizing. Then the pellets were loaded into high purity alumina crucibles, and fired in a horizontal tube furnace under a flow of argon gas. The mixture was first calcined at 600 to 650 °C for several hours to remove the CO_2, and then baked at 800 to 1000 °C for 1 to 3 days. Generally, one to two more grindings and firings were required to achieve a well crystallized product.

For example, the sample of $LiMnO_2$ used for the chemical and magnetic structure determinations described in chapters 4 and 5 was prepared in three small batches of about 20 mmoles (~ 2 g) each. One such batch was made by

combining 1.7882 g of Fisher Scientific Certified Reagent MnO_2 with 0.7615 g of Aldrich 99.997% $Li_2 CO_3$ and firing the mixture in flowing argon for 2 hours at 600 °C followed by 30 hours at 1000 °C. The x-ray diffraction pattern indicated that the dark brown product was orthorhombic $LiMnO_2$, but one very weak additional reflection was observed. The additional reflection occurred at the angle of the strongest peak of $LiMn_2O_4$. The sample was regound and fired again at 1000 °C in argon for a further 24 hours. The product was examined by x-ray diffraction. The resulting powder pattern, figure 3.2.1, is in good agreement with the JCPDF card file for $LiMnO_2$ (#35-749) from the International Centre for Diffraction Data. Figure 3.2.2 shows the trace of an x-ray diffraction pattern of the same sample after 11 months of storage in ambient conditions. The second diffraction pattern is substantially identical to the first. Unlike λ-$Li_2Mn_2O_4$, the orthorhombic form of $LiMnO_2$ is air and moisture stable. Two other batches of $LiMnO_2$ were prepared in an identical manner, and were combined with the first to provide enough material for neutron diffraction.

Another sample of $LiMnO_2$ was prepared from 2.6086 g of MnO_2 and 1.1087 g of Li_2CO_3 by firing overnight at 600 °C and then for 3 days at 900 °C under flowing argon. This material was used in the electrochemical studies described in chapter 6.

Scanning electron microscopy showed that the $LiMnO_2$ particles were layered platelets of varying sizes, typically between 5 and 20 microns. A

measurement of the surface area by krypton gas adsorption, using a Micromeritics ASAP 2000, found an area of 0.306(1) m^2/g of $LiMnO_2$.

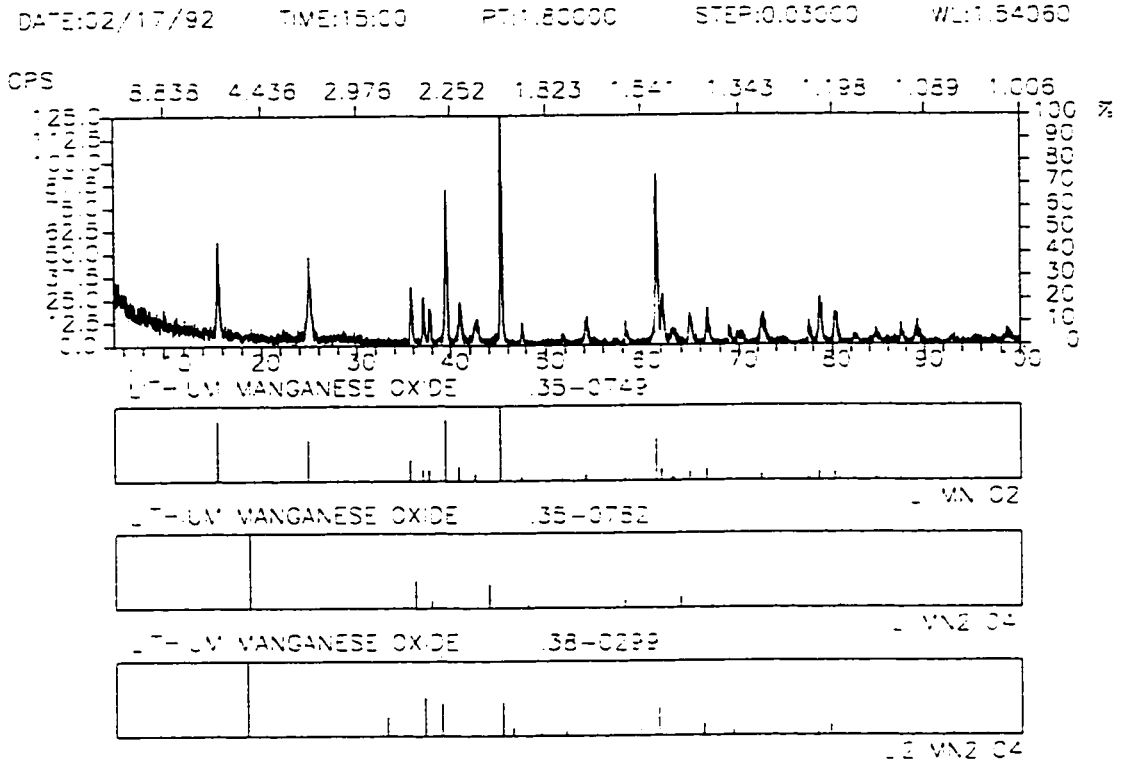

Figure 3.2.1 - X-ray diffraction pattern of orthorhombic $LiMnO_2$

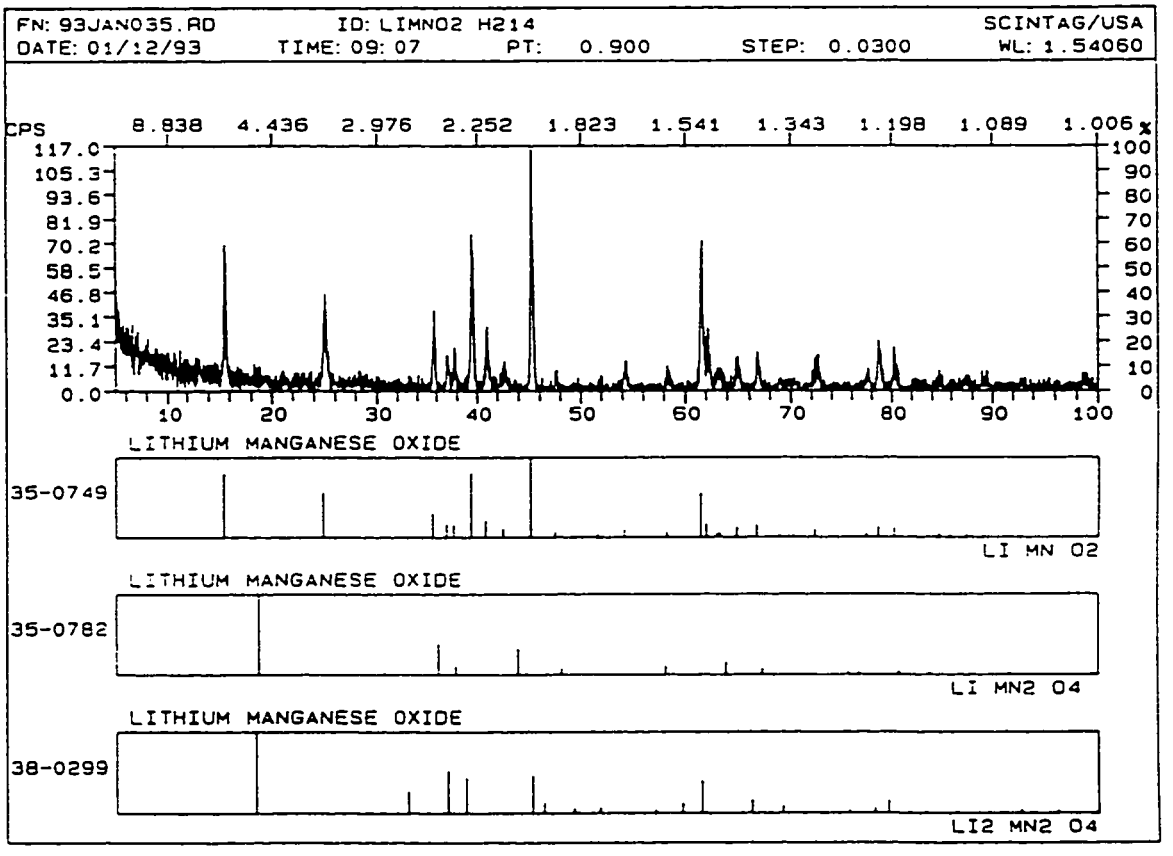

Figure 3.2.2 - Diffraction pattern of same sample of $LiMnO_2$ after 11 months.

3.3 $LiFeO_2$

$LiFeO_2$ is known in three polymorphs, all related to the rock salt structure. The three polymorphs differ in the ordering of the cations within the cubic closest packed oxygen framework. The high-temperature form has a disordered rock salt structure, the low-temperature tetragonal phase has a $LiScO_2$-type structure with ordered cations, and the third modification is a metastable monoclinic structure which is an intermediate product of the transformation of the cubic phase to the tetragonal (Famery *et al 1985).* It was found that a fourth polymorph can be prepared by ion exchange of α-$NaFeO_2$. α-$NaFeO_2$ has a layered 3R-type structure with a cubic closest packed oxygen lattice and is isotropic with $LiCoO_2$ and $LiCrO_2$.

α-$NaFeO_2$ can be made from either cubic closest packed γ-Fe_2O_3 or hexagonal closest packed α-Fe_2O_3 with the appropriate choice of sodium salt and reaction conditions. A second polymorph, β-$NaFeO_2$, has a wurtzite-like structure with oxygens forming hexagonal closest packing. Takeda *et al* (1980) showed that β-$NaFeO_2$ is obtained from reaction, in air, of Na_2CO_3 and α-Fe_2O_3 at 700 °C and from Na_2O_2 and α-Fe_2O_3 up to 400 °C, while α-$NaFeO_2$ was the product from Na_2CO_3 and γ-Fe_2O_3 reacted at 700 °C and from Na_2O_2 and γ-Fe_2O_3 at 300 °C.

For this work, the initial α-$NaFeO_2$ was made from α-Fe_2O_3 (Johnson, Matthey Co. *Specpure*) and NaOH (Anachemia 97%) by solid-phase interaction

in flowing argon in a two-stage heating, 330 °C for 5 hours followed by 500 °C for 24-48 hours. Generally two firings of 24-48 hours each were required to achieve a single phase sample. The reaction was carried out with a 20% excess of NaOH, which was removed from the final product by washing with methanol (to avoid hydrolysis). The product was then dried in air, overnight, at 110 °C.

$LiFeO_2$ was prepared by ion exchange of α-$NaFeO_2$ in molten $LiNO_3$ (Johnson- Matthey 99.8%), at 300 °C, in an argon atmosphere. The inert atmosphere is necessary to prevent the formation of Li_2CO_3. Complete exchange occurred in 48 hours in a fourfold excess of molten $LiNO_3$. The product was allowed to cool to room temperature in the furnace. The $LiFeO_2$ was separated from the residual nitrates by washing with methanol and then dried in air at 110 °C for several hours. The isolated $LiFeO_2$ had a brick red colour.

As shown in figure 3.3.1, the x-ray powder diffraction pattern of $LiFeO_2$ prepared by ion exchange looks very similar to the pattern for 3R-$LiNiO_2$. The diffraction peaks are broad but can be indexed to a cubic cell with a = 8.37 Å, a tetragonal cell with a = 2.95 Å and c = 9.64 Å, or a hexagonal cell with a = 2.96 and c = 14.7 Å.

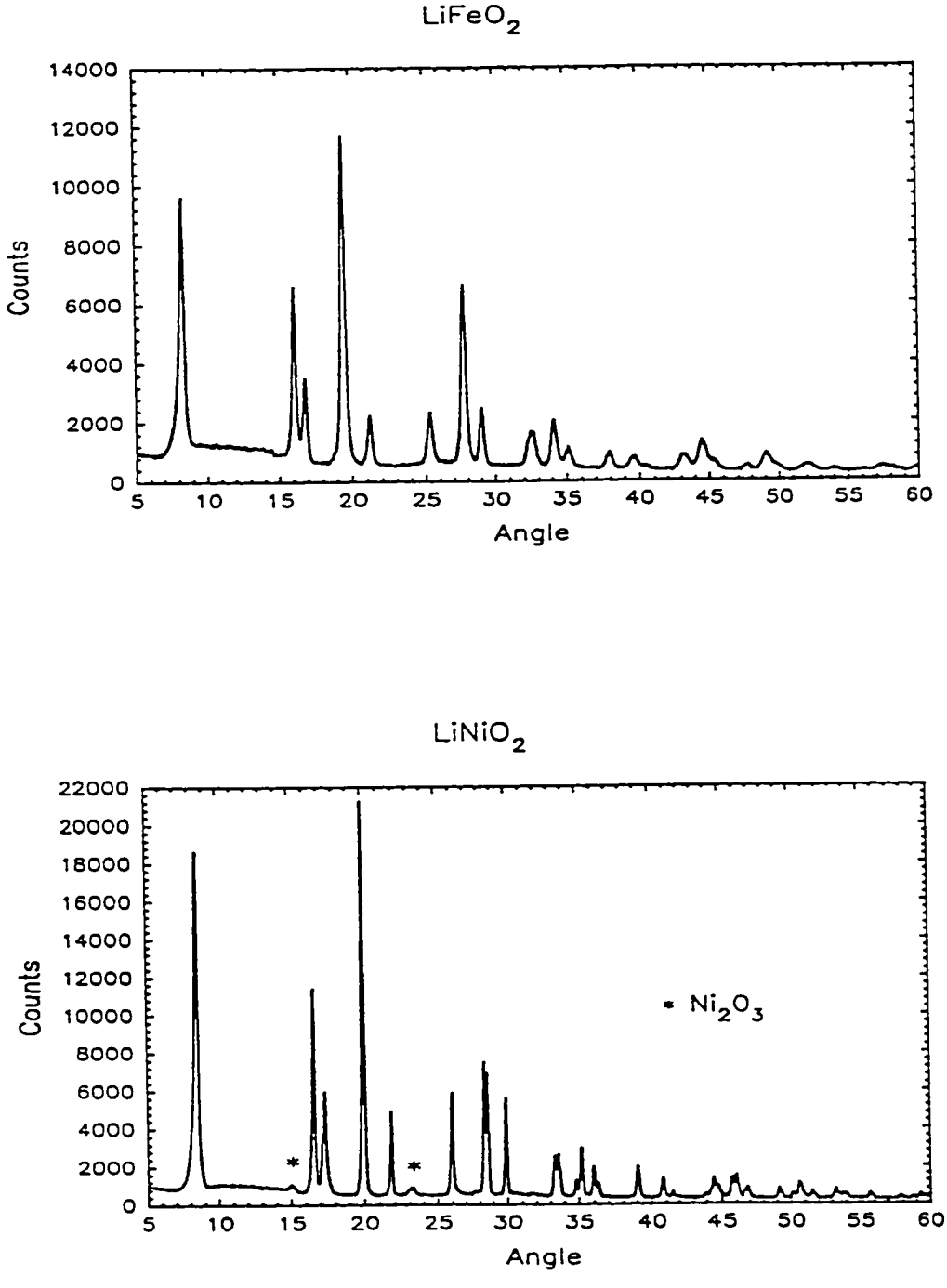

Figure 3.3.1 - Comparison of x-ray diffraction patterns of $LiFeO_2$ and $LiNiO_2$

3.4 3R - $LiNiO_2$

Samples of 3R -$LiNiO_2$ were made from equal weight mixtures of Anachemia reagent grade $LiOH{\cdot}H_2O$ and Aldrich nickel peroxide hydrate. The equal weight mixture was chosen to ensure that there was excess lithium hydroxide in the starting mixture. Each mixture was ground, pelletized and loaded into a gold crucible. The samples were heated under O_2 for 3 hours at 200 °C, followed by about 2 days at 800 °C. The product was washed with water, then ethanol and finally dried for several hours at 110 °C. The x-ray diffraction patterns of all samples could be indexed to a hexagonal cell with a = 2.88 Å and c = 14.2 Å, and were a good match to the JCPDF card file for $LiNiO_2$.

3.5 1T - Li_2NiO_2

The sample of 1T-Li_2NiO_2 used in this study, was prepared by Ulrich von Sacken and C. A. Michal of Moli Energy (1990) Ltd., and Dr. Jeff Dahn of Simon Fraser University. It was made by reacting $LiNiO_2$ with a 1.5 molar excess of Li^+ benzophenone$^-$ in tetrahydrofuran (THF) in an inert atmosphere glove box. After stirring the mixture overnight, the powder was recovered by filtration. The black powder was rinsed with dry THF, and then dried under vacuum. This gave predominantly 1T-Li_2NiO_2 with a small percentage of unreacted $LiNiO_2$. 1T-Li_2NiO_2 prepared in this way is poorly crystalline. Sample crystallinity was improved by a careful annealing which avoided conversion to the orthorhombic

form. This was accomplished by heating the sample at 225 °C for 14 hours under a flow of dry helium. An x-ray powder diffraction pattern taken after the annealing procedure revealed a small amount of decomposition to NiO, which probably resulted from the presence of some moisture in the helium. The full details of the preparation are given in Dahn, von Sacken and Michal 1990.

3.6 $Li_2Ni_yMn_{2-y}O_4$

$LiMnO_2$ has several known forms, none of which have a 3R-type structure like $LiNiO_2$. However, the possibility of forming a solid solution between $LiNiO_2$ and $LiMnO_2$ was worth exploring. The composition range $Li_2Ni_yMn_{2-y}O_4$ (with $0 < y < 2$) was investigated by solid state synthetic techniques. Finely ground powders of $LiNiO_2$ and $LiMnO_2$ (prepared as described earlier), or of MnO_2, NiO and Li_2CO_3 were intimately mixed by grinding and pelletizing, and then fired in an atmosphere of flowing argon, at temperatures ranging from 700 to 1000 °C. The progress of the reaction was monitored by powder x-ray diffraction. Single phase compounds were found over the composition range $1.0 \leq y \leq 1.65$, but for $y < 1.0$, a mixture of products was formed. The 1:1 phase, Li_2NiMnO_4, prepared from $LiMnO_2$ and $LiNiO_2$ reacted in flowing argon at 1000 °C, indexes to a hexagonal cell with a = 2.90 Å and c = 14.3 Å. The relative intensities of the diffraction peaks are consistent with a layered 3R structure, isostructural to $LiCoO_2$ or $LiNiO_2$, see figure 3.6.1. The 1:1 compound has a molar volume of 69.16 $Å^3$ as compared to 67.87 $Å^3$ for $LiNiO_3$ and 73.84 $Å^3$ for

$LiMnO_2$. The expansion of the cell on substitution of Mn for Ni indicates the Mn^{3+} is in the high spin state. Li_2NiMnO_4 was also prepared from MnO_2, NiO, and Li_2CO_3 reacted in an argon atmosphere at 800 °C, see figure 3.6.2. The reflections index to a hexagonal cell with a = 2.91 Å and c = 14.3 Å. However in this sample, the segregation of the lithium and the transition metals into separate layers does not appear to be complete. This is demonstrated by the fact that figure 3.6.2 has relative intensities with more resemblance to rocksalt type α-$LiFeO_2$ than does figure 3.6.1.

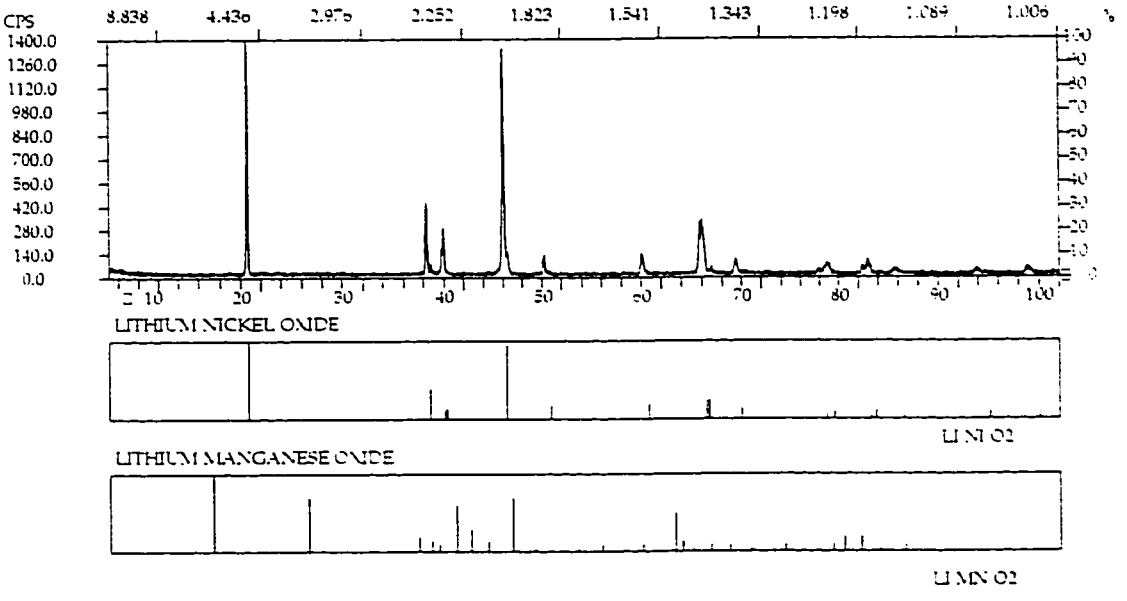

Figure 3.6.1 - Diffraction pattern of Li_2NiMnO_4 prepared at 1000°C.

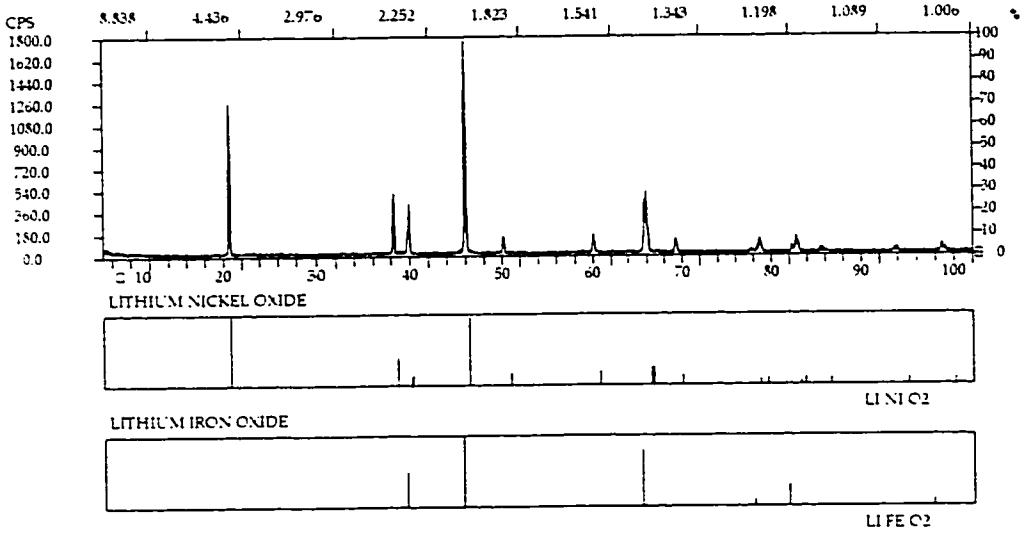

Figure 3.6.2 - Diffraction pattern of Li_2NiMnO_4 prepared at 800°C.

Intermediate compositions between $LiNiO_2$ and Li_2NiMnO_4 formed a solution phase, but exhibited a lesser degree of segregation of the transition metal and lithium atoms into separate layers than was observed for the end members. The powder x-ray diffraction patterns of these intermediate compositions more closely resembled an α-$LiFeO_2$ structure than a 3R structure. as demonstrated by figure 3.6.3. The dimensions of the hexagonal cell for $Li_2Ni_{1.65}Mn_{0.35}O_4$ (a=2.92 Å and c=14.3 Å) and for $Li_2Ni_{1.5}Mn_{0.5}O_4$ (a= 2.91 Å and c=14.3 Å) are very similar to those of Li_2NiMnO_4 (a=2.90 Å and c=14.3 Å). The degree of segregation of lithium atoms into separate layers appears to decrease as the nickel content increases (see figure 3.6.4). The phases with Mn/Ni ratios < 1 do have c/a ratios close to the value for ideal cubic packing, 4.90, and do not

show clear evidence of hexagonal symmetry. Consequently, they may be more accurately described as having a poorly ordered lithiated spinel structure.

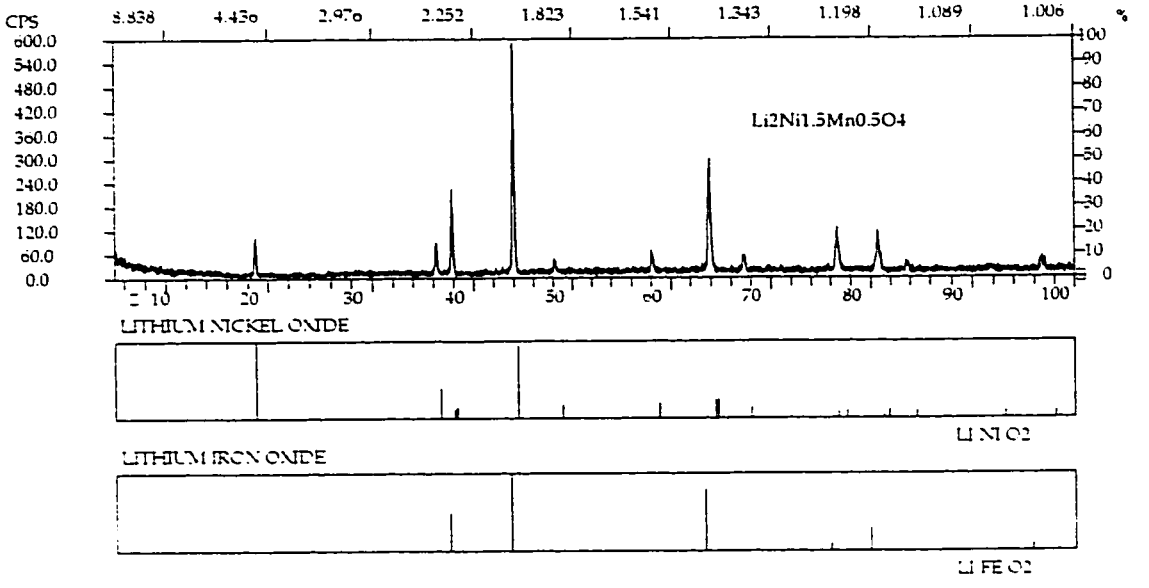

Figure 3.6.3 - X-ray diffraction pattern of $Li_2Ni_{1.5}Mn_{0.5}O_4$

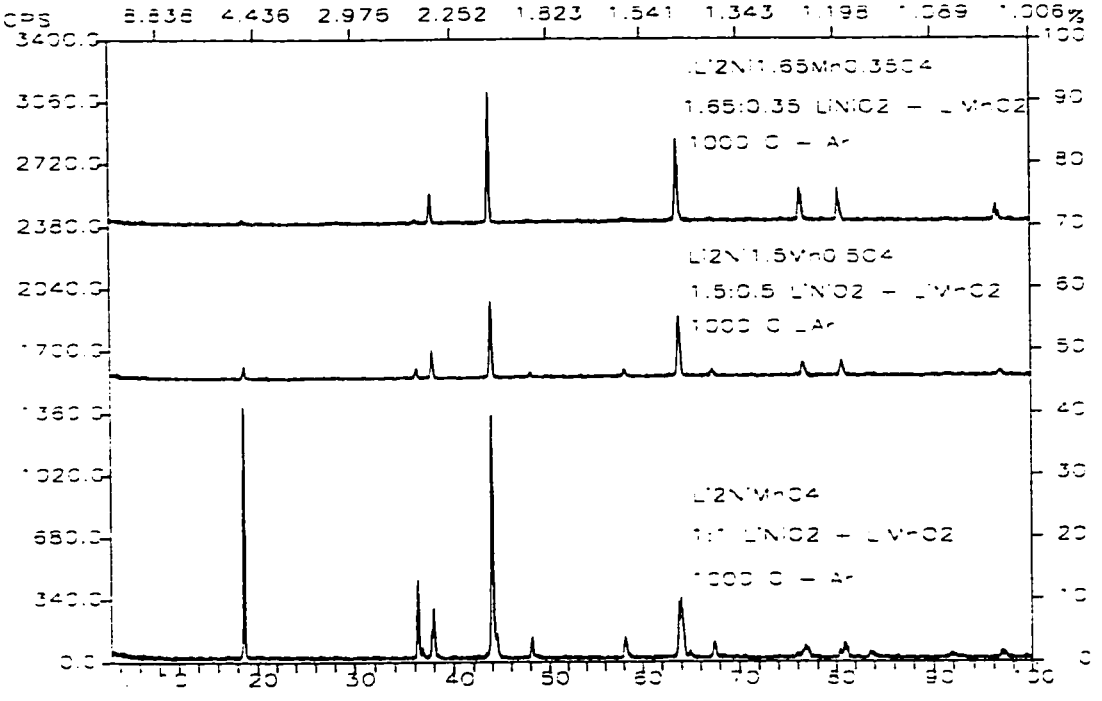

Figure 3.6.4 - Comparison of diffraction peak intensities for $Li_2Ni_yMn_{2-y}O_4$ phases

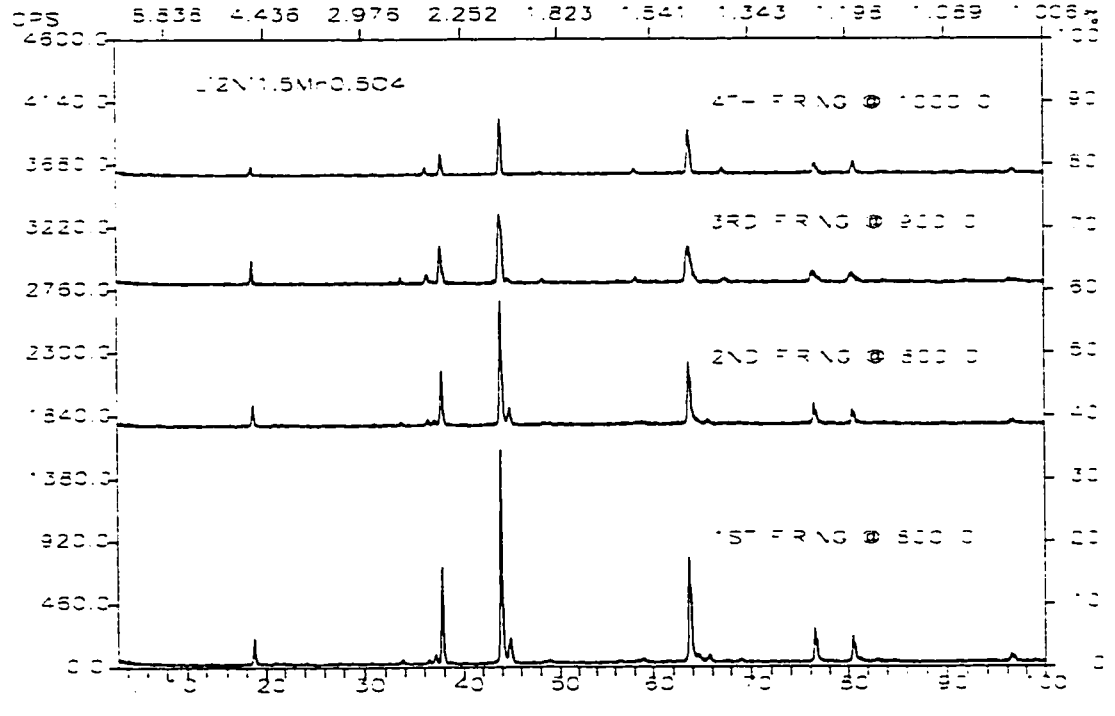

Figure 3.6.5 - Changes in $Li_2Ni_{1.5}Mn_{0.5}O_4$ with annealing temperature.

For the stoichiometry $Li_2Ni_{1.5}Mn_{0.5}O_4$, the preparation temperature appears to be critical. A sample prepared by multiple annealings at 1000 °C (sample H195), apparently adopts a cubic α-$LiFeO_2$ structure in which the lithium and transition metal atoms are randomly distributed over the cation sites. Further annealing at 700 °C does not result in any change in the diffraction pattern. Another sample fired twice at 800 °C (sample H215), has a diffraction pattern which corresponds to a mixture of $Li_xNi_{1-x}O_2$, Li_2MnO_3, and Li_2O, as shown in figure 3.6.5. Increasing the temperature to 900 °C for the third firing results in a diffraction pattern with two extra peaks corresponding to residual Li_2O. A fourth firing at 1000 °C leaves only peaks which can be assigned to a cubic cell with a = 8.243(2) Å, (or a hexagonal cell of dimensions a = 2.913(1) Å and c = 14.28(1) Å). The relative intensities of the peaks suggest a NaCl related structure with limited cation ordering.

Mixtures of $LiMnO_2$ and $LiNiO_2$ containing larger amounts of Mn than Ni were found to disproportionate to either $LiMnO_2$ and a phase, $Li_2Ni_yMn_{2-y}O_4$ with $y \geq 1.0$, or to Li_2MnO_3 and NiO. The products of the disproportionation depended on the stoichiometry of the starting mixture. For example, a 2:3 mixture of $LiNiO_2$ and $LiMnO_2$ resulted in the formation of NiO and Li_2MnO_3 (figure 3.6.6), and a 1:3 mixture of $LiNiO_2$ and $LiMnO_2$ formed a nickel rich solution phase with residual $LiMnO_2$ (figure 3.6.7).

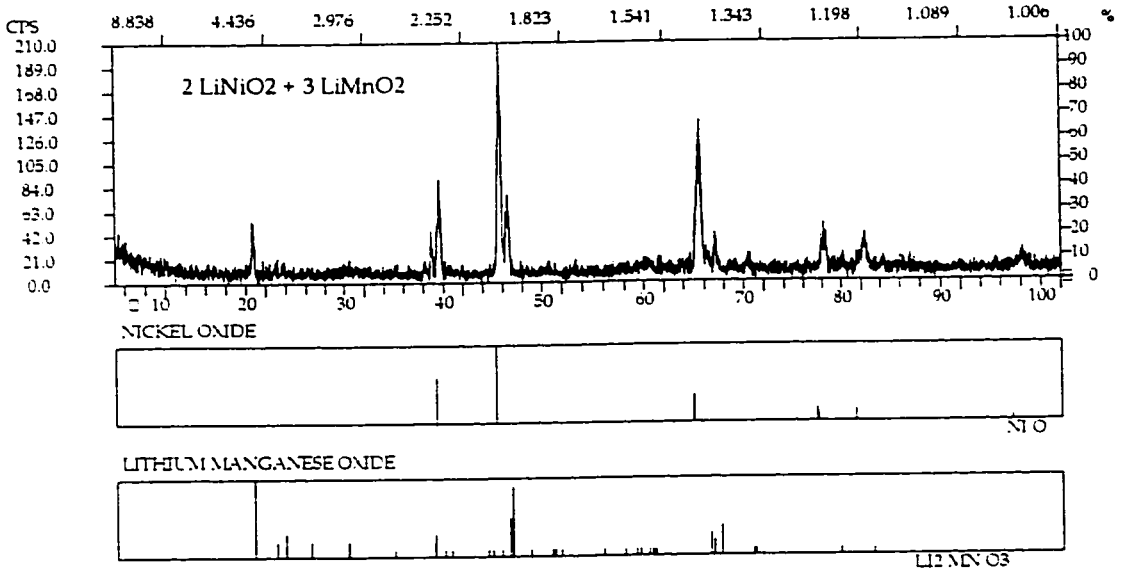

Figure 3.6.6 - Diffraction pattern from 2:3 mixture of $LiNiO_2$ and $LiMnO_2$.

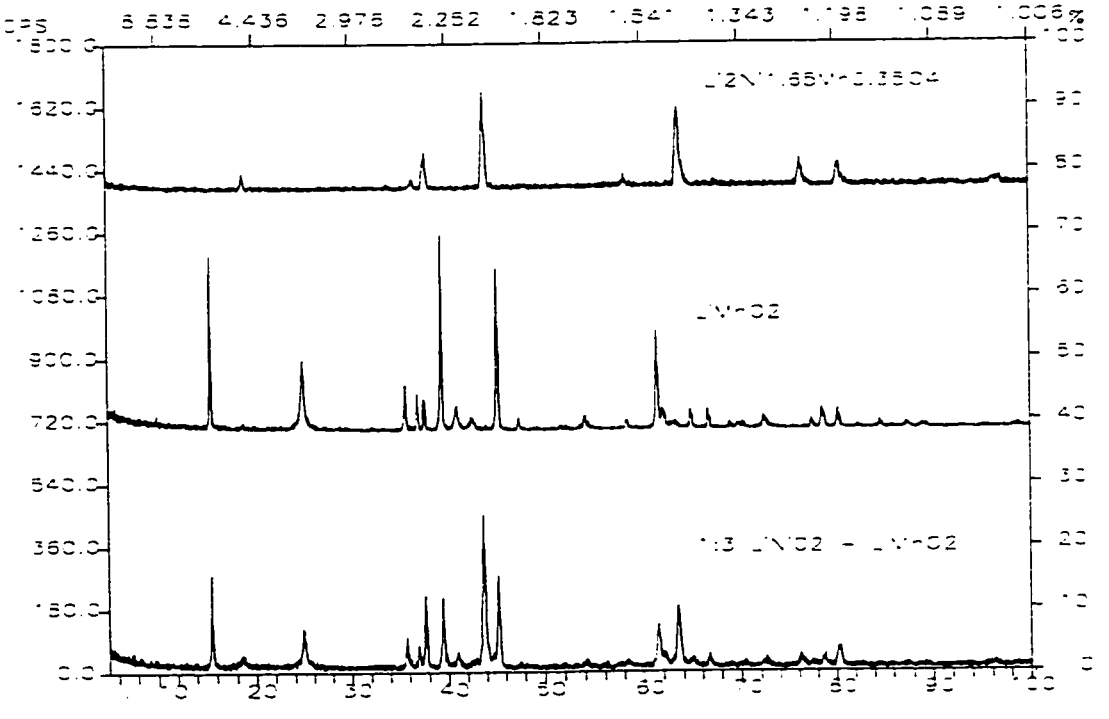

Figure 3.6.7 - Diffraction pattern from 1:3 mixture of $LiNiO_2$ and $LiMnO_2$.

3.7 $Li_2Cr_yMn_{2-y}O_4$

Although $LiMnO_2$ and $LiCrO_2$ have very different structures it was hoped that single phase compounds could be prepared in the series $Li_2Cr_yMn_{2-y}O_4$. Attempts were made to prepare Li_2CrMnO_4 from orthorhombic $LiMnO_2$ and 3R - $LiCrO_2$ (prepared as described earlier), and from Li_2CO_3 (Aldrich 99.997), Cr_2O_3 (Fisher Certified Reagent), and MnO_2 (Fisher Certified Reagent). The powders were intimately mixed, pressed into pellets and loaded into alumina crucibles. They were fired in a flow of argon at 600 °C for 3 hours, and then, at 1000 °C for 4 days. The x-ray diffraction patterns of the two samples from different starting materials, collected after the first firing, were very similar. The lines were, however, quite broad. The samples were ground and fired two more times for 3 days each time at 1000 °C under a flow of argon. This resulted in x-ray powder patterns, figure 3.7.1, with sharp lines which could be indexed to a tetragonal cell of approximate dimensions a = 5.764 Å and c = 8.596 Å, for both samples. The two samples, dark brown in colour, were combined and used as the active material in the cathodes of the three electrochemical cells discussed in chapter 6.

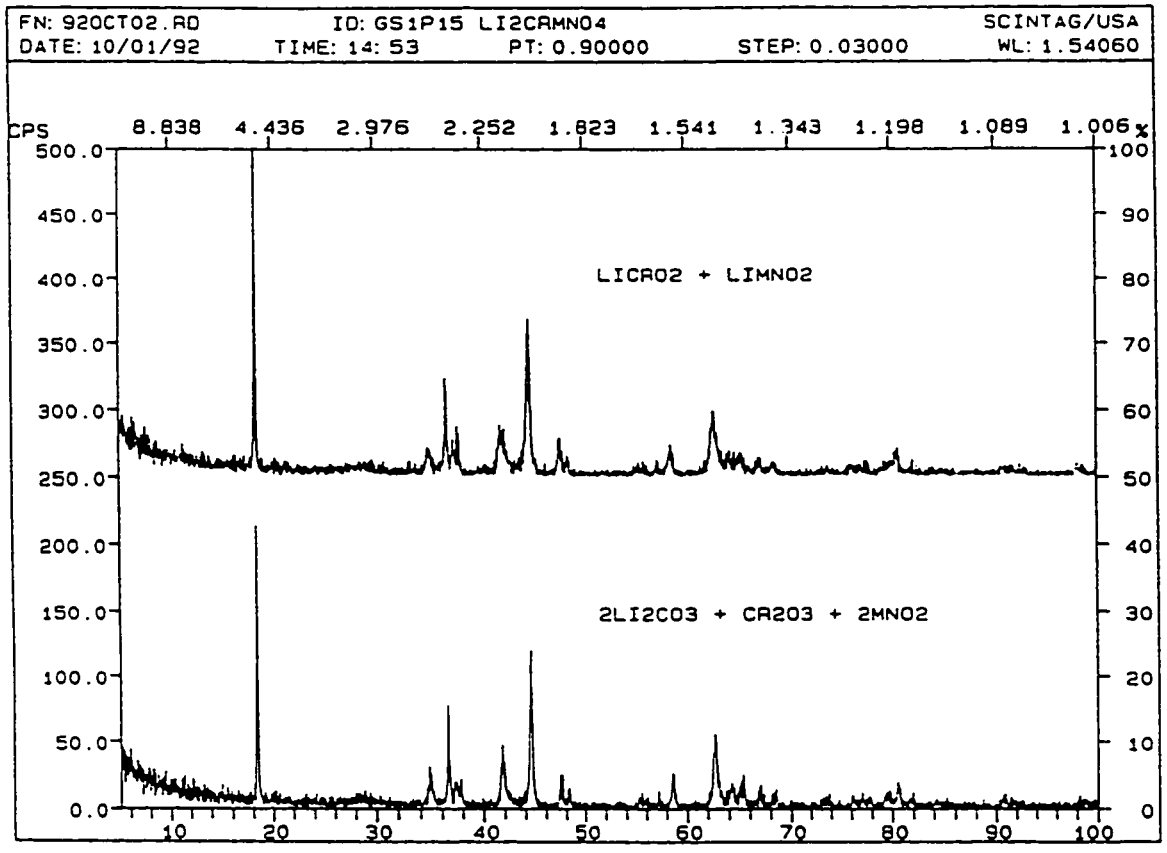

Figure 3.7.1 - X-ray diffraction patterns for two samples of Li_2CrMnO_4.

Similarly, a single phase product of composition $Li_2Cr_{1.5}Mn_{0.5}O_4$ was prepared from 0.1455 g of orthorhombic $LiMnO_2$ and 0.4248 g of 3R-$LiCrO_2$ fired for 3 days, at 1000 °C, in flowing argon. Two subsequent grindings and re-firings were required to achieve an x-ray powder pattern with sharp reflections. The diffraction pattern for $Li_2Cr_{1.5}Mn_{0.5}O_4$ could be indexed to a hexagonal cell of dimensions a = 2.903(5) Å and c = 14.422(4) Å. This represents a small shift from the lattice parameters for $LiCrO_2$ (a = 2.899 Å and c = 14.412 Å). The

relative intensities of the peaks were similar to those of $LiCrO_2$ suggesting that $Li_2Cr_{1.5}Mn_{0.5}O_4$ has a 3R structure. The material had a dark brown colour. To verify that a reaction had indeed occurred, a 3:1 mixture of $LiCrO_2$ and $LiMnO_2$ was ground together and compared to a sample of $Li_2Cr_{1.5}Mn_{0.5}O_4$. The unreacted mixture was much greener in colour than the $Li_2Cr_{1.5}Mn_{0.5}O_4$. In an attempt to determine if some Li_2O might have been lost during the preparation procedure, the $Li_2Cr_{1.5}Mn_{0.5}O_4$ was mixed with an additional 10 mole percent of $LiOH{\cdot}H_2O$ and fired in flowing argon at 800 °C for three days. The relative intensities and positions of the peaks in the diffraction patterns were not changed, but the peaks did sharpen up noticeably. This data, given in figure 3.7.2, indexed with a large figure of merit to a hexagonal cell of dimensions a = 2.905(9) Å and c = 14.444(2) Å.

A larger batch, about 7 g, of $Li_2Cr_{1.5}Mn_{0.5}O_4$ was synthesized for use in electrochemical evaluations. This was prepared from 5.209 g of $LiCrO_2$ and 1.790 g of orthorhombic $LiMnO_2$ by intimately mixing the powders and firing them three times, for three days each, at 1000 °C in argon. The product was reground between the firings. An x-ray powder pattern taken after the third firing showed only reflections which could be indexed to a hexagonal unit cell of dimensions a = 2.909(2) Å and c = 14.442(5) Å.

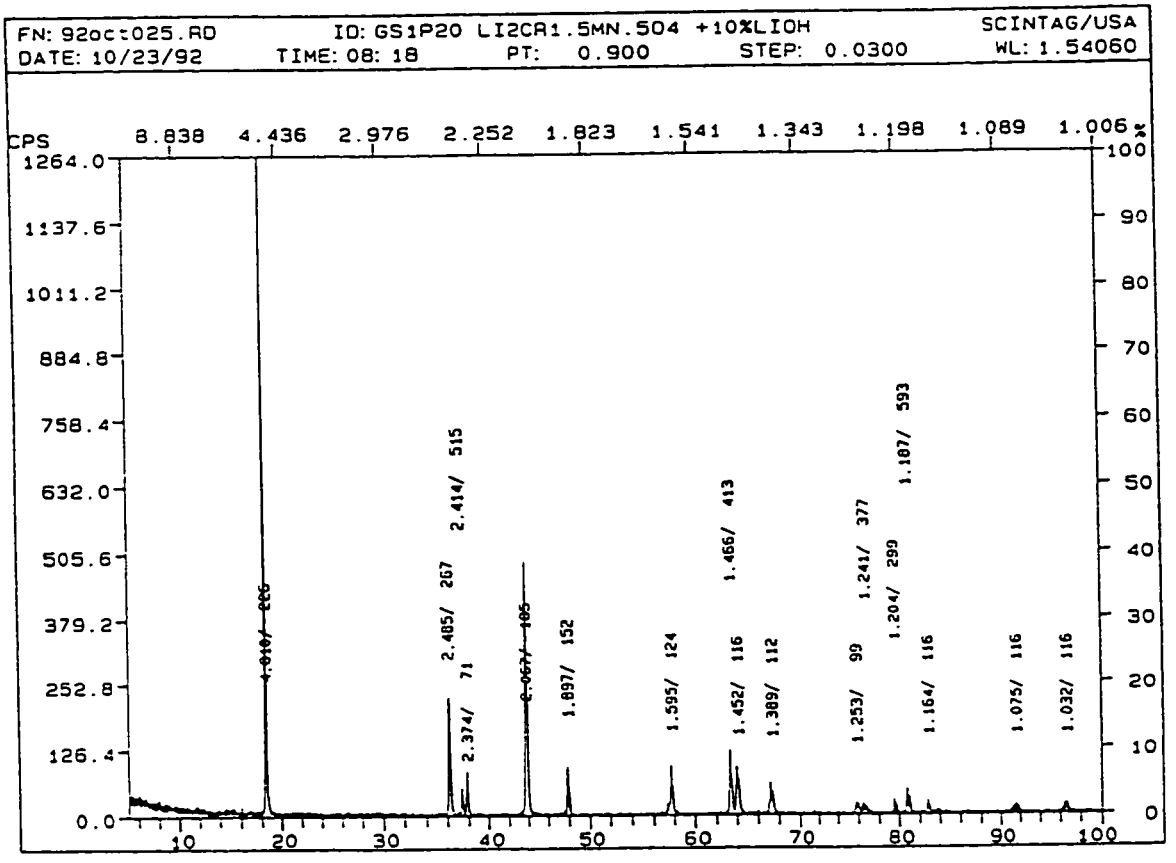

Figure 3.7.2 - X-ray diffraction pattern of $Li_2Cr_{1.5}Mn_{0.5}O_4$.

A sample of $Li_2Cr_{0.5}Mn_{1.5}O_4$ was prepared from 0.3420 g of orthorhombic $LiMnO_2$ and 0.1104 g of 3R-$LiCrO_2$. The intimately mixed powders were fired three times, for three days each, at 1000 °C in a flow of argon gas. The product was dark brown in colour. The x-ray diffraction pattern, for this sample of $Li_2Cr_{0.5}Mn_{1.5}O_4$, still had fairly broad lines after three firings but could be indexed to a tetragonal cell of approximate dimensions a = 5.713 Å and c = 8.952 Å.

A larger sample of $Li_2Cr_{0.5}Mn_{1.5}O_4$ was made from 1.898 g of $LiCrO_2$ and 5.874 g of $LiMnO_2$. It was annealed at 1000 °C in argon for four intervals of 2 to 3 days each with a vigorous regrinding between each firing. Reflections corresponding to residual $LiMnO_2$ were evident in the x-ray powder patterns of the sample until after the fourth firing. The reflections were still somewhat broad after the fourth firing, but they could all be assigned to a tetragonal cell of approximate dimensions a = 5.74 Å and c = 8.95 Å. This sample of $Li_2Cr_{0.5}Mn_{1.5}O_4$ was used for electrochemical evaluations (see chapter 6).

It was found that $Li_2Cr_{0.5}Mn_{1.5}O_4$ can also be made from Li_2CO_3, Cr_2O_3 and MnO_2. A fourth sample of $Li_2Cr_{0.5}Mn_{1.5}O_4$ was made from 2.776 g of Aldrich 99.997% pure Li_2CO_3, 4.900 g of Fisher Certified Reagent MnO_2 and 1.428 g Fisher Certified Reagent Cr_2O_3. The mixture was fired in high purity alumina crucibles under flowing argon. The furnace was held initially at 650 °C for three hours then raised to 1000 °C and left for three days. Two more firings, for three days each at 1000 °C were required to obtain a sample with moderately sharp x-ray diffraction pattern. The final pattern could be approximately indexed to a tetragonal cell of dimensions a = 5.72 Å and c = 8.97 Å. Typical diffraction patterns for $Li_2Cr_{0.5}Mn_{1.5}O_4$, prepared from either precursors, are presented in figure 3.7.3.

A large number of other compositions were prepared in a similar manner from either $LiMnO_2$ and $LiCrO_2$, or from Li_2CO_3, MnO_2 and Cr_2O_3. Single phase products were obtained over the entire composition range. A change of

symmetry occurs between hexagonal $Li_2Cr_{1.4}Mn_{0.6}O_4$ and tetragonal $Li_2Cr_{1.3}Mn_{0.7}O_4$. The extinctions and relative intensities of x-ray powder patterns are consistent with the hexagonal phases having a 3R-type structure like $LiCrO_2$ and the tetragonal phases having a λ-$Li_2Mn_2O_4$ type structure.

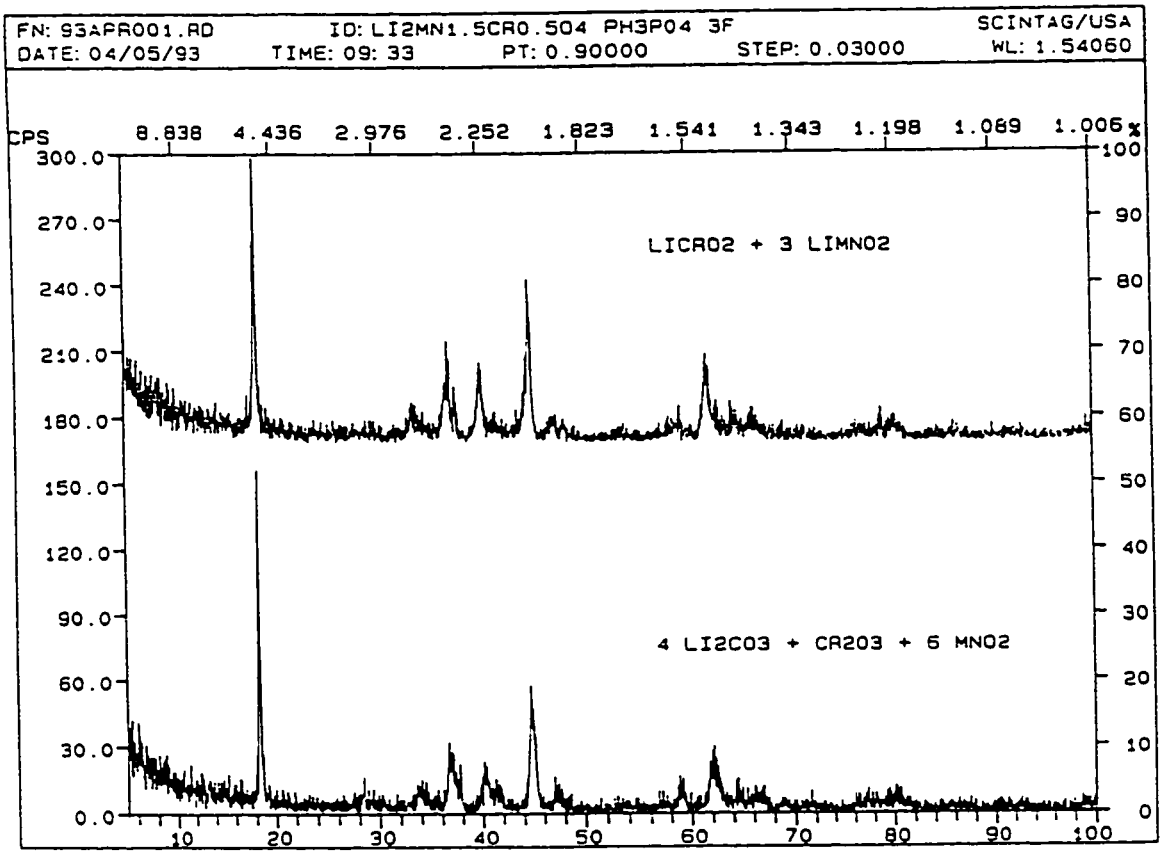

Figure 3.7.3 - X-ray diffraction pattern of $Li_2Cr_{0.5}Mn_{1.5}O_4$.

Chapter 4

Chemical Structures

4.1 Orthorhombic - $LiMnO_2$

A sample of orthorhombic $LiMnO_2$, prepared as described in chapter 3, was examined by powder x-ray and neutron diffraction. A single crystal x-ray study of this phase was reported in 1975 by Hoppe, Brachtel and Jansen. As demonstrated by figure 3.2.1, the powder x-ray diffraction pattern of this sampie matches the JCPDF card file for orthorhombic $LiMnO_2$.

In preparation for an examination of the magnetic structure by low temperature neutron diffraction, a room temperature neutron diffraction data set was collected and refined. The neutron powder diffraction data were collected at the McMaster Nuclear Reactor using 1.39 Å neutrons obtained from a [200] copper monochromator and a detector described by Greedan and O'Reilly (1987). The raw data, collected with a position-sensitive detector, were corrected for the detector geometry according to the procedures of Tompson *et al* (1984). A Rietveld profile refinement program called *Rietan* (Izumi 1989) was used for the structure refinement. The refinement was initiated with the atomic positions of the previous single crystal x-ray refinement. Twenty parameters were allowed to refine: three lattice parameters, four atomic z-coordinates, four isotropic

thermal parameters, a scale factor, a detector zero-point offset, six background parameters and the half-width parameter, w. The observed (symbols) and calculated (line) neutron diffraction patterns are plotted in figure 4.1.1. The refined structure, tabulated in table 4.1.1, agrees well with Hoppe's refinement from single crystal x-ray diffraction data.

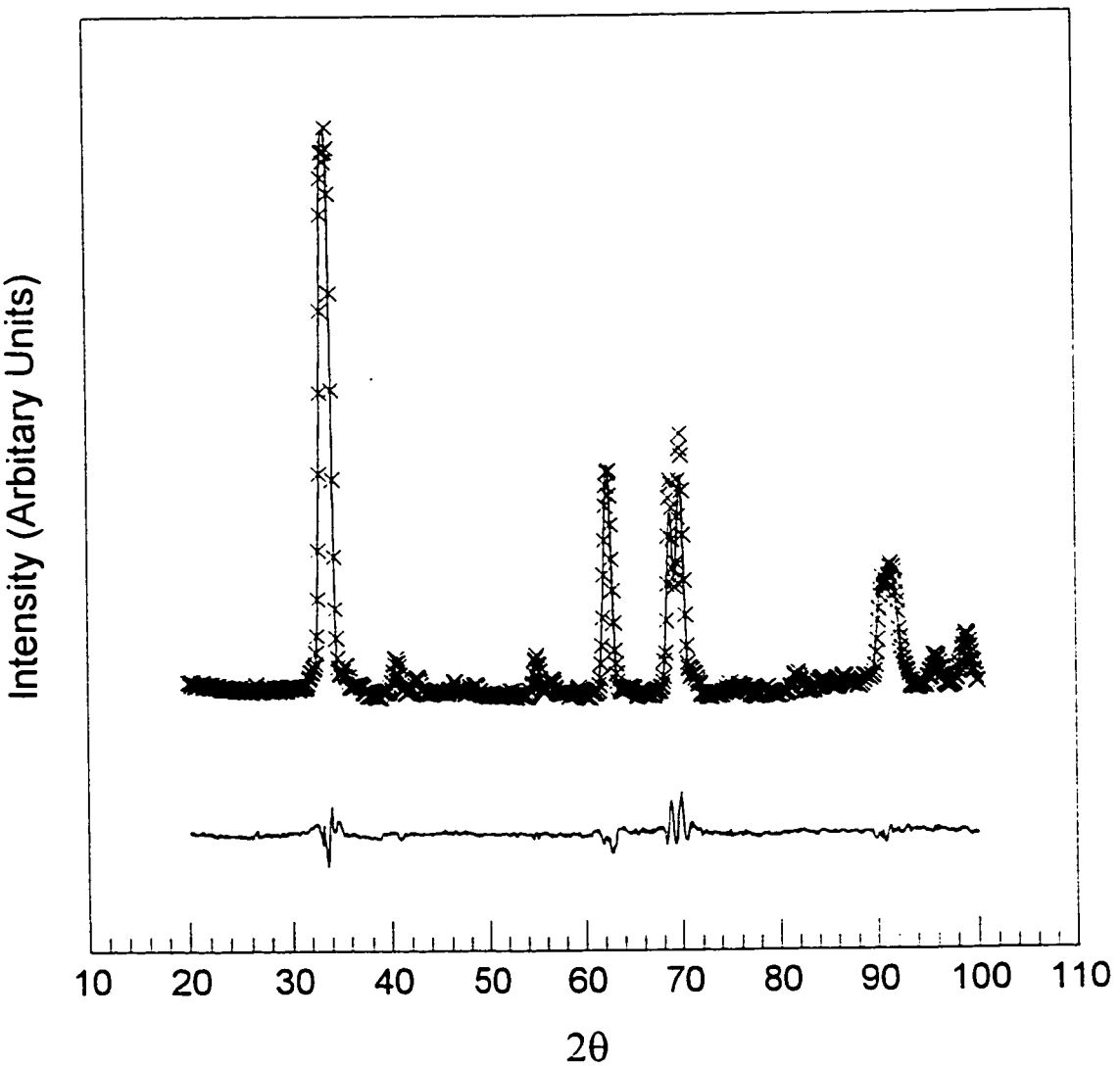

Figure 4.1.1 - Refinement of neutron diffraction data for $LiMnO_2$.

Table 4.1.1 - Rietveld refinement of room temperature neutron diffraction data for $LiMnO_2$.

Atom	x	y	z	B ($Å^2$)	Occup.
Mn (2a)	0.25	0.25	0.632(6)	0.5(4)	1.0
Li (2a)	0.25	0.25	0.10(1)	0.2(7)	1.0
O (2b)	0.25	0.75	0.144(4)	0.4(3)	1.0
O (2b)	0.25	0.75	0.602(5)	0.7(3)	1.0

Space Group Pmmn (D^{13}_{2d}) Wavelength 1.3913 Å

Lattice Parameters: a = 2.8049(3) Å, b = 4.5757(6) Å, c = 5.7495(7) Å

Half-width Parameters: U = 1.50, V = -1.20, W = 0.779(8)

Scattering lengths: Li (-0.190), Mn(-0.373), O (0.5803)

R - factors: Weighted profile R = 7.58 Profile R = 5.84

Bragg R = 4.93 Expected R = 3.42

The bonding in the $LiMnO_2$ structure gives the cations an irregular octahedral coordination with an average manganese - oxygen distance of 2.047 Å and an average lithium - oxygen distance of 2.167 Å. The lithium and manganese atoms each form corrugated layers sandwiched between similar layers of close packed oxygen atoms. The structure is, thus, quite different from that of isostoichiometric λ-$Li_2Mn_2O_4$. The structure of λ-$Li_2Mn_2O_4$ is related to the

spinel structure of $LiMn_2O_4$ in that the lithium atoms occupy the same channels. However, in $LiMn_2O_4$, the lithium atoms occupy tetrahedral sites and the overall symmetry is cubic. In λ-$Li_2Mn_2O_4$ the lithium atoms are in the neighbouring 6-coordinate sites and the overall symmetry is reduced to tetragonal by a Jahn-Teller distortion of the Mn^{3+} ions.

Table 4.1.2 - Bond Lengths and Angles in Orthorhombic $LiMnO_2$

Bond Lengths (Å)

Mn - O (1) x 2	1.904 (38)	Li - O (1) x 2	2.302 (8)
Mn - O (2) x 2	2.294 (6)	Li - O (1) x 2	1.984 (57)
Mn - O (2) x2	1.943 (45)	Li - O (2) x 2	2.214 (66)

Bond Angles (degrees)

O (1) - Mn - O (1)	94.9	O (1) - Li - O (1)	94.5
O (1) - Mn - O (2)	86.4	O (1) - Li - O (1)	167.4
O (1) - Mn - O (2)	178.8	O (1) - Li - O (2)	95.7
O (1) - Mn - O (2)	178.8	O (1) - Li - O (2)	174.3
O (1) - Mn - O (2)	86.4	O (1) - Li - O (2)	85.2
O (2) - Mn - O (2)	92.4	O (2) - Li - O (2)	78.6

4.2 $LiFeO_2$

A phase of stoichiometry $LiFeO_2$ was prepared as described in chapter 3. The x-ray diffraction pattern of this material, shown in chapter 3, is very similar to that of 3R-$LiNiO_2$. However, since the material was made by ion exchange at low temperature, the diffraction pattern has very broad peaks which can be indexed to several possible symmetries, including a cubic cell with a = 8.37 Å, a tetragonal cell with a = 2.95 Å and c = 9.64 Å, or a hexagonal cell with a = 2.96 and c = 14.7 Å. The similarity in peak intensities to that of 3R-$LiNiO_2$ suggests that this phase of $LiFeO_2$ has either a hexagonal 3R-type structure or a cubic spinel-related structure like $Li_2Ti_2O_4$. Reimers, Li and Dahn (1993) have demonstrated that the relative intensities and peak positions of these two structures can be identical. Room temperature neutron diffraction is not able to distinguish between these two structures any better than x-ray diffraction can; however, it is more sensitive to scattering from lithium atoms and can be used to verify their probable locations in the structure.

A neutron diffraction pattern on this phase was collected at the McMaster nuclear reactor on the position sensitive detector described in the preceding section. The pattern, shown in figure 4.2.1, was refined with a Rietveld profile refinement program called Rietan (Izumi 1989). The four small broad peaks in the region between 18 and 30 degrees in 2θ are from Li_2CO_3 formed during the synthesis of the sample. These four peaks are, by far, the strongest intensities in the neutron diffraction pattern of Li_2CO_3. The region

between 18 and 30 degrees was, therefore, excluded in the refinements. Refined structures were calculated with both the hexagonal 3R model and the cubic spinel-related model. The results, shown in figures 4.2.2 and 4.2.3, demonstrate that there is no basis to distinguish between these two models. The details of the refinements are tabulated in tables 4.2.1 to 4.2.4. In addition to the variables indicated, six background parameters were also refined.

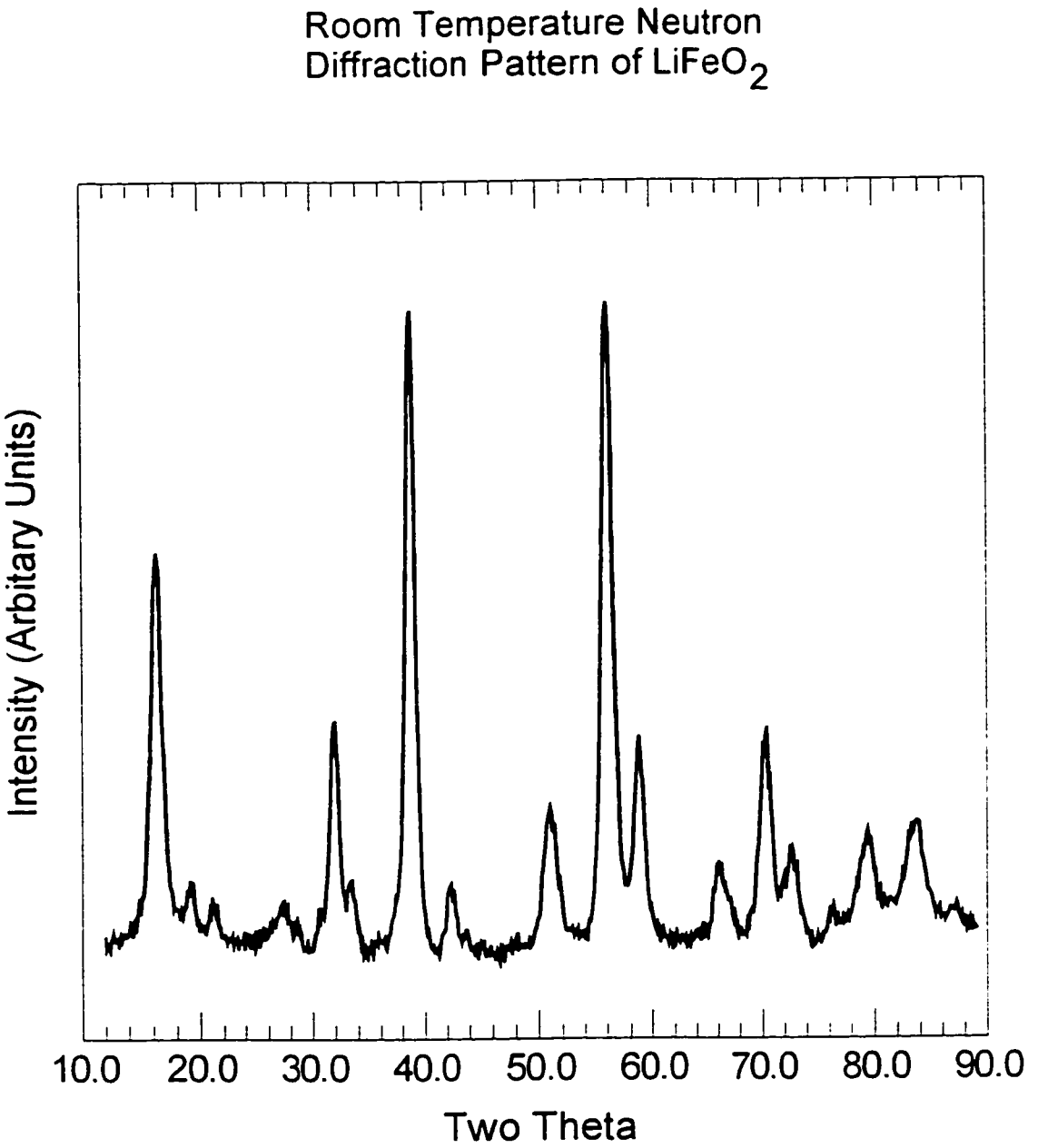

Figure 4.2.1 - Room temperature neutron diffraction pattern of $LiFeO_2$.

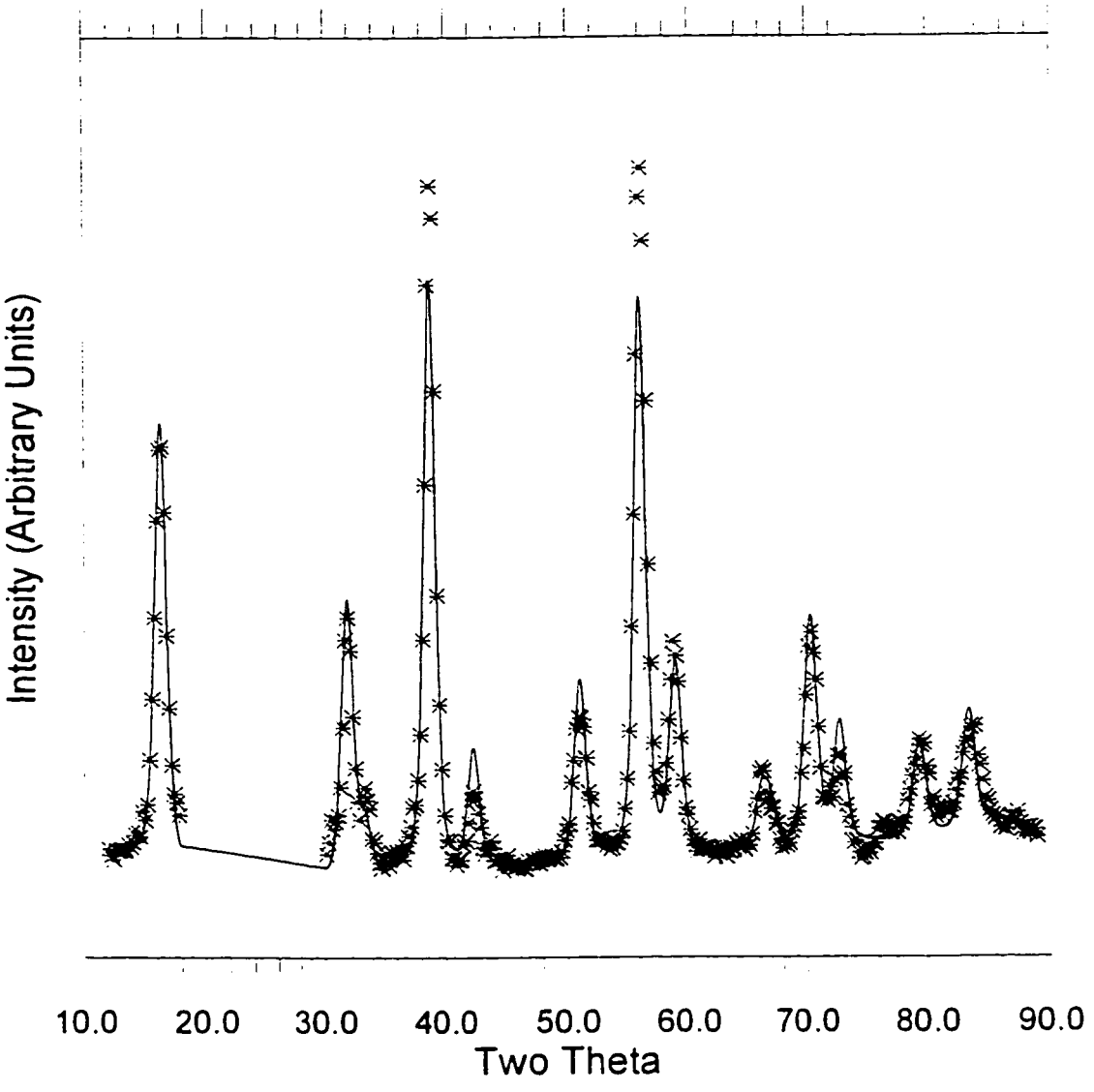

Figure 4.2.2 - Hexagonal model refinement of neutron data for $LiFeO_2$.

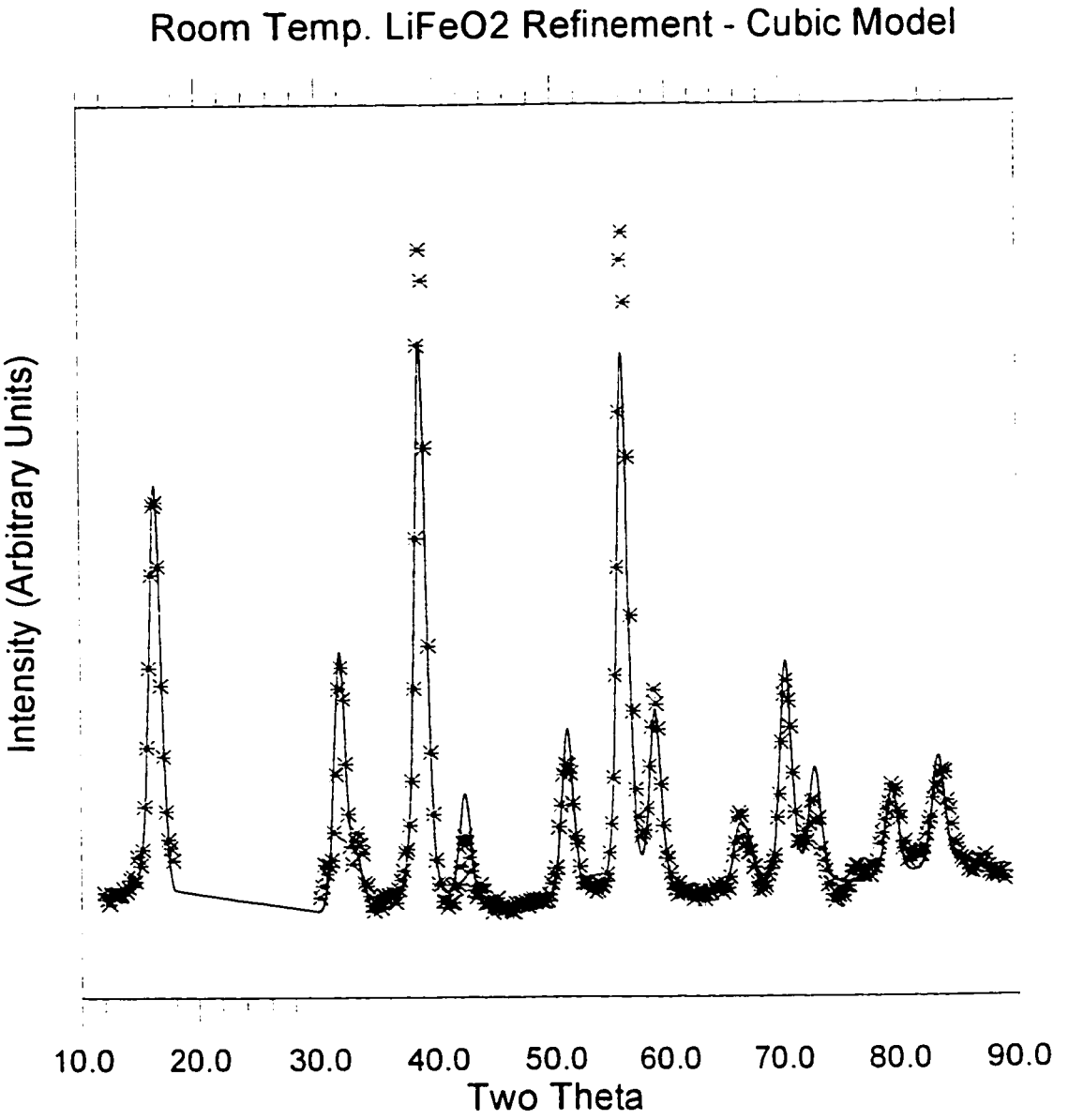

Figure 4.2.3 - Cubic model refinement of neutron data for $LiFeO_2$.

Table 4.2.1 - Rietveld Refinement of Neutron Data Using 3R Model

Space Group R -3 M (D^5_{3d}) Wavelength 1.3951 Å

Cell Parameters: a = 2.956(1) Å and c = 14.530(8) Å

Scattering Lengths: Li (-0.190), Fe (0.954), O (0.5803)

Half-width Parameters: U =1.5, V = -1.2 and W = 1.53(4)

Zero Point Shift = -0.23(1) Scale = 1.15(2)

Atom	x	y	z	B (Å^2)	Occup.
Li (3b)	0.0	0.0	0.5	2.0	1.0
Fe (3a)	0.0	0.0	0.0	1.3(6)	1.0
O (6c)	0.0	0.0	0.255(2)	0.6	1.0

R Factors: R.WP. = 10.44 R.P. = 8.50 R.E. = 2.97

R.I. = 7.95 R.F. = 4.62

A further refinement in which the lithium and iron atoms were allowed to randomly occupy the 3a and 3b sities resulted in a modest improvement in the weighed profile R-factor and a larger increase in the Bragg R-factor (table 4.2.2). However, the refinement suggests that there may be a slight deficiency of lithium in the structure, as prepared. A similar problem occurs in the preparation of 3R-$LiNiO_2$.

Table 4.2.2 - Rietveld Refinement of Neutron Data Using 3R Model with Cation Occupancy Refined

Space Group R -3 M (D^5_{3d}) Wavelength 1.3951 Å

Cell Parameters: a = 2.955(1) Å and c = 14.539(7) Å

Scattering Lengths: Li (-0.190), Fe (0.954), O (0.5803)

Half-width Parameters: U =1.5, V = -1.2 and W = 1.41(3)

Zero Point Shift = -0.23(1) Scale = 1.19(2)

Atom	x	y	z	B ($Å^2$)	Occup.
Li (3b)	0.0	0.0	0.5	2.0	0.92(4)
Li (3a)	0.0	0.0	0.0	2.0	0.04(7)
Fe (3a)	0.0	0.0	0.0	1.3	0.96(7)
Fe (3b)	0.0	0.0	0.5	1.3	0.08(4)
O (6c)	0.0	0.0	0.256(2)	0.6	1.0

R Factors: R.WP. = 9.04 R.P. = 7.50 R.E. = 2.96

R.I. = 9.93 R.F. = 5.67

The refinement using the cubic spinel-related structural model was almost identical to that of the hexagonal 3R model. This refinement allowed six background parameters to refine. The details are given in table 4.2.3.

Table 4.2.3 - Rietveld Refinement of Neutron Data Using Spinel Related Model

Space Group F D -3 M (O^7_h) Wavelength 1.3951 Å

Cell Parameter: a = 8.367(2) Å

Scattering Lengths: Li (-0.190), Fe (0.954), O (0.5803)

Half-width Parameters: U =1.5, V = -1.2 and W = 1.56(4)

Zero Point Shift = -0.25(1) Scale = 0.072(1)

Atom	x	y	z	B (Å^2)	Occup.
Li (16c)	0.0	0.0	0.0	2.0	1.0
Fe (16d)	0.5	0.5	0.5	1.3(6)	1.0
O (32e)	0.254(2)	0.254(2)	0.254(2)	0.6	1.0

R Factors: R.WP. = 10.62 R.P. = 8.52 R.E. = 2.97

R.I. = 7.72 R.F. = 4.33

Refinements which allowed lithium or iron atoms to occupy tetrahedral sites at 0.125, 0.125, 0.125 or at 0.375, 0.375,0.375 resulted in higher R-factors. Allowing the lithium and iron atoms to randomly share the 16 c and 16 d sites resulted in a small improvement in the weighted profile R-factor and a larger

increase in the Bragg R-factor. This refinement, detailed in table 4.2.4, is probably no better than the previous one in table 4.2.3.

Table 4.2.4 - Rietveld Refinement of Neutron Data Using Spinel Related Model with Cation Occupancy Refined

Space Group F D -3 M (O^7_h) Wavelength 1.3951 Å

Cell Parameter: a = 8.365(2) Å

Scattering lengths: Li (-0.190), Fe (0.954), O (0.5803)

Half-width Parameters: U =1.5, V = -1.2 and W = 1.45(3)

Zero Point Shift = -0.25(1) Scale = 0.076(1)

Atom	x	y	z	B (Å^2)	Occup.
Li (16c)	0.0	0.0	0.0	2.0	0.93(3)
Li (16d)	0.5	0.5	0.5	2.0	0.05(6)
Fe (16d)	0.5	0.5	0.5	1.3	0.95(6)
Fe (16c)	0.0	0.0	0.0	1.3	0.07(3)
O (32e)	0.256(2)	0.256(2)	0.256(2)	0.6	1.0

R Factors: R.WP. = 9.32 R.P. = 7.77 R.E. = 2.97

R.I. = 9.66 R.F. = 5.39

Bond distances were calculated for both structural models assuming unmixed cation site occupancies. In both models, the cations are in regular

octaheral sites. For the hexagonal 3R model the lithium - oxygen distance is 2.135 Å and the iron - oxygen distance is 2.051 Å. The structure refined from the cubic spinel related model has very similar bond distances with lithium - oxygen at 2.126 Å and iron - oxygen at 2.059 Å. These are all close to the expected bond distances, 2.14 Å for lithium - oxygen and 2.045 Å for high spin Fe^{3+} - oxygen.

In a further effort to determine whether $LiFeO_2$ adopts a 3R or a lithiated spinel structure, the material was examined by transmission electron microscopy (TEM). The micrographs showed both 4-fold and 3-fold symmetry axes which indexed to a cubic unit cell of axis length 8.36 Å. However, additional studies by x-ray powder diffraction, figure 4.2.4, demonstrated that the same sample of $LiFeO_2$ showed preferred orientation when pressed onto a flat plate before the diffraction spectrum was obtained. These observations can be reconciled by proposing that the $LiFeO_2$, as prepared, contains both crystallites with the 3R and with the lithiated spinel structure.

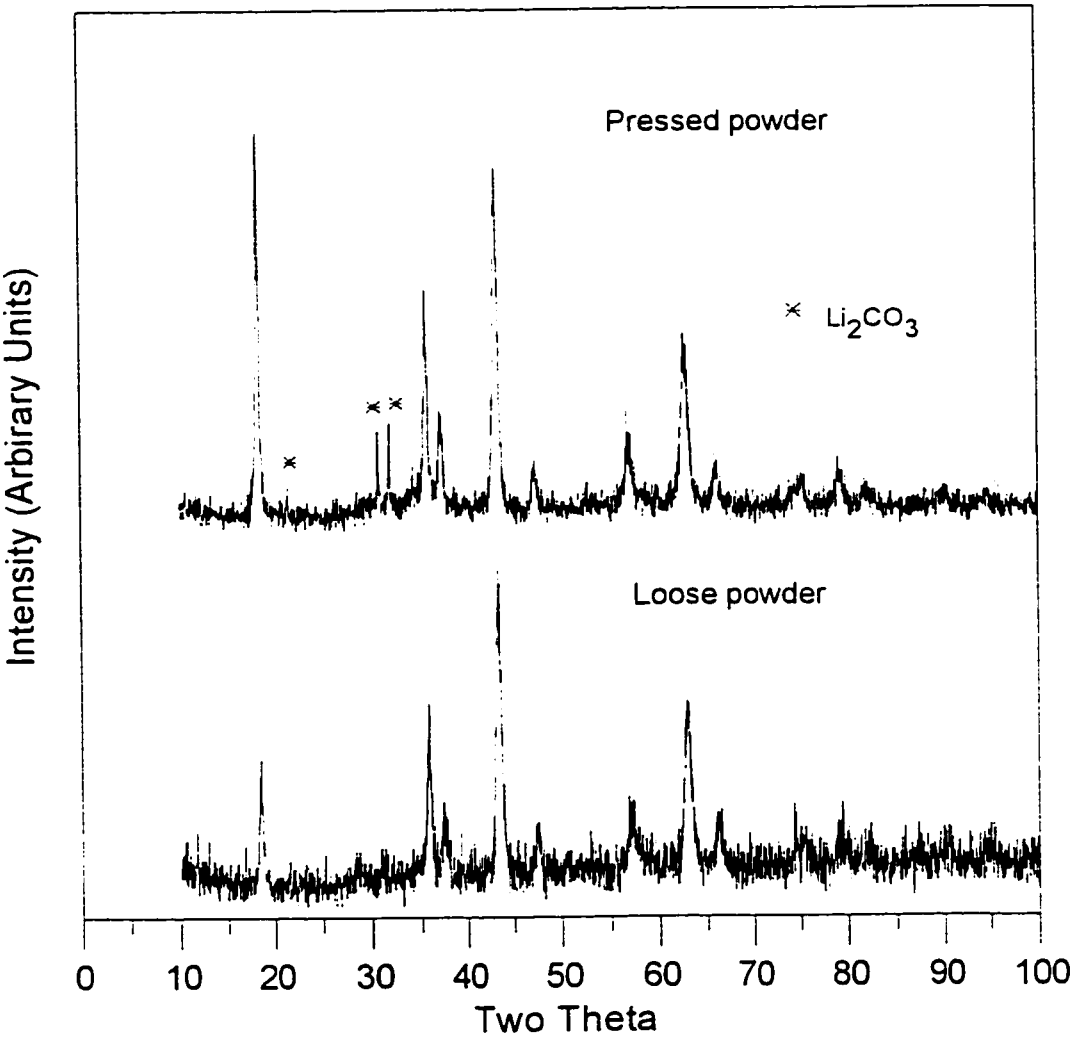

Figure 4.2.4 - X-ray diffraction patterns demonstrating preferred orientation in $LiFeO_2$.

4.3 1T - Li_2NiO_2

A novel phase of Li_2NiO_2 was recently prepared by an electrochemical, *chimie douce* approach (Dahn, von Sacken and Michal 1990). The crystal structure of this new phase was determined by Rietveld profile refinement of powder neutron diffraction data (Davidson *et al.* 1991).

The sample of Li_2NiO_2 provided by Dahn, von Sacken and Michal contained small amounts of $LiNiO_2$ and NiO (about 7% as shown later). The neutron diffractometer was unable to resolve the peaks from the two impurity phases. Therefore, the impurity was represented as arising from a structurally and compositionally related compound, $Li_xNi_{2-x}O_2$, with x chosen to give the strongest peak of this phase as the weighted average of the NiO and $LiNiO_2$ peaks. This procedure required $x = 0.4$. It is not expected that this approximation of two impurity phases by a single compound will affect the structural results obtained for the majority Li_2NiO_2 phase.

A neutron diffraction pattern on this sample was collected at the McMaster nuclear reactor on the position sensitive detector described in the first section. The sample was transferred in a helium filled glove bag to a thin-walled vanadium can with a screw cap. The vanadium can containing the sample was then quickly loaded into the cylindrical aluminum enclosure of the goniometer, and the enclosure was then evacuated. The Li_2NiO_2 structure was refined with a Rietveld-profile refinement program written by Hill and Howard which can refine

two phases simultaneously. This refinement program is an extensively modified version of the one written by Wiles and Young (1981). A two-phase refinement was required to correct for the " $Li_xNi_{2-x}O_2$" also present in the sample.

The observed (symbols) and calculated (line) two-phase neutron diffraction pattern for Li_2NiO_2 and $Li_xNi_{2-x}O_2$ is given in figure 4.3.1. The upper line of arrows corresponds to the Li_2NiO_2 reflections and the lower set to the overlapping strong reflections of $LiNiO_2$ and NiO which have been approximated as $Li_xNi_{2-x}O_2$. The arrow positions include the zero point offset of +0.195 degrees. The difference between the observed and calculated profiles is plotted at the bottom. From the ratio of the scaling factors, the $Li_xNi_{2-x}O_2$ phase (really the combined NiO and $LiNiO_2$ phases) represents about 7% of the sample. Three parameters were refined for the $Li_xNi_{2-x}O_2$ phase: the scale, the theta independent half-width parameter, W, and the lattice parameter.

The structure of the Li_2NiO_2 phase was refined in the space group P-3m1 in accordance with the 1T or CdI_2-type structure previously proposed for this phase (Dahn, von Sacken and Michal 1990). The nickel atom was assigned to the 1a position at (0, 0, 0), and the lithium and oxygen atoms to 2d sites at (1/3, 2/3, 0.6) and (1/3, 2/3, 0.2) respectively, for the initial refinement. In the final refinement, seventeen parameters, including the zero position, three background variables, a scale factor for each phase and a pseudo-Voigt peak shape parameter were varied. The results are listed in table 4.3.1. The large

half-width parameter, W, is probably due to the relatively poor crystallinity of the sample.

This phase of Li_2NiO_2 is isostructural with Li_2VSe_2, having a trigonal CdI_2, or 1T-type, structure completely different from orthorhombic Li_2NiO_2 (Rieck and Hoppe 1972). The 1T- Li_2NiO_2 is composed of hexagonally-close-packed layers of oxygen which alternate with layers of metal atoms in the sequence O-Ni-O-Li-O-Ni-O-Li... . The lithium atoms occupy tetrahedral interstices between the more broadly spaced oxygen layers, while the nickel atoms fill octahedral sites between the alternate, more closely spaced, oxygen layers.

The nickel atoms in 1T- Li_2NiO_2 occupy regular octahedral sites with an oxygen bond distance of 2.1431(7) Å. The lithium tetrahedra are elongated along the c-axis having one Li - O bond of 2.108(2) Å and three of 1.8841(9) Å. The bond distances are comparable to those observed in the isostructural compound Li_2MnO_2 (David *et al* 1983), with Li-O bond lengths of 1.91(5) Å and 1.99(5) Å (x 3). However in Li_2MnO_2, the trigonal distortion of the lithium tetrahedra results in a shorter Li-O bond along the c-axis. The insertion of a second formula unit of lithium into the $LiNiO_2$ structure produces a symmetric expansion of the cell. The Li_2NiO_2 *c/a* ratio, 1.638, is closer to the ideal value, 1.633, for hexagonal close packing than is the axial ratio, 1.660, reported for Li_2MnO_2 (David *el at* 1983).

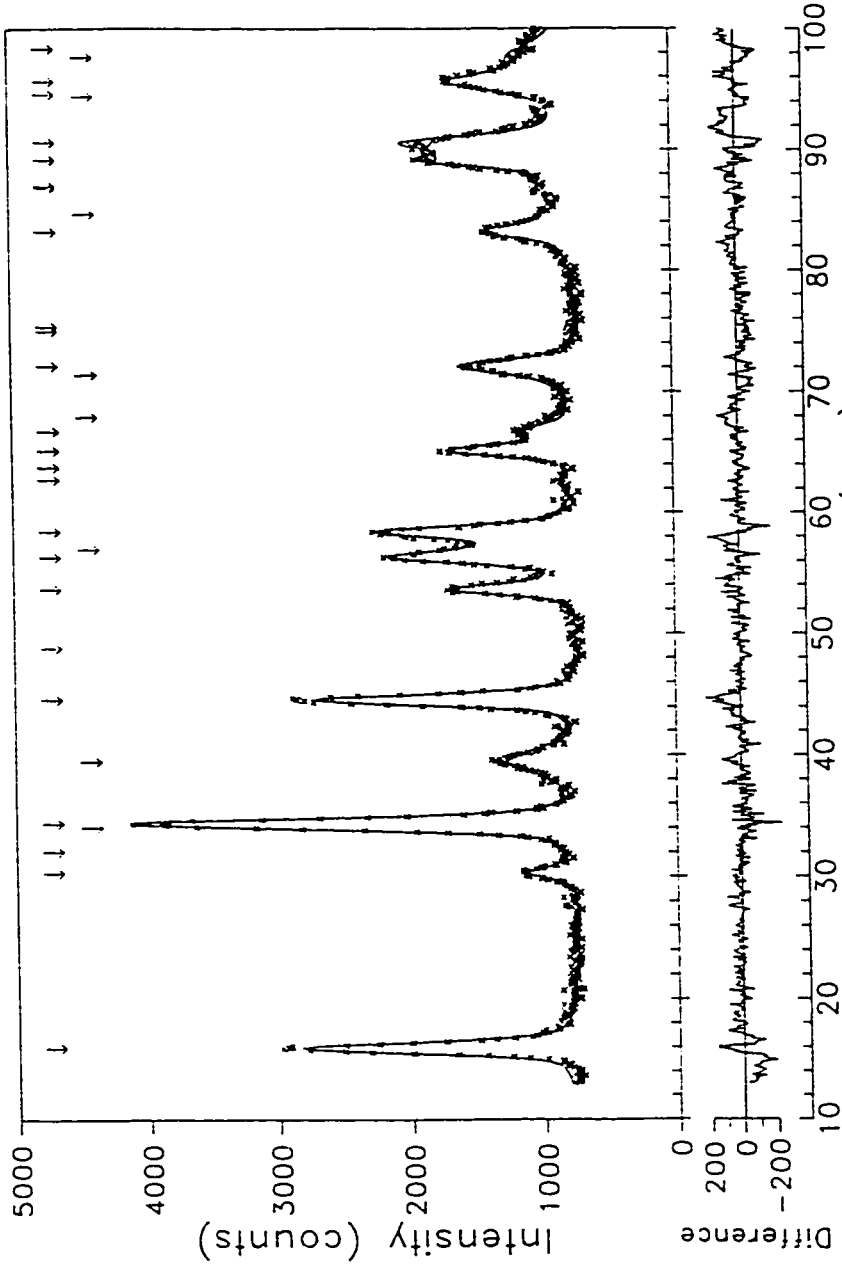

Figure 4.3.1 - Refinement of neutron diffraction data for 1T-Li_2NiO_2.

Table 4.3.1 - Rietveld refinement of room temperature neutron diffraction data for Li_2NiO_2.

Major Phase - Li_2NiO_2 Space Group P-3m1 (D^3_{3d})

Lattice Parameters: a = 3.0954(9) Å and c = 5.070(1) Å

Half-width parameters: U = 1.80, V = -1.20, and W = 1.31(2)

Bragg R-factor = 1.40

Atom	x	y	z	B (Å^2)	Occup.
Ni (1a)	0.0	0.0	0.0	1.0(1)	1.0
Li (2d)	1/3	2/3	0.649(2)	0.4(2)	1.0
O (2d)	1/3	2/3	0.2333(9)	0.4(1)	1.0

Minor Phase - $Li_xNi_{2-x}O_2$ Space Group Fm3m (O^5_h)

Lattice Parameter: a = 4.140(2) Å

Half-width parameters: U = 1.80, V = -1.20, and W = 6.0(4)

Bragg R-factor = 1.20

Atom	x	y	z	B (Å^2)	Occup.
Ni (4a)	0.0	0.0	0.0	1.0	0.80
Li (4a)	0.0	0.0	0.0	1.0	0.20
O (4b)	0.5	0.5	0.5	1.0	1.00

Scattering lengths: Li (-0.203), Ni (1.030), O (0.5805)

Weighted profile R = 5.08 Profile R = 4.02 Expected R = 3.00

4.4 Li_2NiMnO_4

Powder neutron diffraction data were collected for two samples of Li_2NiMnO_4 at the McMaster University Nuclear Reactor using the neutron spectrometer described in section 4.1. Both samples were prepared from a 1:1 mixture of $LiMnO_2$ and $LiNiO_2$ reacted in flowing argon at 1000 °C. The samples were each fired for three 5 day intervals with the products reground and repelletized between each firing. After the second firing, a 25% molar excess of $LiOH.H_2O$ was added to each, to compensate for possible losses of Li_2O by vaporization. After the third firing, the samples were washed with distilled water to remove any unreacted lithium oxide, and then dried, first in air at 110 °C, and then in flowing argon at 300 °C. The x-ray powder diffraction pattern of Li_2NiMnO_4 can be indexed to a hexagonal cell with a = 2.90 Å and c = 14.3 Å. The relative intensities of the diffraction peaks are consistent with a layered 3R structure, isostructural to $LiCoO_2$ or $LiNiO_2$.

The neutron diffraction patterns were analyzed with the Rietveld profile refinement program *Rietan* (Izumi 1989). Fourteen parameters were allowed to vary in the Rietveld refinement: six background parameters, the zero-point shift, the theta independent half-width parameter (W), an overall temperature factor, two cell parameters, the oxygen position, and the occupancy of the two cation sites. The nickel and manganese were treated as a single virtual atom with a scattering length equal to the molar average of its

components. The cation sites were allowed occupancy by both lithium and transition metal atoms, but the occupancies of the both sites were constrained to sum to one. The results of these refinements are shown in the tables 4.4.1 and 4.4.2, and figures 4.4.1 and 4.4.2. The refinement of the occupancies indicates some mixing between the lithium and the transition metal sites, and that the samples contain about 10% less lithium than the stoichiometric composition. Such a loss of lithium is not unusual at the preparation temperature used, and similar problems have been reported in the preparation of $LiNiO_2$. The observed diffraction pattern has weak peaks at angles of approximately 19, 38 , 51 and 90 degrees which cannot be assigned to the given cell dimensions. These additional reflections may be due to a superstructure resulting from ordering of the cations. Low temperature neutron diffraction patterns taken at 100 K and at 10 K showed no indication of long range magnetic ordering.

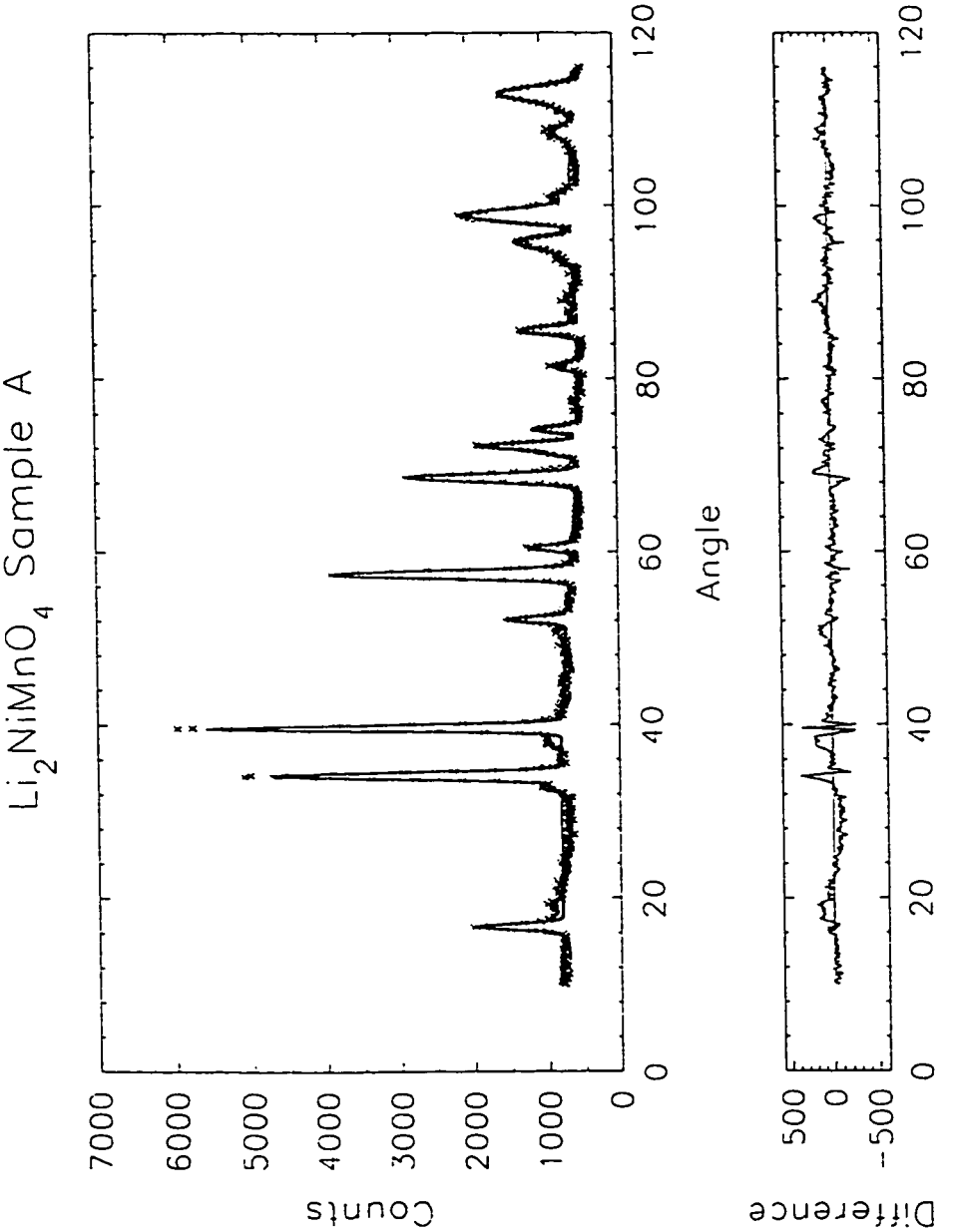

Figure 4.4.1 - Refinement of neutron data for Li_2NiMnO_4 (sample A).

Table 4.4.1 - Rietveld Refinement of Room Temperature Neutron Diffraction Data for Li_2NiMnO_4 (Sample A)

Space Group R -3 m (D^5_{3d}) Wavelength 1.395 Å

Cell Parameters: a = 2.8910(4) Å and c = 14.332(3) Å

Atom	x	y	z	Occup.
0.5 Mn + 0.5 Ni (3a)	0.0	0.0	0.0	0.85(4)
0.5 Mn + 0.5 Ni (3b)	0.0	0.0	0.5	0.25(4)
Li (3a)	0.0	0.0	0.0	0.15(4)
Li (3b)	0.0	0.0	0.5	0.75(4)
O (6c)	0.0	0.0	0.2580(8)	1.0

Overall Temperature Factor 0.9(2) $Å^2$

Half-width Parameters: U = 1.55 V = -1.20 W = 0.76(1)

Scattering Lengths: Li (-0.190), Mn(-0.373), Ni (1.030), O (0.5803)

Weighted profile R = 7.30 Profile R = 5.68

Bragg R = 6.79 Expected R = 3.37

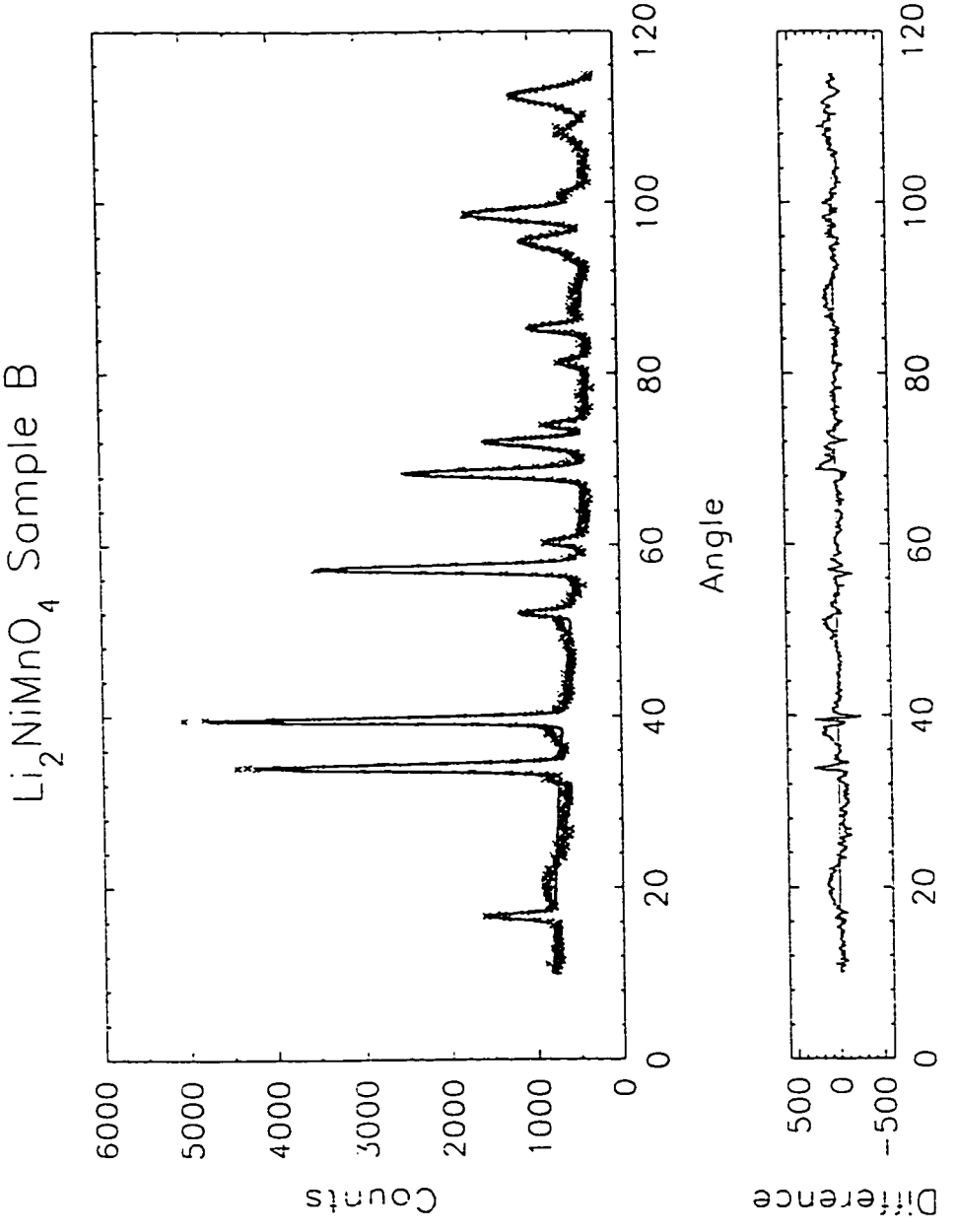

Figure 4.4.2 - Refinement of neutron data for Li_2NiMnO_4 (sample B).

Table 4.4.2 - Rietveld Refinement of Room Temperature Neutron Diffraction Data for Li_2NiMnO_4 (Sample B)

Space Group R -3 m (D^5_{3d}) Wavelength 1.395 Å

Cell Parameters: a = 2.8984(4) Å and c = 14.348(3) Å

Atom	x	y	z	Occup.
0.5 Mn + 0.5 Ni (3a)	0.0	0.0	0.0	0.80(5)
0.5 Mn + 0.5 Ni (3b)	0.0	0.0	0.5	0.29(5)
Li (3a)	0.0	0.0	0.0	0.20(5)
Li (3b)	0.0	0.0	0.5	0.71(5)
O (6c)	0.0	0.0	0.2580(9)	1.0

Overall Temperature Factor 0.9(2) $Å^2$

Half-width Parameters: U = 1.55 V = -1.20 W = 0.80(1)

Scattering Lengths: Li (-0.190), Mn(-0.373), Ni (1.030), O (0.5803)

Weighted profile R = 8.44 Profile R = 6.57

Bragg R = 6.47 Expected R = 3.59

4.5 $Li_2Cr_yMn_{2-y}O_4$

A large number of $Li_2Cr_yMn_{2-y}O_4$ compositions were prepared as described in chapter 3 from either $LiMnO_2$ and $LiCrO_2$, or from Li_2CO_3, MnO_2 and Cr_2O_3. Single phase products were obtained over the composition range $0.1 \leq y \leq 1.9$. A change of symmetry occurs between hexagonal $Li_2Cr_{1.4}Mn_{0.6}O_4$ and, approximately, tetragonal $Li_2Cr_{1.3}Mn_{0.7}O_4$. The crystallographic structures of single phase compositions of $Li_2Cr_yMn_{2-y}O_4$ were investigated by powder x-ray diffraction. Powder x-ray diffraction is useful for determining phase purity, crystallographic unit cell volumes, and approximate crystallographic structures, but can not be relied upon for accurate structural details. Crystallographic unit cell dimensions were refined from powder Guinier diffraction data for a range of compositions. The results of a Guinier diffraction study, listed in table 4.5.1, are as accurate as can be expected from powder diffraction data but may not be the most correct way of describing the crystallographic unit cells. For example, $Li_2Cr_{0.5}Mn_{1.5}O_4$ is listed as having orthorhombic symmetry because a refinement of the diffraction data found the β angle to be 90 degrees within the uncertainty of the measurement. However, a single crystal x-ray diffraction study on this material at a later date may reveal that the beta angle is not exactly 90 degrees. Furthermore, materials prepared for use in electrochemical cells are not usually highly crystalline and therefore have very broad diffraction peaks. In such materials, it is usually not possible to determine small deviations from 90

degrees in the unit cell's angle or small differences in the unit cell's lattice dimensions. Consequently, compositions such as those described in table 4.5.1 as having monoclinic or orthorhombic symmetry, appear to have tetragonal symmetry when they are prepared in a less crystalline form and examined by with a Guinier-De Wolf powder x-ray diffractometer. That is, the diffraction peaks are too broad to determine that the a and b lattice parameters are different from each other, or that one of the unit cell's angle is not exactly 90 degrees.

Table 4.5.1 - Tabulation of Normalized Crystallographic Cell Volumes

Composition	Crystallo-graphic Symmetry	a (Å)	b (Å)	c (Å)	β	Vol. ($Å^3$)
$2\ LiCrO_2$ *	hexagonal	2.899		14.412		69.9
$Li_2Cr_{1.9}Mn_{0.1}O_4$	hexagonal	2.899		14.43		70.1
$Li_2Cr_{1.8}Mn_{0.2}O_4$	hexagonal	2.899		14.46		70.2
$Li_2Cr_{1.5}Mn_{0.5}O_4$	hexagonal	2.907		14.46		70.6
$Li_2Cr_{1.25}Mn_{0.75}O_4$	monoclinic	5.717	5.879	8.50	89.6	71.4
Li_2CrMnO_4	monoclinic	5.708	5.820	8.63	89.8	71.7
$LI_2Cr_{0.5}Mn_{1.5}O_4$	orthorhombic	5.645	5.764	9.01	90.0	73.3
$Li_2Cr_{0.25}Mn_{1.75}O_4$	monoclinic	5.636	5.759	9.09	90.4	73.8
$Li_2Cr_{0.1}Mn_{1.9}O_4$	monoclinic	5.629	5.738	9.17	90.6	74.1
$Li_2Mn_2O_4$ **	tetragonal	5.662		9.274	90	74.3

*JCPDF card file # 24-600

**Thackeray *et al* 1983

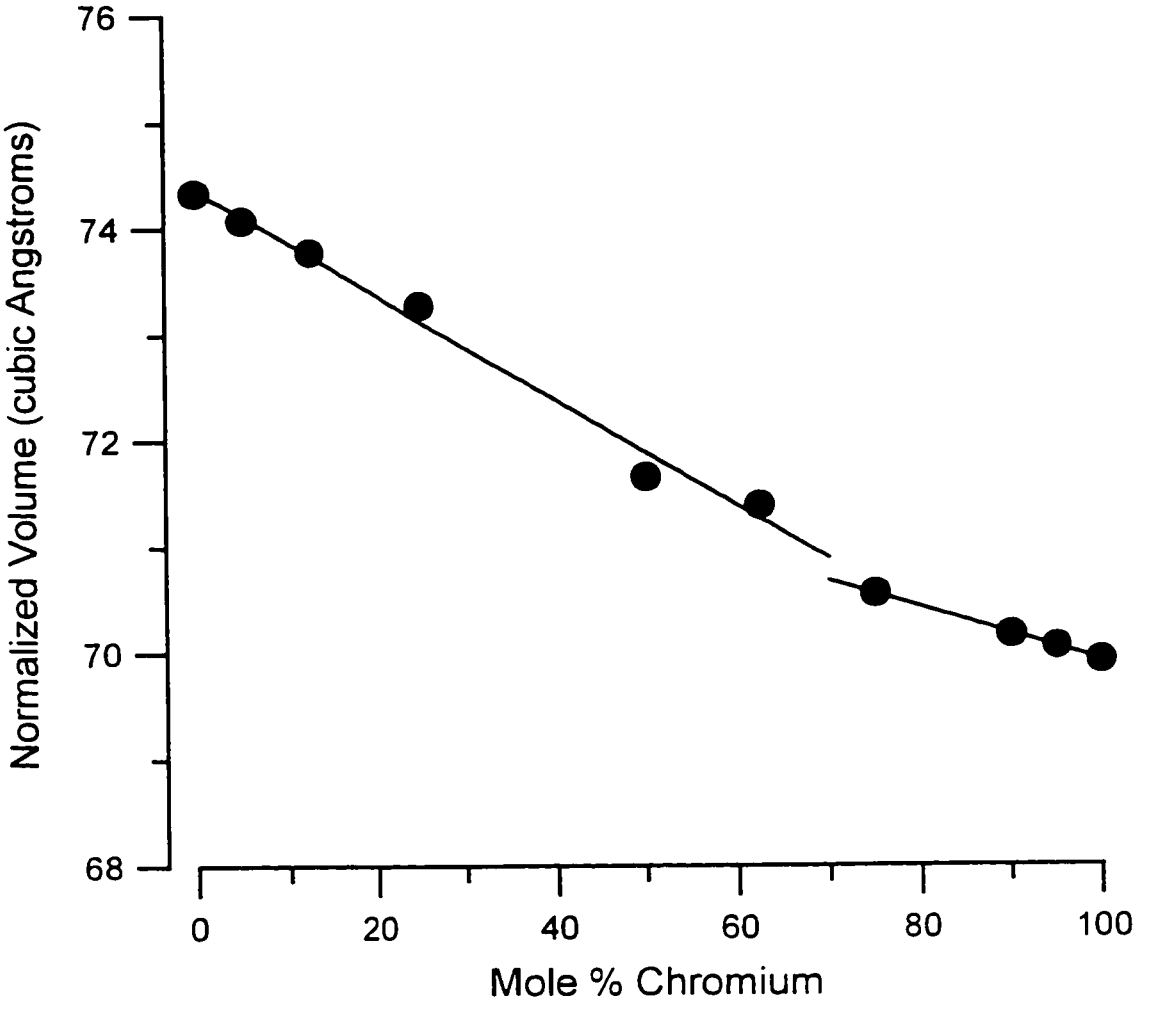

Figure 4.5.1 - Normalized volume versus composition for $Li_2Cr_yMn_{2-y}O_4$ phases.

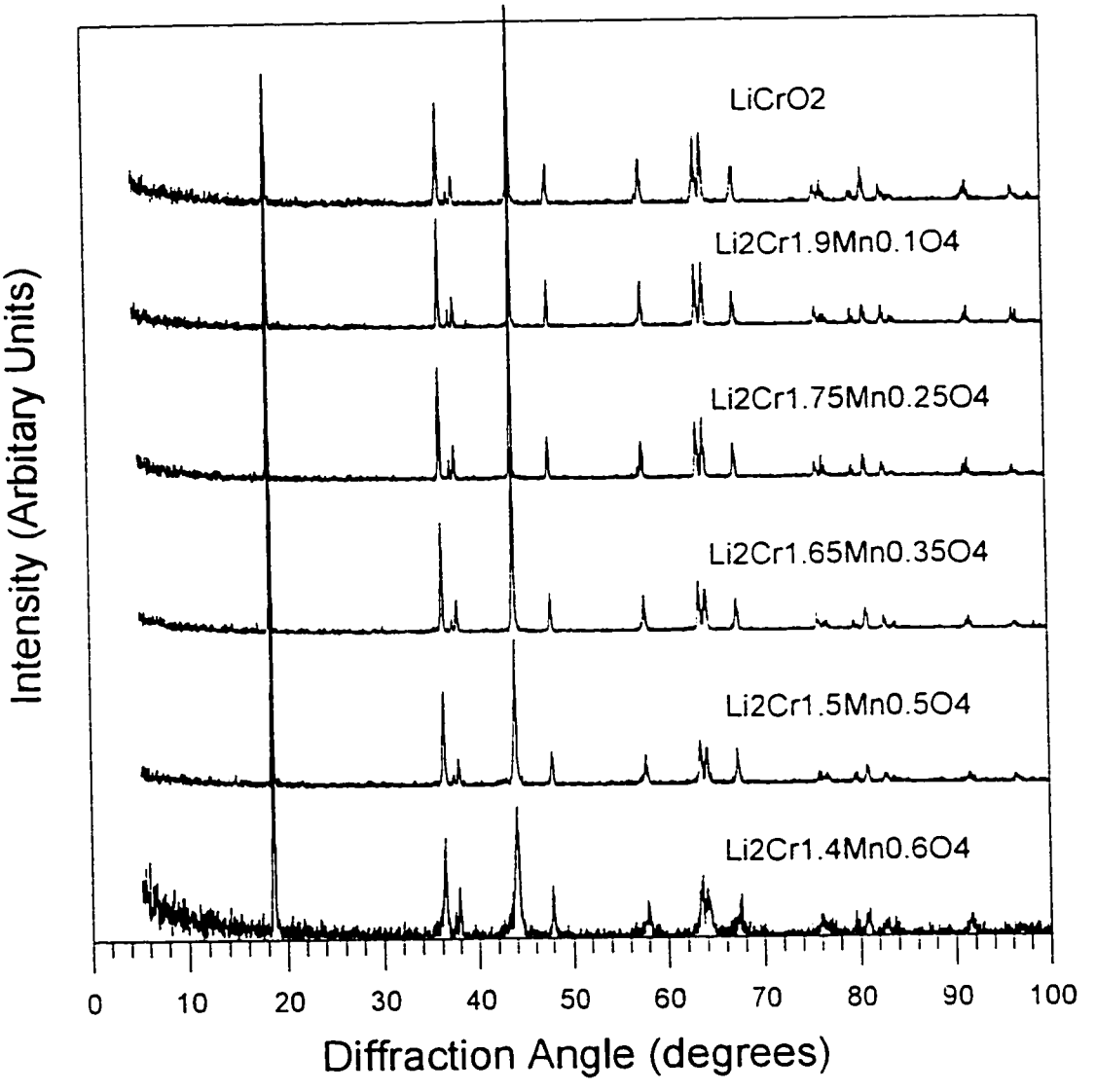

Figure 4.5.2 - Diffraction patterns for $Li_2Cr_yMn_{2-y}O_4$ phases with the 3R structure.

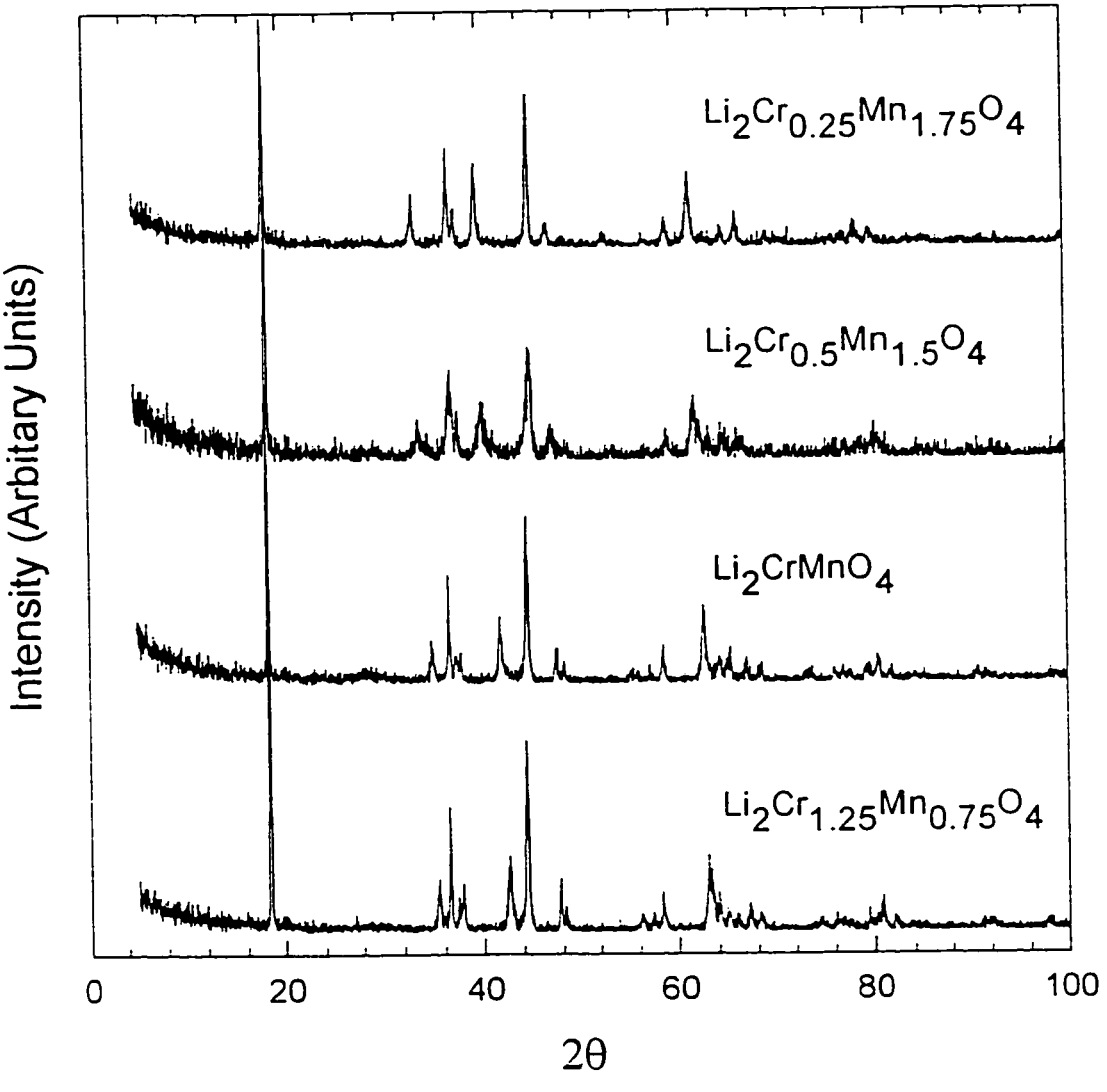

Figure 4.5.3 - Diffraction patterns for $Li_2Cr_yMn_{2-y}O_4$ phases with the lithiated spinel structure.

To simplify the characterization of these materials, a normalized crystallographic unit cell volume is defined. This normalized volume is defined as the crystallographic volume in cubic angstroms containing two lithium atoms, four oxygen atoms and two transition metal atoms in which the transition metal atoms are any combination of chromium and manganese. The hexagonal 3R-type unit cell, such as $Li_2Cr_{1.8}Mn_{0.2}O_4$, contains 2/3 of such a stoichiometric unit while the orthorhombic and monoclinic cell descriptions in table 4.5.1 have 4 stoichiometric units. Table 4.5.1 lists the normalized crystallographic cell volumes as a function of composition, and this data is also plotted in figure 4.5.1. The changes in normalized crystallographic volume as a function of chromium content can be fitted to two linear regions with a change in slope occurring between 62.5 and 75 mole percent chromium. The two linear regions correspond to the two structural types found in these compositions. The hexagonal phases with greater than about 70 mole percent chromium have x-ray powder diffraction patterns with peak intensities resembling those of $LiCrO_2$, and are, consequently, probably isostructural. $LiCrO_2$ has a layered 3R- type structure like that of $LiCoO_2$ and $LiNiO_2$ (Kordes and Petzoldt 1965). Figure 4.5.2 shows the x-ray powder diffraction patterns for a selection of $Li_2Cr_yMn_{2-y}O_4$ phases with a $LiCrO_2$ type structure.

The systematic extinctions and the relative intensities in the x-ray powder diffraction patterns of the nearly tetragonal phases, with less than about 70 mole percent chromium, are very similar to those of λ-$Li_2Mn_2O_4$ which has a

three-dimensional structure with channels of lithium atoms (Thackeray *et al* 1983). The diffraction patterns of a selection of reasonably crystalline samples of $Li_2Cr_yMn_{2-y}O_4$ phases which have the λ-$Li_2Mn_2O_4$ type structure are shown in figure 4.5.3. The similarity between the powder patterns of the $Li_2Cr_yMn_{2-y}O_4$ phases and λ-$Li_2Mn_2O_4$ is not obvious until the reflections in individual powder patterns are indexed. Figures 4.5.4 to 4.5.7 are plots of the individual patterns with the assignment of the major reflections indicated. The stick diagram on the bottom of these graphs is a calculated pattern using the space group and atomic positions of λ-$Li_2Mn_2O_4$ and the approximate tetragonal dimensions of the indicated $Li_2Cr_yMn_{2-y}O_4$ phase. Figure 4.5.8 provides a detailed view of the diffraction patterns of the lithiated spinel phases over the angular range of 30 - 70 degrees in two theta. In these plots the deviation from tetragonal symmetry can be seen in the splitting of the tetragonal 400 reflection into 400 and 040 peaks.

The structure of λ-$Li_2Mn_2O_4$ is tetragonal rather than cubic as a consequence of a cooperative Jahn-Teller distortion caused by the Mn^{3+} ion (Ohzuku, Kitagawa and Hirai 1990). The magnitude of the Jahn-Teller distortion can be quantified by the ratio of the c-axis length to twice the [110] length, calculated as the square root of the sum of the squares of the a and b distances. The farther the ratio is from 1.0 the greater the Jahn-Teller distortion. For simplicity, this ratio will be referred to as the Jahn-Teller ratio. The c-axis distance in λ-$Li_2Mn_2O_4$ is 9.27$\underline{4}$ Å while twice the [110] distance is 8.00$\underline{7}$ Å, and

the Jahn-Teller ratio is 1.158. For compositions with diffraction patterns resembling λ-$Li_2Mn_2O_4$ the changes in the lattice parameters as a function of composition indicates than the magnitude of the Jahn-Teller distortion decreases with increasing chromium content. The Jahn-Teller ratios of selected $Li_2Cr_yMn_{2-y}O_4$ phases are listed in table 4.5.2 and plotted in figure 4.5.9.

In the course of electrochemically cycling a lithium intercalation cathode such as λ-$Li_{2-x}Mn_2O_4$, x can vary from 0 to 2.0. In the case of λ-$Li_{2-x}Mn_2O_4$, for $x \geq 1.0$, the concentration of Mn^{3+} ions is too low to support the deformation and the cooperative Jahn-Teller distortion collapses to form a cubic crystal structure (Ohzuku, Kitagawa and Hirai 1990). For structures with a Jahn-Teller ratio far from 1.0, the change in structure is accompanied by a large change in the crystallographic lattice parameters (Ohzuku, Kitagawa and Hirai 1990). Large changes in lattice parameters result in crystal strain and fracturing, which in turn. diminish the lithium cycleability in the intercalation compound. Compounds with Jahn-Teller ratios closer to 1.0 will, generally, cycle better through this structural transition than those with values far from 1.0. Also in materials in which the concentration of Mn^{3+} ions is diluted by other ions such as Cr^{3+}, the Jahn-Teller distortion will occur at higher lithium ion compositions than in λ-$Li_{2-x}Mn_2O_4$. Thus. in $Li_2Cr_yMn_{2-y}O_4$ phases which have the λ-$Li_2Mn_2O_4$ type structure. the Jahn-Teller distortion should occur at lower values of x as y is increased.

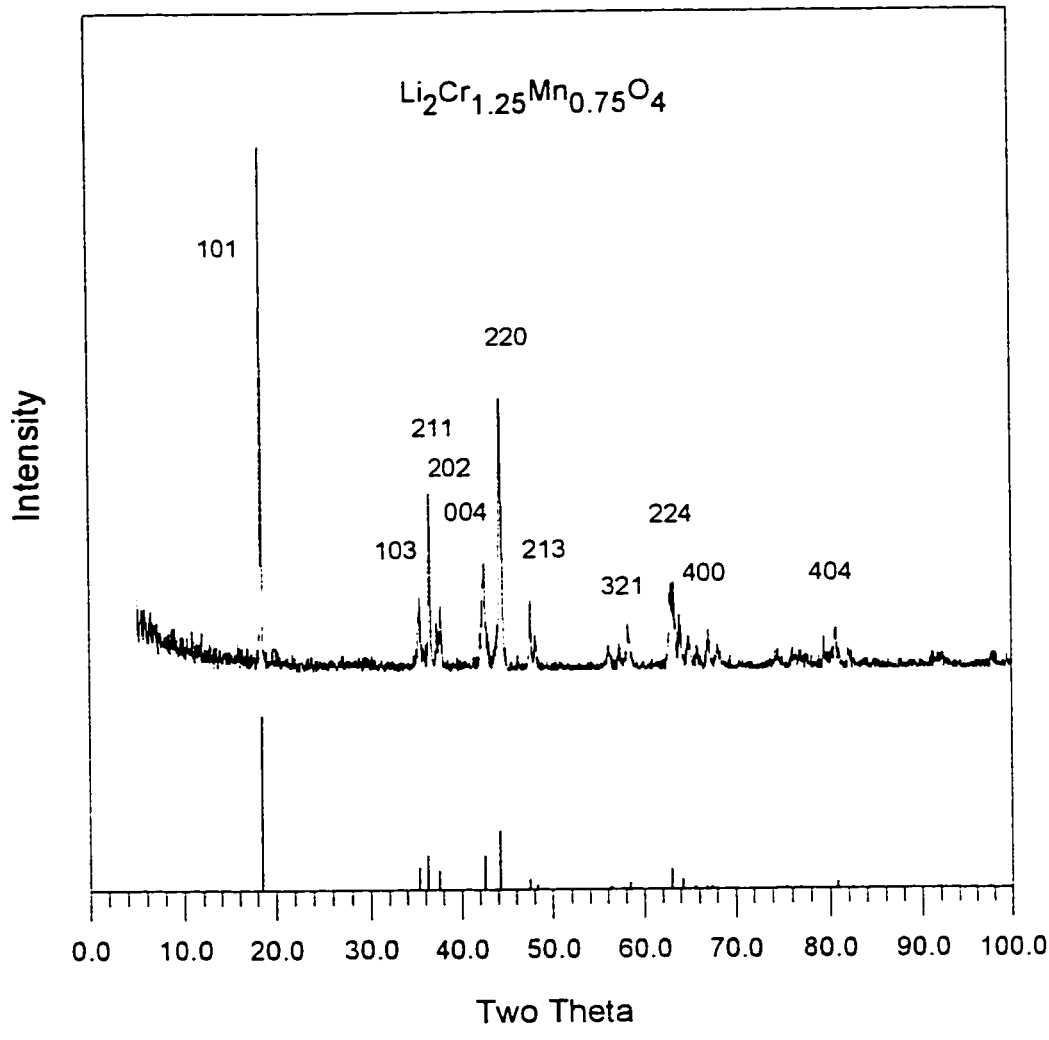

Figure 4.5.4 - Modeling of $Li_2Cr_{1.25}Mn_{0.75}O_4$ to lithiated spinel structure.

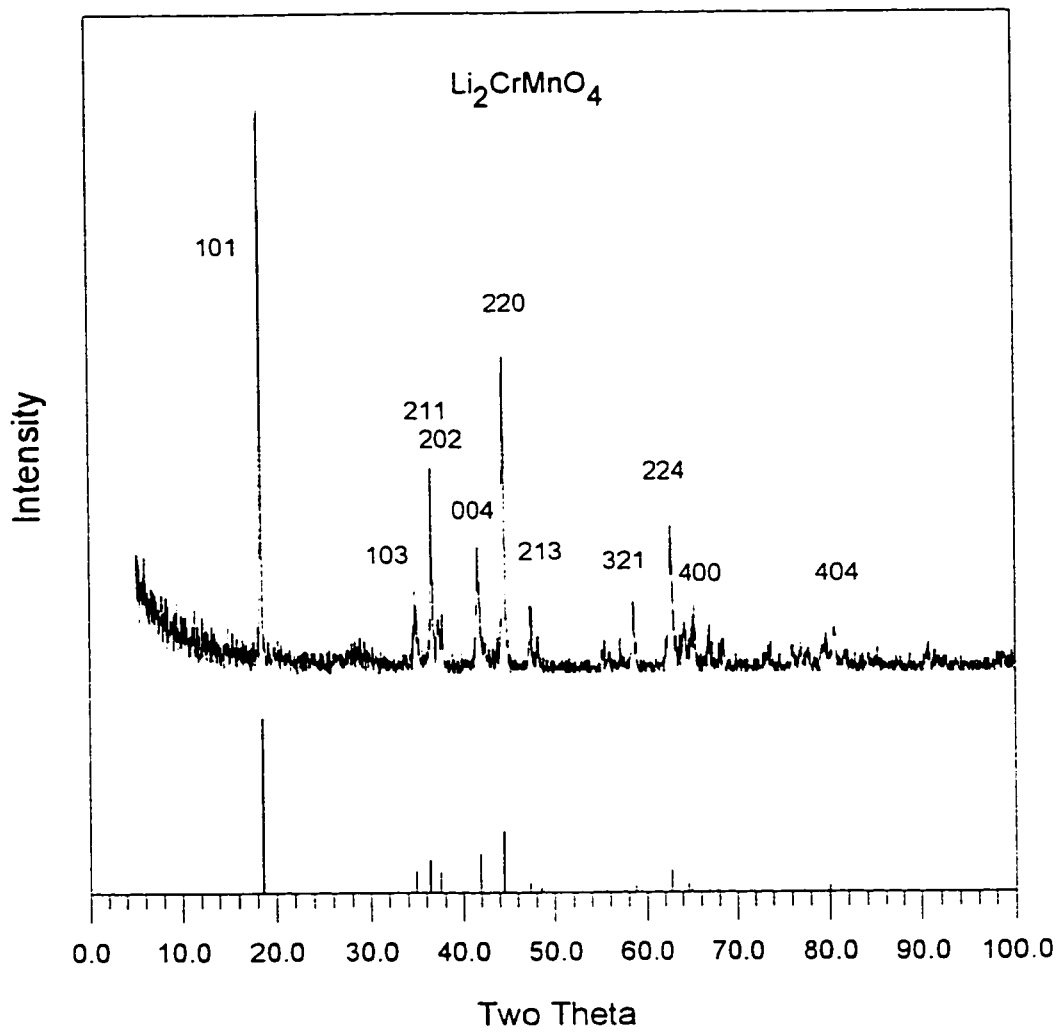

Figure 4.5.5 - Modeling of Li_2CrMnO_4 to lithiated spinel structure.

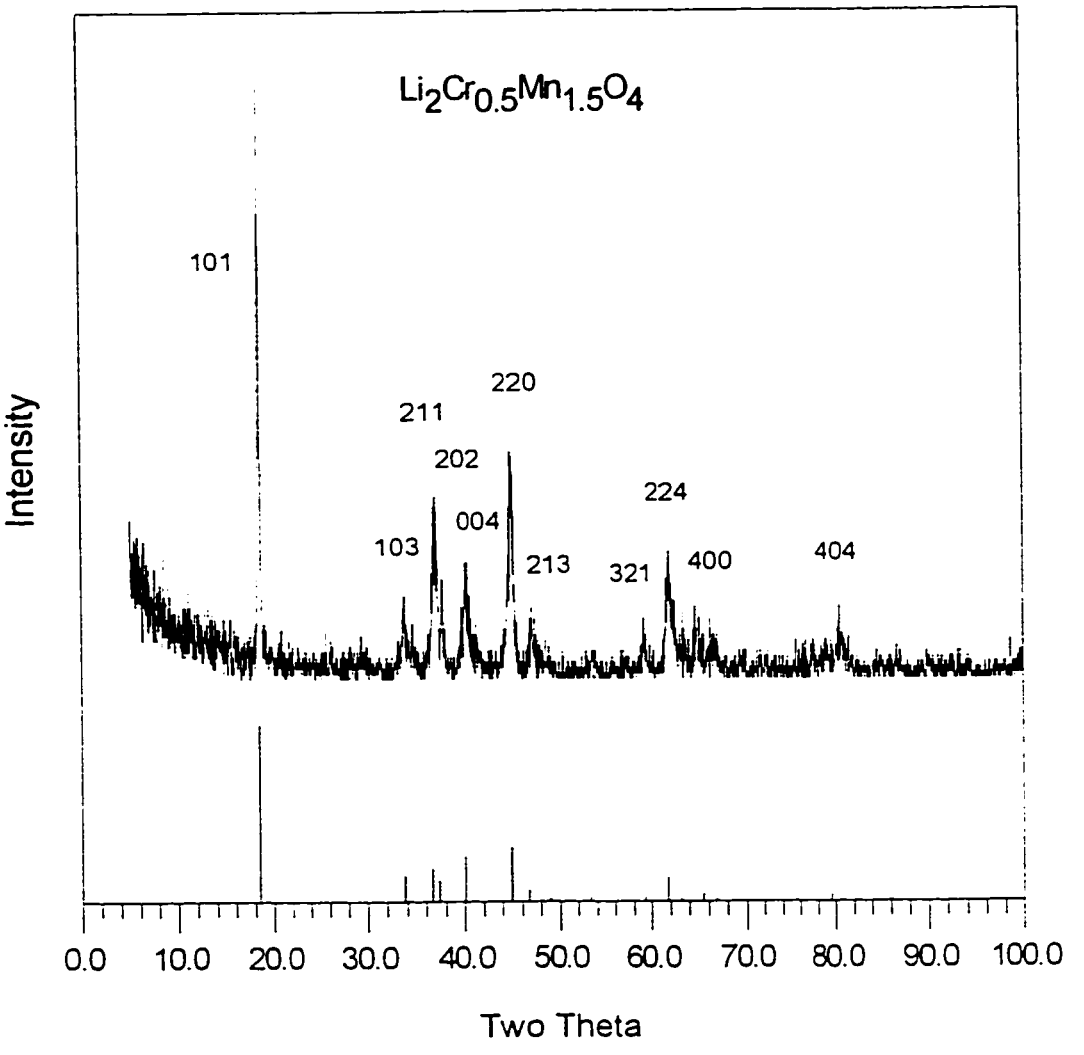

Figure 4.5.6 - Modeling of $Li_2Cr_{0.5}Mn_{1.5}O_4$ to lithiated spinel structure.

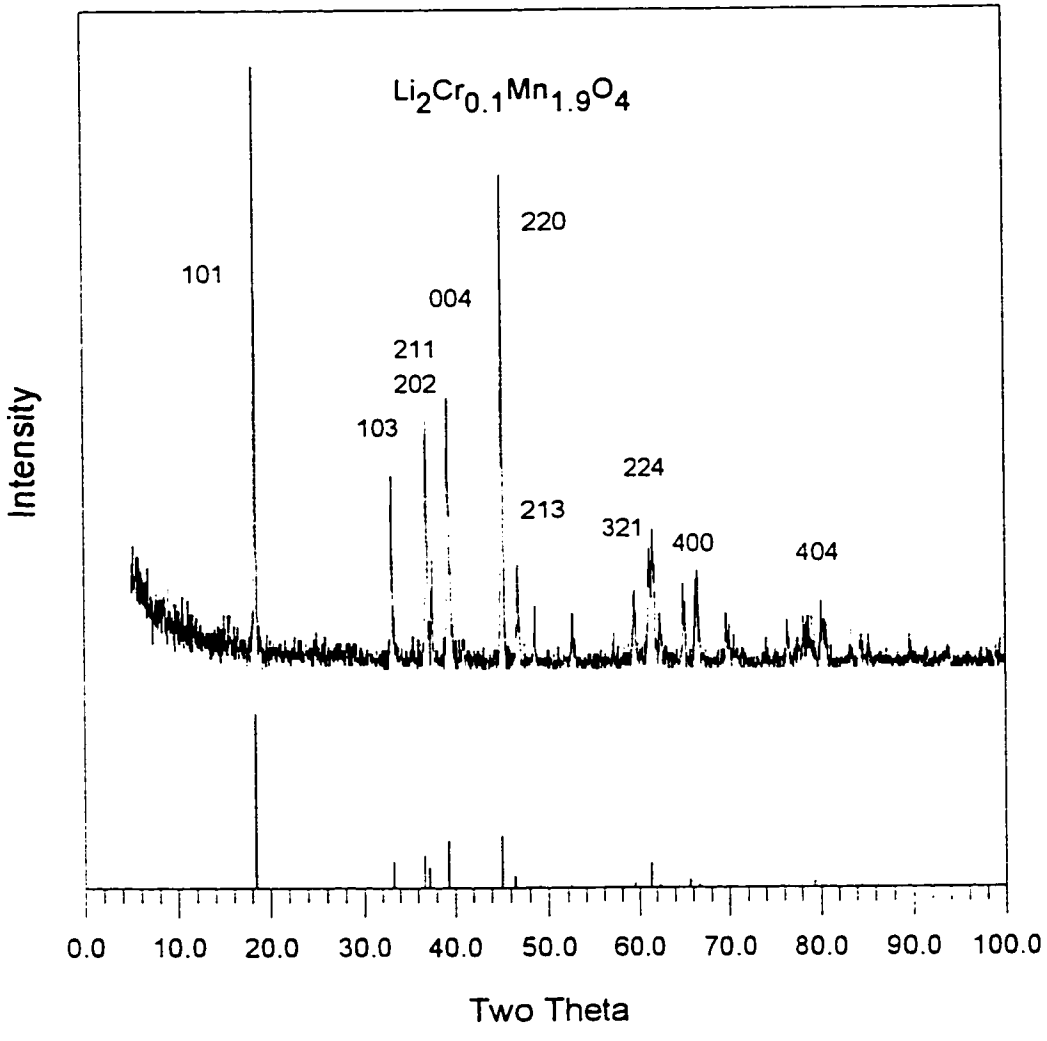

Figure 4.5.7 - Modeling of $Li_2Cr_{0.1}Mn_{1.9}O_4$ to lithiated spinel structure.

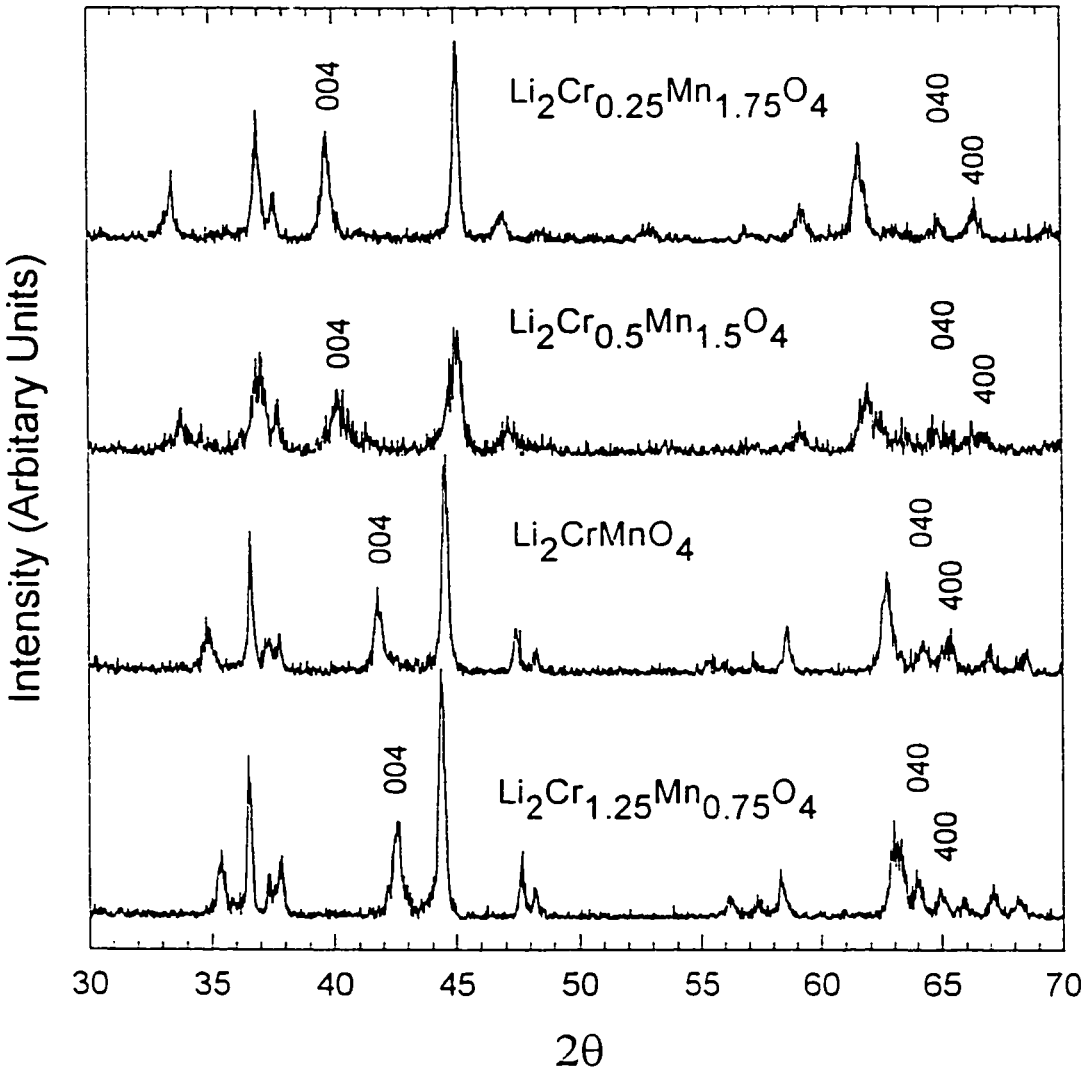

Figure 4.5.8 - Detailed view of diffraction patterns from 30 - 70 degrees.

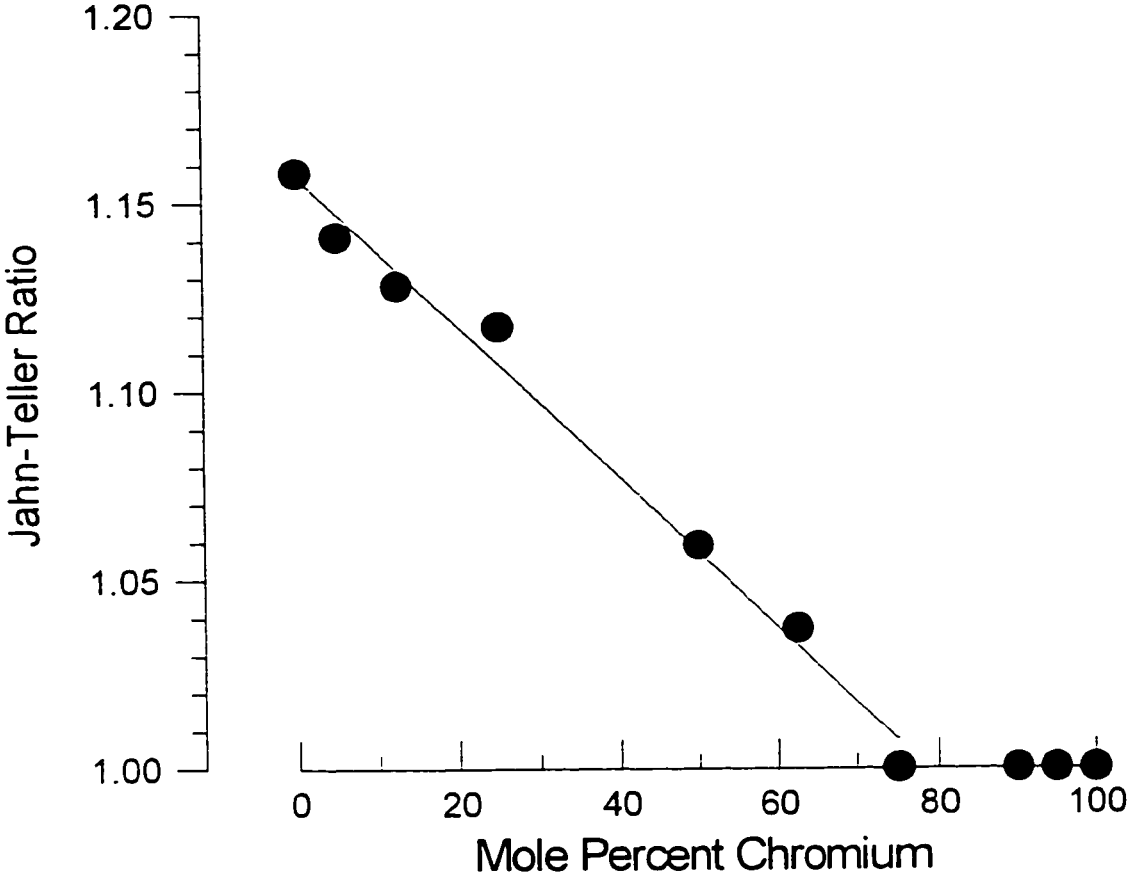

Figure 4.5.9 - Plot of Jahn-Teller ratios versus composition.

Table 4.5.2 - Jahn-Teller Ratios in $Li_2Cr_yMn_{2-y}O_4$ Phases

Composition	a (Å)	b (Å)	c (Å)	beta angle	Jahn-Teller Ratio
$Li_2Cr_{1.25}Mn_{0.75}O_4$	5.717	5.879	8.50	89.6	1.037
Li_2CrMnO_4	5.708	5.820	8.63	89.8	1.059
$LI_2Cr_{0.5}Mn_{1.5}O_4$	5.645	5.764	9.01	90.0	1.117
$Li_2Cr_{0.25}Mn_{1.75}O_4$	5.636	5.759	9.09	90.4	1.128
$Li_2Cr_{0.1}Mn_{1.9}O_4$	5.629	5.738	9.17	90.6	1.141
$Li_2Mn_2O_4$ **	5.662	5.662	9.274	90	1.158

**Thackeray *et al* 1983

The densities of various compositions of $Li_2Cr_yMn_{2-y}O_4$ were measured by helium pycnometry. These measurements corroborate the crystallographic cell volumes determined from powder x-ray diffraction. About 1.0 to 1.2 g of material was required for each density determination. A Micromeritics Accupyc 1330 was used for the measurements. These results and the densities calculated from the normalized crystallographic cell volumes are tabulated in table 4.5.3. The crystallographic densities increase with increasing manganese content. The densities measured by helium pyncometry agree within error with those calculated from the crystallographic volumes. A graphical representation of the data is provided in figure 4.5.10.

Table 4.5.3 - Crystallographic and Measured Densities of $Li_2Cr_yMn_{2-y}O_4$ Phases

Composition	Normalized Crystallo-graphic Volume (A^3)	Molecular Weight (g/mole)	Crystallo-graphic Density (g/cm^3)	Measured Density (g/cm^3)
$2\ LiCrO_2$ *	69.92	181.87	4.319	
$Li_2Cr_{1.9}Mn_{0.1}O_4$	70.05	182.17	4.318	4.322
$Li_2Cr_{1.8}Mn_{0.2}O_4$	70.16	182.46	4.318	
$Li_2Cr_{1.5}Mn_{0.5}O_4$	70.55	183.34	4.315	4.314
$Li_2Cr_{1.4}Mn_{0.6}O_4$				4.296
$Li_2Cr_{1.3}Mn_{0.7}O_4$				4.284
$Li_2Cr_{1.25}Mn_{0.75}O_4$	71.38	184.08	4.282	4.279
Li_2CrMnO_4	71.65	184.82	4.283	4.287
$LI_2Cr_{0.5}Mn_{1.5}O_4$	73.27	186.29	4.222	4.230
$Li_2Cr_{0.25}Mn_{1.75}O_4$	73.77	187.02	4.210	
$Li_2Cr_{0.1}Mn_{1.9}O_4$	74.07	187.46	4.202	4.191
$Li_2Mn_2O_4$ **	74.33	187.76	4.194	

*JCPDF card file # 24-600

**Thackeray *et al* 1983

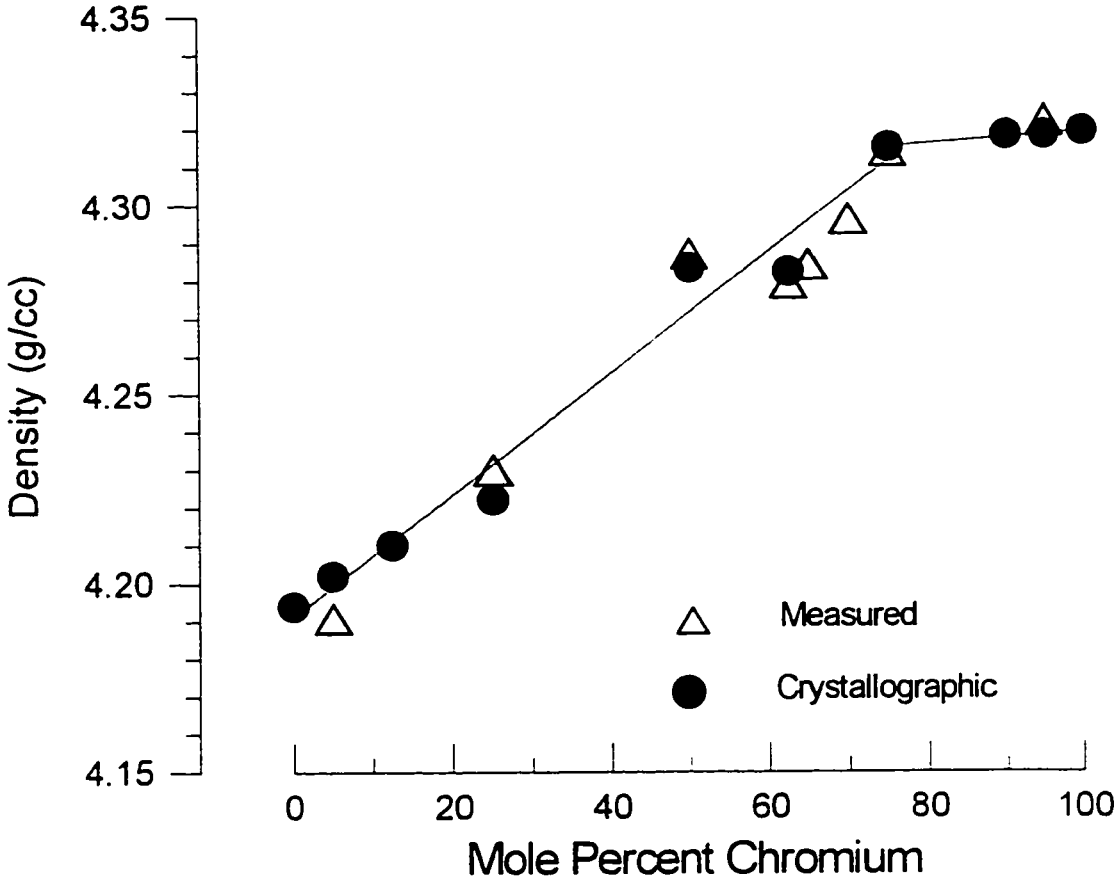

Figure 4.5.10 - Plot of crystallographic and measured densities for $Li_2Cr_yMn_{2-y}O_4$ phases.

Chapter 5

Magnetic Structures and Properties

5.1 Orthorhombic - $LiMnO_2$

The magnetic properties of orthorhombic $LiMnO_2$ were studied by Bongers (1957). He reported that $LiMnO_2$ has a paramagnetic susceptibility corresponding to a high-spin state spin-only value, and that it has an antiferromagnetic transition at about 300 K. A neutron powder diffraction pattern of orthorhombic $LiMnO_2$ was collected over an angular range of about 5 to 55 degrees at 12 K. The sample was contained in a cylindrical aluminum sample holder which was evacuated and back filled with helium gas. The helium gas serves as a heat exchanger during the cooling or warming of the sample. The diffraction pattern was analyzed with the Rietveld profile refinement program *Rietan* written by F. Izumi (1989). This program is capable of modeling neutron scattering from magnetic structures with collinear spin arrangements. The magnetic moment, μ_j, of each magnetic site, and the angle between the spin direction and the unique axes of the lattice can be refined using the equations given by Shirane (1959). In the calculations reported here, the magnetic form factor calculated for Mn^{2+} (Bacon 1975) was used.

The diffraction pattern taken at 12 K indicates a large number of magnetic peaks in addition to those attributable to the chemical structure. All, but one very weak and broad peak at near a 2θ angle of 16 degrees, can be indexed to an F-centered unit cell with dimensions double that of the chemical unit cell along all three axes a, b, and c. The small, broad peak near 16 degrees is also present in diffraction patterns collected at 251 and 271 K.

The simplest possible model for magnetic ordering in orthorhombic $LiMnO_2$ is one in which all neighbouring manganese atoms have spins in opposing directions. This model is represented in figure 5.1.1 with only the manganese atoms shown for clarity. In this model, there are actually two independently ordered sublattices: one involving the manganese atoms at the corners of the chemical unit cell (indicated by the dotted lines), and a second involving the other half of the manganese atoms. Although the chemical symmetry of the 12 K structure is still orthorhombic, the antiferromagnetic ordering of the spins (in the proposed model) reduces the overall symmetry to monoclinic. The proposed magnetic structure can be described with the space group F112 (a non-standard setting of C2). A magnetic structure refinement, based on the proposed magnetic ordering, was carried out in the space group F112 with a magnetic cell of lattice parameters twice that of the chemical cell in all directions. The refinement was initiated with the structural parameters from the room temperature refinement, and with a magnetic moment of 4 μ_B. Thirteen parameters were allowed to refine: the scale factor, the detector zero-point

offset, six background parameters, the theta independent half-width parameter, the three lattice parameters, and the magnetic moment on the manganese atoms. The appropriate spin direction, relative to the lattice parameters, was found by trial and error to be parallel to the b-axis. The results of the refinement are tabulated in table 5.1.1 and demonstrated graphically in figure 5.1.2. The difference between the observed intensities (symbols) and the calculated intensities (line) is plotted below, and the positions of the magnetic and chemical reflections are indicated by the arrows at the top of the figure. Clearly, the proposed magnetic structure is an excellent fit to the observed diffraction pattern. The large peak at about 40.5 degrees is due to the aluminum sample holder. Consequently, this peak and the weak peak at near 16 degrees were excluded from the refinement.

The chemical structure remains the same on cooling to 12 K, with a slight contraction in all three lattice directions, the unit cell volume is reduced by 1.2 %. The magnetic moment of the manganese atoms refined to 3.61(5) μ_B very close to the expected 4 μ_B for high-spin Mn^{3+}. Releasing the spin direction from the b-axis did not improve the fit of the refinement.

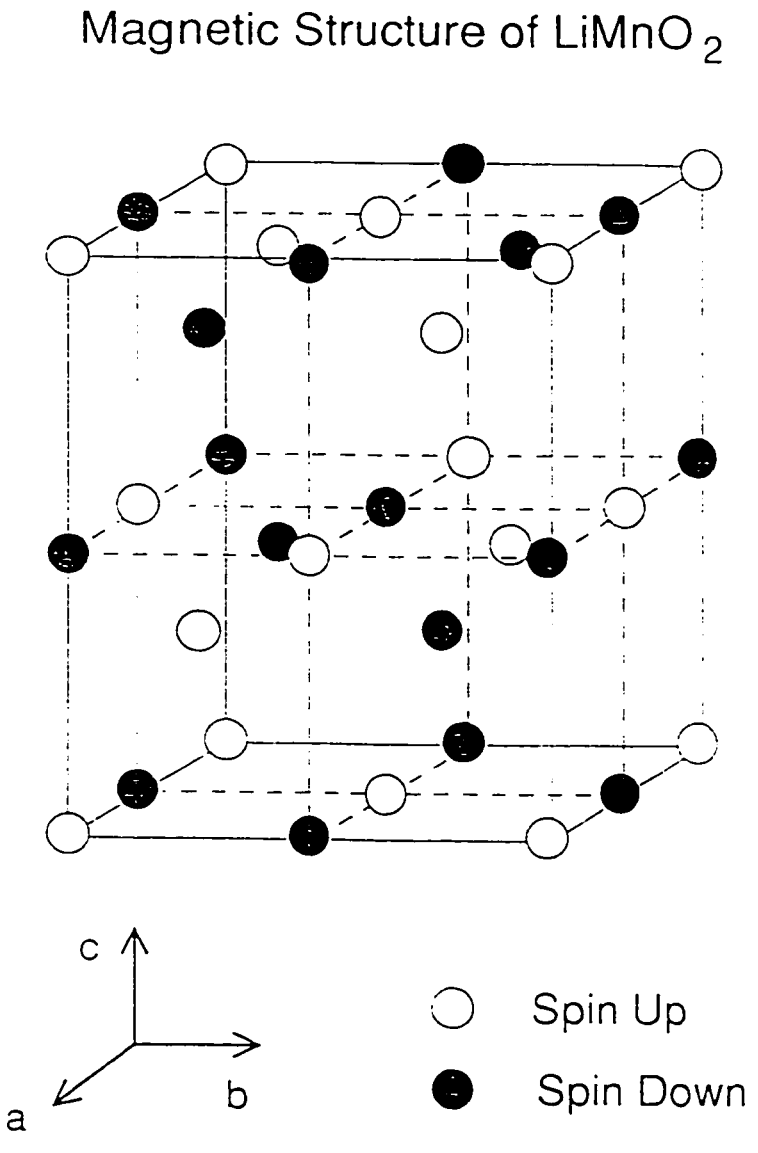

Figure 5.1.1 - Illustration of magnetic structure model for orthorhombic $LiMnO_2$.

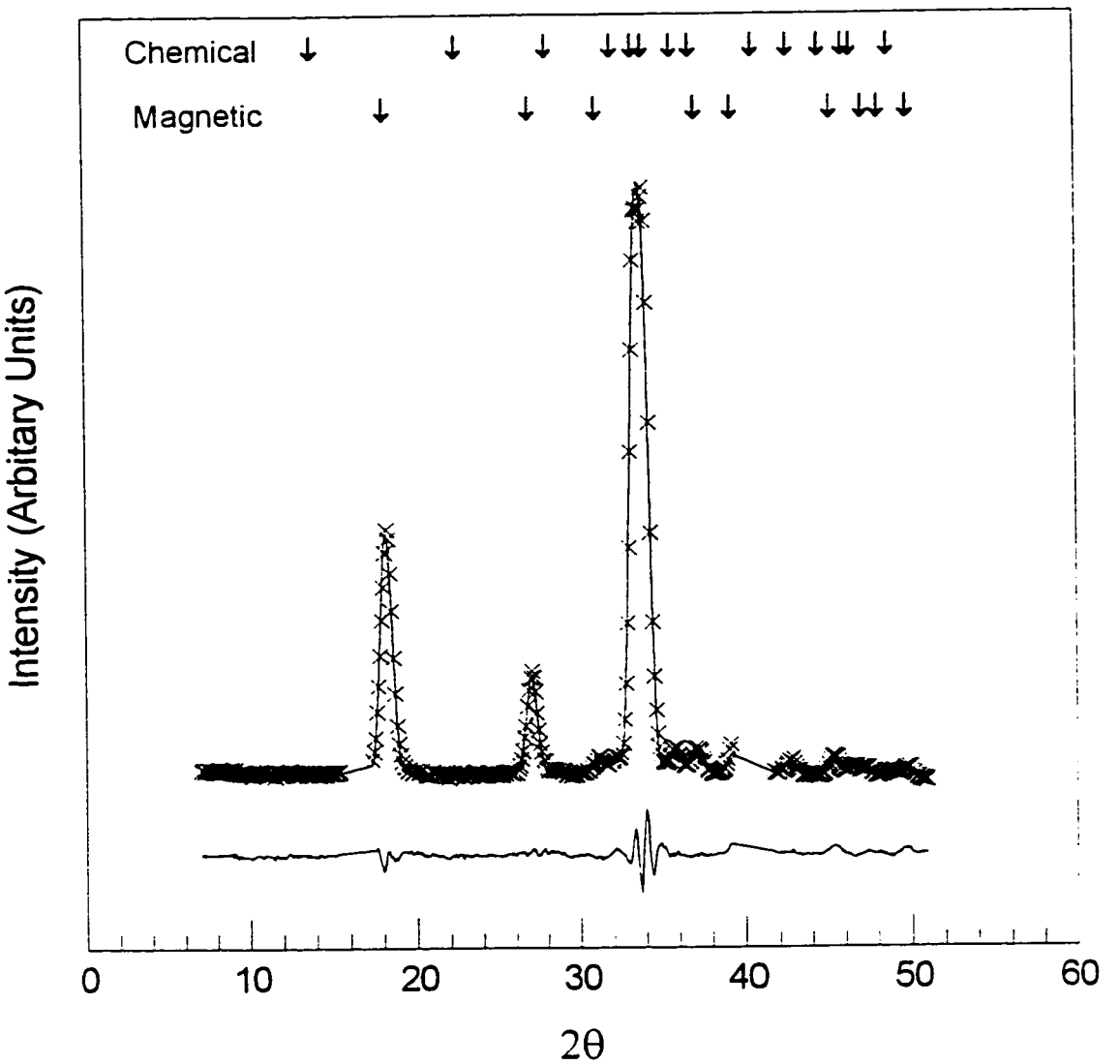

Figure 5.1.2 - Refinement of 12 K neutron data for orthorhombic $LiMnO_2$.

Table 5.1.1 - Rietveld Refinement of 12 K Neutron Diffraction Data for $LiMnO_2$ with Spins Aligned Parallel to the B - axis

Space Group F112 (C^3_2) Wavelength 1.3913 Å

Lattice Parameters: a = 5.604(2) Å, b = 9.072(5) Å and c = 11.473(5) Å

Atom	x	y	z	Moment (μ_B)	Occup.
Mn (4a)	0.0	0.0	0.0	3.61(5)	1.0
Mn (4b)	0.0	0.0	0.5	-3.61(5)	1.0
Mn (4c)	0.25	0.25	0.365	3.61(5)	1.0
Mn (4c)	0.25	0.25	0.865	-3.61(5)	1.0
Li (4a)	0.0	0.0	0.2455		1.0
Li (4b)	0.0	0.0	0.7455		1.0
Li (4c)	0.25	0.25	0.1195		1.0
Li (4c)	0.25	0.25	0.6195		1.0
O (8d)	0.0	0.25	0.4835		1.0
O (8d)	0.0	0.25	0.2545		1.0
O (8d)	0.25	0.0	0.1150		1.0
O (8d)	0.25	0.0	0.3815		1.0

Overall Temperature Factor = 0.05 $Å^2$

Scale = 0.01256(8) Zero-point Offset = 0.02(1)

Half-width Parameters: U = 1.40 V = -1.20 W = 0.82(1)

Scattering lengths: Mn (-0.373), Li (-0.190), O (0.5803)

Weighted profile R = 7.35 Profile R = 5.63

Bragg R = 2.08 Expected R = 2.52

J. E. Greedan and N. P. Raju recently completed a magnetic susceptibility study on the same sample of orthorhombic $LiMnO_2$ (Greedan, Raju and Davidson 1996). Magnetic susceptibility data from 5 K to 350 K at an applied field of 10^{-2} T are shown in figure 5.1.3. The squares and triangles represent zero field cooled and field cooled conditions, respectively. The most prominent features in the susceptibility are a maximum below 50 K and a divergence between the field cooled and zero field cooled susceptibilities below 100 K. No Curie-Weiss behaviour was evident in the susceptibility even up to 350 K. The inset shows the magnetic heat capacity contribution, $d\chi T/dT$ versus T near 260 K. The plot of the inverse of the susceptibility, figure 5.1.4, shows a weak inflection at about 260 K. A precise value for T_N was obtained by fitting data near the ordering temperature to a power law of the type $M = [(T_c - T)/T_c]^{\beta}$ where M is the sublattice magnetization, T_c is the critical temperature and β is the critical exponent. The fitted parameters were found to be $T_N = 261.5(5)$ K and $\beta = 0.376(17)$. The critical exponent value is consistent with a three dimensional Heisenberg model which is reasonable for Mn^{3+}.

An anomaly in the temperature dependence of the magnetic moment below 100 K is seen in a plot of the intensities of the (1/2 1/2 1/2) and the (1/2 1/2 3/2) reflections versus temperature, figure 5.1.5. At higher temperatures the intensities have a Brillioun function like dependence, but below 100 K, a positive and negative deviation is seen in the (1/2 1/2 1/2) and the (1/2 1/2 3/2)

reflections, respectively. This is most likely due to spin canting but it was not possible to determine the canting angle from the neutron data. The angle is likely to be small but it does mean the $LiMnO_2$ is a weak ferromagnet at low temperatures. This feature explains the observed difference, at temperatures below 100 K, in the field cooled and zero field cooled bulk susceptibilities.

In the powder pattern at 271 K (figure 5.1.6), 10 K above T_c, all the magnetic Bragg peaks have disappeared but a broad feature centered around a 2θ value of about 16 degrees which has a distinctly asymmetric shape is still clearly visible. The peak shape with a relatively sharp rise at low angle followed by a more gradual decrease over several degrees to higher angles is characteristic of a Warren type which is a signal of two dimensional correlations. The insert to figure 5.1.6 shows a fit, calculated by Greedan and Raju, of this peak to a Warren function. The peak fit indicates a two dimensional correlation length of 36(1) Å.

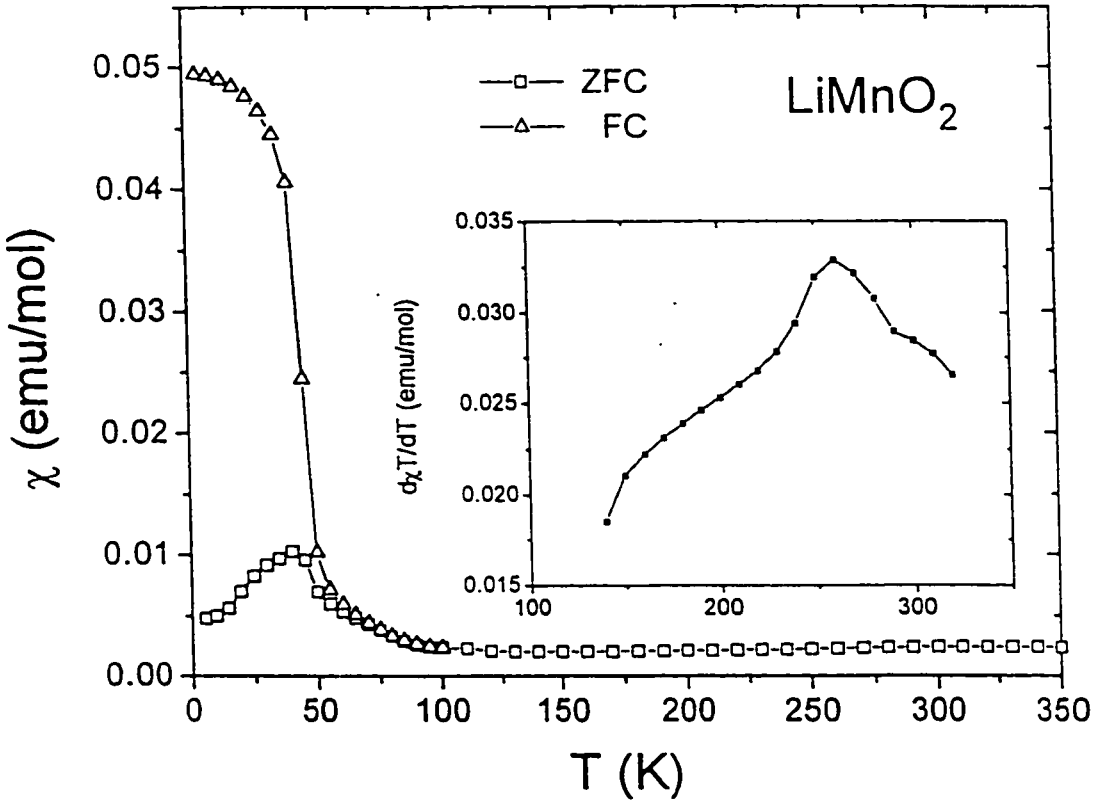

Figure 5.1.3 - Magnetic susceptibility of $LiMnO_2$ at an applied field of 10^{-2} T.

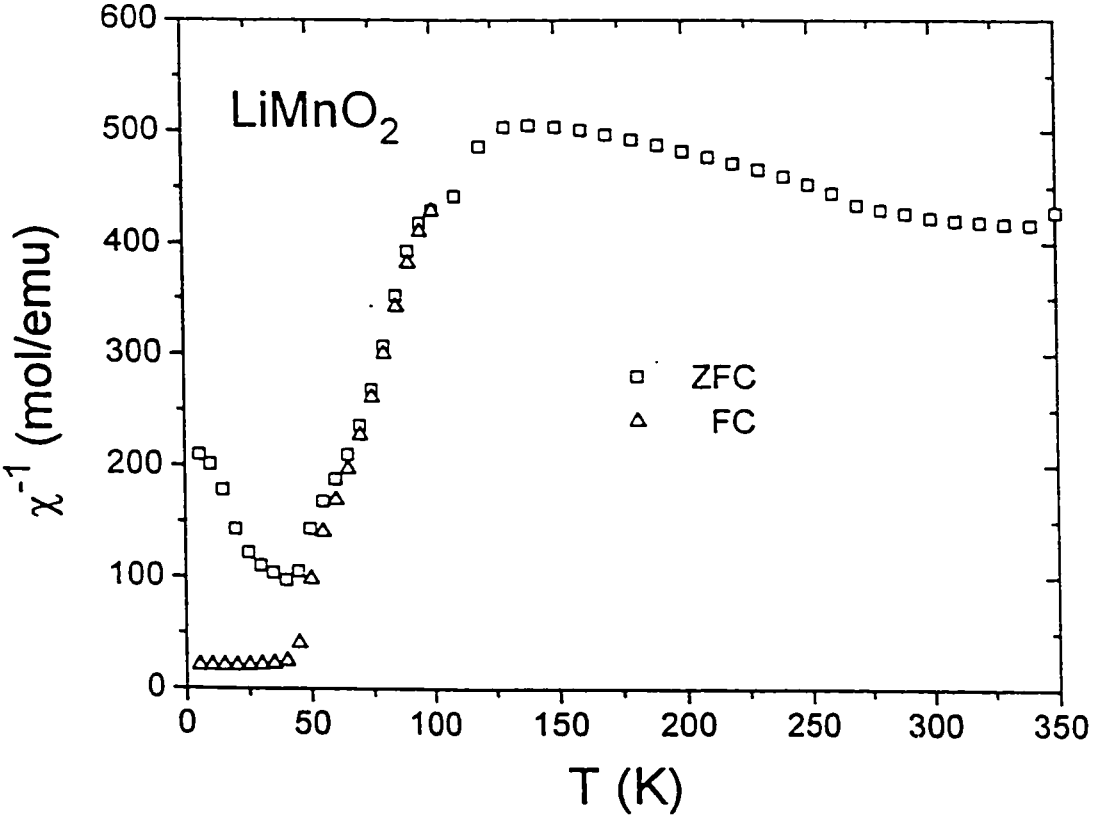

Figure 5.1.4 - Plot of the inverse of the susceptibility of $LiMnO_2$.

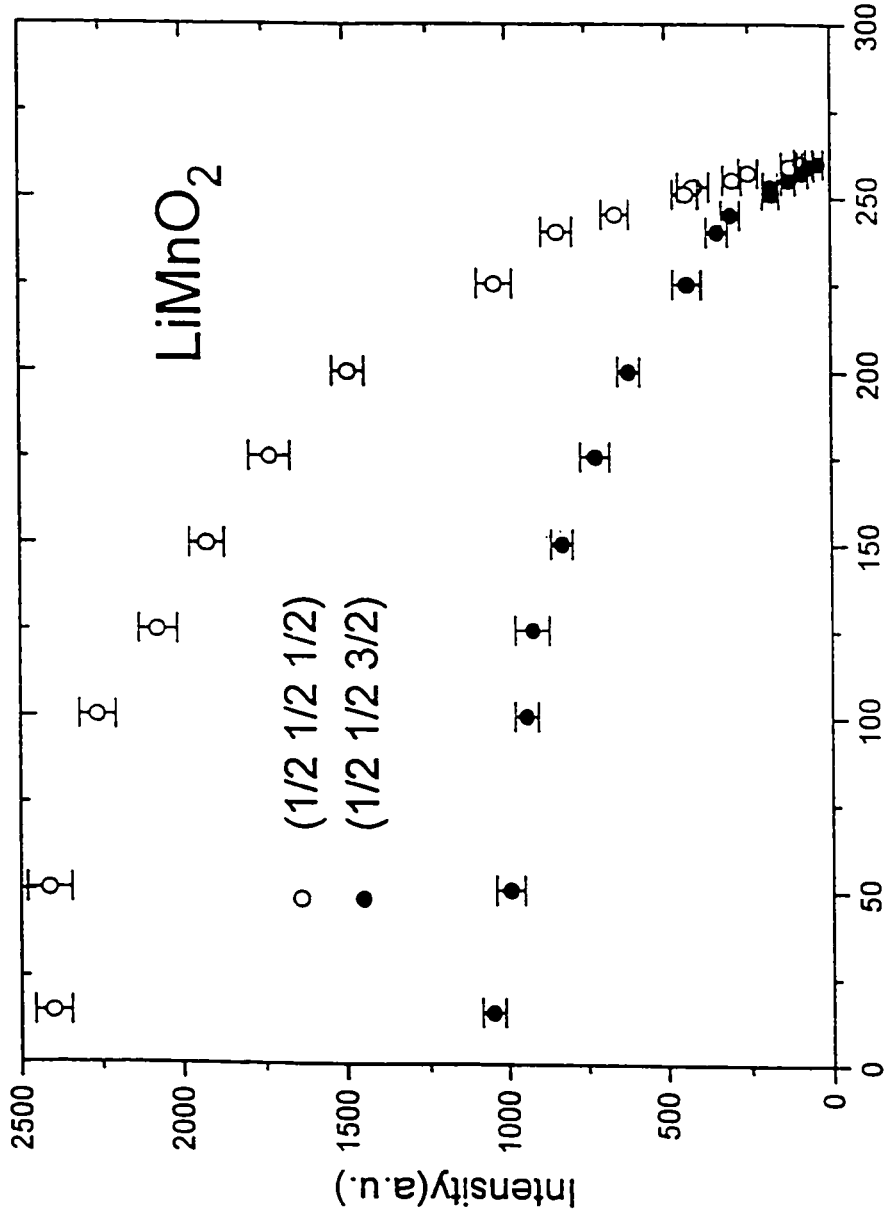

Figure 5.1.5 - Plot of peak intensity versus temperature for the (1/2 1/2 1/2) and (1/2 1/2 3/2) reflections.

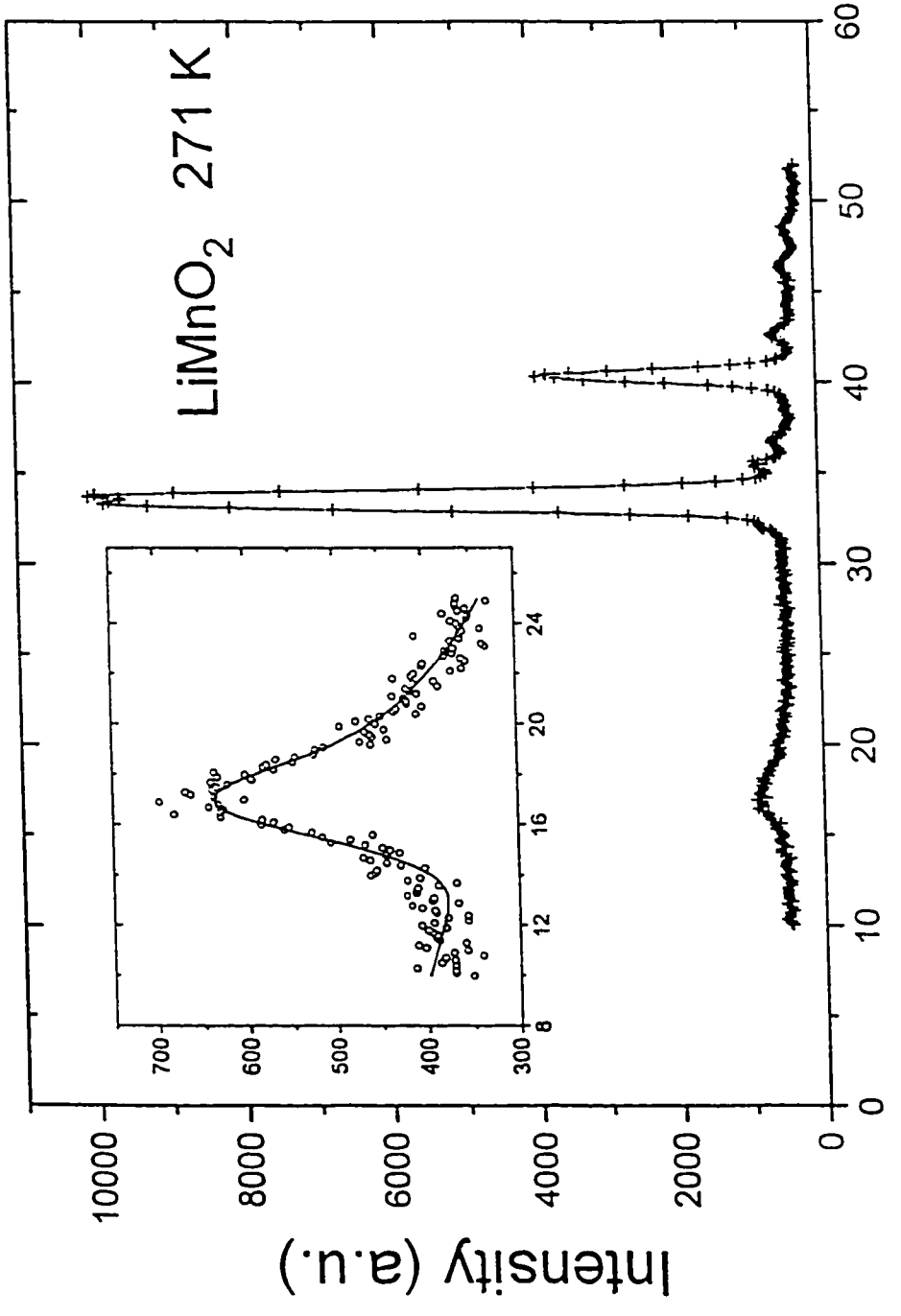

Figure 5.1.6 - Neutron diffraction pattern of $LiMnO_2$ at 271 K and inset showing fit of low angle feature to Warren function.

5.2 $LiFeO_2$

The $LiFeO_2$ phase, prepared by the *chimie douce* procedure of ion-exchange outlined in chapter 3, its powder diffraction pattern can be fit to either a hexagonal 3R-type structure or a cubic spinel-related structure. Magnetic structure is crucially dependent on crystal symmetry and can be used to determine the correct chemical ordering. Therefore, low temperature neutron diffraction data were obtained on this phase of $LiFeO_2$ in an effort to identify both the magnetic and chemical structure of this material.

Neutron powder diffraction data were collected, over a broad range of temperatures, at the McMaster nuclear reactor on the spectrometer described in chapter 4. The sample was contained in a cylindrical aluminum sample holder which was back filled with helium gas. The helium serves as a heat exchanger to ensure thermal equilibration of the sample. The neutron powder diffraction patterns of $LiFeO_2$, shown in figure 5.2.1, for the temperature range 290 K to 10 K indicate only two magnetic peaks, at about 8.9 and 25.0 degrees in 2θ, which begin to form at about 21 K. These peaks are more clearly seen in figure 5.2.2 which plots the difference between the 10 K and 290 K diffraction patterns. The four small broad peaks in the region between 18 and 30 degrees in 2θ are from Li_2CO_3 formed during the synthesis of the sample. These four peaks are, by far, the strongest intensities in the neutron diffraction pattern of Li_2CO_3. The region between 18 and 30 degrees was, therefore, excluded in the structure

refinements. The anomalously high background below about 10 degrees in 2θ is not temperature dependent and may be due to a small amount of absorbed moisture. This background anomaly affects the shape of the magnetic peak about 8.9 degrees in 2θ making it somewhat asymmetrical. A plot of the square root of the intensity of the strongest magnetic reflection against temperature, figure 5.2.3, indicates a critical temperature of 21 K.

A neutron diffraction pattern, shown in figure 5.2.4, was collected over a broader angular range at 10 K. The peak at about 40.7 degrees in 2θ is due to the aluminum sample holder and must be excluded in any structure refinements. Attempts were made to fit the pattern to both the hexagonal 3R-type structure and the cubic spinel-related structure. The rather high background at low angle makes the indexing of the main magnetic peak about 8.9 degrees more uncertain than usual. Depending on the direction of the detector's zero position offset and the fitting of the peak shape, the peak at 8.9 degrees might be either the (1 0 0) reflection of the cubic spinel cell, the (0 0 3/2) reflection of the hexagonal 3R cell. This magnetic peak could also be a (1/6 1/6 0) reflection of the hexagonal cell but it is difficult to envision a model which requires such a large unit cell. Numerous models based on doubling or tripling the dimensions of the cubic chemical cell along one, two or three cell edges were evaluated with the program *Rietan* (Izumi 1989), but none of these resulted in magnetic peaks at the observed diffraction angles. However, a simple anti-ferromagnetic model based on a doubling of the hexagonal chemical cell along the c-axis, with the

spins are aligned perpendicular to the c-axis, resulted in a strong peak near 8.9 degrees, a weak peak near 25.0 degrees and a few other very weak peaks. This magnetic structure was refined using the program *Rietan*.

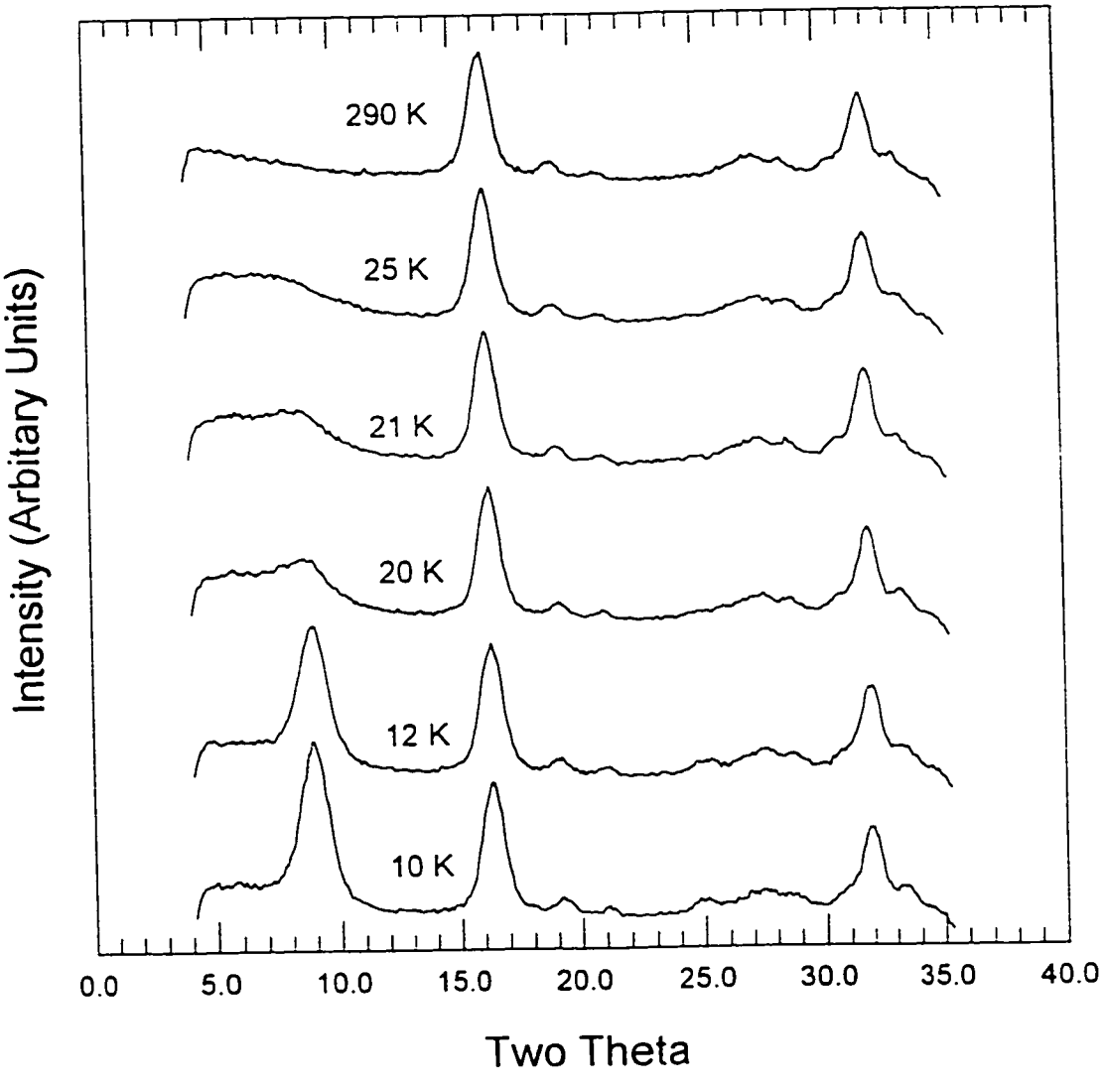

Figure 5.2.1 - Neutron diffraction patterns for $LiFeO_2$ from 10 K to 290 K.

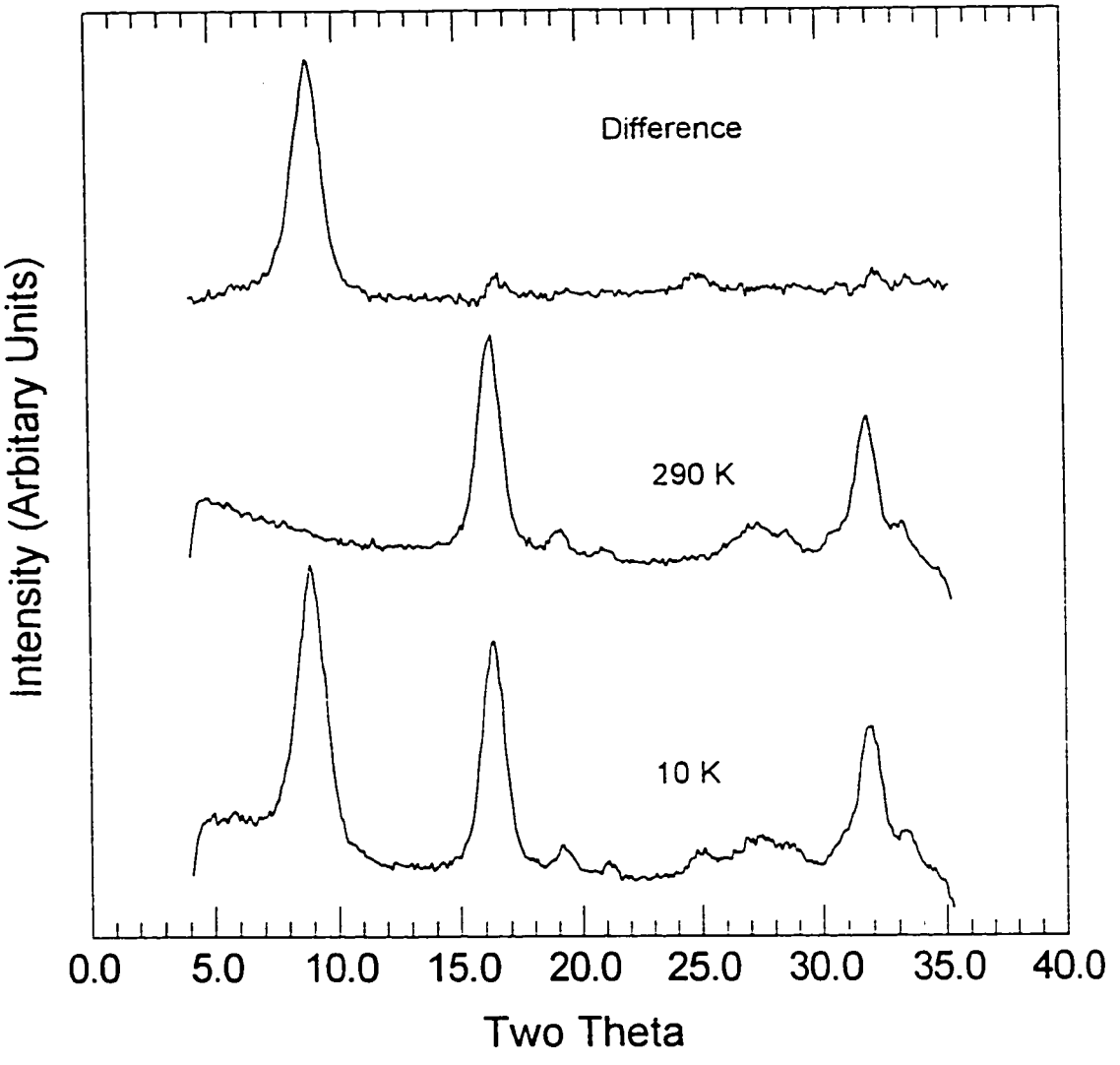

Figure 5.2.2 - Comparison between neutron diffraction patterns for $LiFeO_2$ at 10 K and 290 K.

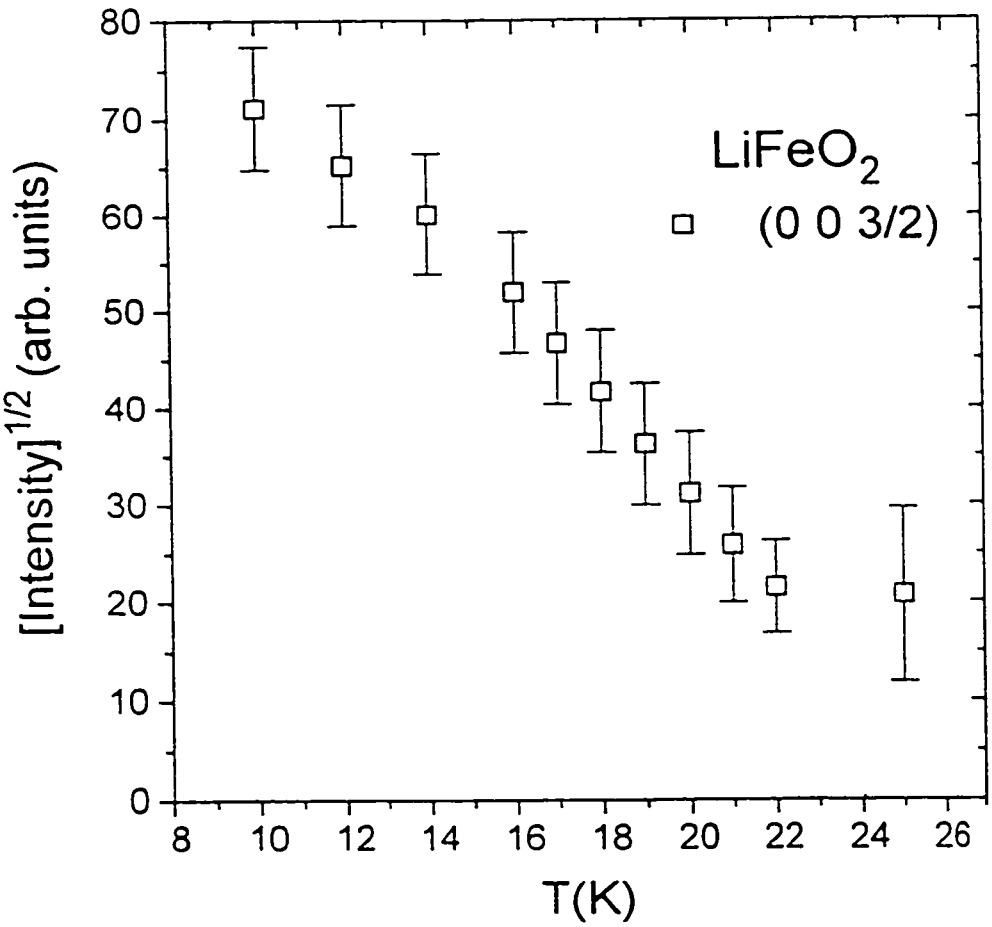

Figure 5.2.3 - Plot of the square root of the intensity of the strongest magnetic reflection versus temperature.

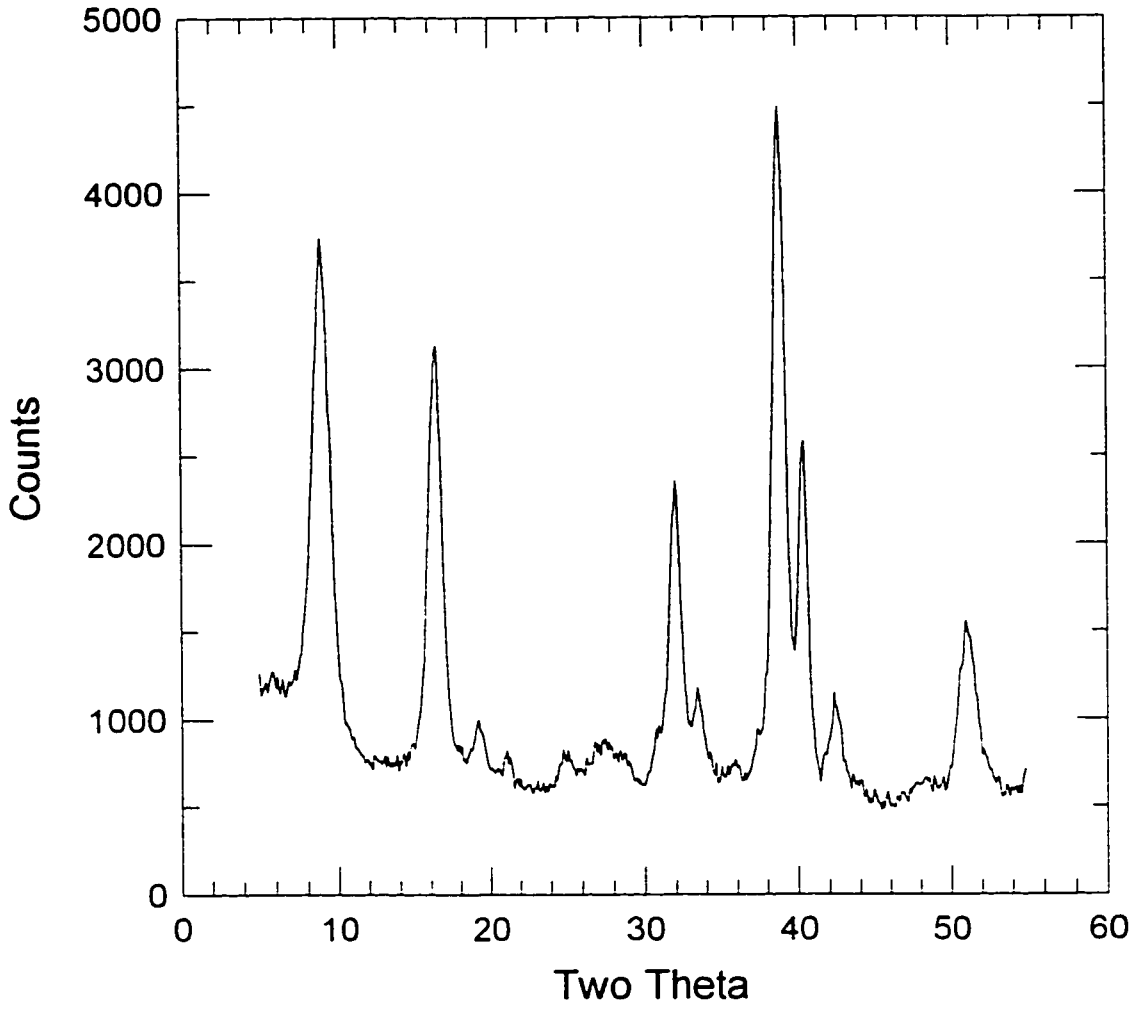

Figure 5.2.4 - Neutron diffraction pattern of $LiFeO_2$ at 10 K over a broader angular range.

In the model, the magnetic peak near 8.9 degrees in 2θ was indexed to the (0 0 3/2) reflection of the chemical cell implying $c_{mag} = 2\ c_{chem}$ or a magnetic sublattice propagation vector k = (00½). The small magnetic peak near 25 degrees was indexed to the (0 0 9/2) reflection. *Rietan* uses the equations given by Shirane (1959) to refine the magnetic moment, μ_j, of each magnetic site, and the angle between the spin direction and the unique axis of the lattice, Φ. For these calculations, the magnetic form factor determined for Fe^{3+} in magnetite (Bacon 1975) was used. The refinement was carried out in the space group R -3 m with $c_{mag} = 2\ c_{chem}$, and the two iron sites, 3a and 3b, were assigned opposing spin orientations.

The iron atoms separated by two layers of lithium and oxygen atoms exhibit ABC stacking in the cubic close packed structure. Within the planes perpendicular to the c-axis, neighboring iron atoms are linked through bonds to oxygen atoms at a bond angle of near 90 °. As the Goodenough-Kanamori rules predict anti-ferromagnetic interactions for a 90° d^5-d^5 system, anti-ferromagnetic order within the planes perpendicular to the c-axis can be anticipated (Goodenough 1963). However, the absence of magnetic reflections assignable to magnetic ordering along the a or b axes suggests that this is not the case for $LiFeO_2$. The observed magnetic reflections indicate anti-ferromagnetic ordering along the c-axis with the spins perpendicular to the c-axis.

As shown by figure 5.2.5, a structural model with the magnetic moments, perpendicular to the c-axis, in ferromagnetically ordered a/b planes, anti-

ferromagnetically aligned along the c-axis, is a reasonable fit to the observed intensities. The difference between the observed intensities (symbols) and the calculated intensities (line) is plotted below, and the positions of the magnetic and chemical reflections are indicated by the arrows at the top of the figure. The details of this Rietveld refinement are tabulated in table 5.2.1. The six background parameters, the scale, the zero-point shift, an asymmetry parameter, the theta independent half-width parameter, two lattice parameters, the position parameter of the oxygen atoms and the magnetic moment of the iron atoms were allowed to refine. The asymmetry parameter is based on the empirical formula of Rietveld (1969) and was only used in fitting the lowest angle peak near 8.9 degrees. The structure remained essentially unchanged on cooling to 10 K except for a small expansion in the cell volume. This apparent increase in cell volume is unlikely to be real. The fit between the calculated and observed patterns is not as good as is generally achieved in single phase highly crystalline materials. However, this low temperature form of $LiFeO_2$ is meta-stable and can only be prepared via *chimie douce*. Consequently, samples of this phase are always of low crystallinity and usually contain small amounts of impurities. Furthermore, a later TEM study on this sample of $LiFeO_2$ showed that it is multi-phase containing some crystallites with the cubic lithiated spinel structure. The magnetic moment refined to $2.5 \pm .4\ \mu_B$, a rather small moment for high spin Fe^{3+}. The expected moment for a high spin d^5 ion is $5\ \mu_B$ However,

10 K is not much below the critical temperature, 21 K, and the ordering may not be complete.

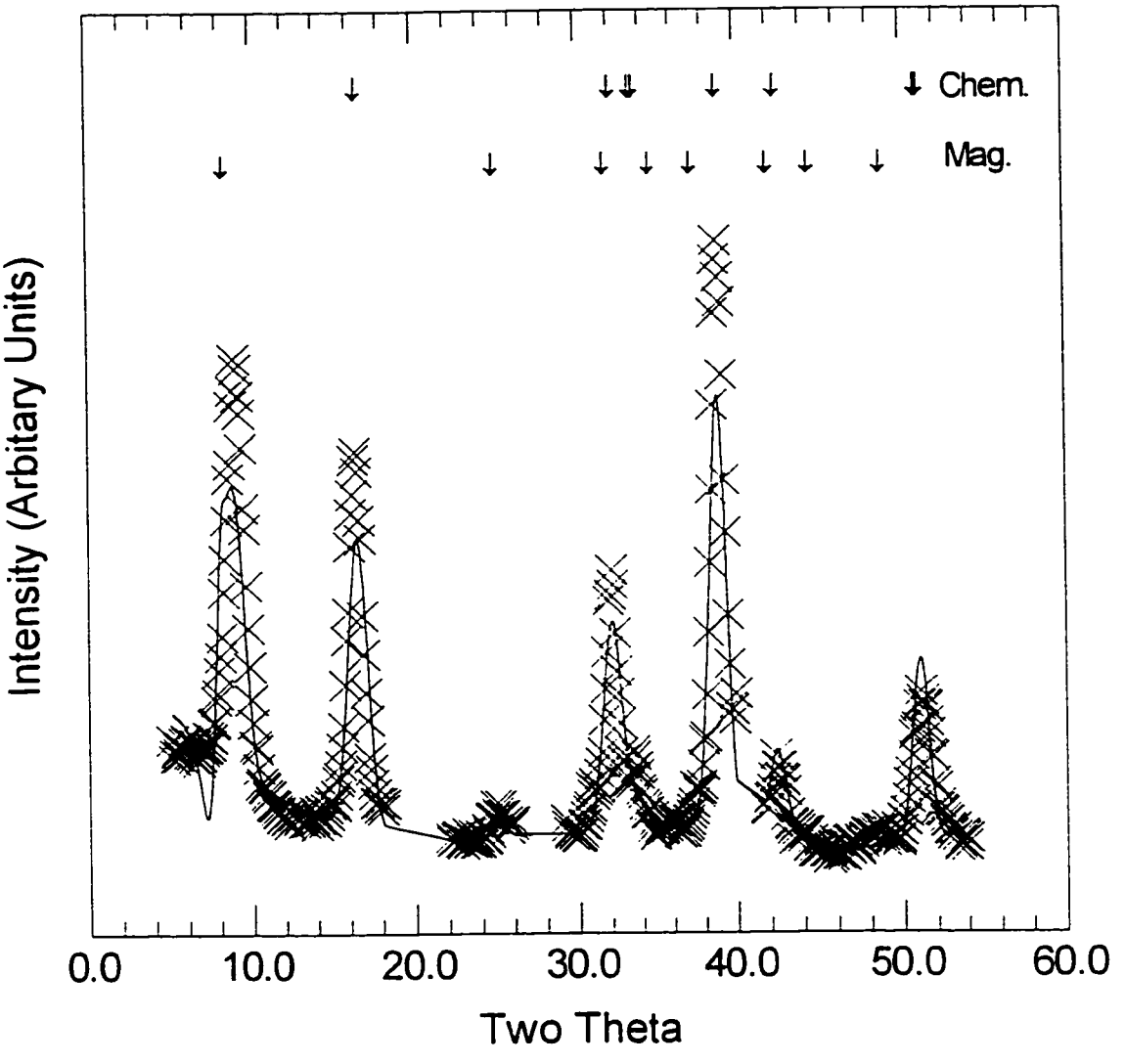

Figure 5.2.5 - Rietveld refinement of 10 K neutron data for $LiFeO_2$.

Table 5.2.1 - Rietveld Refinement of 10 K Neutron Diffraction Data for $LiFeO_2$ with Spins Aligned Perpendicular to the C - axis

Space Group R -3 M (D_{3d}^5) Wavelength 1.3951 Å

Lattice Parameters: a = 2.968(4) Å and c = 29.29(4) Å

Atom	x	y	z	Moment (μ_B)	Occup.
Fe (3a)	0.0	0.0	0.0	2.5(4)	1.0
Fe (3b)	0.0	0.0	0.5	-2.5(4)	1.0
Li (6c)	0.0	0.0	0.25		1.0
O (6c)	0.0	0.0	0.128(2)		1.0
O (6c)	0.0	00	0.628(2)		1.0

Overall Temperature Factor B = 0.05 $Å^2$ Scale = 0.180(5)

Asymmetry Parameter = -0.13(1) Zero-point Offset = 0.09(3)

Half-width Parameters: U = 1.50 V = -1.20 W = 1.13(7)

Scattering lengths: Fe (0.954), Li (-0.190), O (0.5803)

Weighted profile R = 15.11 Profile R = 12.28

Bragg R = 7.29 Expected R = 2.97

5.3 1T - Li_2NiO_2

As demonstrated in chapter 4, the hexagonal phase of Li_2NiO_2 has a 1T structure belonging to the space group P -3 m 1, with a = 3.0954(9) Å and c = 5.070(1) Å at 300 K. The nickel atom occupies the 1a position at (0,0,0), and the lithium and oxygen atoms, the 2d sites at (1/3,2/3,0.649) and (1/3,2/3,0.2333), respectively. As the magnetic atoms are separated by three nonmagnetic sheets, this material could have substantial 2D character in its magnetic properties.

Neutron powder diffraction data were collected at the McMaster Nuclear Reactor on the spectrometer described previously. The sample was held in an aluminum can which was sealed with an indium gasket in a helium atmosphere. The helium serves both as a heat exchange gas and to protect the air and moisture sensitive sample from chemical decomposition.

Neutron powder diffraction patterns of 1T - Li_2NiO_2, shown in figure 5.3.1, for the temperature range 65 K to 10 K indicate only one magnetic peak, at 31.2 degrees in 2θ, which begins to form at about 57 K. The magnetic peak indexes as (10½) relative to the chemical cell implying $c_{mag} = 2\, c_{chem}$ or a magnetic sublattice propagation vector $\vec{k}$ = (00½).

A neutron powder diffraction pattern of Li_2NiO_2 was collected over a broader angular range at 10 K, and was analyzed with the Rietveld profile refinement program *Rietan* written by F. Izumi (1989). The magnetic moment, μ_j,

of each magnetic site, and the angle between the spin direction and the unique axis of the lattice, Φ, can be refined using the equations given by Shirane (1959). For these calculations, the magnetic moment of the nickel ion was taken as 2 μ_B, and the magnetic form factor determined for Ni^{2+} in NiO by Alperin (1962) was used . The refinement was carried out in the chemical space group P -3 m 1 but with $c_{mag} = 2\ c_{chem}$, and the two nickel sites, 1a and 1b, were allowed different spin orientations. Figure 5.3.2 is the $11\bar{2}0$ projection of the doubled 1T cell with the c-axis vertical. The dashed line indicates the hexagonal cell. The nickel atoms separated by two layers of lithium and oxygen atoms exhibit AAA stacking in the hexagonal close packed structure. Within the planes perpendicular to the c-axis, neighboring nickel atoms are linked through bonds to oxygen atoms at a bond angle of 92.5 °. As the Goodenough-Kanamori rules predict ferromagnetic interactions for a 90° d^8-d^8 system, ferromagnetic order within the planes perpendicular to the c-axis can be anticipated (Goodenough 1963). The absence of magnetic superlattice reflections assignable to expansion of the a or b axes supports this view, as do the bulk magnetic properties reported in the following section.

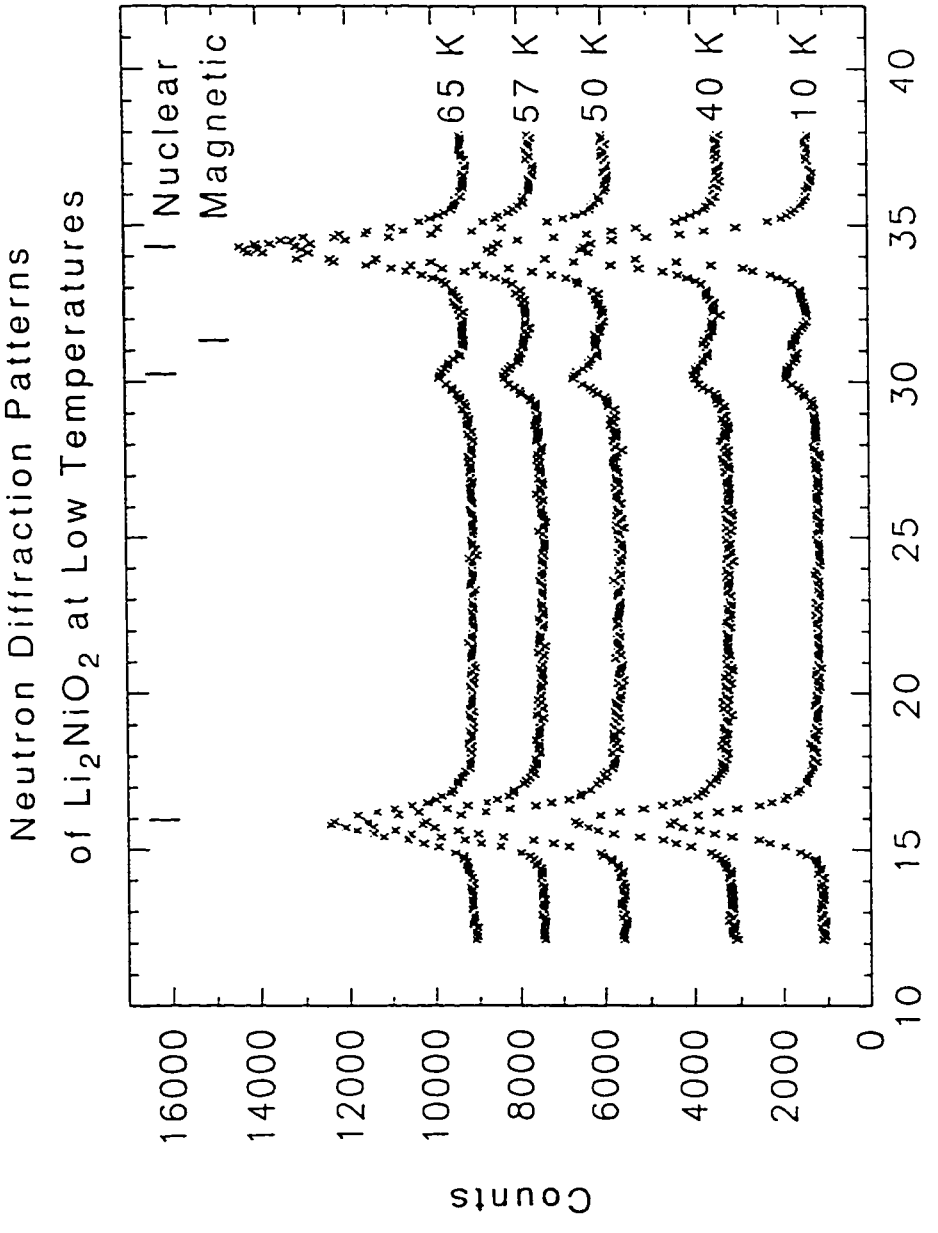

Figure 5.3.1 - Neutron diffraction patterns for 1T- Li_2NiO_2 from 10 to 65 K.

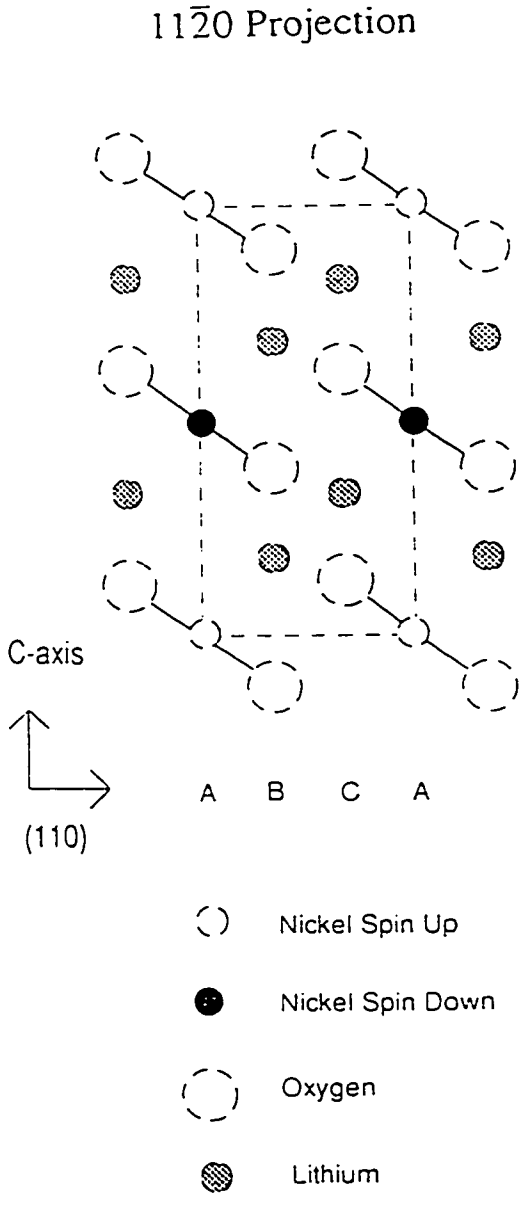

Figure 5.3.2 - 11 $\bar{2}$ 0 projection of magnetic crystallographic unit cell.

Thus, two structures, based on antiferromagnetically coupled ferromagnetic sheets, one with spins normal to c and the other with the spins parallel to c were refined. The results are shown in figures 5.3.3 and 5.3.4. The peak at 40 degrees is due to the aluminum container and the shoulder at 39 degrees results from residual NiO and $LiNiO_2$ from the synthesis of the material (Davidson *et al* 1991). Neither $LiNiO_2$ nor NiO contribute to the peak at 31.5 degrees in 2θ. For $LiNiO_2$, no magnetic Bragg scattering has been observed at any temperature or angle (Hirakawa and Kadowaki 1986). The low temperature neutron diffraction pattern of NiO was investigated by Roth (1958). As shown by figure 5.3.4, the model with the magnetic moments parallel to the c axis is a good fit to the observed intensities. The details of this Rietveld refinement are tabulated in table 5.3.1. The atomic positions were fixed at the sites determined previously from the room temperature powder neutron diffraction data (Davidson *et al* 1991). The three background parameters, the scale, the zero-point shift and two lattice parameters were allowed to refine. The structure remained unchanged on cooling to 10 K. However, both the a and c axes shrank slightly, thereby reducing the cell volume by 1.2%. Releasing the magnetic moment for refinement gave a value of $1.40 \pm 0.49\ \mu_s$ with no improvement in the profile fit.

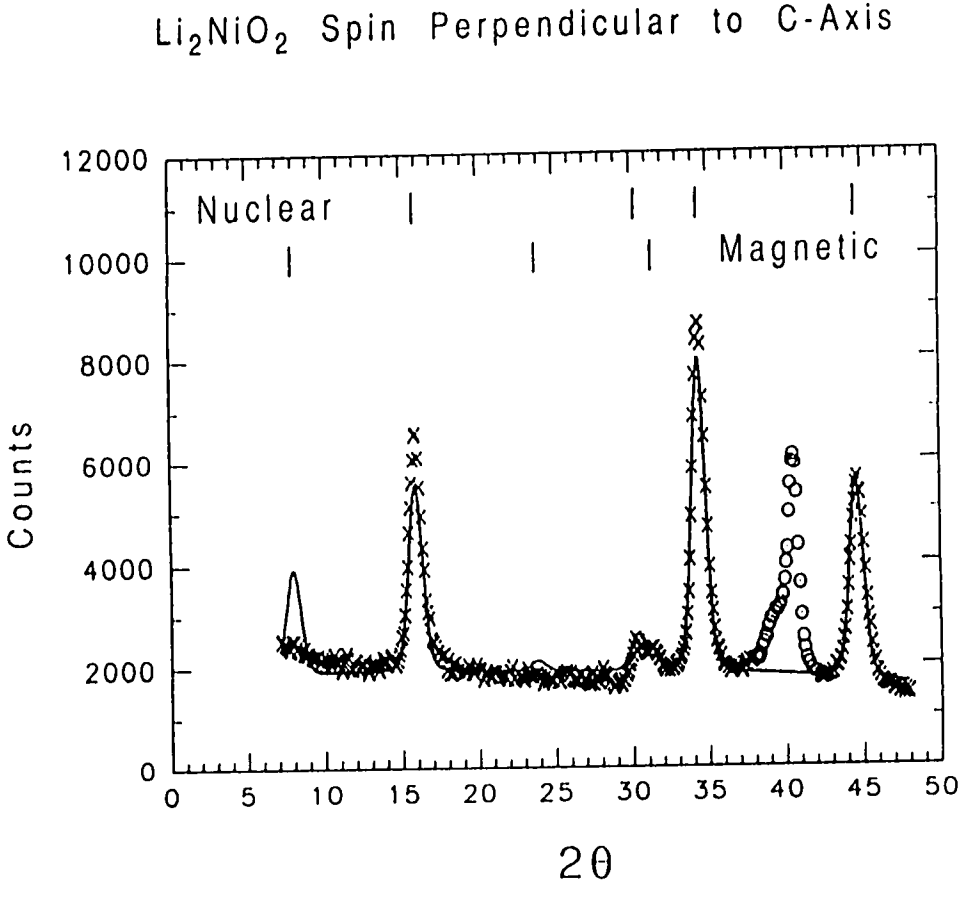

Figure 5.3.3 - Rietveld refinement fit of 10 K neutron diffraction data with the spin perpendicular to the c-axis for 1T-Li_2NiO_2.

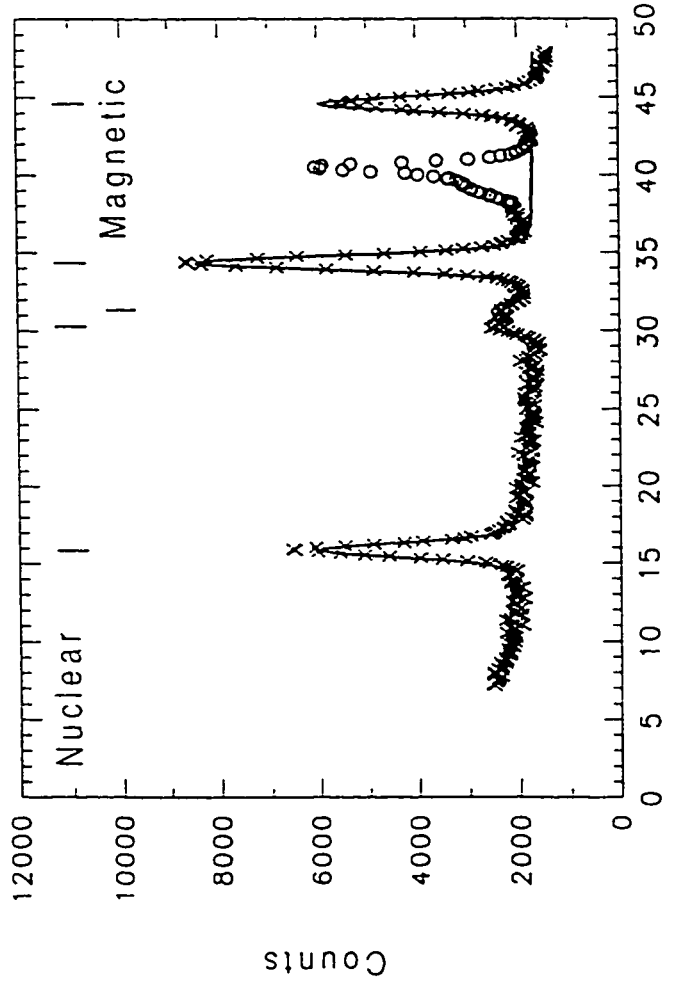

Figure 5.3.4 - Rietveld refinement fit of 10 K neutron diffraction data with the spin parallel to the c-axis for 1T-Li_2NiO_2.

Table 5.3.1 - Rietveld Refinement of 10 K Neutron Diffraction Data for Li_2NiO_2 with Spins Aligned Parallel to the C - axis

Space Group P-3m1 (D^3_{3d})

Lattice Parameters a = 3.080(2) Å and c = 10.118(8) Å

Atom	x	y	z	Moment (μ_B)	Occup.
Ni (1a)	0.0	0.0	0.0	2.0	1.0
Ni (1b)	0.0	0.0	0.5	-2.0	1.0
Li (2d)	1/3	2/3	0.3245		1.0
Li (2d)	1/3	2/3	0.8245		1.0
O (2d)	1/3	2/3	0.1167		1.0
O (2d)	1/3	2/3	0.6167		1.0

Overall Temperature Factor B = 0.05 $Å^2$

Half-width Parameters: U = 1.80 V = -1.20 W = 1.31

Scattering lengths: Ni (1.030), Li (-0.190), O (0.5803)

Weighted profile R = 6.01 Profile R = 4.79

Bragg R = 3.56 Expected R = 2.00

Bulk magnetization studies on 1T-Li_2NiO_2 further demonstrated the 2D character of this material (Davidson *et al* 1993). Dc magnetization was measured in a *Quantum Design* SQUID magnetometer. For the magnetization measurements, 16.01 mg of 1T-Li_2NiO_2 were contained in a crimp seal aluminum TGA capsule, which had been filled and sealed in a helium atmosphere glove box.

An apparent susceptibility can be calculated by dividing the dc-magnetization by the applied field, M/H. The plot of M/H against temperature, figure 5.3.5, is indicative of an antiferromagnet with a T_N of 64 K, but as the inset figure shows, the magnetization does not fit Curie-Weiss behaviour. In the plot of magnetic moment versus applied field to 2.0 Tesla, figure 5.3.6, the moment is linearly dependent on the applied field for T = 10 K and 30 K. Hence the magnetic behaviour is consistent with long range antiferromagnetic ordering (LRAFO) for $T < T_N$. However, when the applied field is raised to 5.0 Tesla the observed moments, shown in figure 5.3.7, are much larger than expected based on a linear extrapolation of the lower field data. In fact, at 5.0 Tesla, the actual moments are quite substantial, 1.27 μ_B / Ni^{+2} at 10 K. The change in slope of the magnetic moment between 2.0 and 5.0 Tesla and the large observed moments at high field indicate a metamagnetic transition. Replotting the moment versus field data as moment versus temperature (figure 5.3.8) shows that the maximum disappears for the B = 5.0 Tesla case. The small quantities of NiO and $LiNiO_2$ present in our sample are not expected to interfere with interpretation of the

magnetization studies. NiO is an antiferromagnet with a T_N = 523 K.(Kondoh 1960) In a recent study of $LiNiO_2$ (Reimers *et al* 1993), the observed values of the molar susceptibility were lower by a factor of 5 or more than those of Li_2NiO_2 at the same temperature. Thus the contribution of $LiNiO_2$ to the measured magnetization of our sample would be at the 1-2% level.

The M/H versus T data for $T > T_N$ show that the measured M/H values are always higher than the values predicted by the Curie Law and that M/H is field dependent. This can only be due to ferromagnetically coupled domains or clusters of subcritical size within the layers. The domain size distribution and moment distribution are temperature and field dependent. The moment versus field curves for T = 65 K and 100 K (figure 5.3.6) show curvature consistent with ferromagnetic correlations. At 65 K, the moment versus field data shows a smooth increase up to 5.0 Tesla where a large moment of about 1.0 μ_B / Ni^{2+} is found. The 100 K data show a slope change between the ranges below 2.0 Tesla and above 2.0 Tesla indicating a more complex short range ordered microstructure. Even at T = 300 K, the apparent susceptibility, M/H, is different for an applied field of 0.01 Tesla and 1.0 Tesla. The non-linear field dependence at T = 300 K indicates that the short range ferromagnetic order persists above room temperature.

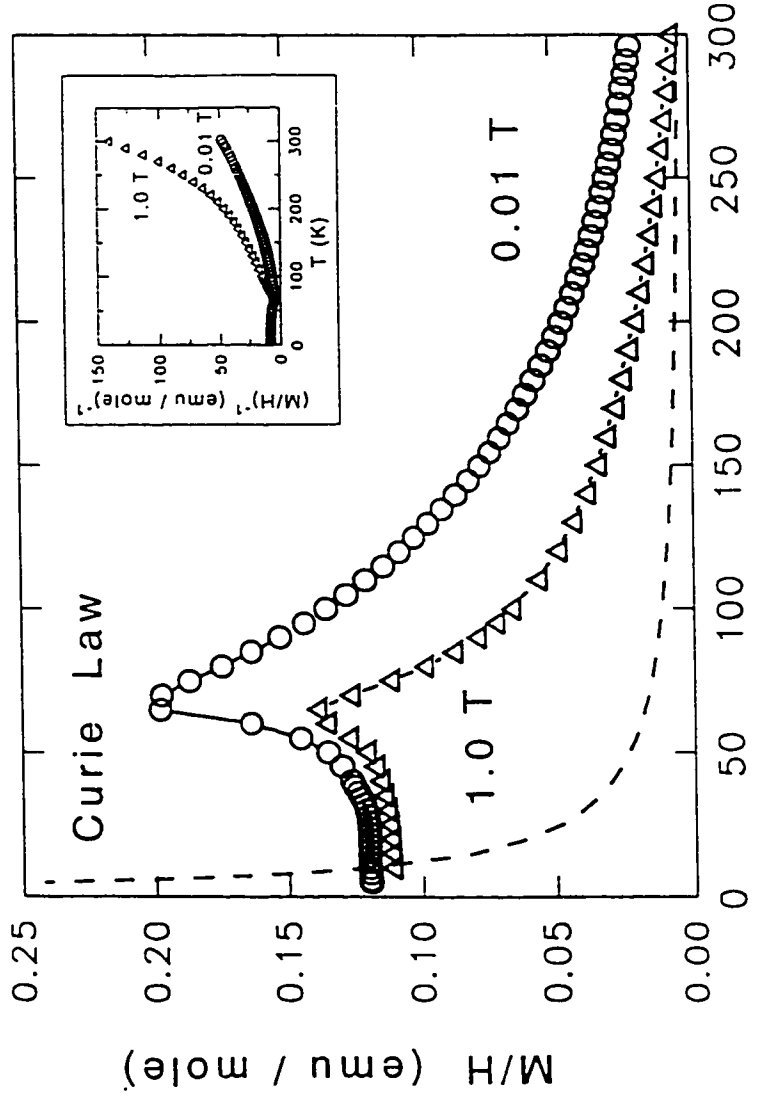

Figure 5.3.5 - Magnetization divided by applied field versus temperature for applied fields of 0.01 T and 1.0 T for 1T-Li_2NiO_2.

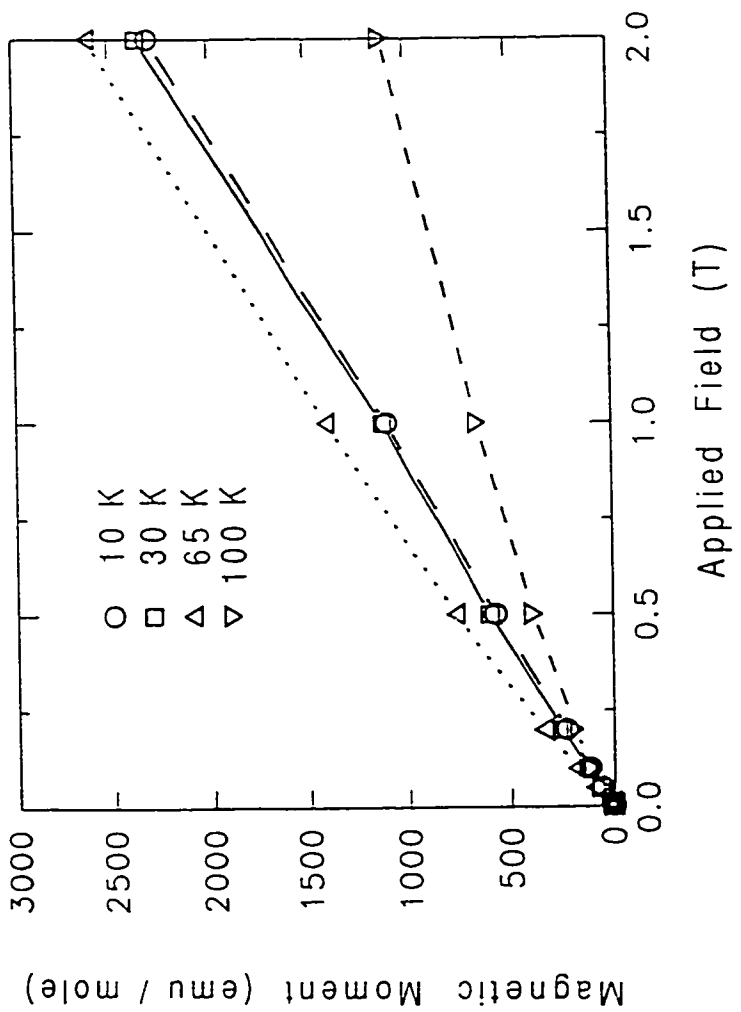

Figure 5.3.6 - Magnetic moment data for 1T-Li_2NiO_2 as a function of temperature versus applied field to 2.0 T.

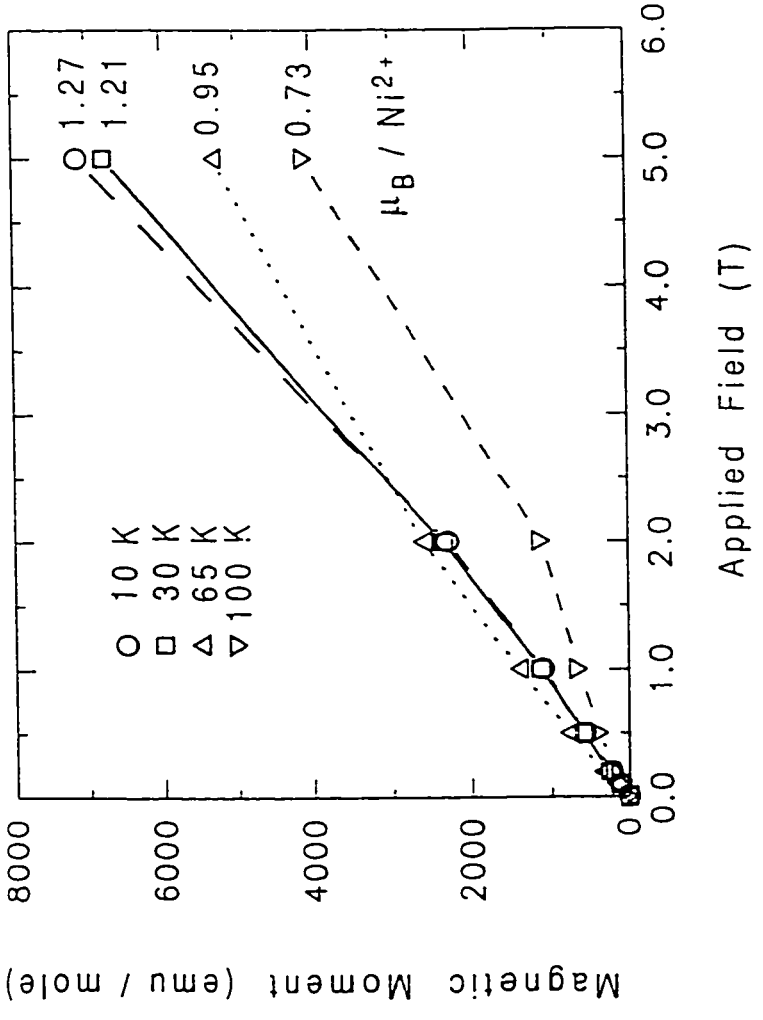

Figure 5.3.7 - Magnetic moment data for 1T-Li_2NiO_2 as a function of temperature versus applied field to 5.0 T.

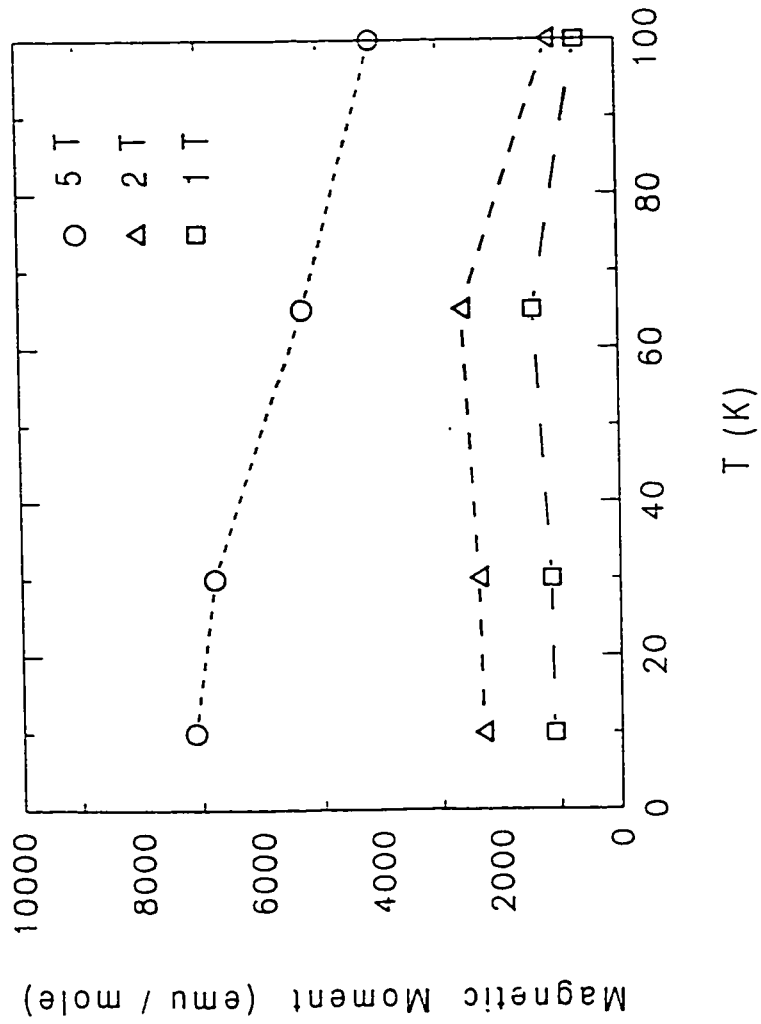

Figure 5.3.8 - Magnetic moment data for 1T-Li_2NiO_2 replotted versus temperature for various applied fields.

Chapter 6

Electrochemistry

6.1 Orthorhombic - $LiMnO_2$

Lithium ion cells were assembled with cathodes containing orthorhombic $LiMnO_2$ formed by reacting stoichiometric amounts of Li_2CO_3 and β-MnO_2 in a manner, as described in chapter 3. These cathodes were prepared by drying a slurry made from orthorhombic $LiMnO_2$ with two weight percent of ethylene propylene diene monomer (EPDM) and 10 wt.% *Super S* carbon black in cyclohexane. The carbon anodes were made from petroleum coke, with 2 wt.% of EPDM and 5 wt.% of *Super S* carbon black. The electrolyte used was a 50/50 mixture by volume of propylene carbonate and dimethoxyethane containing 1 M $(CF_3SO_2)_2N^- Li^+$.

Two coin cells were assembled, as described in chapter 2, with cathodes containing orthorhombic $LiMnO_2$. The first cell had a 0.045" thick anode weighing 0.354 g made with *Conoco XP* coke, and a cathode of 0.024" thickness, weighing 0.329 g. The cell completed 49 cycles between 1.8 and 4.0 volts at a current of 0.25 mA. The cell was stopped half way into the 50^{th} charge. After a period of relaxation, the open circuit voltage of the cell was 3.04 volts. The cell was disassembled and the cathode pellet was examined by powder x-

ray diffraction. The trace of the diffraction pattern, shown in figure 6.1.1, matches the JCPDF card file for $LiMn_2O_4$.

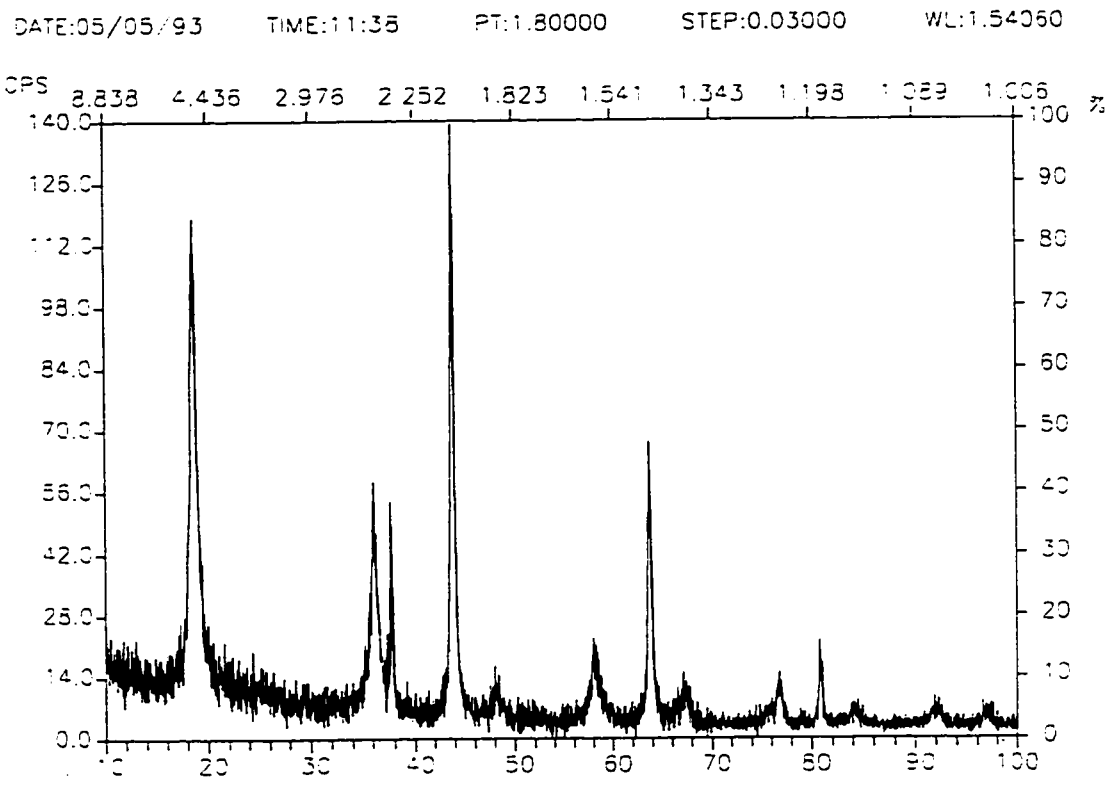

Figure 6.1.1 - X-ray diffraction pattern of $LiMnO_2$ cathode from cell at 3.04 V.

The second cell had a 0.056" thick anode weighing 0.428 g and a cathode of 0.014" thickness and 0.190 g weight. A capacity of 33.7 mAh was required to charge the cell to 4.0 volts at 0.28 mA. This corresponds to a 70% depth of charge of the cathode and to a composition of $Li_{0.3}MnO_2$ in the active material. This cell was cycled between 1.2 and 3.8 volts at 0.20 mA. The cell was stopped after completing the fifth charge. After a period of relaxation the

open circuit voltage of the cell was 3.5 volts. The cell was opened and the cathode was extracted for analysis by x-ray powder diffraction. The trace of the diffraction pattern is shown in figure 6.1.2. The peaks correspond to a cubic unit cell with a = 8.143(3) Å. The diffraction pattern matches that described for $Li_{0.6}Mn_2O_4$ by Ohzuku, Kitagawa and Hirai (1990).

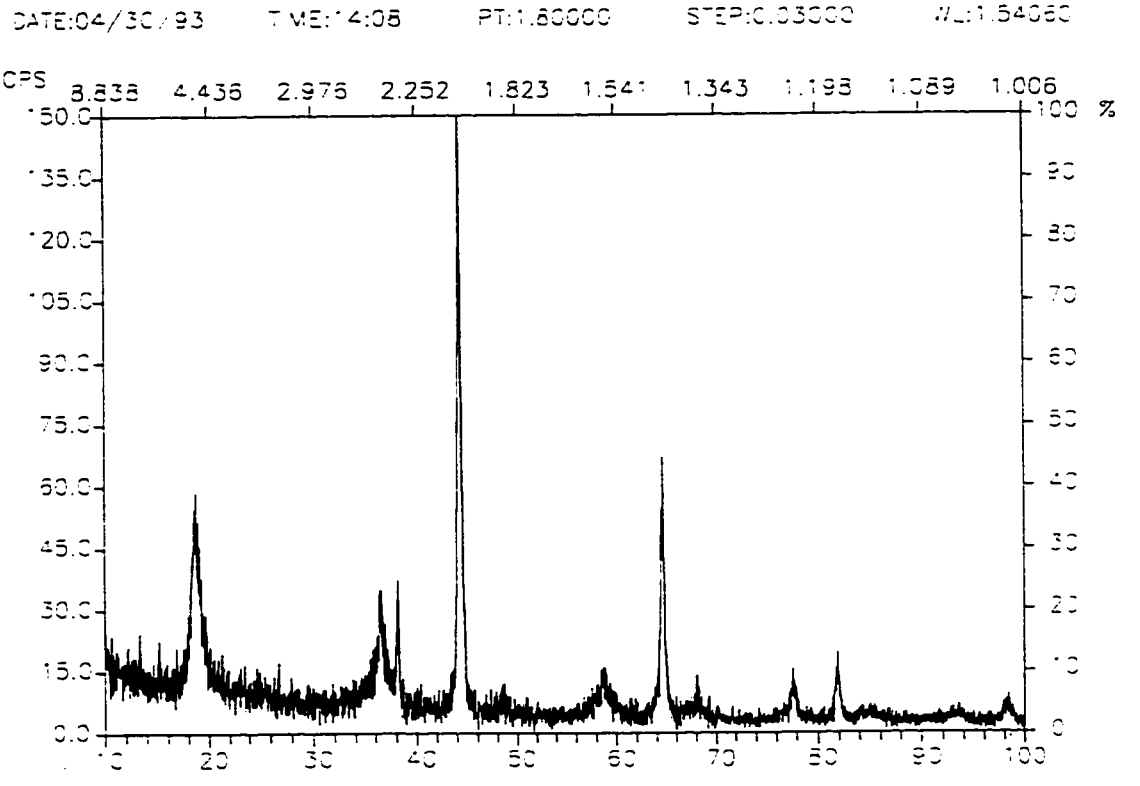

Figure 6.1.2 - X-ray diffraction pattern of $LiMnO_2$ cathode from cell charged to 3.8 V.

These results demonstrate that orthorhombic $LiMnO_2$ undergoes an irreversible phase change to the spinel related form on being charged beyond a

critical composition. On cycling a third $LiMnO_2$ coin cell between a lower voltage limit of 1.5 v and upper voltage limits which increased on each successive cycle it was found that phase conversion occurs when between 40 to 50% of the lithium has been de-intercalated from the $LiMnO_2$ structure. As shown in figure 6.1.3, the first two cycles, to voltage limits of 3.0 and 3.5 volts, respectively, showed very high irreversible capacities. The second charge pushed the cathode to 40% of its theoretical capacity. The third charge to a voltage limit of 3.8 volts, indicated by the plus symbols in figure 6.1.3, took the cathode to 46% of its nominal capacity. The subsequent discharge, however, provided 12% more capacity than the charge had consumed. The fourth and fifth cycles to 4.0 volts provided further small gains in discharge capacity relative to the prior charge. The first two discharges show no evidence of the higher voltage plateau (above 3.6 V) associated with lithium occupation of tetrahedral sites. Although it is difficult to see on the figure, the third discharge shows a small amount of the high voltage plateau indicating that the conversion to spinel $Li_{1-x}Mn_2O_4$ began on the third charge.

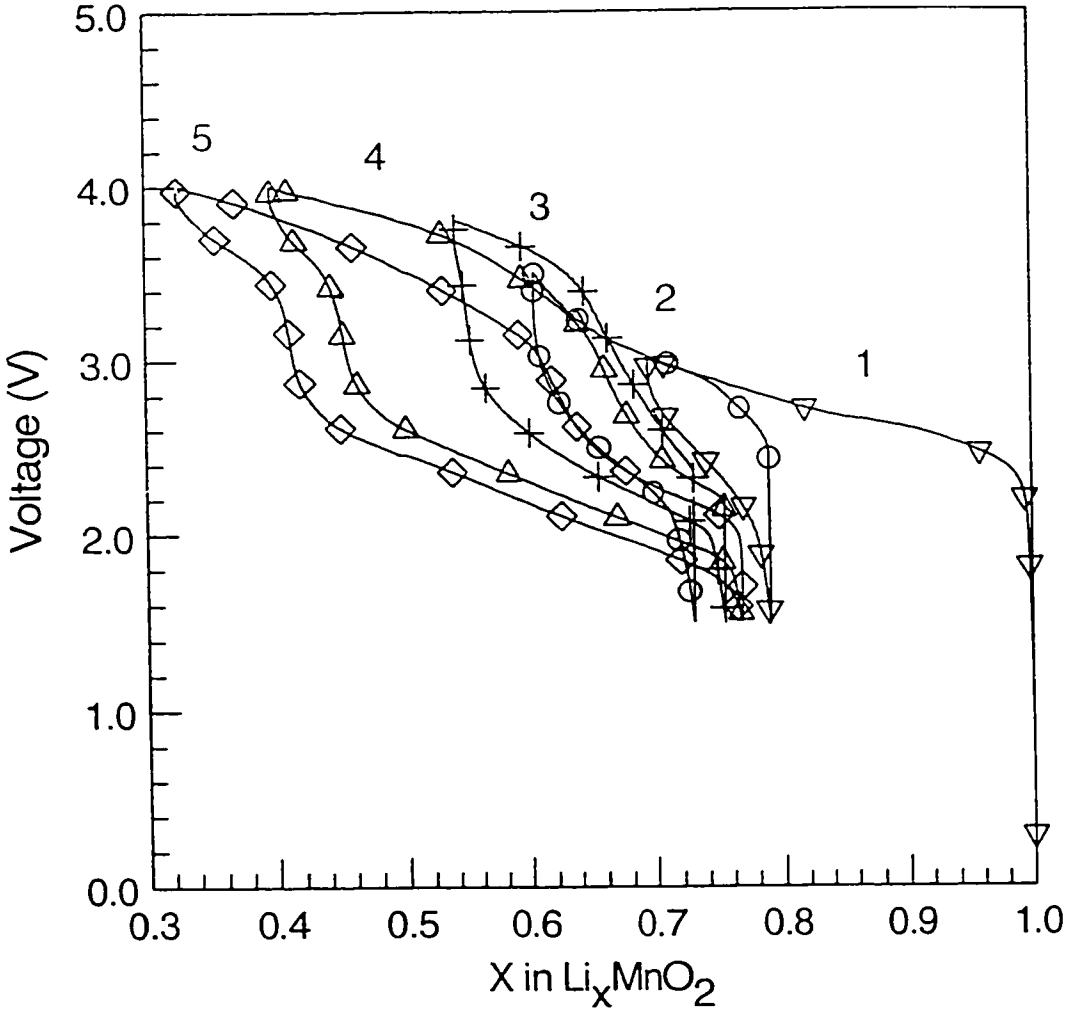

Figure 6.1.3 - First five cycles of a coke/$LiMnO_2$ cell cycle to progressively higher voltage limits.

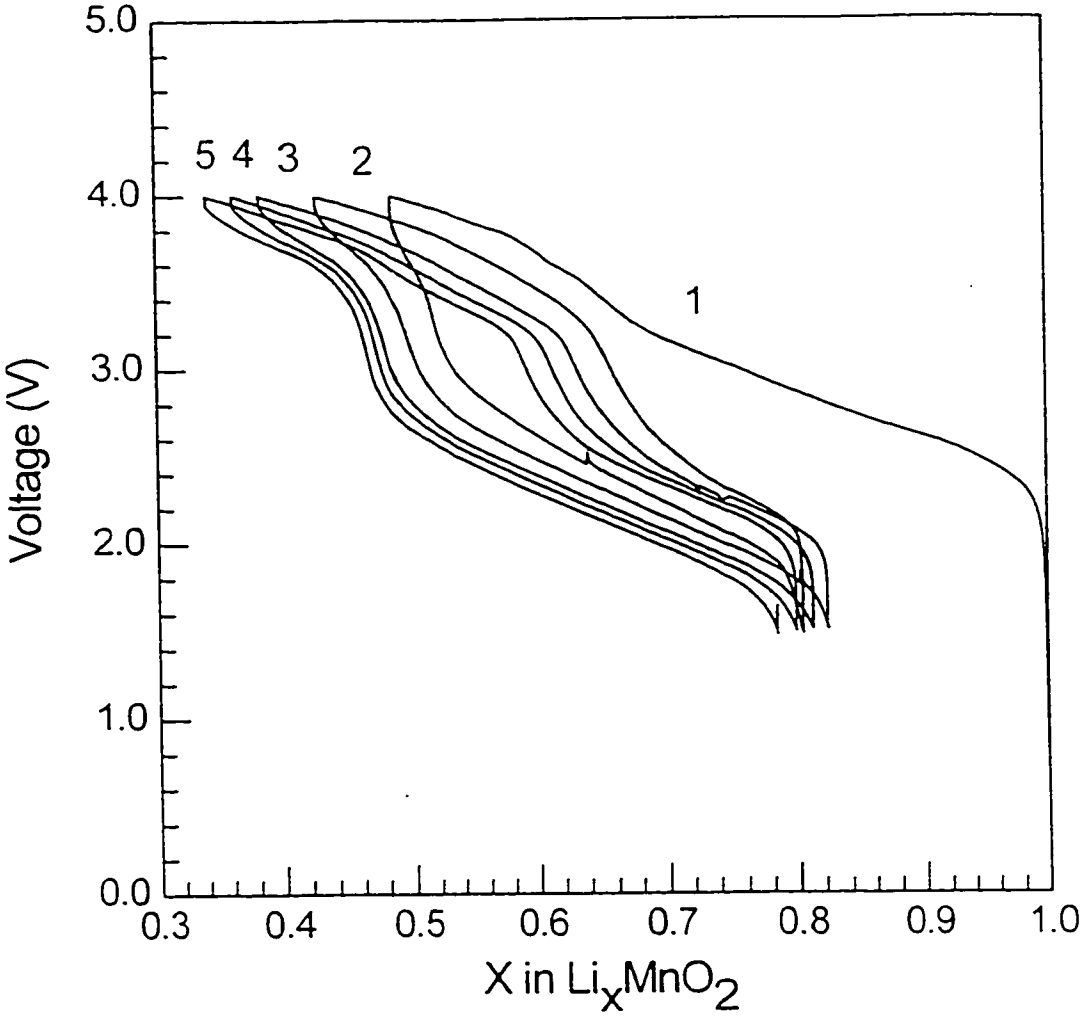

Figure 6.1.4 - First five charge/discharge cycles of a coke/$LiMnO_2$ cell cycled between voltage limits 1.5 and 4.0 V.

Figure 6.1.4 shows the first five cycles for a cell cycled at 100 hour rate between voltage limits of 1.5 and 4.0 volts. The anomalies in the first discharge and in the third charge are due to brief, accidental, power interruptions. The low rate is necessary for the rather thick (~ 1 mm) electrodes used in this experiment. Except for the lower upper voltage limit, the voltage curves are very similar to those shown for λ-$Li_2Mn_2O_4$, in figure 6 of Tarascon and Guyomard (1991).

The coincidence of the phase conversion with increased reversible capacity suggests that it is critical to the functioning of $LiMnO_2$ based cathodes, and may explain previous negative reports regarding the electrochemical activity of high temperature $LiMnO_2$. Lithium ion cells built with high temperature $LiMnO_2$ cathodes and carbon coke anodes have been cycled to more than 100 cycles without serious reduction in their reversible capacity. Figure 6.1.5 is a plot of capacity, in mAh per gram of $LiMnO_2$, versus cycle number for a typical coin cell with relatively thick electrodes (~1 mm). This cell was cycled at 1.27 mA/g for the first 8 cycles and then at 2.53 mA/g to the 55^{th} cycle. The cell was cycled at constant current to 4.0 volts. On the 35^{th} discharge the lower voltage limit was reduced from 1.5 to 1.0 volts, resulting in a modest increase in capacity, and finally, on the 55^{th} cycle the rate was changed back to 1.27 mA/g. The large reduction in capacity on increasing the rate from 1.27 mA/g to 2.53 mA/g reflects the fact that the coin cell format uses rather thick electrodes, approximately 1 mm. The first cycle had an irreversible capacity loss of 79 mAh/g, which is

believed to be due to lithium being consumed in the formation of a passivation film on the coke anode. At 1.26 mA/g, the cycleable capacity of this coin cell is about 132 mAh/g of $LiMnO_2$, which when summed with the irreversible capacity loss on the first cycle, 211 mAh/g, is still much less that the theoretical capacity of $LiMnO_2$, 285 mAh/g, but comparable to the capacity to 4.0 volts in a lithium ion cell with a λ-$Li_2Mn_2O_4$ cathode and a coke anode (Tarascon and Guyomard 1991). The upper voltage limit, of 4.0 volts, is required to prevent decomposition of the electrolyte. As demonstrated later, more capacity is obtained with orthorhombic $LiMnO_2$ cathodes when the electrolyte had a greater stability range.

Lithium ion cells with coke anodes and a cathode of either orthorhombic $LiMnO_2$ or λ-$Li_{2-x}Mn_2O_4$ have a first cycle, coulombic inefficiency of 45-80 mAh/g of active material, as shown in figure 6.1.4. This irreversible loss of capacity was, initially, attributed solely to the formation of a passivation film on the surface of the coke. However later studies with thin electrodes in cells with metallic lithium anodes showed a similar irreversible capacity on their first cycle.

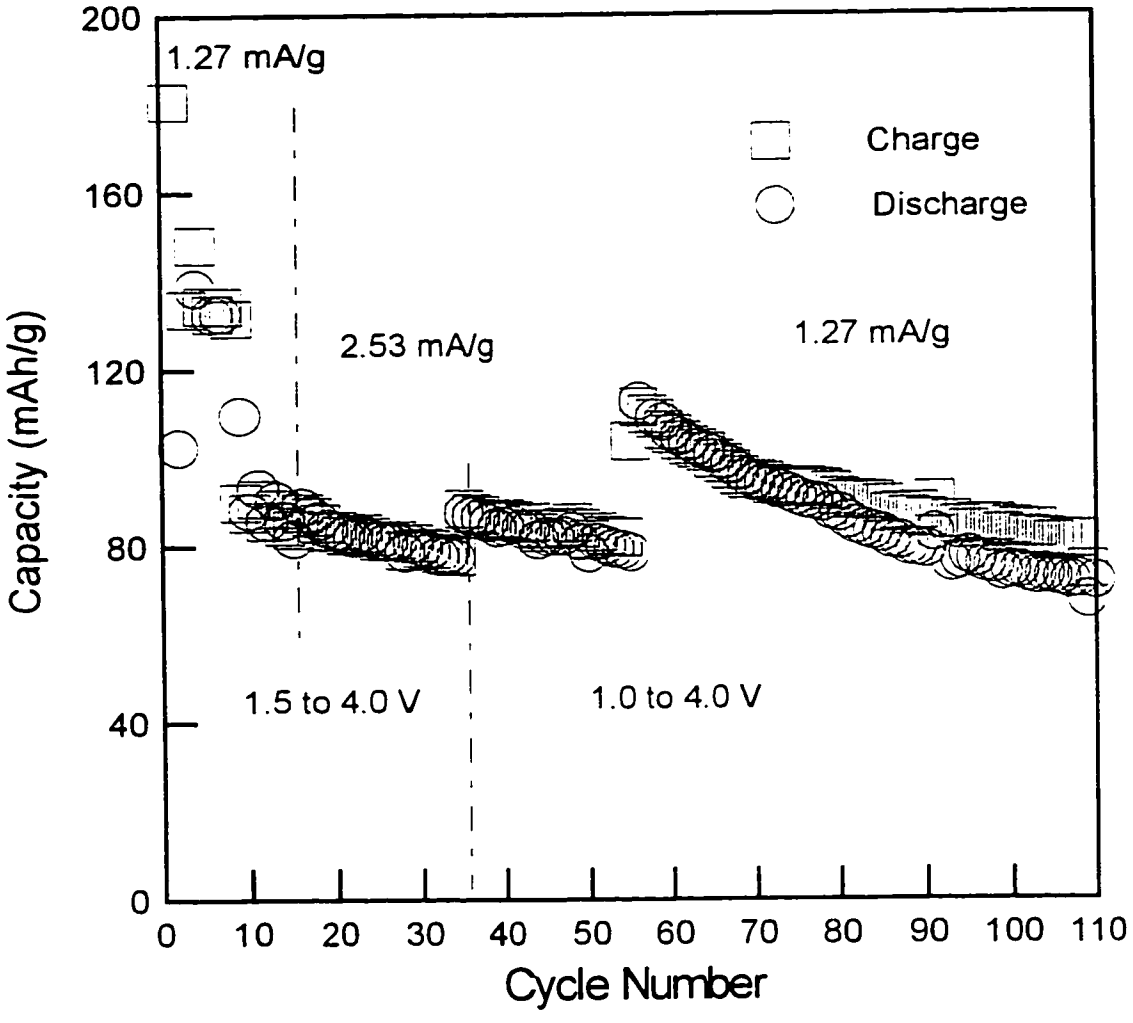

Figure 6.1.5 - Charge and discharge capacities as function of cycle number for a coke/$LiMnO_2$ coin cell.

Figure 6.1.6 shows voltage profiles of the first cycle for several Li/$LiMnO_2$ cells cycled at different rates in 1M $LiPF_6$ EC/DMC (1/2) between 2.5 and 4.2 volts. The most remarkable feature of these plots is that, even with a lithium anode, there is a large difference in the capacity of the first charge and the first discharge. Both the charge and discharge capacities are very dependent on the current. Constant rate studies in the coke/ $LiMnO_2$ cells showed that the discharge capacity is critically dependent on charging the cell enough to convert the orthorhombic $LiMnO_2$ to spinel $LiMn_2O_4$. It appears that this phase transition has slow kinetics and the extent of the phase transition during the first cycle is highly dependent on the cycling rate. At a current of 14.2 mA/g of $LiMnO_2$, only a very small amount of orthorhombic $LiMnO_2$ is converted to the spinel phase on the first charge. This is evident from the fact that the charge voltage increases with a steep slope at the cut-off voltage of 4.2 volts and the subsequent discharge shows very little reversible capacity from the cell. On the other hand. the cell cycled at 0.7 mA/g shows a clear difference in that the charge voltage curves over to form a plateau before it reaches the cut-off voltage of 4.2 volts. In addition, a substantial amount of reversible capacity is obtained on the subsequent discharge. The cells cycled at 3.6 mA/g and 1.4 mA/g fall between the two extreme cycling rates mentioned above. At higher currents the phase conversion takes several cycles to complete.

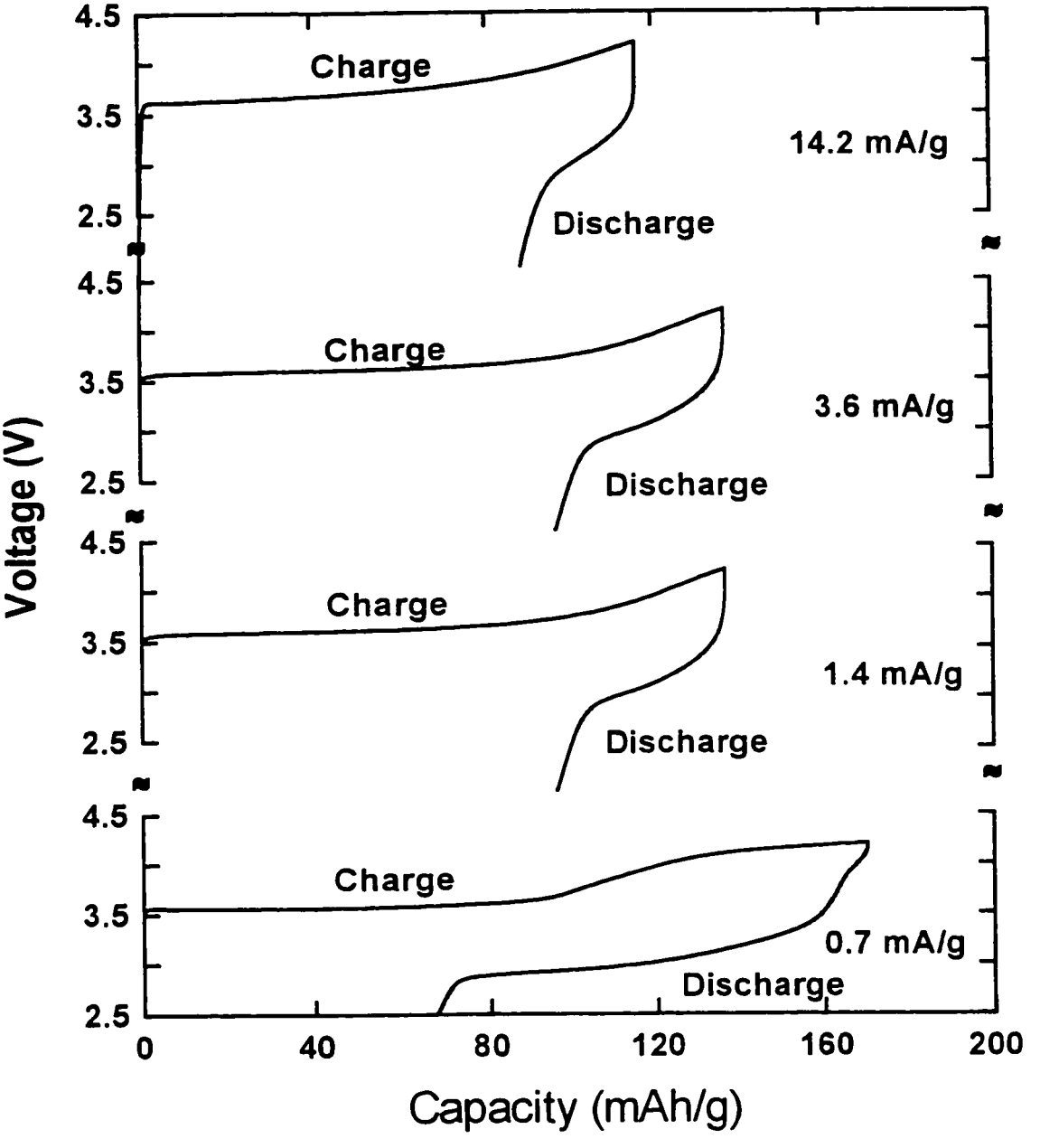

Figure 6.1.6 - First cycle voltage profiles for Li/$LiMnO_2$ cells cycled at different rates.

It is not surprising that the kinetics of the phase conversion is slow since it involves a massive rearrangement of the cations in the structure. A detailed mechanism has been proposed by Gummow, Liles and Thackeray (1993). The first cycle capacity loss in $Li/LiMnO_2$ cells was somewhat unexpected. The rate dependence of the capacity loss suggests that it is a kinetic rather than a thermodynamic limitation.

After a few cycles in which the spinel phase was formed in-situ, some cells were cycled progressively to a higher charge cut-off voltage. Figure 6.1.7 shows typical voltage profiles of a $Li/LiMnO_2$ cell cycled at 3.56 mA/g of $LiMnO_2$ in 1M $LiPF_6$ in EC/DMC (1/2) to different charge voltage limits while keeping the discharge cut-off voltage at 2.5 volts. The discharge profiles essentially follow the same shape as reported for λ-$Li_2Mn_2O_4$ with a first order phase transition occurring in the relatively flat lower plateau near 3 volts and a homogenous phase transition occurring in the more sloping upper plateau near 4 volts (Ohzuku, Kitagawa and Hirai 1990). Not surprisingly, the capacity gain by cycling to a higher voltage mainly occurs at the higher voltage plateau near 4 volts. The delithiation of the cathode is almost completely reversible for all voltage limits tested except a small loss of capacity when a cell is charged to a higher voltage presumably due to increased electrolyte decomposition at higher voltage. The charge and discharge capacities of the various cycles are listed in table 6.1.1.

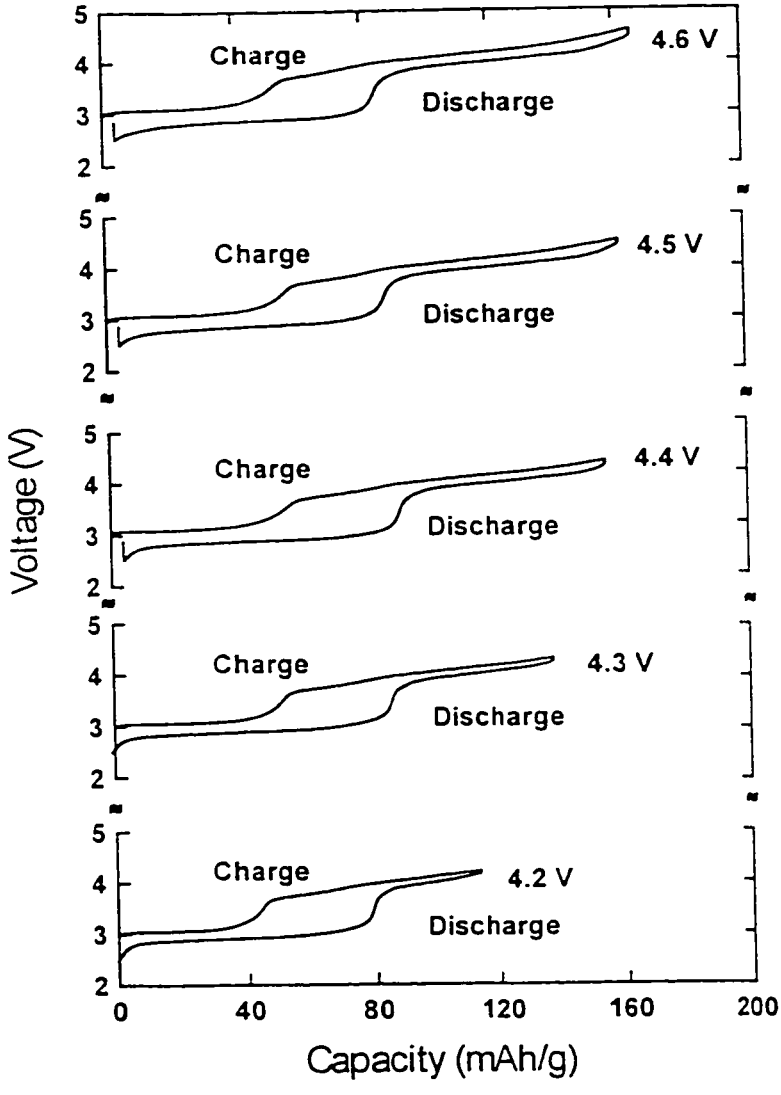

Figure 6.1.7 - Voltage profiles of a Li/$LiMnO_2$ cell cycled to progressively higher charge limits.

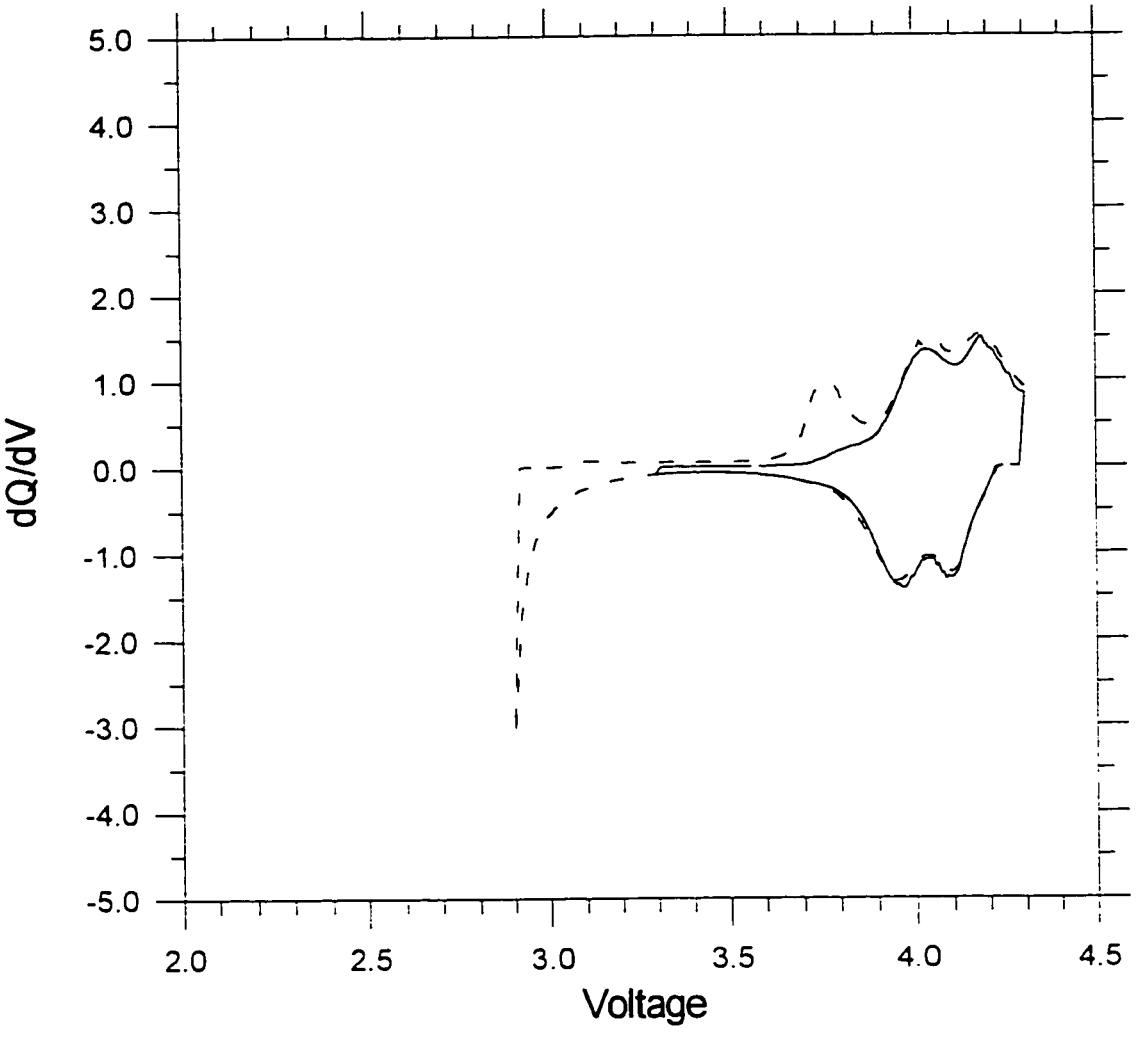

Figure 6.1.8 - Derivative plot of cycling curve for a Li/$LiMnO_2$ cell conditioned by cycling over upper plateau only before cycling to 2.9V.

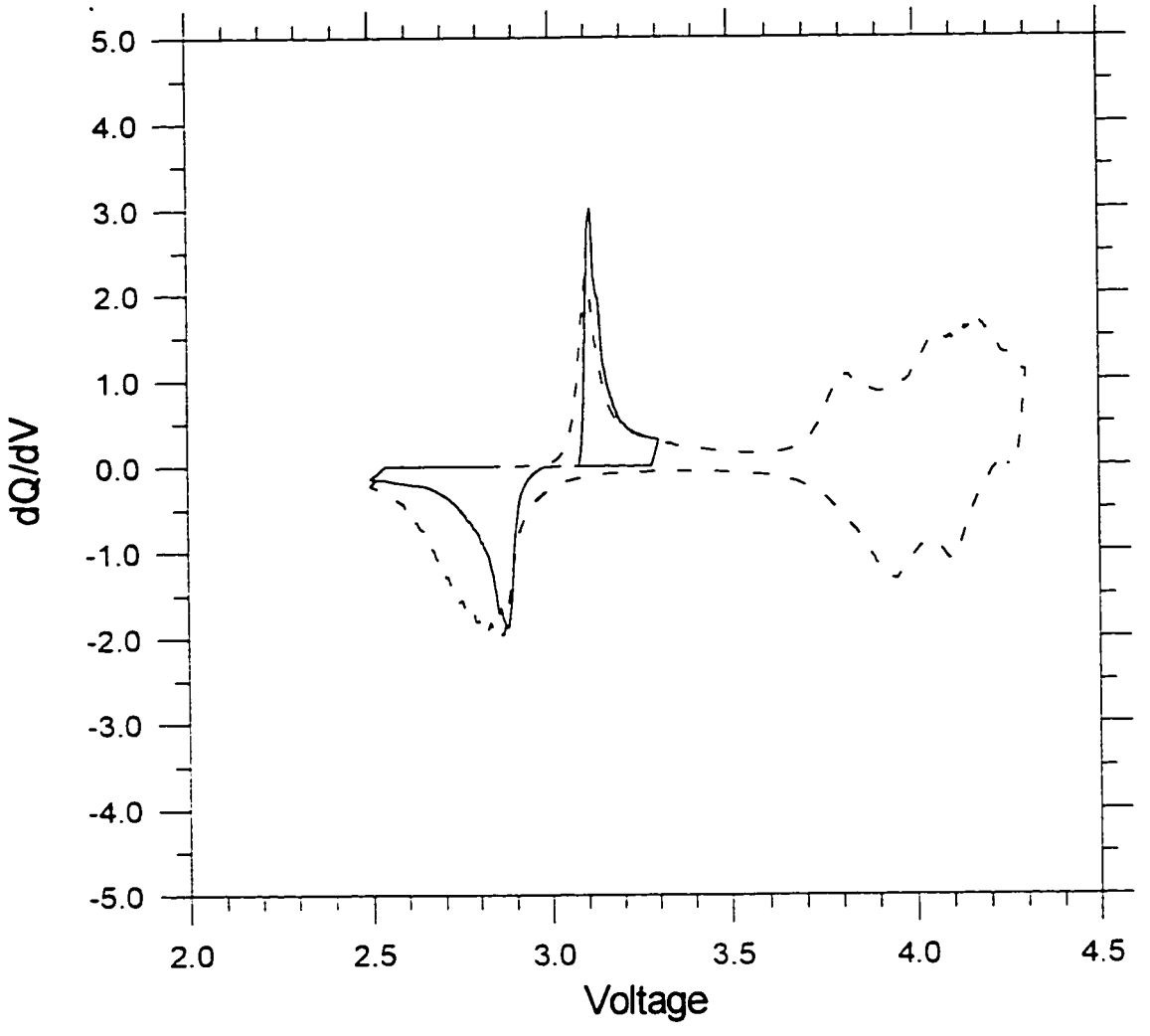

Figure 6.1.9 - Derivative plot of cycling curve for a Li/$LiMnO_2$ cell conditioned by cycling over lower plateau only before cycling to 4.3V.

The hysteresis in the voltage profiles is about the same regardless of the voltage limit on charge. Lithium removed from the cathode near 3.8 volts, on charge, is re-inserted on discharge in the 2.9 volt plateau. This region was explored further by cycling over restricted voltage ranges. The data was plotted as a derivative, dQ/dV, the change in capacity divided by the change in voltage, versus voltage to emphasize the more subtle changes in slope of the cycling curves. Figure 6.1.8 shows a dQ/dV plot for a Li/$LiMnO_2$ cell cycled initially between 4.3 and 3.3 volts, and then discharge to a lower limit of 2.9 volts and recharge back to 4.3 volts. The peak at 3.8 volts on charge is only present if the subsequent discharge went into the lower plateau region. In a later cycle, shown as a dQ/dv plot in figure 6.1. 9 , this same cell was cycled between 2.5 and 3.3 volts, and then charged to 4.3 volts and discharged back to 2.5 volts. The figure shows that the shape and magnitude of the lower plateau peak is critically dependent on charging the cell into the upper plateau. Consequently, the hysterisis in the voltage curves of the Li/$LiMnO_2$ cells is due to some of the lithium being inserted into more energetic sites on charge and then relaxing to sites of lower energy before the cell is discharged. The upper voltage plateau of λ-$Li_2Mn_2O_4$ is known to be due to insertion/extraction of lithium ions from the tetrahedral (8a) sites of the cubic spinel, and the lower plateau to insertion/extraction of lithium ions from octahedral (16c) sites in the tetragonally distorted lithiated spinel structure (Ohzuku, Kitagawa and Hirai 1990). However, the change in slope associated with the hysteresis portion of the charge profile

of the Li/$LiMnO_2$ cells suggests that a different crystallographic process is occurring than in the subsequent charge region. The process at 3.8 V could be due to extraction of lithium from a more hindered octahedral site, such as the 16d site.

The electrochemical behaviour of $LiMnO_2$ was further investigated at a voltage below 2.5 volts after the spinel phase was formed in-situ. This was carried out by first charging the cell to 4.2 volts in the manner described above, followed by discharging the cell to 1.0 volts. Figure 6.1.10 shows voltage profiles of a cell cycled between 4.2 and 1.0 volts. Once again, the discharge plateau near 2.9 volts is shown to be strongly rate dependent, but the charging hysteresis is independent of rate over the current range studied. In addition, a capacity of about 65 mAh/g is observed between the voltage range 2.5 and 1.0 volts. The discharge capacity below 2.5 volts is independent of the cycling rates from 14.2 to 3.6 mA/g and is almost completely reversible. However, this "extra" capacity between 2.5 and 1.0 volts appears in the recharge at 3.05 volts. In fact, cells discharged to 1.0 volts and then monitored for voltages changes in the absence of current flow were found to relax to greater than 2.0 volts in 3.5 hours, and reach a maximum of 2.94 volts after about 80 hours. Charge and discharge capacities of Li/$LiMnO_2$ cells cycled at different rates and voltage limits in various electrolytes are given in table 6.1.1. Depending on the electrolyte used and the cycling rate, the total reversible capacity is between 1.0 and 4.4 volts,

under our non-optimized conditions, can be as high as 90% of the theoretical capacity of $LiMnO_2$.

Table 6.1.1 - Charge and discharge capacities of $Li/LiMnO_2$ cells cycled at different rates and voltage limits in a variety of electrolytes.

Electrolyte (1M salt)	Voltage (V)	Rate (mA/g)	Charge Capacity (mAh/g)	Discharge Capacity (mAh/g)
$LiPF_6$ EC/DMC (1/2)	4.2-2.5	3.56	119	113
	4.3-2.5	3.56	138	138
	4.4-2.5	3.56	155	152
	4.5-2.5	3.56	161	157
	4.6-2.5	3.56	165	164
$LiPF_6$ EC/DMC (1/2)	4.2-1.0	3.56	203	199
	4.3-1.0	3.56	214	210
	4.3-1.0	1.78	255	227
	4.4-1.0	3.56	225	220
	4.5-1.0	3.56	235	227
$LiClO_4$ EC/DMC (1/2)	4.4-1.0	3.56	269	257
$LiClO_4$ PC/DME (1/1)	4.2-1.0	1.78	219	208
	4.4-1.0	1.78	248	230
$LiClO_4$ PC/EC (1/1)	4.2-1.0	1.78	228	224
	4.3-1.0	1.78	246	243
	4.4-1.0	1.78	253	250

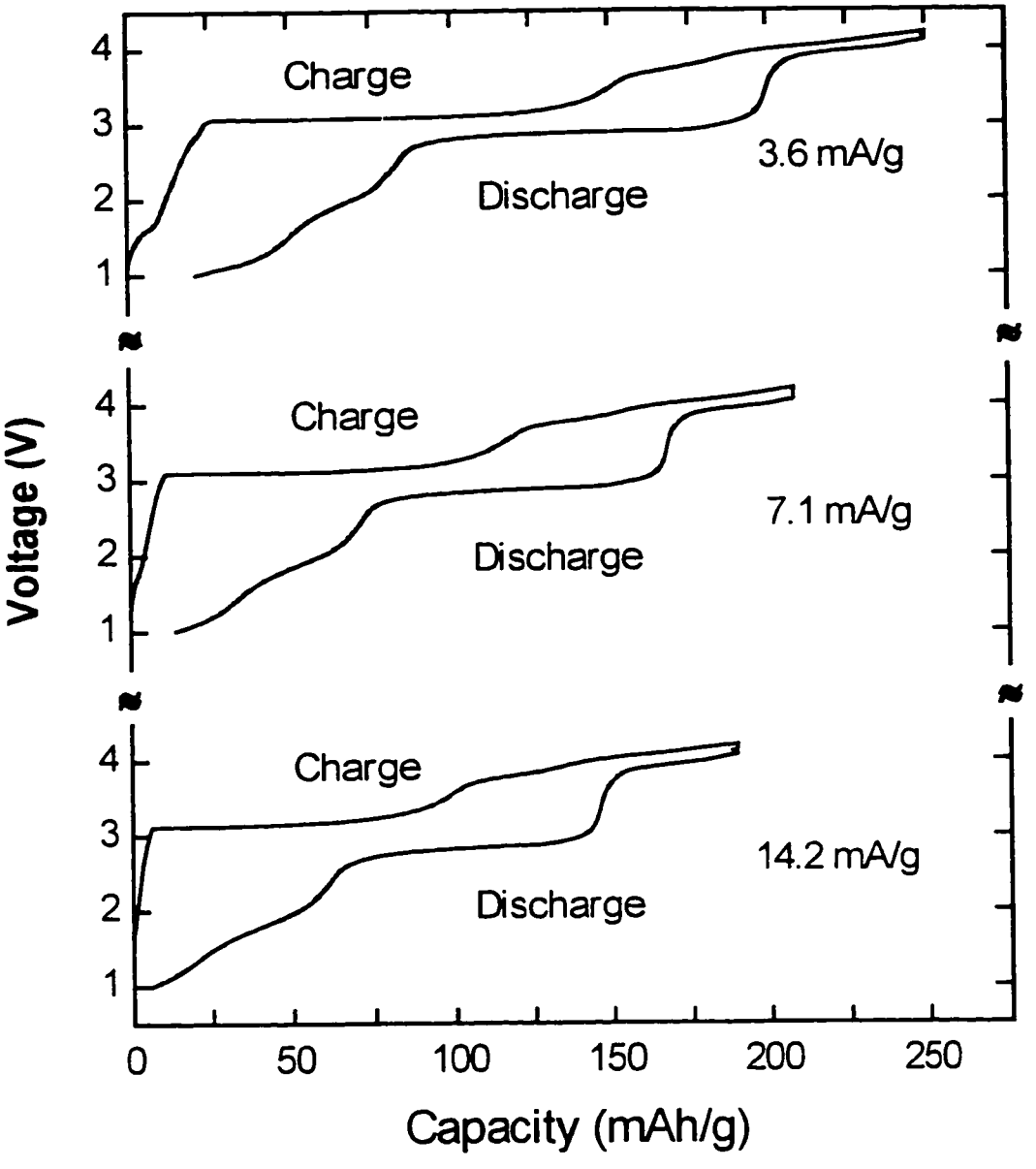

Figure 6.1.10 - Voltage profiles for a Li/$LiMnO_2$ cell cycled between 1.0 and 4.2 volts at various rates.

The spinel-related structure of $LiMnO_2$ after the *in-situ* phase transition was confirmed again by the x-ray diffraction. This was carried out by first cycling the cell for a number of cycles and allowing a complete phase transition as indicated by the voltage profile. A cell was then taken apart after charging it to 4.2 volts. The cathode was completely extracted from the separator before obtaining the diffraction data listed in table 6.1.2. The x-ray diffraction pattern indexed to a cubic crystallographic unit cell with a lattice parameter of 8.174(1) Å. This corresponds to a composition of $Li_xMn_2O_4$ in which x = 0.87 (Ohzuku, Kitagawa and Hirai 1990). The relative intensities of the peaks are a reasonable match to the predicted diffraction pattern except that the (111) reflection is weaker than expected. This is most probably due to x-ray absorption which will have the strongest effect on the lowest angle peak.

Two other cells which had been cycled between 4.6 and 1.0 volts were disassembled after being discharged to 1.0 volts. The cathodes were extracted from the coin cells and sealed in polyethylene bags in an argon filled glove box. Neither cathode could be removed from the attached separator. The peaks at 4.8 Å and at 2.46 Å overlapped with peaks associated with the separator and could not be resolved with any accuracy. These peaks were not used in the calculation of the lattice parameters. The x-ray powder diffraction patterns of the two cathodes were quite similar. Both patterns indexed to tetragonal cells but the unit cells dimensions were slightly different. The diffraction pattern of the cathode from the first cell refined to lattice parameters of a = 5.636 (4) Å and

c = 9.190 (6) Å, and that of the second cell, to a = 5.658 (2) Å and c = 9.232 (4) Å. These are comparable to the tetragonal lattice parameters of λ-$Li_2Mn_2O_4$ at a = 5.646 Å and c = 9.250 Å (Ohzuku, Kitagawa and Hirai 1990). The diffraction pattern of the second cathode, listed in table 6.1.2, is a good match to the pattern calculated for λ-$Li_2Mn_2O_4$ on the basis of the structural data in Ohzuku, kitagawa and Hirai (1990), with the notable exception that the (004) and (224) reflections are much more intense in our diffraction pattern. This may indicate that the crystals of λ-$Li_2Mn_2O_4$ formed *in-situ* in a pressed cathode are not randomly oriented.

Thus, orthorhombic $LiMnO_2$ can be cycled over a large composition range (about 90 % of its theoretical capacity), but about 25 % of this capacity is delivered below 2.5 volts versus metallic lithium. Since the capacity below 2.5 volts is not as sensitive to rate as the capacity of the 2.9 volt plateau, the lower voltage capacity is likely to be due to the formation of a metastable phase which is richer in lithium than the bulk of the cathode. Over time, normally several hours, the cell voltage rises to 2.9 volts as the lithium concentration in the cathode equilibrates to form λ-$Li_{2-x}Mn_2O_4$. Consequently, it has not been possible to identify the metastable phase by *ex-situ* x-ray diffraction technique, but one possibility is, Li_2MnO_2. This phase has a trigonal crystal structure consisting of hexagonally-close-packed anions with octahedrally coordinated Mn^{2+} ions in alternate basal planes and Li^+ ions in tetrahedral sites of the other basal planes

(David, Goodenough, Thackeray and Thomas 1983). A similar chemistry occurs in lithium cells with $LiNiO_2$ cathodes in which Li_2NiO_2 is formed on over-discharge (Dahn, von Sacken, and Michal 1990).

Table 6.1.2 - X-ray diffraction data for cathodes extracted from cycled coin cells after charging to 4.2 volts and after discharging to 1.0 volts.

Cathode at 4.2 volts $Li_{0.87}Mn_2O_4$			Cathode at 1.0 volts $Li_2Mn_2O_4$		
d (Å)	(hkl)	Relative Intensity	d (Å)	(hkl)	Relative Intensity
a = 8.174 (1) Å	F d-3m	Cu K_α	a = 5.658 (2) Å c = 9.232 (4) Å	$I4_1/amd$	Cu K_α
4.685	111	91	4.8 *	101	40
2.456	311	52	2.691	103	10
2.355	222	14	2.46 *	211	15
2.040	400	100	2.407	202	11
1.875	331	5	2.302	004	100
1.574	511	33	1.999	220	23
1.444	440	72	1.510	224	23
1.381	531	22	1.414	400	7
1.233	622	15	1.350	206	< 5
1.179	444	14	1.222	422	< 5
1.145	551	< 5	1.207	404	6
1.064	553 + 731	< 5	1.154	008	< 5
1.022	800	9			

* Peaks marked with an asterisk overlapped with peaks from the separator and are not accurate. These peaks were not used in the calculation of the lattice parameters.

6.2 $LiFeO_2$

A sample of $LiFeO_2$, prepared as described in chapter 3, was incorporated into the cathode of a coin cell with a carbon coke anode. Both the cathode and the coin cell were assembled as described for $LiMnO_2$. Attempts to charge the cell at even a modest current resulted in a rapid polarization of the cell to voltages corresponding to decomposition of the electrolyte. Furthermore, charging the cell did not result in any charge retention.

It was pointed out in chapter 4 that the sample of $LiFeO_2$ used in this study is a two-phase mixture. It contains both of crystallites with the layered 3R structure and with the lithiated spinel structure. In either structure, the lithium atoms have unhindered pathways for motion in and out of the structure. The two most probable explanations for the lack of electrochemical activity in $LiFeO_2$ are that either the Fe^{3+}/Fe^{4+} couple has a potential beyond the stability range of the electrolyte, or $LiFeO_2$ is too poor an electronic conductor to be useful as an electrochemical intercalation compound. The chemical potential of the Fe^{3+}/Fe^{4+} couple in a lithium intercalation electrode is apparently not known, as it has never been successfully exploited in this way. It is reasonable to expect that it will be similar to the potentials observed for the electrochemical oxidation of $LiCoO_2$ and $LiNiO_2$. However, even as a finely ground powder, $LiFeO_2$ has a brick red colour, which suggests that it is not a good electronic conductor.

6.3 $Li_2Ni_yMn_{2-y}O_4$

The preparation of phases within the solid state solution, $Li_2Ni_yMn_{2-y}O_4$, was discussed in chapter 3. Two of these phases, Li_2NiMnO_4 and $Li_2Ni_{1.5}Mn_{0.5}O_4$, were evaluated as cathodes in lithium ion cells with carbon coke anodes. The cells were assembled and tested in the same manner as were those built with $LiMnO_2$ cathodes.

Li_2NiMnO_4, prepared at 1000 $^{\circ}C$ from $LiMnO_2$ and $LiNiO_2$, was evaluated in a coin cell with a petroleum coke anode and an electrolyte solution of 1M Lithium Bis-(trifluoromethylsulfonyl) imide in a 1:1 mixture of propylene carbonate and dimethoxyethane. The cell contained a 0.3296 g cathode of 0.024" thickness containing 10 weight % carbon black and 2 weight % EPDM binder. The 0.3543 g coke anode had a thickness of 0.047" and contained 5% carbon black and 2% EPDM. The cell was cycled at 5.8 mA/g of Li_2NiMnO_4 between voltage limits of 2.0 and 4.0 volts. The first and third charge and discharge cycles are shown in the accompanying figures 6.3.1 and 6.3.3. The cell capacity is given in units of mAh/g of active cathode material. For comparison, figure 6.3.2 provides a typical first cycle plot for a similarly prepared lithium ion cell with a $LiCoO_2$ cathode. Li_2NiMnO_4 has a theoretical capacity of 280 mAh/g, assuming all the lithium in the structure could be reversibly cycled. Figure 6.3.1 shows that, on the first charge, half of the lithium was removed from the cathode before the cell reached the limiting potential of 4.0 volts. The

subsequent discharge recovered 68% of the first charge capacity. The capacity loss between the first charge and the first discharge is believed to be due to an irreversible reaction on the carbon anode. The first cycle cell voltage was lower than in the comparative coke/$LiCoO_2$ cell. The cell capacity was initially higher, but it faded faster than for similar cells containing $LiCoO_2$ cathodes. By the third cycle the reversible capacity is only 74 mAh/g of Li_2NiMnO_4.

The resistivities of cathode pellets containing Li_2NiMnO_4 and $Li_2Ni_{1.5}Mn_{0.5}O_4$ were measured with a four point probe method and compared with similarly prepared pellets containing either $LiNiO_2$ or $LiCoO_2$ (figure 6.3.4). The higher electrical resistivity of Li_2NiMnO_4 may in part explain why cells with cathodes containing Li_2NiMnO_4 have a larger internal resistance and more rapid capacity fade than those containing $LiCoO_2$. The cathode pellets containing $Li_2Ni_{1.5}Mn_{0.5}O_4$ had a lower resistivity than those containing either $LiNiO_2$ or $LiCoO_2$. This material was also tested in a coin cell. The cell reached the cutoff voltage of 4.0 v at a charge capacity of 20.9 mAh. This capacity is equivalent to removing only 22% of the lithium from the cathode. The cell charged at a higher than normal voltage, and had virtually no discharge capacity. This suggests that the charge capacity involved a decomposition of the electrolyte rather than the electrochemical extraction of lithium from the $Li_2Ni_{1.5}Mn_{0.5}O_4$ structure. The difficulty in electrochemically extracting lithium ions from $Li_2Ni_{1.5}Mn_{0.5}O_4$ may be related to the larger degree of site sharing between the lithium and transition metals atoms in this structure (see chapter 4). A lesser degree of ordering

between the transition metal atoms and the lithium atoms onto separate crystallographic sites will result in a shortening or elimination of pathways for lithium ion mobility.

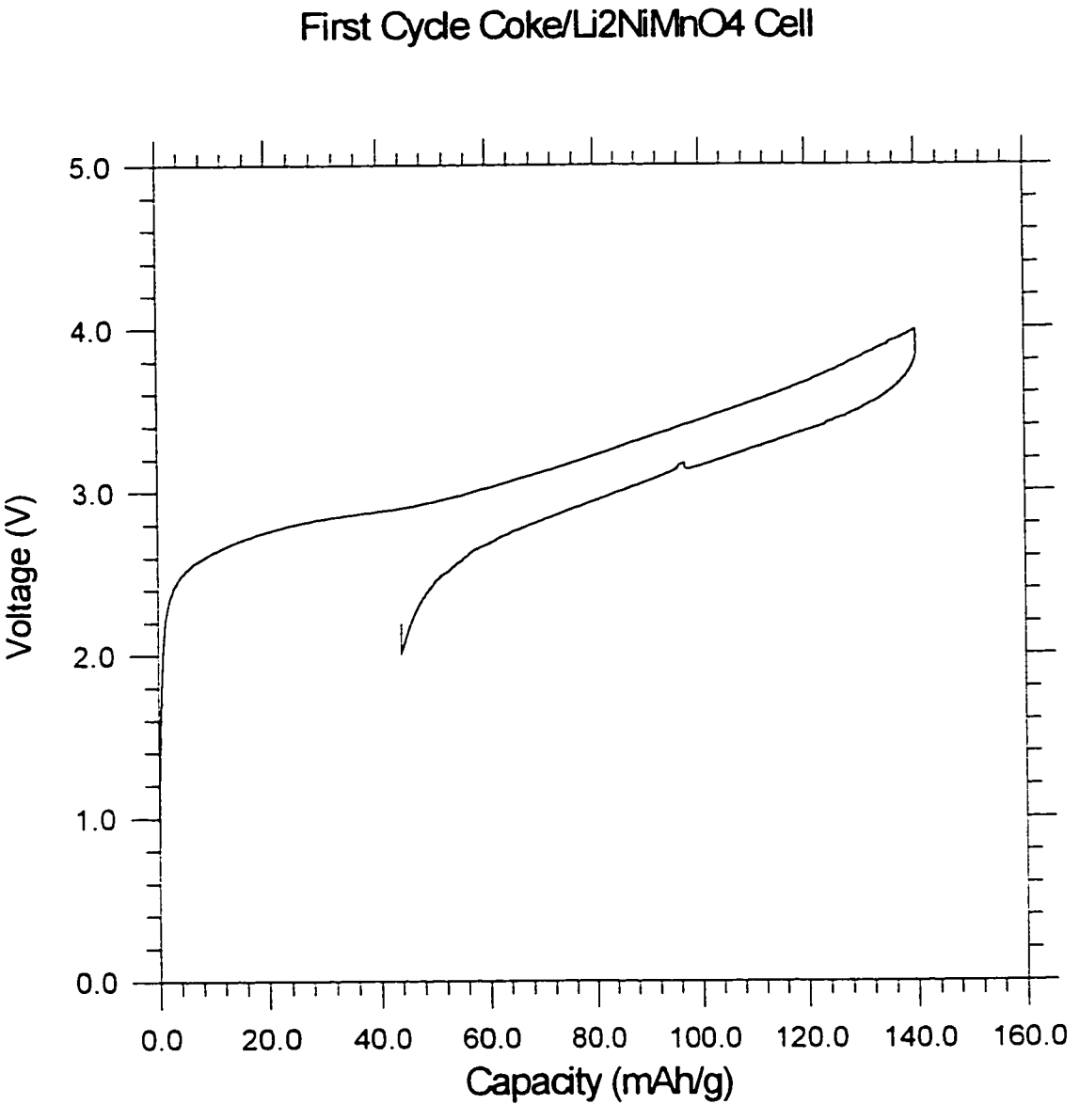

Figure 6.3.1 - Voltage profile of the first charge and discharge of a coke/Li_2NiMnO_4 coin cell.

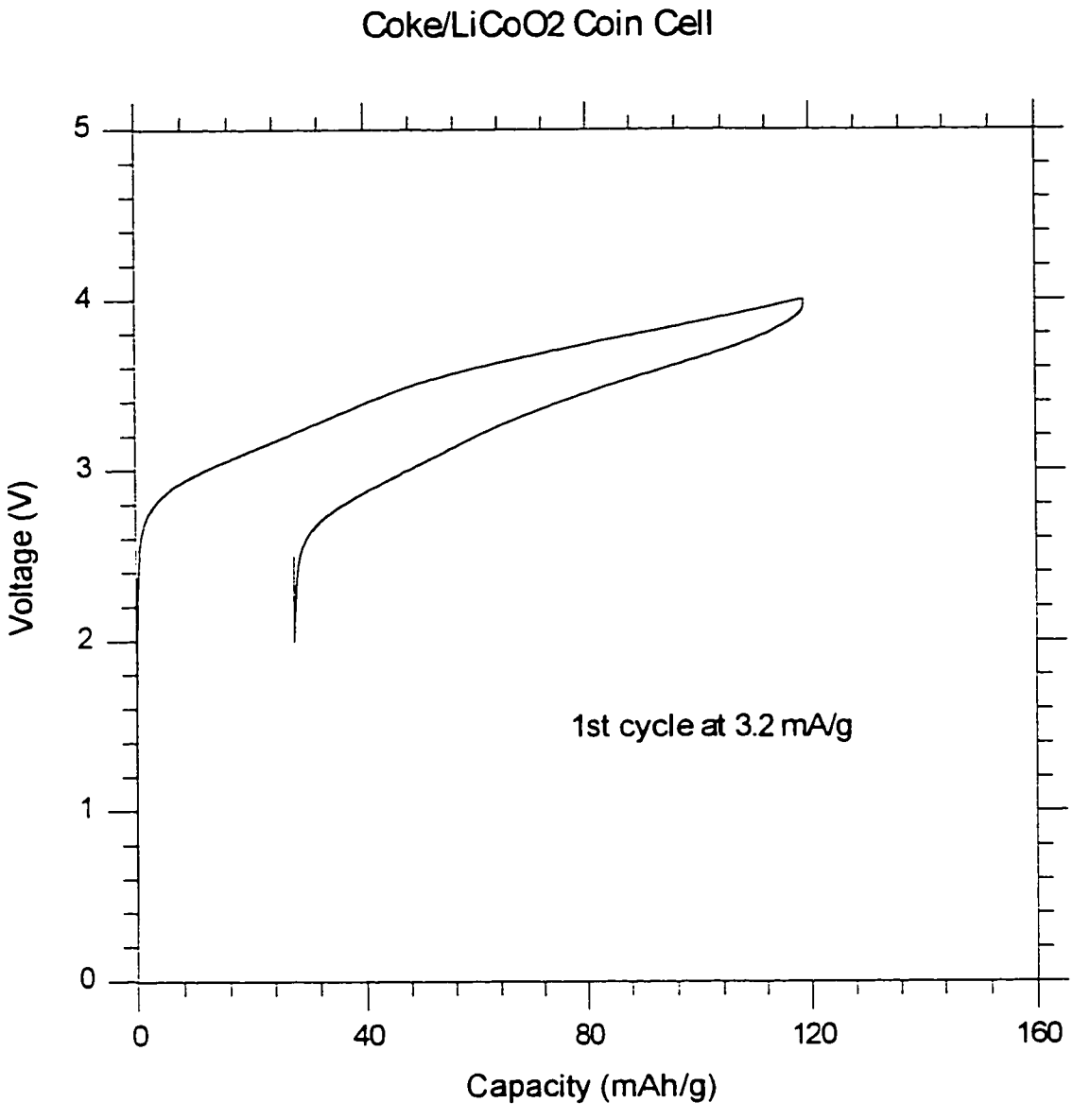

Figure 6.3.2 -Comparative plot of the first cycle voltage profile for a typical coke/$LiCoO_2$ coin cell.

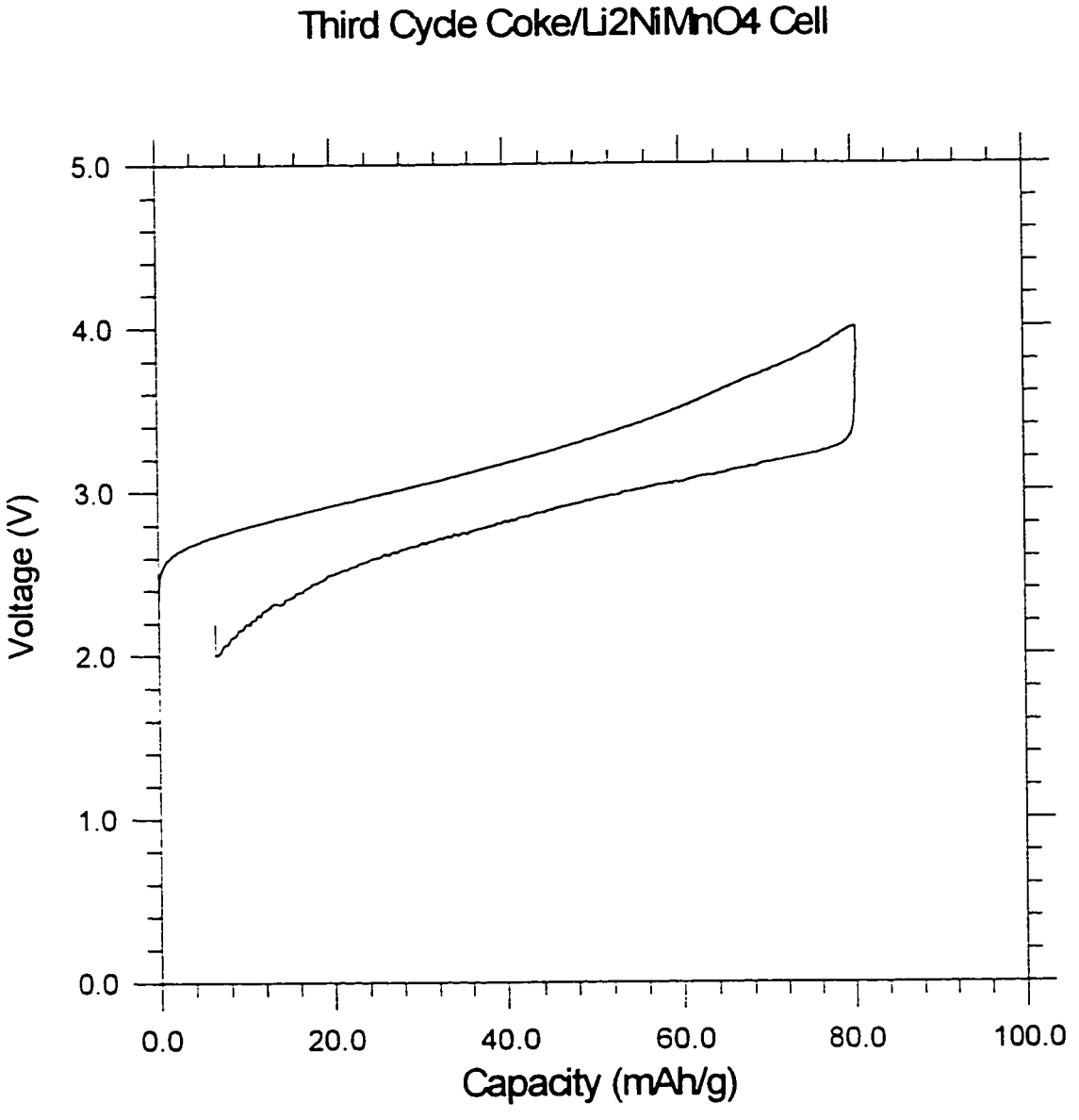

Figure 6.3.3 - Voltage profile of the third cycle of a coke/Li_2NiMnO_4 coin cell

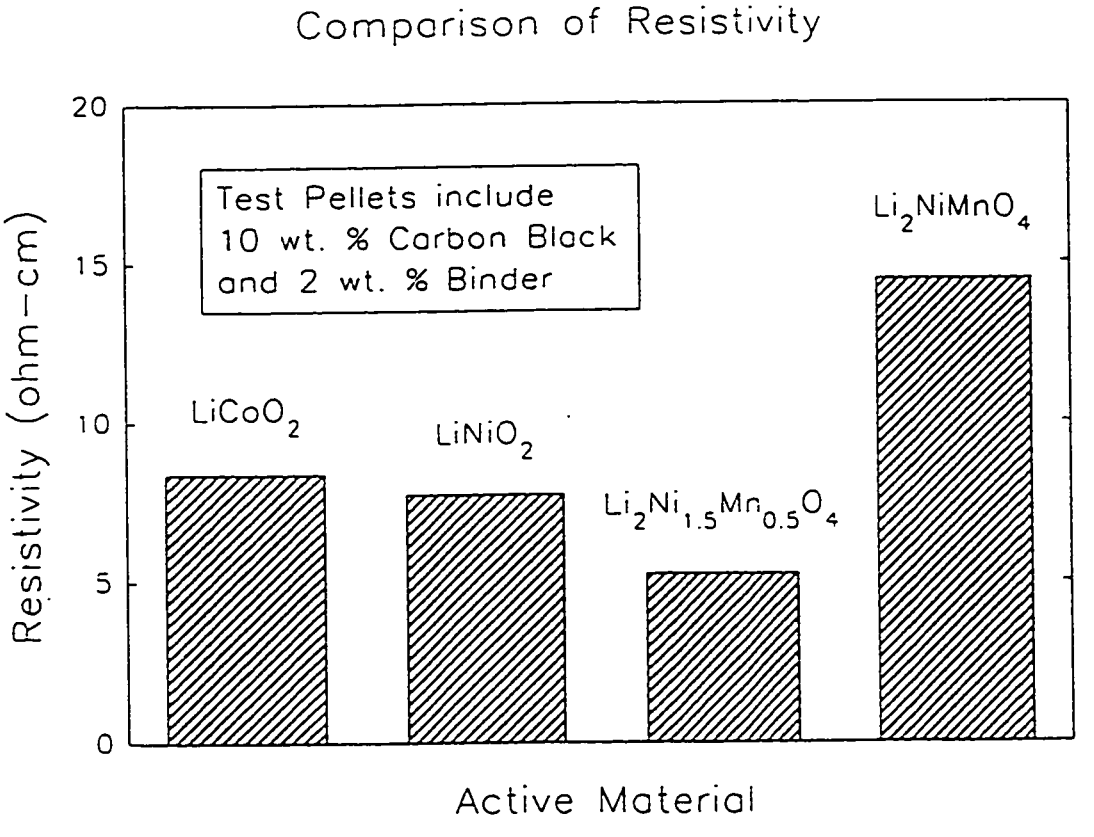

Figure 6.3.4 - Comparison of resistivity between cathodes based on $Li_2Ni_yMn_{2-y}O_4$ phases and those based on $LiCoO_2$ or $LiNiO_2$.

6.4 $Li_2Cr_yMn_{2-y}O_4$

As reported earlier, 3R-$LiCrO_2$ and orthorhombic $LiMnO_2$ were found to be completely miscible. Phases over the range of compositions, $0.1 \leq y \leq 1.9$, were fabricated into cathodes and tested in coin cells.

Compositions in which greater than 75% of the transition metal is chromium show a strong dependence between composition and colour. The colour darkens with decreasing chromium content, changing from brown for $Li_2Cr_{1.9}Mn_{0.1}O_4$ to black for $Li_2Cr_{1.5}Mn_{0.5}O_4$. Compositions in which greater than 75% of the transition metal is chromium did not perform well in coin cell tests. The internal impedance of the coin cells, with greater than 75% chromium, increased with increasing chromium concentration. The dependence of colour and cell impedance on chromium content suggests that the electronic conductivity increases with increasing manganese substitution.

Cells assembled with $Li_2Cr_yMn_{2-y}O_4$ based cathodes in which $y \leq 1.5$ showed capacities and cycle lives comparable to, or better than, that those with $LiCoO_2$ or $LiNiO_2$ based cathodes. Details of several experiments are given below to illustrate the electrochemical performance.

$Li_2Cr_{1.5}Mn_{0.5}O_4$ was prepared from 5.209 g of $LiCrO_2$ and 1.790 g of orthorhombic $LiMnO_2$. The sample was fired three times, for three days each, at 1000 $^{\circ}C$ and was reground between the firings. An x-ray powder pattern taken after the third firing showed only reflections which could be indexed to a

hexagonal unit cell of dimensions a = 2.909(2) Å and c = 14.442(5) Å. This sample was used as the active material in the cathodes of three coin cells. The cathodes were prepared by drying a slurry made from 6.595 g of $Li_2Cr_{1.5}Mn_{0.5}O_4$ with two weight percent of ethylene propylene diene monomer (EPDM) and 10 wt.% *Super S* carbon black in cyclohexane. The carbon anodes were made from petroleum coke, with 2 wt.% of EPDM and 7.5 wt.% of *Super S* carbon black.

In the first cell, the anode had a thickness of 0.043" and a weight of 0.325 g, which corresponds to a capacity of 54.7 mAh to a composition of LiC_{12}. The cathode was 0.033" thick and weighed 0.483 g which corresponds to a theoretical capacity of 124.3 mAh if all the lithium ions in the cathode can be reversibly cycled. The cell was charged at 1.8 mA to 4.0 volts consuming a capacity of 56 mAh. This capacity corresponds to the cathode material being oxidized to the composition $Li_{1.1}Cr_{1.5}Mn_{0.5}O_4$ and represents a capacity density of 132 mAh/g of $Li_2Cr_{1.5}Mn_{0.5}O_4$. It also represents a nominal depth of charge on the anode of 102%. However, some of the anode reaction is known to be irreversible, and is assumed not to be lithium intercalation. On discharging the cell to 2.0 volts at 1.8 mA, a capacity of 31 mAh was achieved with an average cell voltage of around 3.2 volts. By the 24^{th} cycle at 1.8 mA, the reversible capacity had decreased to 23.3 mAh. Reducing the current to 0.45 mA resulted in an increase in the reversible capacity to 36 mAh. After an additional five cycles at 0.45 mA, the cell has a reversible capacity of 32.5 mAh between 2.0 and 4.0 volts.

A second cell was built with a 0.040" thick anode weighing 0.302 g, and a 0.036" thick cathode weighing 0.495 g. This corresponds to an anode capacity of 50.8 mAh to LiC_{12} and a cathode capacity of 127.4 mAh assuming all the lithium in the cathode can be cycled. The cell was charged at 1.8 mA to 4.0 volts consuming a capacity of 53 mAh. This capacity corresponds to a 42% depth of charge on the cathode or an end of charge composition of $Li_{1.16}Cr_{1.5}Mn_{0.5}O_4$. The first discharge produced 31 mAh to a limit of 2.0 volts at a current of 1.8 mA. A subsequent cycle at 0.45 mA resulted in a discharge capacity of 44 mAh, which is a capacity density of 101 mAh/g of $Li_2Cr_{1.5}Mn_{0.5}O_4$. A typical charge and discharge cycle for this cell is shown in figure 6.4.1.

The third cell was assembled with a 0.053" thick anode weighing 0.391 g, and a 0.021" cathode weighing 0.269 g. The cell required 38.1 mAh to charge to 4.0 v at 0.45 mA. The first charge pushed the cathode to a 55% depth of discharge. The cell delivered 24.2 mAh at 0.45 mA on the subsequent discharge to a voltage cutoff of 1.2 v. Thus, the capacity density of active cathode material, $Li_2Cr_{1.5}Mn_{0.5}O_4$, for the charge and discharge were 161 mAh/g and 102 mAh/g, respectively.

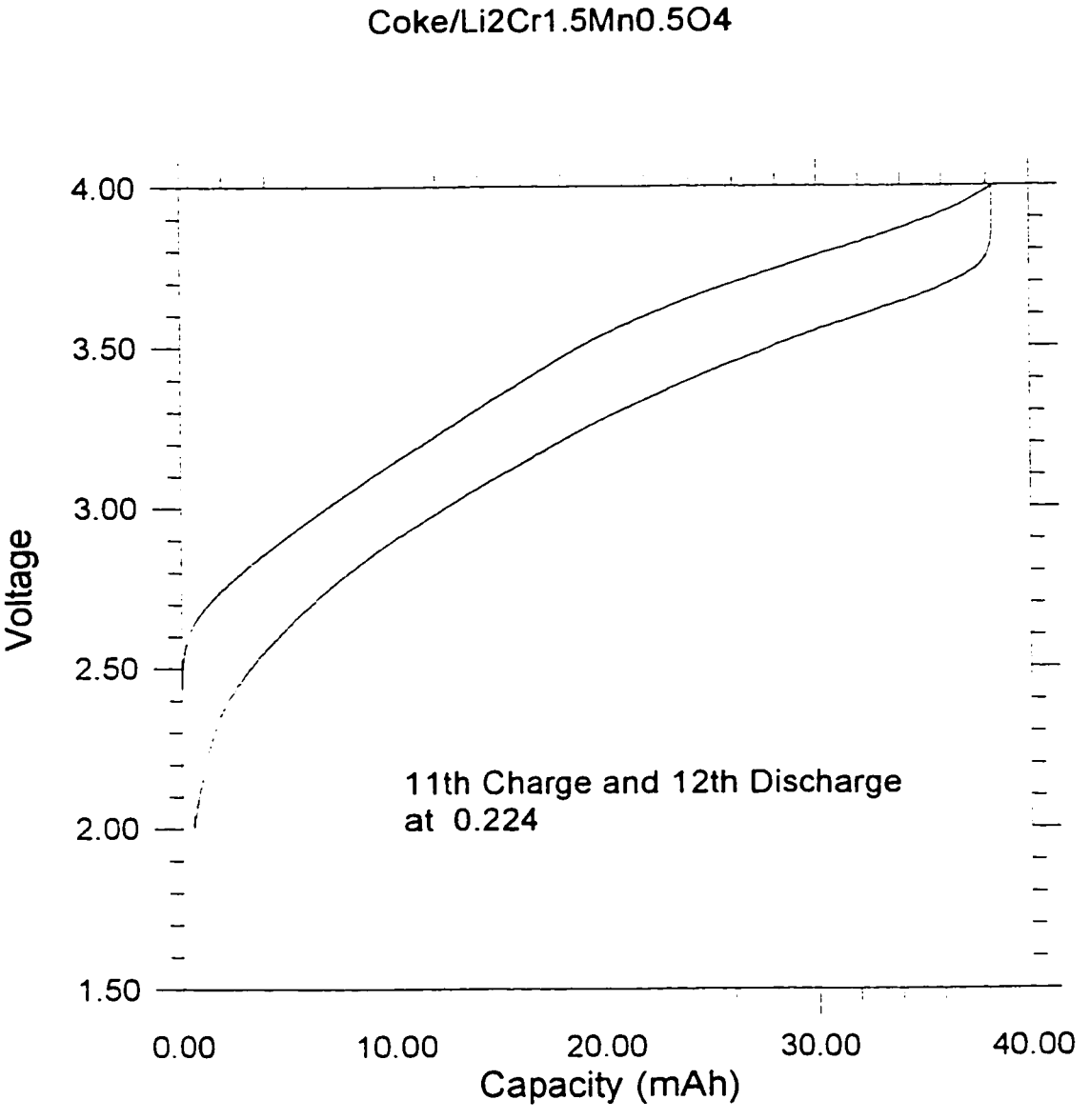

Figure 6.4.1 - Voltage profile of a coke/ $Li_2Cr_{1.5}Mn_{0.5}O_4$ coin cell.

Two batches of Li_2CrMnO_4 were combined to prepared the cathode mixture which was evaluated in coin cells. The first sample was prepared by mixing 0.771 g of $LiCrO_2$ with 0.798 g of orthorhombic $LiMnO_2$. The second sample of Li_2CrMnO_4 was prepared by combining 0.798 g of Li_2CO_3 with 0.823 g of Cr_2O_3 and 0.937 g of MnO_2. X-ray powder diffraction patterns were obtained for both samples after the first firing. The patterns were very similar, but the diffraction peaks were broad. The samples were fired two more times, for three days each, at 1000 °C and were reground between the firings. X-ray powder patterns taken after the third firing showed both samples to have virtually identical diffraction patterns but the reflections were still somewhat broad. The diffraction peaks could be indexed to a tetragonal unit cell of dimensions a = 5.76 Å and c = 8.60 Å.

The two samples were combined and used as the active material in the cathodes of three coin cells. The cathodes were prepared by mixing 3.084 g of Li_2CrMnO_4 with 2 wt.% EPDM and 10 wt.% *Super S* carbon black. The anodes were made from petroleum coke, with 2 wt.% of EPDM and 7.5 wt.% of *Super S* carbon black. Both the anode and cathode pellets were formed in the same manner as those for the $Li_2Cr_{1.5}Mn_{0.5}O_4$ cells, and the same electrolyte solution. and cell assembly procedure, was used. The first cell had a 0.320 g anode of 0.042" thickness, and a 0.033" thick cathode weighing 0.384 g. The cell required 53.1 mAh to charge to 4.0 v at 1.8 mA. This corresponds to a 54% depth of charge on the cathode, or a capacity density of 157 mAh/g of Li_2CrMnO_4. The

subsequent discharge to 1.8 v at 1.8 mA yielded 30.6 mAh. After a rest period the cell was discharged again at 0.45 mA to 1.8 v which produced a further 3.9 mAh for a total of 34.5 mAh. Later cycles at 0.45 mA produced a reversible discharge capacity of 39.5 mAh.

The second cell had a 0.042" thick anode weighing 0.316 g and a cathode of 0.034" thickness weighing 0.383 g. The cell was charged at 1.8 mA to a capacity limit of 49 mAh which corresponds to 50% depth of charge on the cathode. The cell reached the capacity limit at a voltage of 3.9 v. The first discharge at 1.8 mA yielded 26.8 mAh to 1.8 v. After a rest period, the cell was discharged a further 6.8 mAh at 0.18 mA to 1.8 v. Subsequent cycles at 0.225 mA produced a reversible capacity of 43 mAh. This represents a 44% depth of discharge on the cathode, or a capacity density of 127 mAh/g of Li_2CrMnO_4. Figure 6.4.2 shows a typical charge and discharge cycle for this cell.

The third cell was assembled with a 0.052" thick anode weighing 0.369 g and a 0.022" thick cathode weighing 0.252 g. The first charge at 0.45 mA to 4.0 v required 47.4 mAh. This capacity represents a 73.5% depth of charge on the cathode and a capacity density of 214 mAh/g of Li_2CrMnO_4. The subsequent discharge at 0.45 mA produced 30.1 mAh to a 1.2 v limit, with almost all of the capacity being achieved above 1.9 v. After a period of rest, the cell was discharge again at 0.23 mA to 1.2 v, providing a further 1.6 mAh. The total discharge capacity, 31.7 mAh, corresponds to a 49% depth of discharge on the cathode and to a reversible capacity density of 143 mAh/g of Li_2CrMnO_4.

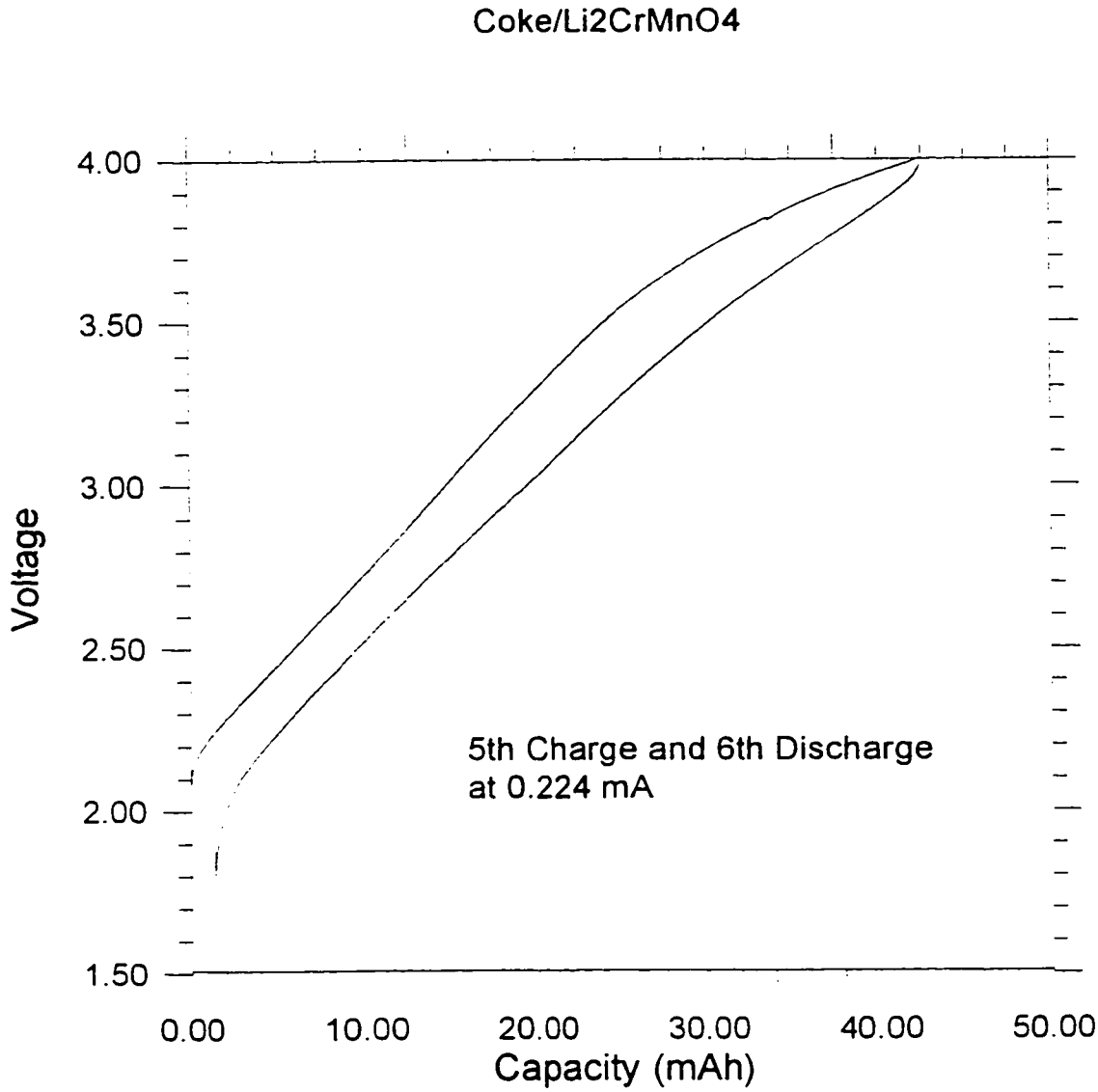

Figure 6.4.2 - Voltage profile of a coke/ Li_2CrMnO_4 coin cell.

$Li_2Cr_{0.5}Mn_{1.5}O_4$ was prepared from 1.898 g of $LiCrO_2$ and 5.874 g of orthorhombic $LiMnO_2$. Finely ground powders of the reagents were intimately mixed and pelletized. Then they were fired in high purity alumina crucibles in a horizontal tube furnace under a flow of inert gas. The furnace was held at 600 °C for 4 hours before heating and holding it at 1000 °C for 3 days. Three further annealings at 1000 °C for 2 to 3 days each were required to obtain an x-ray diffraction pattern with moderately sharp peaks. The sample was reground between each firing. The x-ray diffraction pattern of the final product could be indexed to a tetragonal unit cell of approximate dimensions a = 5.74 Å and c = 8.95 Å.

Two coin cells were built, in the same manner as described above, with cathodes fabricated from $Li_2Cr_{0.5}Mn_{1.5}O_4$ and petroleum coke anodes. The cathode mixture was prepared from 5.113 g of $Li_2Cr_{0.5}Mn_{1.5}O_4$ with 2 wt.% EPDM and 10 wt.% *Super S* carbon black. The first cell had a 0.045" thick anode weighing 0.355 g, and a 0.418 g cathode which was 0.031" thick. A capacity of 64.2 mAh was required to charge the cell to a 60% depth of charge on the cathode. The cell was charged at 0.45 mA and reached the required capacity at a potential of 3.83 v. On being discharged to 1.5 v at 0.45 mA, the cell produced 41.4 mAh, with almost all the capacity being delivered above 2.0 v. A typical charge and discharge cycle for this cell is shown in figure 6.4.3.

The second cell had a 0.374 g cathode of 0.026" thickness and a 0.049" thick anode weighing 0.398 g. A capacity of 72.3 mAh was needed to charge the

cell to 4.0 v at 0.45 mA. This corresponds to a 75% depth of charge on the cathode, or a capacity density of 217 mAh/g of $Li_2Cr_{0.5}Mn_{1.5}O_4$. A capacity of 49 mAh was recovered on the subsequent discharge at 0.45 mA to 1.5 v.

Figure 6.4.4 illustrates the variation in the capacity versus voltage plots as a function of the composition. The capacity accessible below 4.0 volts increases with increasing manganese composition. The average voltage of the cell increases with increasing chromium substitution. The step in the voltage curves for compositions in which greater than 80% of the transition metal sites are occupied by manganese is similar to that observed in cells with cathodes based on orthorhombic $LiMnO_2$ and λ-$Li_2Mn_2O_4$. Ohzuku, Kitagawa and Hirai (1990) have shown that, for λ- $Li_2Mn_2O_4$, this voltage step is due to the deformation of the MnO_6-octahedra from O_h-symmetry to D_{4h}-symmetry at a critical concentration of the Jahn-Teller ion Mn^{3+}.

A step in the voltage curve is also observed in cells with $Li_2Cr_yMn_{2-y}O_4$ based cathodes in which greater than 75% of the transition metal sites are occupied by manganese. The voltage step occurs at a deeper depth of charge for $Li_2Cr_yMn_{2-y}O_4$ than for $LiMnO_2$, and the depth of charge at which it occurs increases with increasing chromium content.

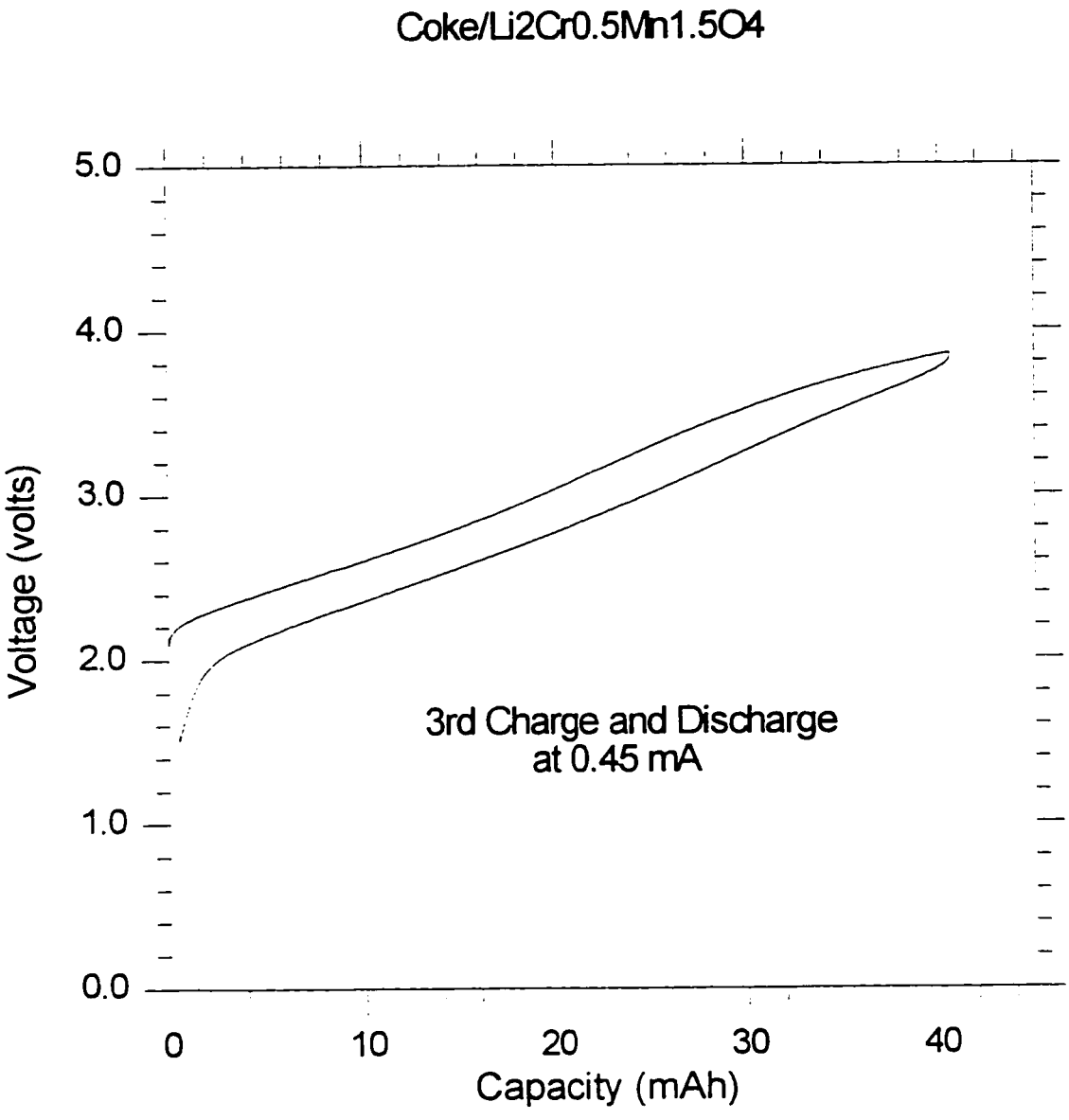

Figure 6.4.3 - Voltage profile of a coke/ $Li_2Cr_{0.5}Mn_{1.5}O_4$ coin cell.

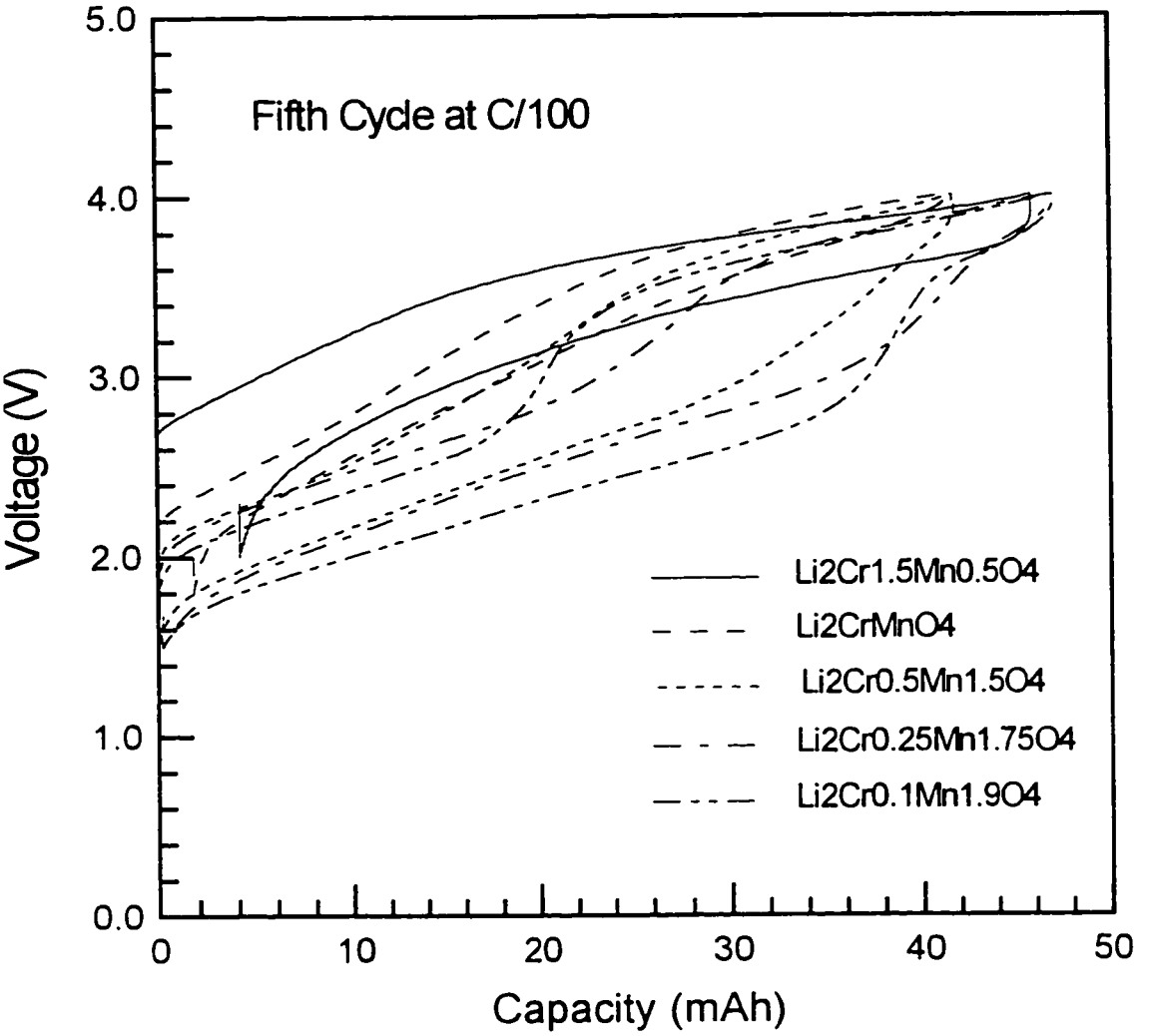

Figure 6.4.4 - Voltage profiles of the fifth charge/discharge cycle for coin cells with $Li_2Cr_yMn_{2-y}O_4$ cathodes and coke anodes.

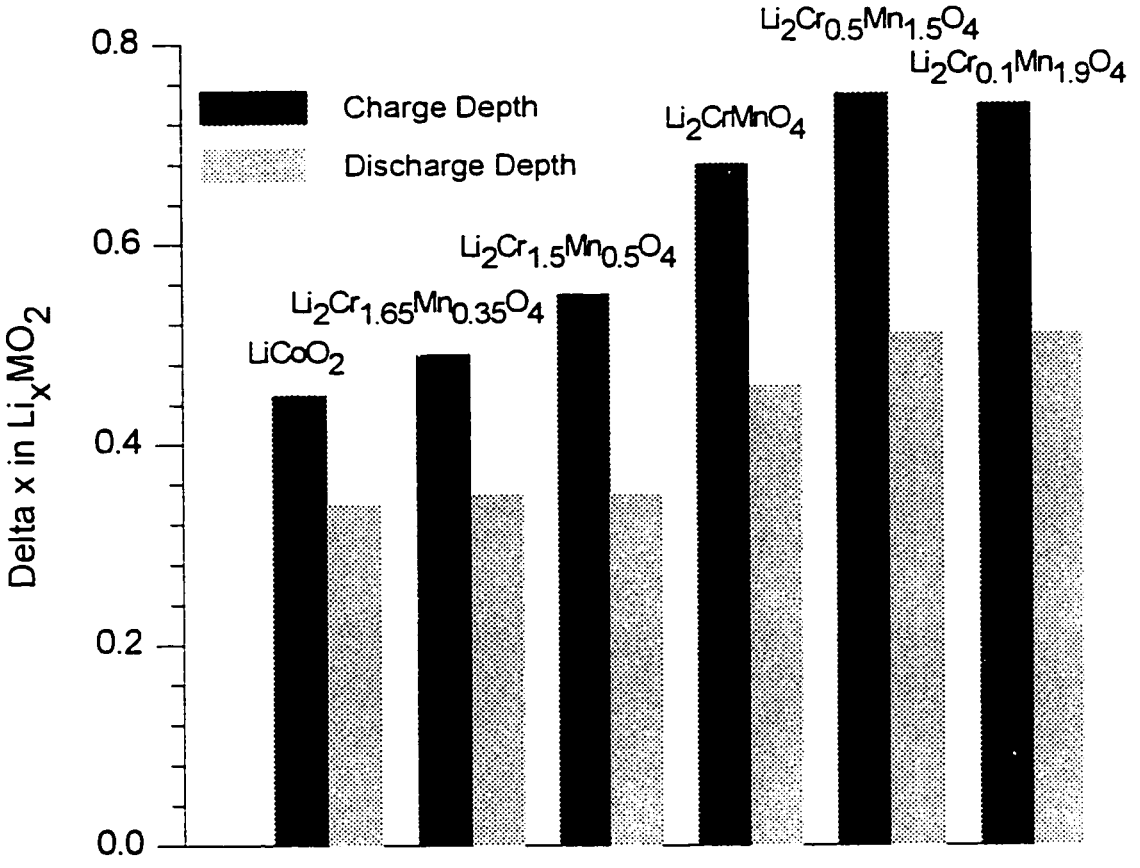

Figure 6.4.5 - Comparison of charge and discharge cathode utilization in lithium ion cells cycle between 1.5 and 4.0 V at 100 hour rate.

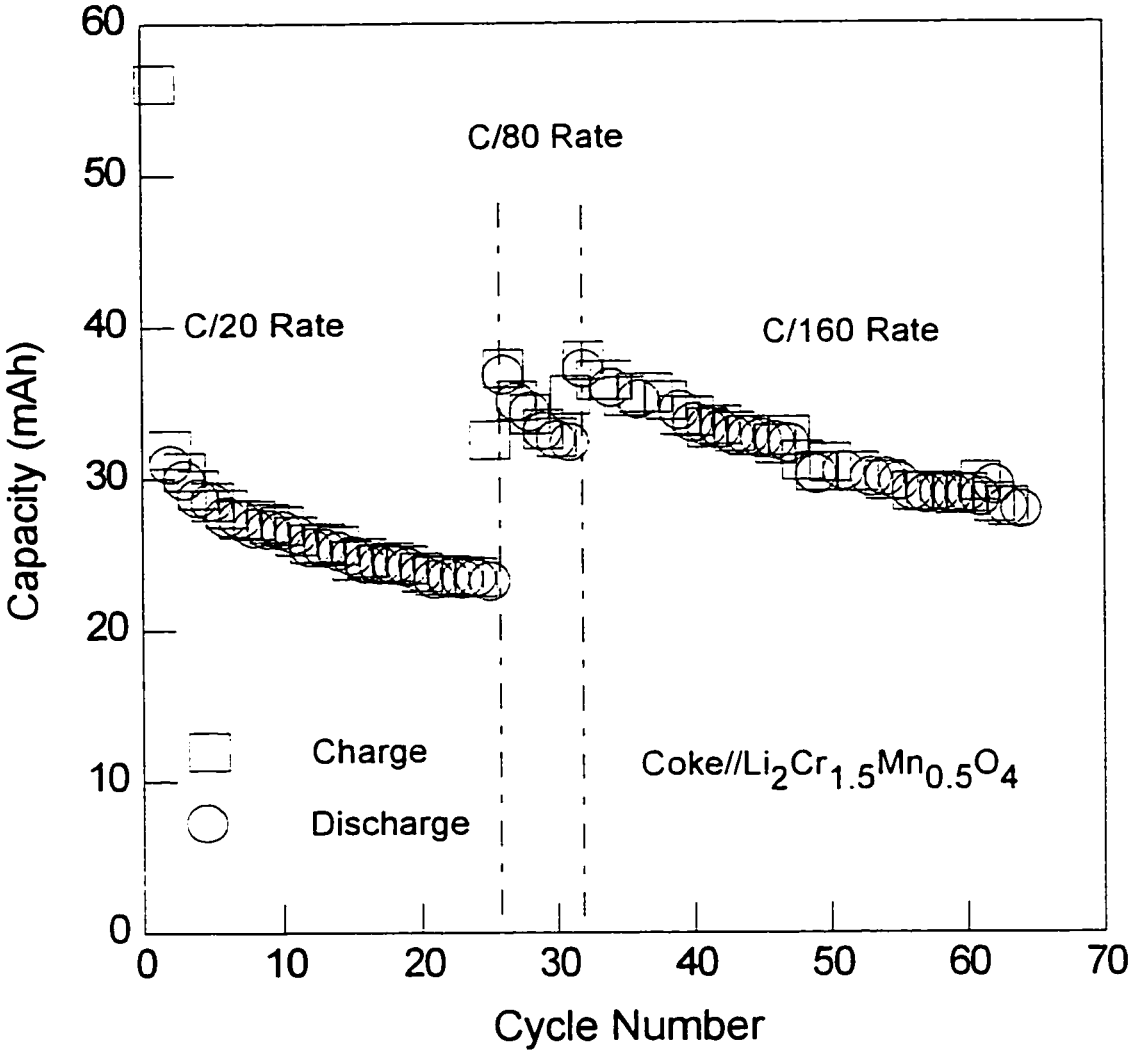

Figure 6.4.6 - Charge and discharge capacities as a function of cycle number for a coke/$Li_2Cr_{1.5}Mn_{0.5}O_4$ coin cell.

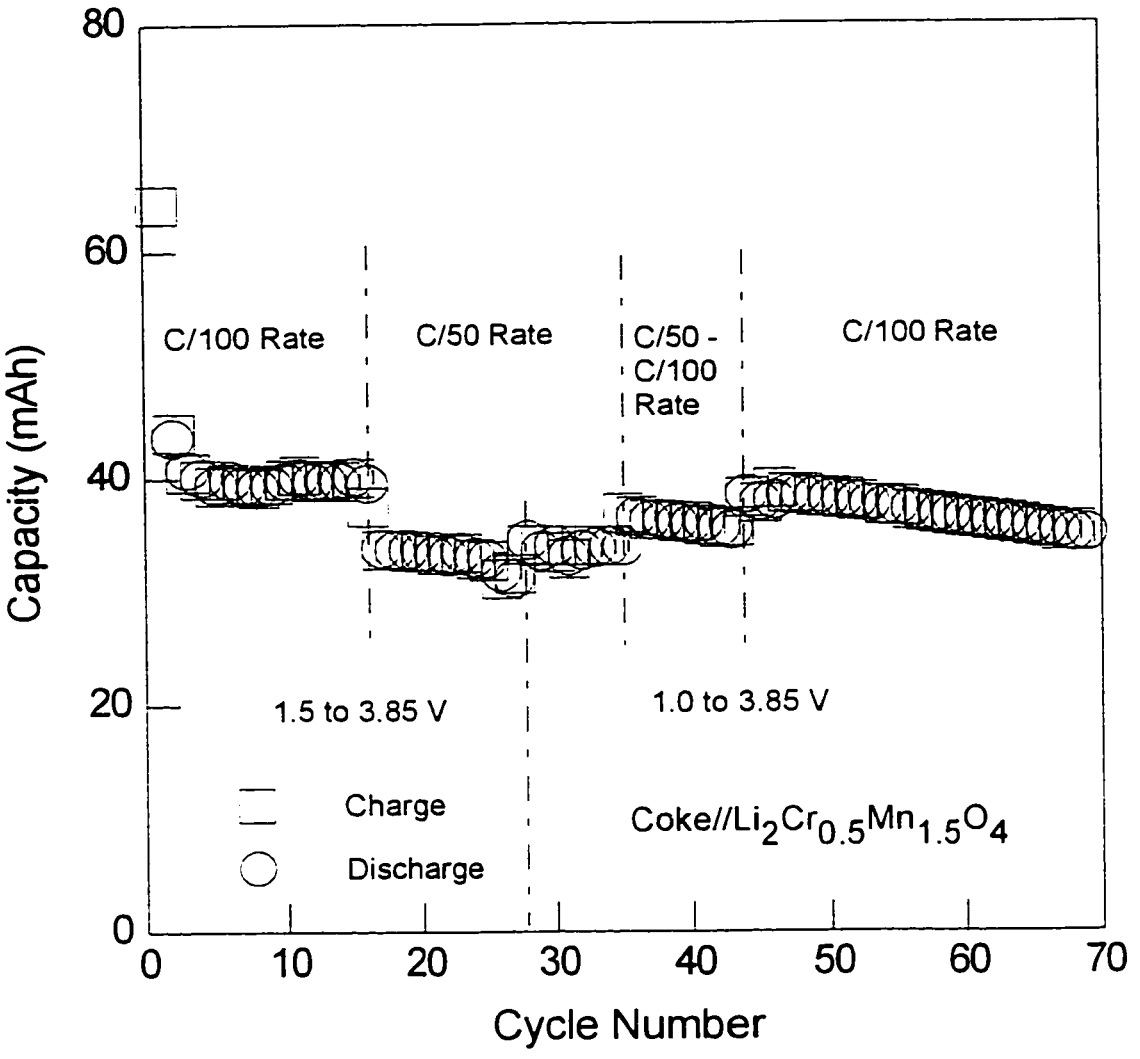

Figure 6.4.7 - Charge and discharge capacities as a function of cycle number for a coke/$Li_2Cr_{0.5}Mn_{1.5}O_4$ coin cell.

Figure 6.4.5 compares the accessible cathode capacity, in terms of percent lithium cycled, on the first charge and discharge of lithium ion cells with petroleum coke anodes. The anode to cathode weight ratios were chosen to optimize the cathode capacity accessible below 4 volts. These results are, however, each based on only one or two cells and may have a significant margin of variability. In all cases the reversible capacity, or discharge capacity, is at least as good as that of a similar $LiCoO_2$ cell. Compositions of $Li_2Cr_yMn_{2-y}O_4$ with a spinel-related structure have greater capacity to 4.0 volts than those with a 3R-type hexagonal structure. This could be due to either differences the intrinsic stability of the de-intercalated structure or to increases in cell potentials with increasing chromium content. The irreversible capacity losses, the difference between the charge depth and the discharge depth, are larger for all $Li_2Cr_yMn_{2-y}O_4$ compositions than for cells with $LiCoO_2$ cathodes, but are comparable to that expected for a λ-$Li_2Mn_2O_4$ lithium ion cell cycled to 4.0 volts (Tarascon and Guyomard 1991). Figures 6.4.6 and 6.4.7 demonstrate that lithium ion cells with $Li_2Cr_yMn_{2-y}O_4$ cathodes can be cycled to greater than 60 cycles at modest rates. The cycling rates were varied over the course of the experiment to examine the effect of rate on capacity and cycle life. The rate designation C/100 means that it took 100 hours to fully discharge, or charge, the cell. The cell containing a $Li_2Cr_{1.5}Mn_{0.5}O_4$ cathode, figure 6.4.6, was cycled between voltage limits of 1.8 and 4.0 volts. The voltage limits of the $Li_2Cr_{0.5}Mn_{1.5}O_4$ cell, figure 6.4.7, were changed from 1.5 to 3.85 volts to 1.0 to 3.85 volts on

the 28th cycle. The coin cell format, 2325, required that the electrodes have thickness on the order of 1 mm. Thinner electrodes were expected to have better rate capabilities.

The addition of stainless steel disc springs and spacers inside the coin cell assembly made it possible to work with thinner electrodes. Thinner cathodes based on the higher manganese compositions of $Li_2Cr_yMn_{2-y}O_4$ with y = 0.1, 0.5, 1.0 and 1.5 were evaluated in coin cells with lithium counter electrodes. Lithium anodes simplify the interpretation of the potential versus capacity curves because the potential of the anode remains constant. Consequently, the observed changes in potential reflect changes in lithium ion activity in the cathode as a function of its lithium composition.

The thin electrodes were prepared by the slurry cast method described in chapter 2. An electrolyte solution 1 M $LiClO_4$ in a 1:1 mixture of EC/DME was used. The thinner electrodes did not have much better rate capabilities. This suggests that the rate is limited by kinetics of the lithium ion mobility in the $Li_2Cr_yMn_{2-y}O_4$ compounds themselves. Figures 6.4.8 - 6.4.10 are plots of cell potential against capacity in mAh per gram of active cathode material for cells cycled at constant current between 2.5 and 4.2 volts. The trends in the electrochemistry as a function of composition are the same as was observed in the cells with coke anodes. The average cell potential increases with increasing chromium content. The cell with $Li_2Cr_{0.5}Mn_{1.5}O_4$ cathode has a cycle curve like that of λ-$Li_2Mn_2O_4$ with two voltage plateaus. A fourth cell with a cathode based

on $Li_2Cr_{0.1}Mn_{1.9}O_4$ and a lithium anode was cycled between 2.5 and 4.4 volts. The cycle plot of this cell, figure 6.4.11, as expected, also has two plateaus but the transition between the plateaus is much sharper and more like that of λ-$Li_2Mn_2O_4$. Figure 6.4.11 can be compared to the middle plot in figure 6.1.6 for a Li/$LiMnO_2$ cell cycle between 2.5 and 4.4 volts. The figures are similar except that the cell with the $Li_2Cr_{0.1}Mn_{1.9}O_4$ cathode has more capacity in the lower voltage plateau and a broader cycling hysteresis. The chemistry of the electrochemical reactions within the cathodes has are not yet been determined. The shape of the first charge curves for the compositions with $y \leq 1.0$ is different from that of subsequent cycles. This indicates that a phase transition is occurring on the first charge. Preliminary *ex-situ* x-ray diffraction studies of previously cycled cathodes confirm that a structure change has occurred.

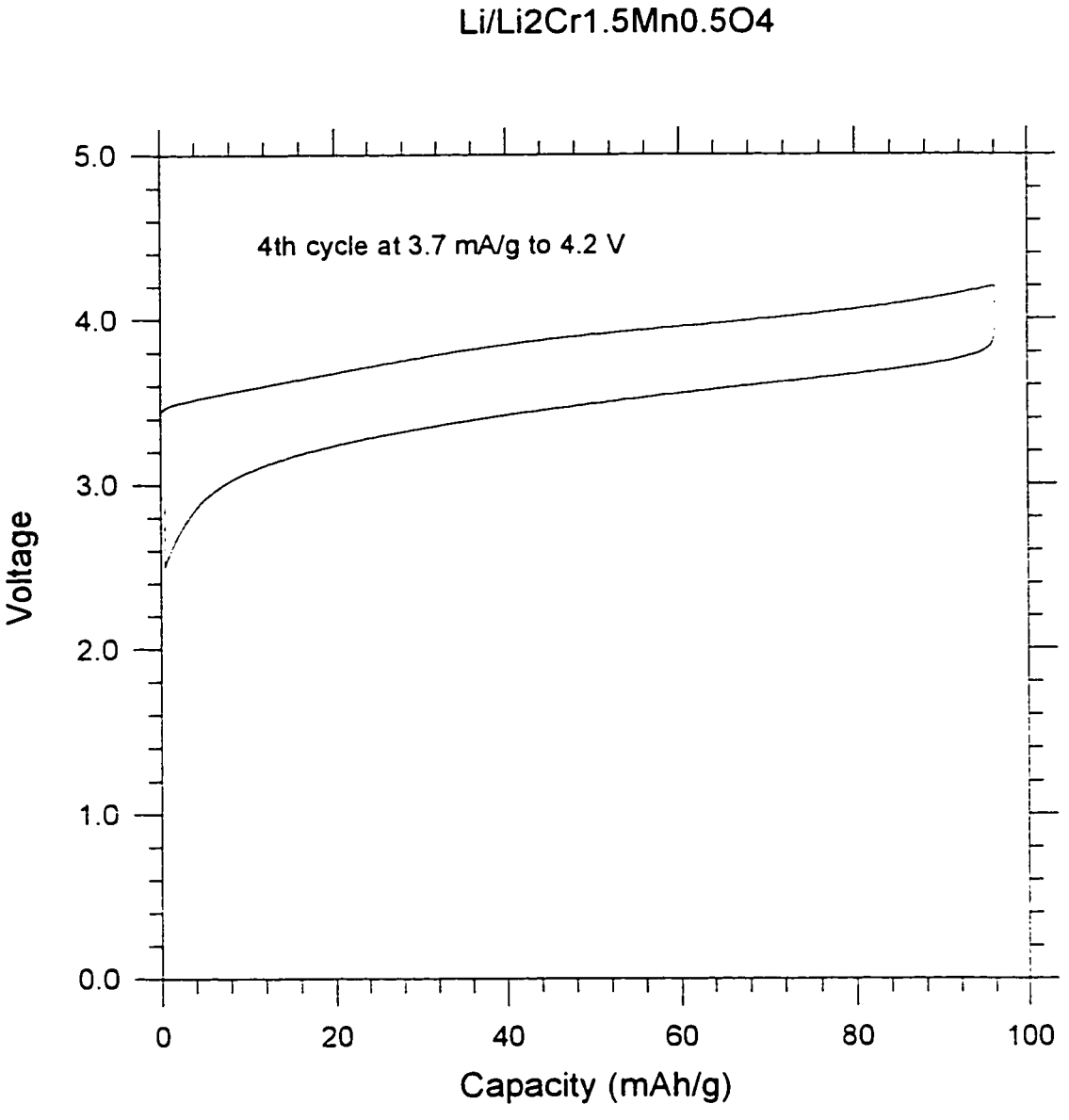

Figure 6.4.8 - Voltage profile for the 4th cycle of a Li/$Li_2Cr_{1.5}Mn_{0.5}O_4$ cell.

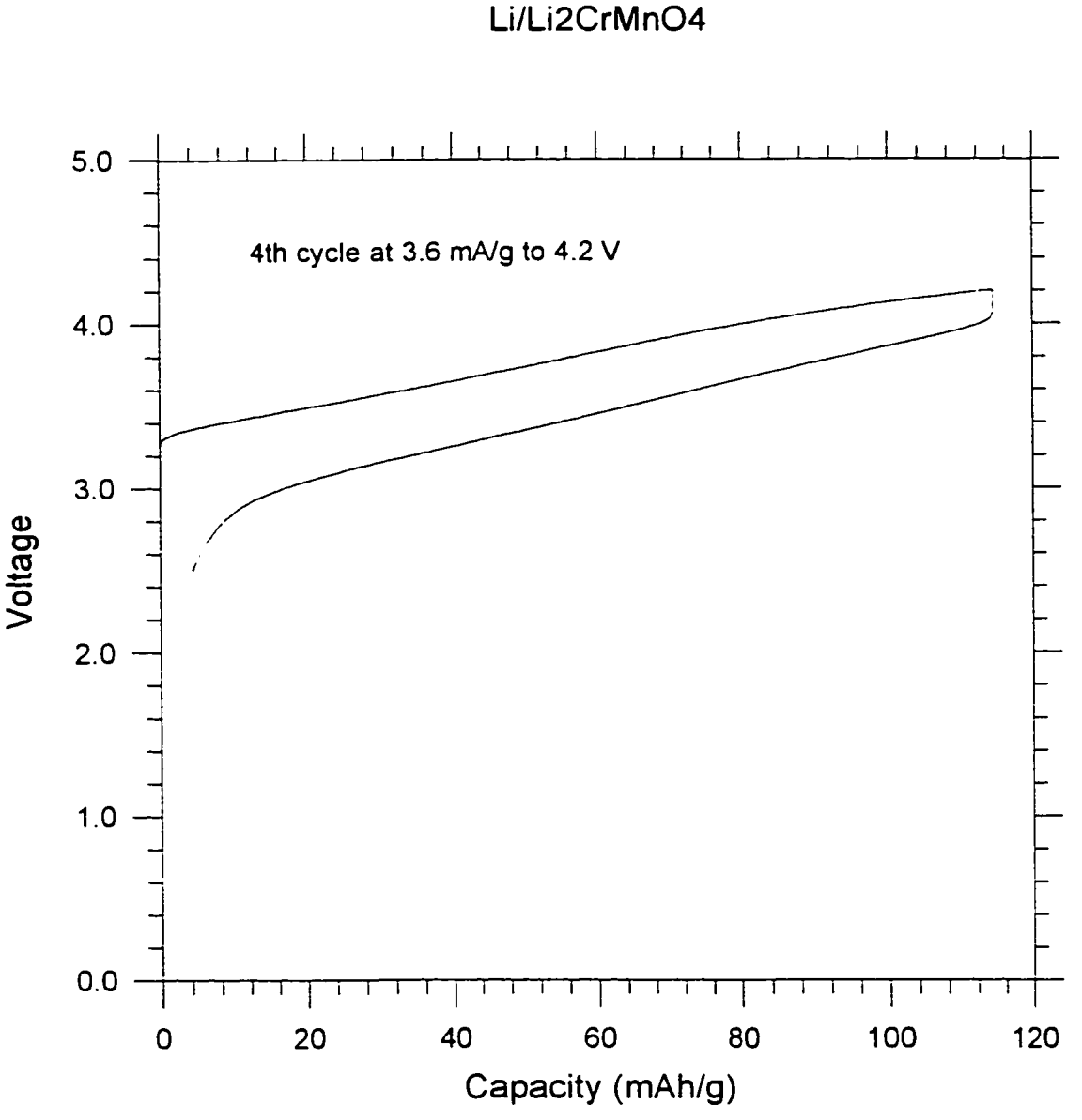

Figure 6.4.9 - Voltage profile for the 4th cycle of a Li/Li_2CrMnO_4 cell.

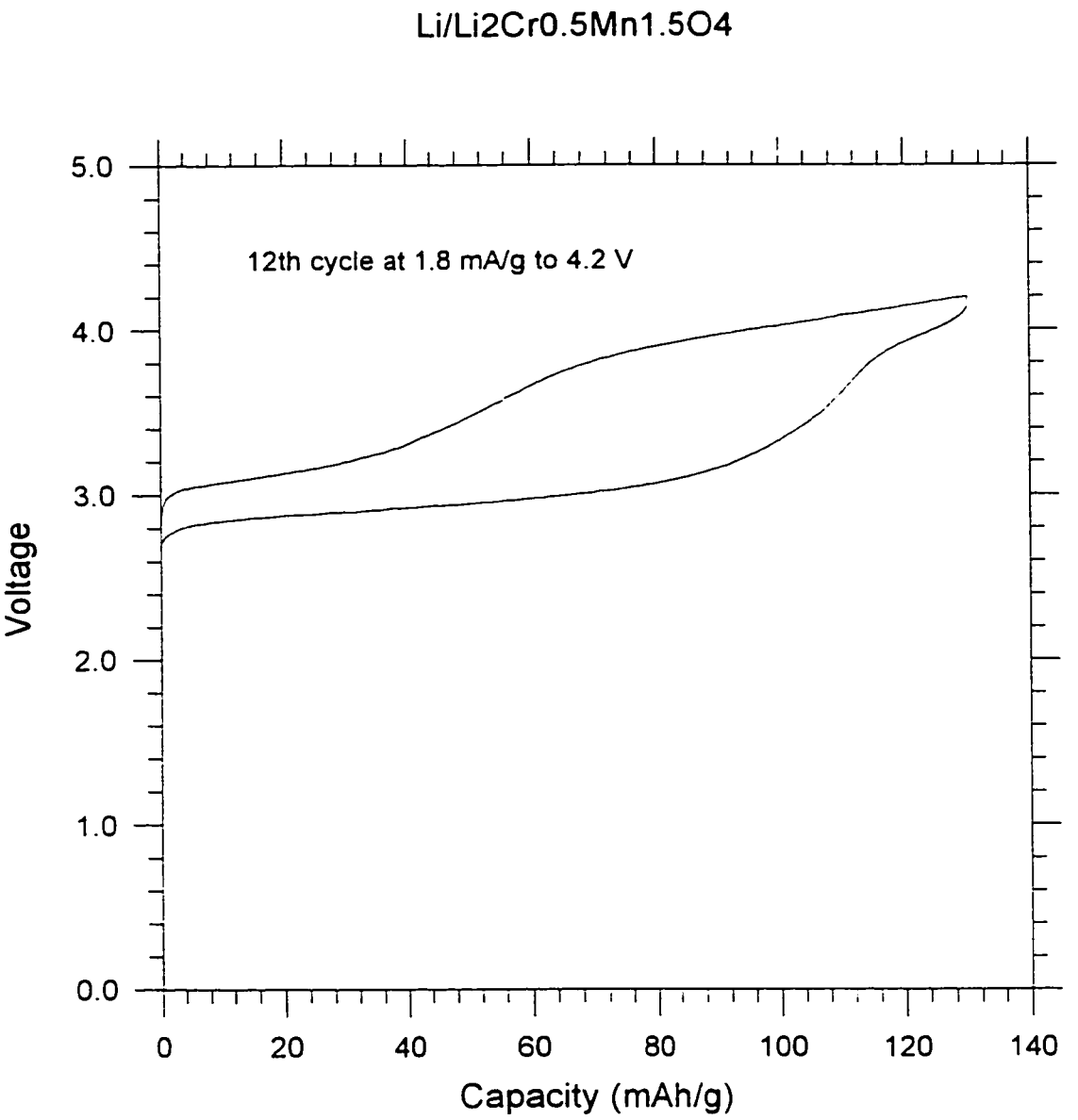

Figure 6.4.10 - Voltage profile for the 12th cycle of a Li/$Li_2Cr_{0.5}Mn_{1.5}O_4$ cell.

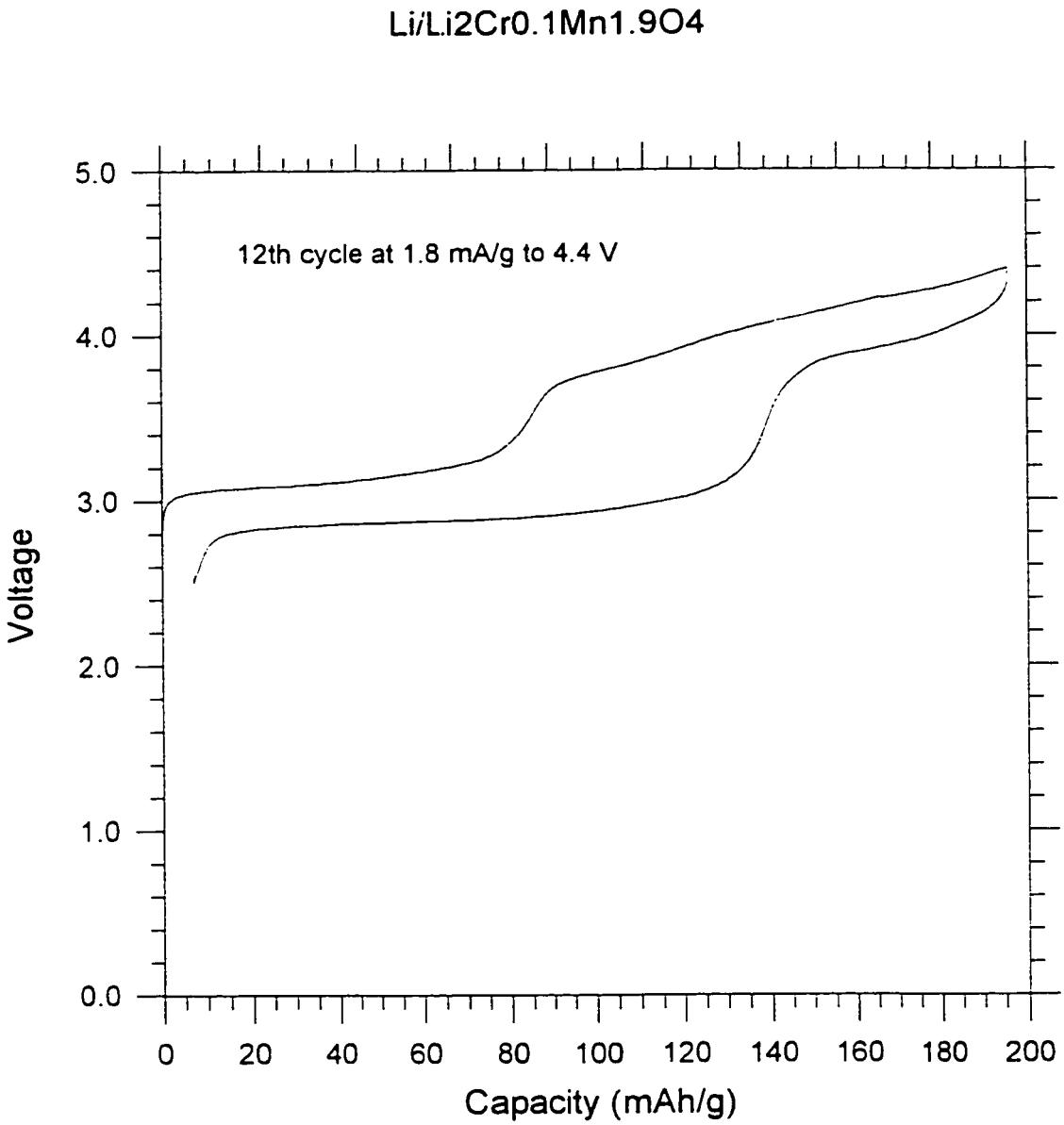

Figure 6.4.11 - Voltage profile for the 12th cycle of a Li/$Li_2Cr_{0.1}Mn_{1.9}O_4$ cell.

Chapter 7

Discussion

7.1 Orthorhombic $LiMnO_2$

$LiMnO_2$ is known to exist in several phases. Two phases, whose crystal structures have been well characterized, are a high temperature orthorhombic phase and a tetragonal phase. Both structures involve cubic closest packing but they differ in the arrangement of the ordering of the lithium and manganese cations. The tetragonal form is normally written as λ-$Li_2Mn_2O_4$. It has an atacamite-type structure which is often referred to as being spinel related or a lithiated spinel. Another type of lithium manganate, $LiMn_2O_4$, has a true spinel structure.

Both $LiMn_2O_4$ and λ-$Li_2Mn_2O_4$ have been used as cathodes in lithium ion cells (Tarascon and Guyomard 1991 and Guyomard and Tarascon 1992). λ-$Li_2Mn_2O_4$ has twice the nominal capacity of $LiMn_2O_4$ but it is reported to be hygroscopic and metastable (Mosbah, Verbaere and Tournoux 1983). λ-$Li_2Mn_2O_4$ is prepared by electrochemically, or chemically, intercalating lithium into the $LiMn_2O_4$ spinel structure.

The structure of the high temperature orthorhombic phase of $LiMnO_2$ was determined in detail by Hoppe, Brachtel and Jansen, (1975). This structure

is described by the space group Pmnm and has unit cell dimensions a = 4.572 Å, b = 5.757 Å and c = 2.805 Å. The first practical demonstration of the use of $LiMnO_2$, having this structure, as the active material in the cathode of a lithium ion cell was reported at the 7th International Meeting on Lithium Batteries (Davidson, McMillan, Murray and Greedan 1995).

Ohzuku, Ueda and Hirai (1992) have demonstrated the use of a low temperature form of orthorhombic $LiMnO_2$, prepared by reacting an equimolar mixture of γ-MnOOH and $LiOH \cdot H_2O$ at 450 °C, as the active cathode material in a reversible lithium ion cell. More recently, Reimers Fuller, Rossen and Dahn (1993) developed improvements on Ohzuku's synthesis and found that LT-$LiMnO_2$ can be prepared at very low temperature (100 °C) by ion exchange. However, they found that well crystallized $LiMnO_2$ prepared at 450 °C had much poorer electrochemical behavior than more disordered material prepared at 350 °C. Gummow, Liles and Thackeray (1993) studied $LiMnO_2$ prepared at moderate (600-620 °C) temperatures from γ-MnO_2 and LiOH in argon with carbon added as a reducing agent. Both Reimers and Gummow stated, without giving direct evidence, that orthorhombic $LiMnO_2$, which is conventionally synthesized at high temperatures, does not show good electrochemical activity.

The orthorhombic $LiMnO_2$, used in this thesis, was prepared by a classical high temperature solid state reaction, and was verified as having Hoppe's structure by neutron diffraction. The neutron diffraction data also confirms the purity of our sample. Neutron diffraction is often a more rigorous

test of sample purity because it probes the entire sample volume. No additional phases were detected and the refined unit cell parameters and atomic positions agreed very well with the previous determination.

The electrochemical studies, in chapter 6, demonstrated that cathodes based on the high temperature form of orthorhombic $LiMnO_2$ have good capacity and cycle life. X-ray diffraction studies on materials recovered from cycled cells also revealed that the orthorhombic $LiMnO_2$ prepared at high temperature converts to $Li_{1-x}Mn_2O_4$ on being charged to greater than about 50% of its theoretical capacity (285 mAh/g). This transition is essential to the functioning of orthorhombic $LiMnO_2$ as a practical cathode material. However, unlike λ-$Li_2Mn_2O_4$, orthorhombic $LiMnO_2$ has been found to have long term stability in ambient conditions and is easily prepared in a one step reaction.

Although there has recently been substantial interest in the electrochemical properties of orthorhombic $LiMnO_2$, the magnetic properties had not been investigated in detail. There are several features of the $LiMnO_2$ structure which suggest that it might have interesting magnetic properties. Since Mn^{3+} is a Jahn-Teller ion, $3d^4$, the local environment around the manganese ions is tetragonally distorted. The two axial bonds along the b-axis are longer, 2.294(6) Å, than the two nearly equal pairs of equatorial bonds at 1.90(4) and 1.94(4) Å. The disorder of the oxygen sublattice in $LiMnO_2$ causes the Li - O and Mn - O layers to fold into a corrugated pattern. $LiMnO_2$ can be regarded as having a distorted and unusual ordering of the rock-salt structure. More typical

ordered rock-salt phases, such as $LiCrO_2$ have layers of nearly regular edge-sharing octahedra which stack in the direction normal to the close-packed oxygen layers, resulting in rhombohedral symmetry. The stacking direction in $LiMnO_2$ is nearly 45° to that of a typical 3R-phase.

The manganese sublattice can be viewed in two ways: as a distorted hexagonal motif lying normal to the c-axis with a fold angle of 111°, or as two sets of linear chains of Mn-atoms running in the direction of the a-axis. The hexagonal view, shown in figure 7.1.1, is built of edge sharing isosceles triangles with one edge at the a-axis distance of 2.805 Å and the other two at 3.09 Å with angles of 63°, 63° and 54°. The corrugated Mn - O layers are separated by interleaving Li - O layers with a closest interlayer Mn - Mn distance of 5.00 Å. Alternatively, in the linear chain view, shown in figure 7.1.2, the Mn - Mn distance within the chains is 2.805 Å and the Mn - Mn distance between the two chains at z = 1/3 and z = 2/3 is 3.09 Å. The Mn - O octahedra share edges and the intra and inter chain Mn - O - Mn angles are very similar at 93.2(2)° and 92.8(4)°, respectively.

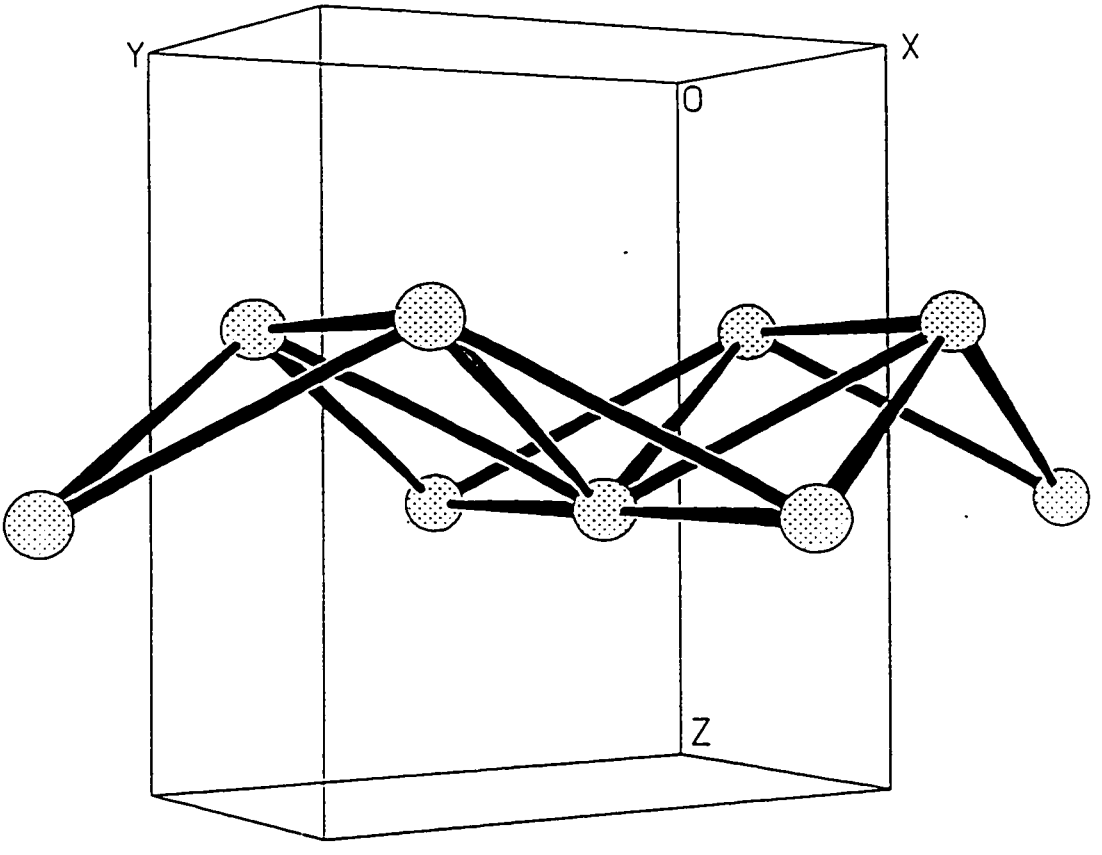

Figure 7.1.1 - Hexagonal view of orthorhombic $LiMnO_2$ structure.

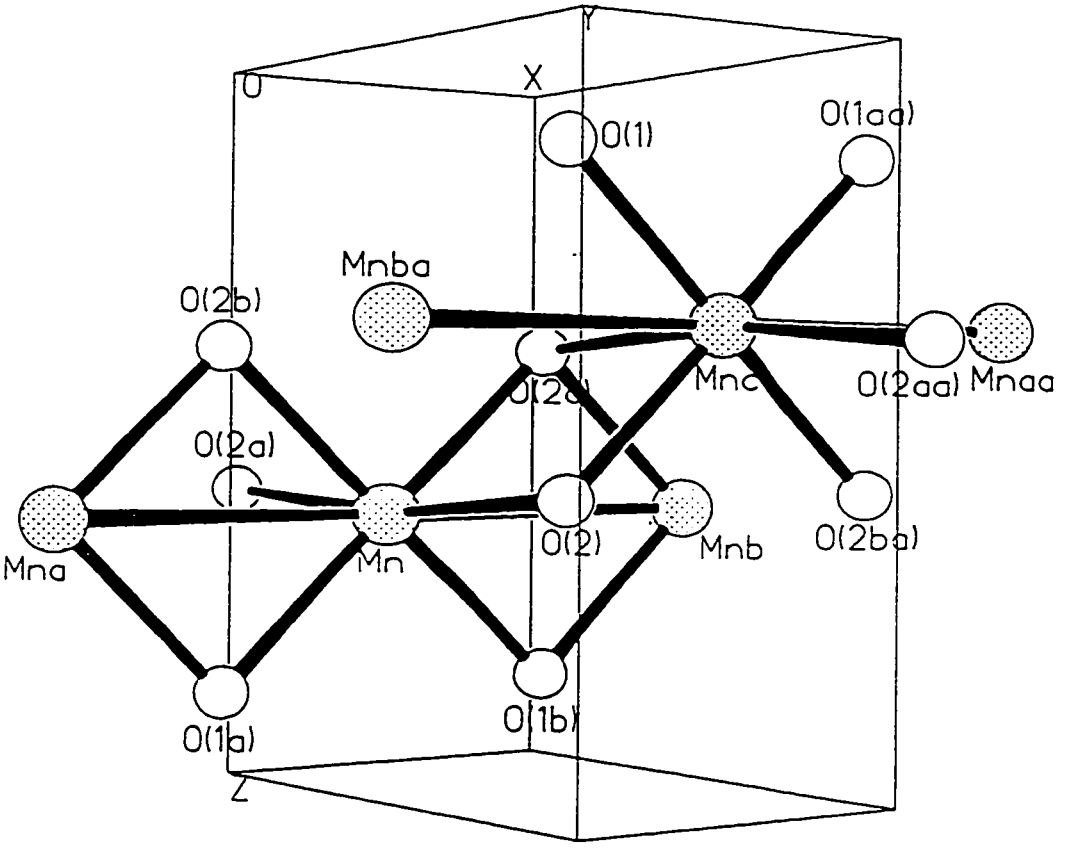

Figure 7.1.2 - Linear chain view of orthorhombic $LiMnO_2$ structure.

The magnetic exchange pathways in this material can be understood by considering the orbital symmetries involved in the interactions. The tetragonal elongation of the Mn - O octahedra means the Mn^{3+} configuration is $t_{2g}^3 d_{z2}^1 d_{x2-y2}^0$. The intrachain 90° Mn - O - Mn interaction involves the empty d_{x2-y2} orbitals and can be expected to be weak. The intra chain Mn - Mn interaction occurs via the half-filled $t_{2g}(d_{xz})$ orbitals and should be strongly antiferromagnetic. The interchain interaction also involves a 90° Mn - O - Mn pathway but since it involves the d_{z2} - O - d_{x2-y2} orbitals it should be weak and according to the Goodenough-Kanamori rules, ferromagnetic. Therefore, it is expected that the strongest exchange interaction should be an antiferromagnetic Mn - Mn interaction along the a-axis chains.

The geometric relationship between the two interwoven chains is also important. The manganese atoms in adjacent chains are displaced along the c-axis and along the a-axis by (1/2 0 0) such that an atom in one chain centres two spins in the adjacent chain. Thus, if the ordering along the a-axis chains is antiferromagnetic, then the interchain coupling will be subject to symmetry cancellation.

Low temperature neutron powder diffraction on orthorhombic $LiMnO_2$ revealed a magnetic structure with a propogation vector of k = (1/2,1/2,1/2) and antiferromagnetic coupling in all three lattice directions. The magnetic moment refined to 3.61(5) μ_B, close to the expected spin-only value for high-spin Mn^{3+},

and has a preferred direction parallel to the b-axis. The magnetic structure can be viewed as consisting of two symmetry independent sublattices represented by the two sets of a-axis chains. The interaction along the a-axis chains is antiferromagnetic as expected.

From the symmetry considerations discussed above, it is expected that the magnetic correlations would be one-dimensional, with cross-overs to two and ultimately, three dimensionality as the temperature is lowered. The three dimensional ordering at low temperature is clearly established by the low temperature neutron diffraction pattern. Evidence for two dimensional ordering is evident from the Warren peak in the neutron diffraction patterns and from the susceptibility measurements. The absence of Curie-Weiss behaviour in the susceptibility even up to 350 K indicates the importance of short range magnetic correlations.

7.2 $LiFeO_2$

Since this work was completed another group has published a study on the structure and properties of $LiFeO_2$ prepared at low temperature by ion-exchange (Shirane, Kanno, Kawamoto, Takeda, Takano, Kamiyama and Izumi 1995). They obtained "layered" $LiFeO_2$ by a reaction of α-$NaFeO_2$ in molten LiCl/KCl. They also found that Rietveld refinement of neutron diffraction data could not clearly distinguish between the two probable structural models. Their lattice parameters : a = 8.3787(8) for the cubic model, and a= 2.9532(7) and c =

14.531(4) for the hexagonal model, are in very good agreement with those reported in chapter four. Shirane *et al* (1995) also examined their material by Mössbauer spectroscopy and measured its magnetization with a SQUID magnetometer. The Mössbauer spectrum at 300 K consisted of two quadrupole doublets with a relative abundance of 80:20, while at 4 K two magnetically split patterns are superimposed at a ratio of 88:12. The isomer shift and magnetic hyperfine field were both characteristic of trivalent Fe ions in oxides. From these results the authors concluded that their sample was two-phase containing both layered and lithiated spinel phases. They attributed the major component to the layered $LiFeO_2$ and the minor one to the spinel phase. Their magnetization study found an anomaly attributed to antiferromagnetic ordering near 19 K and a small magnetic hysteresis at and below 300 K which the authors proposed was due to the spinel phase component of their sample being a ferrimagnet.

The low temperature neutron diffraction study of $LiFeO_2$ reported in chapter 5 found the onset of antiferromagnetic ordering at about 21 K in good agreement with Shirane *et al* (1995). As in the work of Shirane *et al*, the sample of $LiFeO_2$ prepared for this study was found to be two-phase. On the basis of the material's extreme susceptibility to preferred orientation (see figure 4.2.5), it can be concluded that the spinel phase is a minor component. This view is supported by the low temperature neutron diffraction which shows strong antiferromagnetic ordering at 10 K. The isostructural precursor, α-$NaFeO_2$, has an antiferromagnetic transition temperature of about 11 K (Ichida, Shinjo, Bando

and Takada 1970). This difference in T_N can be attributed to $LiFeO_2$ having a smaller lattice volume.

The magnetic structure of $LiFeO_2$ is remarkably similar to that of 1T-Li_2NiO_2. Both consist of ferromagnetically ordered layers of metal atoms with antiferromagnet coupling between the consecutive sheets. The main difference between the two magnetic structures is that in 1T-Li_2NiO_2 the spins are aligned parallel to the c-axis while in $LiFeO_2$ the spins align perpendicular to the c-axis. Although $LiFeO_2$ has a cubic-close-packed structure and 1T-Li_2NiO_2 is composed of hexagonally-close-packed layers, the structures are similar in that they both consist of sheets of transition metal cations well isolated from each other by a thick oxygen-lithium-oxygen sandwich. This gives the structures distinctly two-dimensional character. Similar types of magnetic ordering occur in the trigonal transition metal halides such as $NiCl_2$, $CoCl_2$, $FeCl_2$, $CoBr_2$, and $FeBr_2$ (Goodenough 1963). These structures are formed from three layer, halide - transition metal - halide sandwiches stacked perpendicular to the trigonal c-axis and held together by rather weak Van der Waals bonding. The chlorides have a $CdCl_2$ structure with cubic-close-packed layers which is related to the 3R-structure by filling the octahedral sites of the Van der Waals gap with lithium atoms. The bromides have hexagonally -close-packed layers to which 1T-Li_2NiO_2 is related by filling the tetrahedral sites between the layers with lithium atoms.

Since O^{2-} is a considerably smaller anion that Cl^- and Br^-, the near neighbour distance in the layered transition metal oxides will be smaller than in the halides. The next nearest neighbour distances will be longer in the lithiated metal oxides than in the metal halides. Consequently, it is expected that the near neighbour interactions will have a respectively greater influence on the magnetic ordering than the next nearest neighbour interactions in the oxides than in the halides. However, the ordering in $LiFeO_2$ seems to be opposed to this logic.

The rhombohedral $LiFeO_2$ structure is made up of almost regular FeO_6 octahedra with bonding angles of 92.2°, 87.8° and 179.9°, and a bond distance of 2.051 Å. The FeO_6 octahedra form layers normal to the rhombohedral axis by sharing faces. In $LiFeO_2$ the nearest neighbour and next nearest neighbour Fe - Fe distances are 2.956(1) Å and 5.120(2) Å, respectively. The Fe - O - Fe bond angle for nearest neighbour interaction is 92.2°. The oxygen bond length in $LiFeO_2$ confirms that the Fe^{3+} ions are in the high spin state and have the configuration $t_{2g}^3e_g^2$. According to the Goodenough-Kanamori rules (Goodenough 1963), the 90 ° $3d^5$-O-$3d^5$ interaction will occur via overlap of the half-filled t_{2g} orbitals of the cations and anti-ferromagnetic ordering is expected. However, the only magnetic ordering model which resulted in a reasonable fit to the low temperature neutron diffraction pattern of $LiFeO_2$ requires ferromagnetic ordering within the Fe^{3+} layers. Ferromagnetic interactions in 90 ° $3d^5$-O-$3d^5$ bonds have been observed previously. The best known cases are MnO, which has a rock-salt structure, and rutile MnF_2. In MnO ferromagnetic ordering is

observed in the sheets of Mn^{2+} perpendicular to the 3-fold axis with successive metal layers coupled antiferromagnetically. The strongest magnetic interaction in MnO is the 180° Mn - O - Mn superexchange for which the Goodenough-Kanamori rules require antiferromagnetic odering. In MnO, the stronger requirement for antiferromagnetic ordering between the manganese layers, apparently overwhelms the weaker 90 ° Mn - O - Mn interaction. Although the overall ordering in MnF_2 is antiferromagnetic, nuclear magnetic resonance experiments (Owen, Brown, Coles and Stevenson 1962) have shown that the 90 ° Mn - F - Mn interactions along the c-axis are ferromagnetic. Goodenough attributed this to stronger than expected $\rho\sigma$, $\rho\sigma$ correlation superexchange (Goodenough 1963). The 90 ° exchange through oxygen between face-sharing iron atoms is also ferromagnetic in compounds such as β-$Fe_2(PO_4)O$ in which Fe^{2+} and Fe^{3+} share a common site (Ijjaali *et al* 1990). This is because the easiest electron to transfer from high spin Fe^{2+} to a neighbouring Fe^{3+} is the minority spin electron. This mechanism maintains the maximum exchange energy and is only possible if the two ions are aligned ferromagnetically.

The refinement of the room temperature neutron diffraction pattern of $LiFeO_2$ (chapter 4) indicated that there is a small degree of cation mixing on the 3a and 3b crystallographic sites. The occupancy refinement also suggested that the sample studied is slightly deficient in lithium and has a stoichiometry of $Li_{0.96}Fe_{1.04}O_2$. The presence of Fe^{2+} on the 3a sites and of either Fe^{3+} or Fe^{2+} on the 3b sites could have a strong influence on the magnetic ordering. The 3a and

3b sites are separated by a distance of 2.963(1) Å at an angle of 176.8° through the intervening oxygen. For high spin $3d^5$ ions, the 180 ° cation - anion - cation superexchange is strong and antiferromagnetic for both another $3d^5$ cation and a $3d^6$ cation such as Fe^{2+}.

Electrochemical studies on $LiFeO_2$ found that the material could not be oxidized within the potential stability range of electrolytes commonly used in lithium ion batteries. This behaviour could be due either to a very high oxidation potential or to poor electronic conductivity.

7.3 1T-Li_2NiO_2

The magnetic behaviour of 1T-Li_2NiO_2 is best described by division into two regimes, long range antiferromagnetic order for T < about 60 K and short range ferromagnetic order for T > 60 K. The long range antiferromagnetic state is well characterized by the neutron powder diffraction data. The magnetic structure consists of ferromagnetic sheets coupled antiferromagnetically with a moment direction parallel to the c-axis and a moment value close to 2.0 μ_B. The ordering onset temperature from the neutron data, T_N = 57 to 60 K, is a bit lower than the temperature of the maximum value of M/H, but this is not unusual.

The dc-magnetization measurements on 1T-Li_2NiO_2 at applied fields up to 2.0 Tesla indicate antiferromagnetic ordering with a T_N of 64 K. Somewhere between 2.0 Tesla and 5.0 Tesla a metamagnetic transition occurs such that by 5.0 Tesla the magnetic behaviour is dominated by short range ferromagnetic

coupling. Even in the low field range, up to 2.0 Tesla, there is clear evidence of ferromagnetic correlations in the magnetic data collected at or above 65 K.

These results can be compared to those for the anhydrous dichlorides of the first row transition metals e.g. $FeCl_2$, $CoCl_2$ and especially $NiCl_2$. These materials have the layer-type $CdCl_2$ structure which is similar to that of 1T-Li_2NiO_2. The three dihalides mentioned have strong ferromagnetic intraplanar exchange and weak interplanar antiferromagnetic exchange (Starr *et al* 1940, Bizette *et al* 1956 and Birgeneau *et al* 1972). At zero applied field the ground state magnetic structures consist of antiferromagnetically coupled ferromagnetic layers as found for 1T-Li_2NiO_2 (Wilkinson *et al* 1959 and Billerey *et al* 1977). All show metamagnetic transitions at low temperatures. For example the critical field for $FeCl_2$ at 4.2 K is 1.1 Tesla (Jacobs and Lawrence 1967). Of the group $NiCl_2$ has the highest antiferromagnetic transition temperature of 52 K, remarkably close to the 65 K reported here for 1T-Li_2NiO_2. Presumably, the strong intraplanar ferromagnetic correlations result from the 90° M-Cl-M linkages. Evidence for the presence of short range ordered ferromagnetic clusters above the long range ordering temperature has been found in $FeCl_2$ from small angle neutron scattering (Billerey *et al* 1977). Similar short range order is reported here for 1T-Li_2NiO_2. The main difference between $NiCl_2$ and 1T-Li_2NiO_2 is the preferred direction for the Ni^{2+} moments which is normal to the c-axis in the former and parallel to the c-axis in the latter.

7.4 $Li_2Ni_yMn_{2-y}O_4$

During the course of this work, studies on the structure and electrochemistry of solid solution phases of $Li_xMn_yNi_{1-y}O_2$ were reported by Rossen, Jones and Dahn (1992). They reported single phase compositions for $0 \leq y \leq 0.5$ and x near 1. Their samples were prepared in air or oxygen at temperatures between 500 and 900 °C. The lattice parameters of crystallographic unit cells for all their samples were quite close to those of $LiNiO_2$ and did not vary smoothly with changes in the nickel manganese ratio. The authors explained this by proposing that the manganese cations are in a low spin 3+ state. Since the crystal ionic radii of low spin Ni^{3+} at 0.70 Å and low spin Mn^{3+} at 0.72 Å are very similar little change in the lattice parameters would be expected with increasing manganese composition. However even a difference of 0.02 Å in the crystal ionic radius should result in a significant change in the lattice parameters of the crystallographic unit cell when the Ni/Mn ratio is close to one. The authors themselves note that the x-ray diffraction patterns indicate that their samples contains contain $LiMnO_2$, $LiMn_2O_4$ and in some cases Li_2MnO_3 as impurities. In the synthesis conditions used, compounds containing Mn^{3+} would tend to oxidize to Mn^{4+}. Since the x-ray data were collected using a copper anode source, the peaks from manganese containing compounds would be severely diminished in intensity by fluorescence. Consequently the concentrations of manganese containing impurities would be greater than the

relative intensities of the associated peaks would suggest. In their electrochemical studies of these samples, the discharge capacities decrease linearly with increasing manganese composition. An addition study with purer samples is clearly justified.

In the lithium nickelate, $LiNiO_2$, the ordering of the cations is generally less than perfect. That is some lithium ions are found in the "nickel" layer and some nickel atoms are found in the "lithium" layer. (Pickering, Lewandowski, Jacobson and Goldstone 1992) In addition, even with very careful preparation the Li/Ni ratio is generally slightly less than 1.0, so a small amount of Ni^{2+} is also present. Li, Reimers and Dahn [1992] determined the unit cell dimensions and ordering parameters of $Li_xNi_{2-x}O_2$ for a broad range of x. They found that the crystallographic lattice expands in all directions as x decreases form near 1 to about 0.2 and the ordering of the lithium and nickel cations into separate layers also decreases. For example they found $Li_{0.9}Ni_{1.1}O_2$ to have a hexagonal unit cell of dimensions a = 2.8854(1) Å and c = 14.213(1) Å with about 2 % of the lithium atoms located in the "nickel" layer and 11 % of the nickel atoms in the "lithium" layer.

The samples of $Li_2Ni_yMn_{2-y}O_4$ in this work were prepared in an inert atmosphere to prevent further oxidation of the Mn^{3+}. Single phase compounds were only obtained for Mn/Ni ratios between 1 and about 0.21. The x-ray diffraction patterns of the phases with Mn/Ni ratios less than 1 indicated that these compositions had a substantial degree of cation mixing between the

lithium ions and the transition metal ions. Consequently, they have structures which lie between a cation ordered and a disordered NaCl type phase. Two samples of nominal composition Li_2NiMnO_4 were examined by neutron powder diffraction. The diffraction patterns of both samples were refined by Rietveld profile analysis to acceptable R-factors using a model isostructural to 3R-$LiNiO_2$, in which the nickel and manganese cations were assumed to randomly share the same sites. The Rietveld analysis showed that both samples contain less lithium than the target composition, Li_2NiMnO_4, and that there is considerable mixing between the lithium and transition metal layers. The only experimentally significant difference between the two refinements is in the lattice parameters with sample B having significantly larger unit cell dimensions than sample A. This may be due to a difference in the degree of cation ordering between the 3a and 3b sites, or to a small difference in the composition, but the large standard deviation in the refinement of the site occupancies makes it impossible to be certain. Since both samples were prepared in the same manner and from the same precursors, the difference must be due to relatively subtle changes in their preparation. The Rietveld refinement indicates a composition of $Li_{1.8}M^{2+}_{0.4}M^{3+}_{1.8}O_4$ which can also be expressed as $Li_{0.9}M^{2+}_{0.2}M^{3+}_{0.9}O_2$ to facilitate comparison with previous studies. Table 7.4.1 provides a comparison of lattice parameters and bond distances in the two samples of $Li_{1.8}Ni_{1.1}Mn_{1.1}O_4$ with those of related phases. The two samples of composition $Li_{1.8}Ni_{1.1}Mn_{1.1}O_4$ have larger unit cell dimensions than $Li_{0.9}Ni_{1.1}O_2$, or even $Li_{0.8}Ni_{1.2}O_2$, consistent with Mn^{3+}

having a larger crystal radius than Ni^{3+}. Both samples A and B also have larger lattice parameters than the $LiNi_{0.7}Mn_{0.3}O_2$ and $Li_{1.1}Ni_{0.5}Mn_{0.5}O_2$ samples prepared and studied by Rossen, Jones and Dahn (1992), which is surprising since these compositions contain more of the larger cation, lithium.

Table 7.4.1 - Comparison of Bond Lengths in "Li_2NiMnO_4" to Related Phases

Composition	Lattice Parameters		Bond Distances (Å)		Reference
	a (Å)	c (Å)	3a - 6c	3b - 6c	
$Li_{1.8}Ni_{1.1}Mn_{1.1}O_4$	2.8910(4)	14.332(3)	1.988(6)	2.121(7)	Sample A
$Li_{1.82}Ni_{1.09}Mn_{1.09}O_4$	2.8984(4)	14.348(3)	1.992(7)	2.125(8)	Sample B
$LiNi_{0.7}Mn_{0.3}O_2$	2.878	14.22	1.9770	2.1090	Rossen *et al*
					(1992)
$Li_{1.1}Ni_{0.5}Mn_{0.5}O_2$	2.870	14.20	1.9718	2.1038	Rossen *et al*
					(1992)
$LiNiO_2$	2.8762(1)	14.190(1)	1.9741(2)	2.1073(3)	Li *et al*
					(1992)
$Li_{0.9}Ni_{1.1}O_2$	2.8854(1)	14.213(1)	1.9811(2)	2.1111(3)	Li *et al*
					(1992)
$Li_{0.8}Ni_{1.2}O_2$	2.8898	14.220	1.9860(4)	2.1106(4)	Pickering *et al*
					(1992)

To properly compare the transition metal to oxygen bond distances it is necessary to correct for the lithium occupancy in both the 3a and 3b sites. Table 7.4.2 lists the contribution of the transition metal cations to the average oxygen bond distances for both the 3a and 3b sites. These values were calculated using the refined, or reported, cation occupancies and assumed that lithium has an average oxygen bond distance of 2.14 Å.

The crystal radii of O^{2-}, Li^{+}, low spin Ni^{3+}, low spin Mn^{3+}, Ni^{2+}, and low spin Mn^{2+} in six-fold coordination are 1.26, 0.88, 0.70, 0.72, 0.83 and 0.81 Å, respectively (Shannon and Prewitt 1969 and 1970). In six-fold coordination, low spin Ni^{3+} - oxygen and low spin Mn^{3+} - oxygen should have average bond

distances of 1.96 Å and 1.98 Å, respectively, and Ni^{2+} - oxygen and low spin Mn^{2+} - oxygen distances are expected to be 2.09 Å and 2.07 Å, respectively.

The bond distances of the 3a sites in the two samples of $Li_{1.8}Ni_{1.1}Mn_{1.1}O_4$ are consistent with both Ni^{3+} and Mn^{3+} being in the low spin state. High spin state Ni^{3+} and Mn^{3+} with crystal radii of 0.74 and 0.79 Å, respectively, (Shannon and Prewitt 1969) would be too large for the 3a site. The 3a site is also too small to have a significant amount of either Ni^{2+} or Mn^{2+}. The 3b sites of $Li_{1.8}Ni_{1.1}Mn_{1.1}O_4$ samples are large enough for the transition metal cations present to be mostly Ni^{2+} and Mn^{2+}. Thus in $Li_{1.8}Ni_{1.1}Mn_{1.1}O_4$, the M^{2+} cations tend to order on the larger 3b cation site. Table 7.4.2 provides a comparison to the transition metal cation's contribution to the bond distances in the related phases. In all cases the bonding of the 3b site is too small for Ni^{3+}, Mn^{3+}, or even Mn^{4+}, with a crystal radius of 0.680 Å (Shannon and Prewitt 1969). The bonding of the 3a sites in the two phases studied in detail by Rossen *et al* (1992) is also too small for even low spin Mn^{3+} but might be explained by the presence of Mn^{4+}. This further suggests that the samples of $Li_xNi_yMn_{1-y}O_2$ used in the study of Rossen *et al* (1992) were multi-phase.

Table 7.4.2 - Comparison of transition metal bonding in "$Li_2Ni_yMn_{2-y}O_4$" phases.

	$Li_{1.8}Ni_{1.1}Mn_{1.1}O_4$		$LiNi_{0.7}Mn_{0..3}O_2$	$Li_{1.1}Ni_{0.5}Mn_{0.5}O_2$	$Li_{0.9}Ni_{1.1}O_2$
Reference	Sample A	Sample B	Rossen *et al*	Rossen *et al*	Li *et al*
			(1992)	(1992)	(1992)
Site 3a					
Mole Fraction					
[M] 3a	0.85(4)	0.80(5)	0.91	0.85	0.983(8)
[Li] 3a	0.15(4)	0.20(5)	0.09	0.15	0.017(8)
Bond Lengths					
3a - 6c (Å)	1.988(6)	1.992(7)	1.977	1.972	1.9811(2)
M - O (Å)	1.96(1)	1.96(1)	1.961	1.943	1.978(1)
Site 3b					
Mole Fraction					
[M] 3b	0.25(4)	0.29(5)	0.12	0.07	0.085(3)
[Li] 3b	0.75(4)	0.71(5)	0.88	0.93	0.915(3)
Bond Lengths					
3b - 6c (Å)	2.121(7)	2.125(8)	2.109	2.104	2.1111(3)
M - O (Å)	2.06(1)	2.09(1)	1.882	1.629	1.857(4)

The preliminary electrochemical evaluation of Li_2NiMnO_4 as a thick electrode in a lithium ion cell with a coke anode showed that it can be electrochemically cycled over about half its original lithium composition. The potential curve is not as smooth in slope as in comparative coke/$LiCoO_2$ cells and lies at a lower voltage. The chemistry of the lithium cycling processes in Li_2NiMnO_4 has not been studied yet.

$Li_2Ni_{1.5}Mn_{0.5}O_4$ was also evaluated as a cathode in a lithium ion cell and found to be electrochemically inactive under typical cell cycling conditions. The poor electrochemical performance is due to the lack of clear pathways for lithium ion mobility in a phase in which the cations are less ordered.

7.5 $Li_2Cr_yMn_{2-y}O_4$

Phases in the solid state solution series $Li_2Cr_yMn_{2-y}O_4$ were prepared as single phase compounds over the range $0 < y < 2$. These represent a series of new compounds. The unit cell volume decreases smoothly with increasing chromium content as Cr^{3+}, with a smaller ionic radius, is substituted for Mn^{3+}. The x-ray powder diffraction patterns of phases in the range $1.4 \leq y < 2$ are similar to that of $LiCrO_2$ with the exception that the reflections are shifted to lower diffraction angles, corresponding to larger unit cell size. The magnitude of the shift increases as y decreases from 2 to 1.4. The x-ray powder diffraction patterns of $Li_2Cr_yMn_{2-y}O_4$ phases over the range $0 < y \leq 1.3$ resemble the diffraction pattern of λ-$Li_2Mn_2O_4$, which has a tetragonal unit cell with an

atacamite-type structure. Although the structure of these phases has not been determined in detail, the x-ray diffraction patterns can be approximately indexed to tetragonal unit cells with dimensions slightly smaller than λ-$Li_2Mn_2O_4$. High resolution Guinier diffraction on well crystallized samples demonstrated that the materials actually have orthorhombic or monoclinic symmetry, depending on the composition. However, the a and b axes have only slightly different dimensions and monoclinic angle, β, is not far from 90 °. Poorly crystallized samples such as those used in electrochemical studies have broad peaks which can be indexed to tetragonal unit cells.

The use of related phases such as $LiMn_{2-x}Cr_xO_{4.35}$ with x ~ 0.2 - 0.4 (Pistoria, Wang and Wang 1992), and $LiCr_xMn_{2-x}O_4$ where 0 < x < 1 (Wang, Xia, Li and Zhao 1992) as cathodes in secondary lithium batteries which have a metallic lithium anode have been described previously. In the latter case, electrochemical insertion of one mole equivalent of lithium into $LiCr_xMn_{2-x}O_4$ would result in a phase of the same stoichiometry, although not necessarily the same structure, as one of those described here. However, the authors only managed to electrochemically insert about 0.4 mole equivalents of lithium.

$LiCrO_2$, olive green in colour, is too poor an electronic conductor to be useful in an electrochemical cell. Doping with a small amount of Mn (10 % or perhaps less) dramatically improves the material's electronic conductivity as evidenced by its colour. Both $LiMn_2O_4$ and λ-$Li_2Mn_2O_4$ have been used as cathodes in lithium ion cells. λ-$Li_2Mn_2O_4$ has twice the nominal capacity of

$LiMn_2O_4$ but it is reported to be hygroscopic and metastable (Mosbah, Verbaere and Tournoux 1983). λ-$Li_2Mn_2O_4$ converts to the orthorhombic form, $LiMnO_2$, at about 500 °C. It is prepared by electrochemically, or chemically, intercalating lithium into the $LiMn_2O_4$ spinel structure.

Substituting Cr^{3+} for Mn^{3+} in $Li_2Mn_2O_4$ with Cr was found to stabilize the lambda structure. $Li_2Cr_yMn_{2-y}O_4$ with $0.1 \leq y \leq 1.3$, which can be prepared at 1000 °C, is less tetragonally distorted than λ-$Li_2Mn_2O_4$ but otherwise structurally similar. However, $Li_2Cr_yMn_{2-y}O_4$ with $0.1 \leq y \leq 1.3$ is simple to prepare, and is air and thermally stable. Greater chemical stability often results in enhanced safety in electrochemical cells.

Phases of $Li_2Cr_yMn_{2-y}O_4$ were formed into cathodes and evaluated in lithium ion cells with coke based anodes. The electrochemical potential of $Li_2Cr_yMn_{2-y}O_4$ varies more smoothly with state of charge than does the potential of λ-$Li_{2-x}Mn_2O_4$ which has a distinct step at $x = 1$. $Li_2Cr_yMn_{2-y}O_4$ has a higher average discharge potential and energy density than λ-$Li_2Mn_2O_4$. The potentials and shapes of the charge/discharge cycles vary with composition in a regular manner over the full range of $Li_2Cr_yMn_{2-y}O_4$ compositions, $0.1 \leq y \leq 1.9$. Phases with the 3R structure, $1.4 \leq y \leq 1.9$, have capacities similar to isostructural $LiCoO_2$ in which only about half the lithium ions can be cycled reversibly. However, the cells with cathodes based on $Li_2Cr_yMn_{2-y}O_4$ in which $y > 1.5$ showed high internal impedance. This is presumably due to poorer electronic

conductivity as evidenced by a lightening in the colour of the compounds as the chromium content is increased. Phases with the lithiated spinel structure, $0.1 \leq y \leq 1.3$, have larger discharge capacities. In fact, $Li_2Cr_{0.1}Mn_{1.9}O_4$ can be reversibly cycled over 75% of its theoretical capacity.

Chapter 8

Conclusions

It has been demonstrated for the first time, in this work, that cathodes based on the high temperature orthorhombic form of $LiMnO_2$ have good capacity and cycle life. X-ray diffraction and electrochemical studies have revealed that cathodes prepared from orthorhombic $LiMnO_2$ undergo a structural change on being charged beyond a certain potential in which the original structure is converted to spinel $Li_{1-x}Mn_2O_4$. High temperature orthorhombic $LiMnO_2$ has long term stability in ambient conditions, is easily prepared in a one step reaction, and consequently, proves to be a practical and convenient precursor to λ-$Li_2Mn_2O_4$ in lithium ion cells.

Orthorhombic $LiMnO_2$ can be cycled over a large composition range (about 90 % of its theoretical capacity), but about 25% of this capacity is delivered below 2.5 volts versus metallic lithium. In a lithium ion cell, the $LiMnO_2$ cathode capacity below 2.5 volts is a good match to the irreversible capacity needed to passivate the carbon anode. However, improved anode/electrolyte formulations may, in future, lessen the capacity loss due to anode passivation. Since the capacity below 2.5 volts is not as sensitive to rate as the capacity of

the 2.9 volt plateau, the lower voltage capacity is believed to be due to the formation of a metastable phase which is richer in lithium than the bulk of the cathode, such as Li_2MnO_2.

The kinetics of the initial phase transition to the spinel form and of re-insertion of the last 25% or so of the Li^+ ions into the λ-$Li_{2-x}Mn_2O_4$ structure are undesirably slow. In the spinel phase $LiMn_2O_4$, small modifications to the stoichiometry have been shown to have a dramatic affect on the electrochemical performance in the 4 volt region (Guo and Dahn 1996). Clearly, similar studies on the orthorhombic phase are warranted. Alternatively, using a slightly higher temperature for the first forming cycle or preparing the material as crystallites of smaller size might improve the kinetics of both the phase conversion and the re-insertion process.

The magnetic properties of orthorhombic $LiMnO_2$ were investigated in detail for the first time. The lack of Curie-Weiss behaviour in the susceptibility even up tp 350 K indicates the importance of short range magnetic correlations. As the temperature is lowered a long range order grows at the expense of the short range correlations. At a Neel temperature ot 261.5 K an antiferromagnetic order sets in. The magnetic structure was solved from neutron diffraction data and has a magnetic propogation vector of k = (1/2 1/2 1/2) and a magnetic moment of 3.65(2) Bohr magnetons with a preferred direction parallel to the b-axis. The neutron diffracton data also provided evidence of two dimensional correlations above T_c at 271 K in the presence of a Warren line shape feature at

a lower diffraction angle than the Bragg magnetic reflections. The complex behaviour in the relatively simple material, $LiMnO_2$ is due to the distortion of the ordered NaCl type structure by the presence of the Jahn-Teller ion, Mn^{3+}. Crystallographic distortions due to the presence of Mn^{3+} result in a Mn sublattice which is strongly coupled along the a-axis and a folded, distorted hexagonal symmetry normal to the c-axis. This results in short range correlations which persist to temperatures in excess of 350 K. The details of the magnetic behaviour are consistent with the expectation that intrachain coupling along the a-axis will be the strongest interaction and antiferromagnetic, and that the structure will evolve by interchain coupling to form layers and finally, interlayer coupling.

$LiFeO_2$ prepared at low temperature by ion exchange has proven to be another example of a material which can exist in both the layered 3R structure and the cubic lithiated spinel structure. Powder diffraction techniques are only able to distinguish between the two structures when there is a significant deviation from the idea close packed structure. The three techniques applied to distinguishing between the two structural models: transmission electron microscopy, forced crystallite alignment, and low temperature magnetic neutron scattering, yielded apparently conflicting conclusions. The results are reconciled by concluding that the $LiFeO_2$ sample contains both crystallites with the 3R structure and with the lithiated spinel structure.

A sample of a low temperature form of Li_2NiO_2 was prepared by Dr. Ulrich von Sacken and C. A. Michal of Moli Energy (1990) Ltd. and Dr. Jeff Dahn then, at Simon Fraser University, by careful chemical lithiation of $LiNiO_2$. Refinement of room temperature neuton diffraction data confirmed their expectation that this phase has a 1T, Li_2VSe_2 type structure, with nearly ideal hexagonal-close-packing.

The magnetic behaviour of 1T-Li_2NiO_2 was examined by dc magnetization measurements and low temperature neutron diffraction. The magnetic structure, refined from low temperature neutron diffraction data, has a magnetic propogation vector k = (0 0 1/2) and a magnetic moment of 1.4(5) Bohr magnetons with a perferred direction parallel to the c-axis. The low temperature magnetic structure is formed by antiferromagnetic coupling of alternate, ferromagnetically aligned, nickel layers, lying normal to the c-axis. The dc magnetization measurements showed an applied field and temperature dependence indicative of a competition between long range antiferromagnetic ordering and short range ferromagnetic coupling, resulting in a metamagnetic transition at an applied field strength somewhere between 2.0 and 5.0 Tesla. The dc-magnetization measurements at 2.0 Tesla indicate antiferromagnetic ordering with a T_N of 64 K, but at temperatures greater than 65 K there is clear evidence of ferromagnetic correlations. The behaviour of 1T-Li_2NiO_2 is similar to that of the structurally related transition metal dichlorides, $FeCl_2$, $NiCl_2$ and $CoCl_2$.

Within the series $Li_2Ni_yMn_{2-y}O_4$ only the composition with y = 1 was investigated in detail. This phase has a rhombohedral, ordered NaCl structure like $LiCoO_2$ and $LiNiO_2$. However, in Li_2NiMnO_4 the cation ordering is not ideal and there is some mixing between the lithium and transition metal layers. A Rietveld refinement of neutron diffraction data also showed that the samples prepared for this study were slightly deficient in lithium. An analysis of the bond lengths in Li_2NiMnO_4 confirmed an earlier study's proposal that both the Ni^{3+} and Mn^{3+} are in the low spin state. Li_2NiMnO_4 was the only composition which showed reversible electrochemical behaviour.

This thesis presented a new series of compounds, $Li_2Cr_yMn_{2-y}O_4$, wherein $0.1 \leq y \leq 1.9$. This series consists of two solid solutions regions with a cross-over occurring at a composition near y = 1.4. The chemical structure of these phases was identified by x-ray powder diffraction. Phases with $y \geq 1.4$ are iso-structural to the end member of the solid solution, $LiCrO_2$, in which the lithium and transition metal cations form alternating layers normal hexagonal c-axis to the between the sheets of cubic-close -packed oxygen atoms. These phases showed that substituting a small amount of manganese (10% or perhaps less) for chromium in $LiCrO_2$ dramatically changes the material's colour and electrochemical activity. The phases with $y < 1.4$ are essentially iso-structural to the other end member of the solid state solution λ-$Li_2Mn_2O_4$ in which the lithium ions and transition metal ions are arranged in interleaving chains within the cubic-close-packed oxygen framework. The resulting structures are distorted

from cubic symmetry, as is λ-$Li_2Mn_2O_4$, by the presence of the Jahn-Teller ion, Mn^{3+}. Although electrochemically useful, λ-$Li_2Mn_2O_4$ is metastable must be prepared by chemically, or electrochemically, intercalating lithium ions into $LiMn_2O_4$. It can not be prepared by direct solid state chemical reaction, and once synthesized, it is not stable in ambient conditions. $Li_2Cr_yMn_{2-y}O_4$ phases with the λ-$Li_2Mn_2O_4$ type structure are prepared by high temperature solid state reaction and are both thermodynamically and air stable. These phases demonstrate that substituting even a small amount of chromium for manganese in λ-$Li_2Mn_2O_4$ stabilizes the structure. $Li_2Cr_yMn_{2-y}O_4$ phases have been shown to be practical materials for use as cathodes in lithium ion cells. The compositions with $y < 1.65$ were found to be particularly useful as cathodes in lithium ion type, electrochemical cells. These phases have electrochemical capacities comparable to, or better than, the materials presently being used in commercial lithium ion batteries. The enhanced thermal stability of $Li_2Cr_yMn_{2-y}O_4$ phases relative to λ-$Li_2Mn_2O_4$ may also improve the safety of lithium ion cells.

Bibliography

Alperin H. A., *J. Phys. Soc. Japan* , **17**, Suppl. B-111, 12 (1962).

Anderson J. C. and Schieber M., *J. Phys. Chem. Solids* , **25**, 961 (1964).

Bacon G. E., *"Neutron Diffraction"*, pp. 227-228, Clarendon Press, Oxford (1975).

Bertrand J. A., Ginsberg A. P., Kaplan R. I., Kirkwood C. E., Martin R. L. and Sherwood R. C., *Inorganic Chemistry* , **10**, 240 (1971).

Billerey D., Terrier C., Mainard R. and Meriel P., *Comptes Rend. Ser. B*, **284**, 495 (1977).

Birgeneau R. J., Yelon W. B., Cohen E. and Makovsky J., *Phys. Rev.* , **B5**, 2607 (1972).

Bizette H., Terrier C. and Tsai B., *Compt. Rend.* , **243**, 895, 1295 (1956).

Bongers P. F., *Thesis*, Univ. of Leiden, (1957).

Clearfield A., *Ann. Rev. Mater. Sci.* , **14**, 205 (1984).

Dahn J. R., von Sacken U. and Michal C. A., *Solid State Ionics* , **44**, 87 (1990).

Dahn J. R., Sleigh A. K., Shi H., Reimers J. N., Zhong Q., and Way B. M., *Electrochimia Acta*, **38**, 1179 (1993).

David W. I. F., Goodenough J. B., Thackeray M. M. and Thomas M. G. S. R., *Revue de Chimie Minerale* , **20**, 636 (1983).

David W. I. F., Thackeray M. M., De Picciotto L. A. and Goodenough J. B., *J. Solid State Chem.*, **67**, 316 (1987).

Davidson I. J. and Greedan J. E., *J. Solid State Chem.* **51**, 104 (1984).

Davidson I., Greedan J. E., von Sacken U., Michal C. A. and Dahn J. R., *Solid State Ionics* , **46**, 243 (1991).

Davidson I. J., Greedan J. E., von Sacken U., Michal C. A. and McKinnon W. R., *J. Solid State Chem.*, **105**, 410 (1993).

Delmas C. and Saadoune I., *Solid State Ionics*, (1992).

Famery R., Bassoul P. and Queyroux F., *J. Solid State Chem.*, **57**, 178 (1985).

Goodenough J. B., *"Magnetism and the Chemical Bond"*, Interscience, New York (1963).

Greedan J. E. and O'Reilly A. H., *Physical Review* , **B35**, 8770 (1987).

Greedan J. E., Raju N. P. and Davidson I. J., submitted to *J. Solid State Chem.*, July 1996.

Guo Y. and Dahn J. R., *J. Electrochem. Soc.*, **143**, 100 (1996).

Gummow R. J., Liles D.C. and Thackeray M. M., *Mat. Res. Bull.*, **28**, 1249 (1993).

Guyomard D. and Tarascon J. M., *J. Electrochem. Soc.*, **139**, 937 (1992).

Hewston T.A. and B. L. Chemberland, *J. Phys. Chem. Solids* , **48**, 97 (1987).

Hill R. J. and Howard C. J., *Program forRietveld Analysis of Fixed Wavelength X-ray and Neutron Powder Diffraction Patterns - Version LHPM 1*, AAEC (Lucas Heights Research Laboratories, N.S.W., Australia).

Hirakawa K. and Kadowaki H., *Physica* , **136B**, 335 (1986).

Hoppe R., Brachtel G. and Jansen M., *Z. Anorg. Allg. Chem.*, **417**, 1 (1975).

Ichida T., Shinjo T., Bando Y. and Takada T., *J. Phys. Soc. Japan*, **29**, 795 (1970).

Ijjaali M., Malaman B., Gleitzer C., Warner J. K., Hriljac J. A. and Cheetham A. K., *J. Solid State Chem.*, **86**, 195 (1990).

Izumi F., *Rietan - Rietveld Analysis System,* National Institiute for Research in Inorganic Materials, 1-1 Namiki, Tsukuba-shi, Ibaraki 305, Japan (1989).

Jacobs I. S. and Lawrence P. E., *Phys. Rev.* , **164,** 866 (1967).

Johnston W. D. and Heikes R. R., *J. Am. Chem. Soc.* , **78**, 3255 (1956).

Kittel C., *"Introduction to Solid State Physics"*, Wiley, New York (1976).

Kondoh H., *J. Phys. Soc. Japan* , **15**, 1970 (1960).

Kordes V. E. and Petzoldt J., *Zeit. Anorganische und Allgemeine Chemie*, **335**, 138 (1965).

Li W., Reimers J. N. and Dahn J. R., *Phys. Rev. B*, **46**, 3236 (1992).

Mosbah A., Veraere A. and Tournoux M., *Mater. Res. Bull.*, **18**,1375 (1983).

Murphy D. W. and Christian P. A., *Science* , **205**, 651 (1979).

Ohzuku T., Kitagawa M., and Hiria T., *J. Electrochem.Soc*. (1989).

Ohzuku T., Kitagawa M. and Hirai T., *J. Electrochem. Soc.*, **137**, 769 (1990).

Ohzuku T., Ueda A., and Hirai T., *Chem. Express*, **7**, 193 (1992).

Owen J., Brown M. R., Coles B. A. and Stevenson R. W. H., *J. Phys. Soc. Japan*, **17** Suppl. B-1, 428 (1962).

Pickering I. J., Lewandowski J. T., Jacobson A. J. and Goldstone J., *Solid State Ionics*, (1992).

Pistoria G., Wang G. and Wang C., *Solid State Ionics*, **58**, 285 (1992).

Reimers J. N. and Dahn J. R., *J. Electrochem. Soc.*, (1992).

Reimers J. N., Dahn J. R., Greedan J. E. , Stager C. V., Liu G., Davidson I., and von Sacken U., *J. Solid State Chem.* , **102**, 542 (1993).

Reimers J. N., Li W. and Dahn J. R., *Phys. Rev. Letters*, (1993).

Reimers J. N., Fuller E. W., Rossen E., and Dahn J. R., *J. Electrochem. Soc.*, **140**, 3396 (1993).

Rieck H. and Hoppe R., *Z. Anorg. u Allg. Chemie* , **392**, 193 (1972).

Rietveld H. M., *J. Appl. Cryst.*, **2**, 65 (1969).

Rossen E., Jones C. D. W. and Dahn J. R., *Solid State Ionics*, **57**, 311 (1992).

Roth W. L., *Physical Review* , **110**, 1333 (1958).

Shannon R. D. and Prewitt C. T., *Acta Crystallogr.*, **B25**, 925 (1969).

Shannon R. D. and Prewitt C. T., *Acta Crystallogr.*, **B26**, 1046 (1970).

Shirane G., *Acta Crystallogr.* , **12**, 282 (1959).

Shirane T., Kanno R., Kawamoto Y., Takeda Y., Takano M., Kamiyama T., and Izumi F., *Solid State Ionics*, **79**, 227 (1995).

Starr C., Bitter F. and Kaufmann A. R., *Phys. Rev.* , **58**, 977 (1940).

Takeda Y., Akagi J., Edagawa A., Inagaki M. and Naka S., *Mat. Res. Bull.*, **15** 1167 (1980)

Tarascon J. M. and Guymond D., *J. Electrochem. Soc.*, **138**, 2864 (1991).

Thackeray M. M., David W. I. F., Bruce P. G. and Goodenough J. B., *Mat. Res. Bull.*, **18**, 461 (1983).

Thomas J. M., *Phil. Trans. Roy. Soc.* , **277**, 251 (1974).

Tompson C. W., Mildner D. F. R., Mehregang M., Sudol J., Berliner R. and Yelon W. B., *J. Appl. Crystallogr.* , **17**, 385 (1984).

Wang B., Xia Y., Li F. and Zhao D., *J. Power Sources*, **43-44**, 539 (1993).

Wells A. F., *"Structural Inorganic Chemistry"*, Clarendon Press, Oxford (1975).

Werner P-E., Eriksson L. and Westdahl M., *J. Appl. Crystallogr.* , **18**, 367 (1985).

Whittingham M. S., *Prog. Solid State Chem.* , **12**, 41 (1978).

Wiles D. B. and Young R. A., *J. Appl. Crystallogr.*, **14**, 149 (1981).

Wilkinson M. K., Cable J. W., Wollan E. O. and Koehler W. C., *Phys. Rev.*, **113**, 497 (1959).

Wyckoff R. W. G., *Crystal Structures* (2nd edn.), Vol. 2, p. 312, Interscience, New York (1964).

IMAGE EVALUATION TEST TARGET (QA-3)

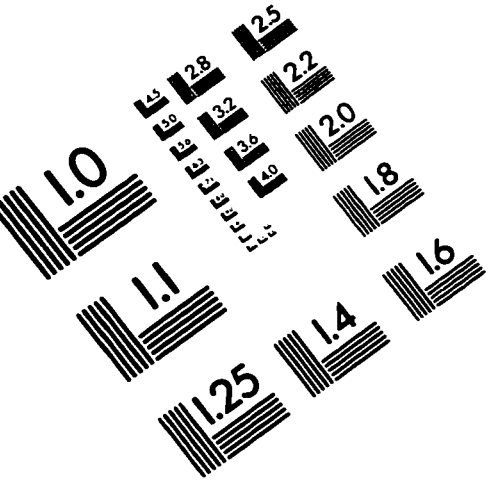

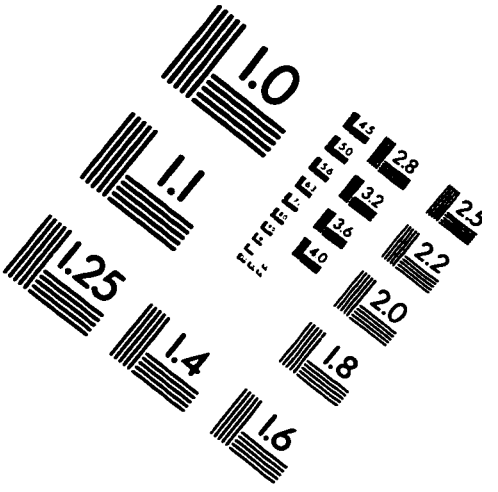

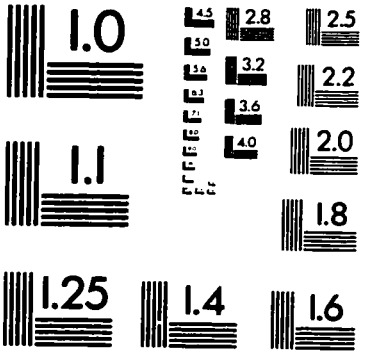

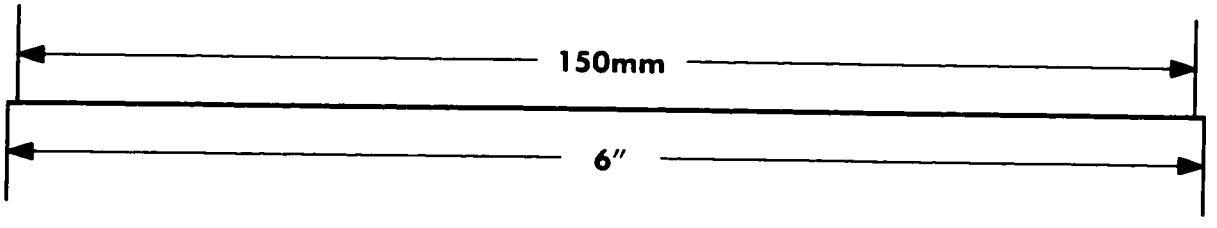

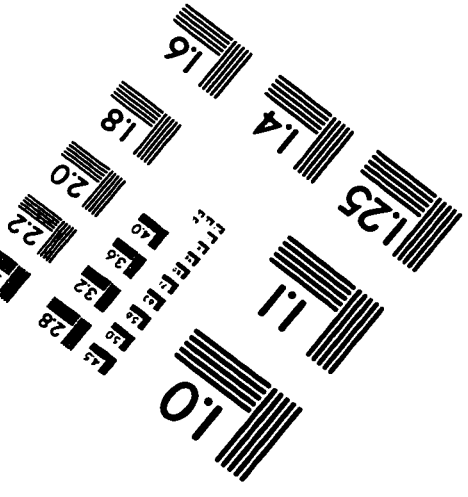

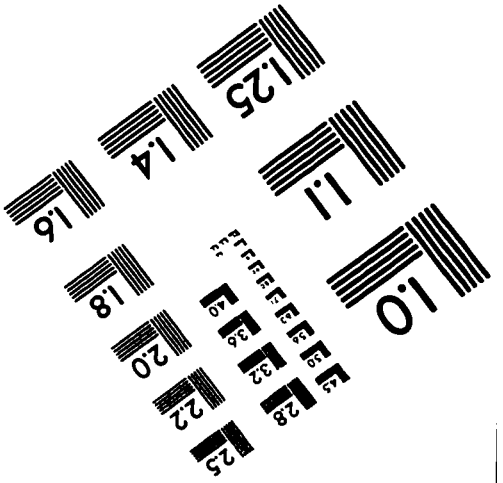

APPLIED IMAGE, Inc
1653 East Main Street
Rochester, NY 14609 USA
Phone: 716/482-0300
Fax: 716/288-5989